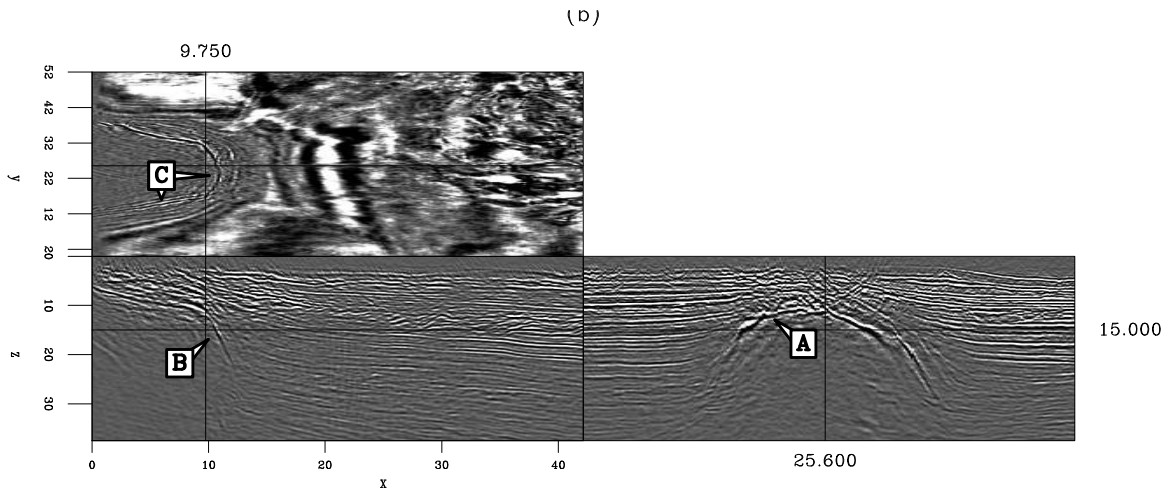
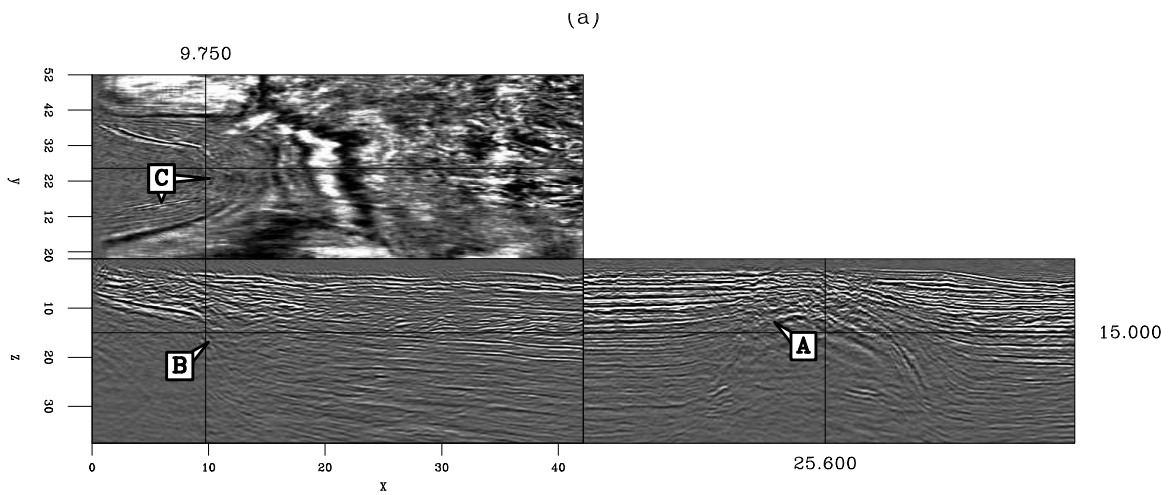


STANFORD EXPLORATION PROJECT

Gabriel Alvarez, Gboyega Ayeni, James Berryman, Biondo Biondi, Robert Clapp, Bill Curry, William Curry, John Etgen, Roland Günther, Claudio Guerra, Pierre Jouselin, Oliver Pell, Guojian Shan, Jeff Shragge, Yaxun Tang, Alejandro Valenciano, Madhav Vyas, and Ben Witten

Report Number 129, April 2007



Copyright © 2007

by the Board of Trustees of the Leland Stanford Junior University

Stanford, California 94305

*Copying permitted for all internal purposes of the Sponsors of
Stanford Exploration Project*

Preface

The electronic version of this report¹ makes the included programs and applications available to the reader. The markings [ER], [CR], and [NR] are promises by the author about the reproducibility of each figure result. Reproducibility is a way of organizing computational research that allows both the author and the reader of a publication to verify the reported results. Reproducibility facilitates the transfer of knowledge within SEP and between SEP and its sponsors.

ER denotes Easily Reproducible and are the results of processing described in the paper. The author claims that you can reproduce such a figure from the programs, parameters, and makefiles included in the electronic document. The data must either be included in the electronic distribution, be easily available to all researchers (e.g., SEG-EAGE data sets), or be available in the SEP data library². We assume you have a UNIX workstation with Fortran, Fortran90, C, X-Windows system and the software downloadable from our website (SEP makerules, SEPlib, and the SEP latex package), or other free software such as SU. Before the publication of the electronic document, someone other than the author tests the author's claim by destroying and rebuilding all ER figures. Some ER figures may not be reproducible by outsiders because they depend on data sets that are too large to distribute, or data that we do not have permission to redistribute but are in the SEP data library.

CR denotes Conditional Reproducibility. The author certifies that the commands are in place to reproduce the figure if certain resources are available. SEP staff have only attempted to make sure that the makefile rules exist and the source codes referenced are provided. The primary reasons for the CR designation is that the processing requires 20 minutes or more, or commercial packages such as Matlab or Mathematica.

M denotes a figure that may be viewed as a movie in the web version of the report. A movie may be either ER or CR.

NR denotes Non-Reproducible figures. SEP discourages authors from flagging their figures as NR except for figures that are used solely for motivation, comparison, or illustration of the theory, such as: artist drawings, scannings, or figures taken from SEP reports not by the authors or from non-SEP publications.

Our testing is currently limited to LINUX 2.6 (using the Intel Fortran90 compiler), but the code should be portable to other architectures. Reader's suggestions are welcome. For more information on reproducing SEP's electronic documents, please visit [<http://sepwww.stanford.edu/research/redoc/>](http://sepwww.stanford.edu/research/redoc/).

¹<http://sepwww.stanford.edu/private/docs/sep129>

²http://sepwww.stanford.edu/public/docs/sepdata/lib/toc_html/

Jon Claerbout
April 2, 2007

Rosemary Knight, Geophysics Chair

Dear chairperson Knight,

This letter from me to you is required by the faculty guide.

I am planning to retire from Stanford University within 30 days of Biondo returning from sabbatical and resuming his academic duties here.

I expect to execute the paperwork on or about January 15, 2008.

I plan to make myself available to Biondo for part-time teaching.

Sincerely,



Jon Claerbout

—

SEP-129 — TABLE OF CONTENTS

Imaging

<i>Shan G., Clapp R., and Biondi B.</i> , 3D plane-wave migration in tilted coordinates	1
<i>Shragge J. and Shan G.</i> , Prestack depth migration in elliptic coordinates	17
<i>Etgen J. T.</i> , A tutorial on optimizing time domain finite-difference schemes: "Beyond Holberg"	31
<i>Valenciano A. A.</i> , Two-way vs. one-way: Understanding the approximations	41
<i>Shan G.</i> , Optimized implicit finite-difference migration for TTI media: A 2D synthetic dataset	55

Inversion

<i>Valenciano A. A.</i> , Target-oriented wave-equation inversion: Sigsbee model	63
<i>Curry W.</i> , Non-stationary interpolation in the f-x domain	73
<i>Curry W.</i> , Interpolation with pseudo primaries: Revisited	83
<i>Ayeni G. and Biondi B.</i> , Seismic monitoring of sub-salt reservoirs: Time-lapse wave-equation inversion	93

Velocity

<i>Shragge J.</i> , Transmission wavefield velocity analysis	107
<i>Witten B.</i> , ℓ_1 regularized inversion	115
<i>Günther R.</i> , Full-volume dip corrections for velocity analysis and MVA	127
<i>Berryman J. G.</i> , Aligned vertical fractures,	137

Gathers

<i>Clapp R. G.</i> , Moveout analysis with flattening	147
<i>Tang Y.</i> , Selective stacking in the reflection-angle and azimuth domain	157

<i>Jousselin P. and Biondi B.</i> , Anisotropic migration velocity analysis from residual moveout transformation in angle-domain common-image gathers	177
<i>Alvarez G.</i> , Mapping of 3-D multiples to image space: An example with a Gulf of Mexico dataset.....	199
<i>Vyas M.</i> , Improving multiple prediction in image space using ADCIGs for limited-offset recordings	211
<i>Guerra C.</i> , Residual multiple attenuation using AVA modeling	231

Computers

<i>Witten B., Curry B., and Shragge J.</i> , A New Build Environment for SEP	245
<i>Pell O. and Clapp R. G.</i> , Accelerating subsurface offset gathers for 3D seismic applications using FPGAs.....	251
SEP Articles Published or In Press, 2006-07	263
SEP Phone Directory	265
Research Personnel	269

3D plane-wave migration in tilted coordinates

Guojian Shan, Robert Clapp, and Biondo Biondi

ABSTRACT

We develop 3D plane-wave migration in tilted coordinates for anisotropic media. We transform the recorded surface data to plane-wave data by slant-stack processing. Both the source plane-wave and its corresponding slant-stacked data are extrapolated into the subsurface within a tilted coordinates system whose direction depends on the propagation direction of the plane-wave. Images are generated by cross-correlating these two wavefields. A real dataset from Gulf of Mexico shows that this technique can image steeply dipping salt flanks and faults, even though the one-way wave equation operator is used for the wavefield extrapolation.

INTRODUCTION

Kirchoff migration has been widely applied in seismic processing due to its relative cheap cost and flexibility. However, it can not provide reliable images where there is strongly lateral velocity variation because of its high-frequency assumption. Wave-equation migration, which is performed by recursive wavefield extrapolation, has been demonstrated to overcome these limitations and produce better images in areas of complex geology.

It is well known that waves propagate upward and downward simultaneously. Reverse-time migration (Whitmore, 1983; Baysal et al., 1983; Biondi and Shan, 2002), which solves the full wave equation directly and mimics wave propagation naturally, is still too expensive for today's computing facilities. As a result, downward continuation methods (Claerbout, 1985), which are based on one-way wave equation wavefield extrapolation and much cheaper than reverse-time migration, are widely used in the industry.

Conventional downward continuation method extrapolates wavefields using the one-way wave equation in Cartesian coordinates. For a medium without lateral variation, the phase-shift method (Gazdag, 1978) can be applied, and one-way wave equation can model waves propagating in a direction up to 90° away from the extrapolation direction. But in a laterally varying medium, it is very difficult to model waves propagating in a direction far from the extrapolation direction using the one-way wave equation. A lot of effort has been made to improve the accuracy of the wavefield-extrapolation operator in laterally varying media, including Fourier finite-difference (Ristow and Ruhl, 1994; Biondi, 2002), general screen propagator (de Hoop, 1996; Huang and Wu, 1996), and optimized finite difference (Lee and Suh, 1985) with phase correction (Li, 1991). Even if we could model waves accurately up to 90 degree using the one-way wave equation in laterally varying media, overturned waves, which travel downward

first and then curve upward, are filtered away during the extrapolation. This is because only down-going waves are allowed in the source wavefield and only up-going waves are allowed in the receiver wavefield in downward continuation. But overturned waves and waves propagating in a high angle direction play a key role in imaging the steeply dipping reflectors. As a consequence, imaging steeply dipping reflectors, such as salt flank and faults, remain a major problem in downward continuation.

Some work has been done to image the steeply dipping reflectors with one-way wave equation by coordinate transformation. This includes tilted coordinates (Higginbotham et al., 1985; Etgen, 2002), the combination of downward continuation and horizontal continuation (Zhang and McMechan, 1997), or wavefield extrapolation in general coordinates such as ray coordinates (Nichols, 1994) and Riemannian coordinates (Sava and Fomel, 2005; Shragge, 2006).

Plane-wave source migration (Whitmore, 1995; Rietveld, 1995; Duquet et al., 2001; Liu et al., 2002; Zhang et al., 2005) has been demonstrated as a useful tool in seismic imaging. Shan and Biondi (2004) perform 2D plane-wave migration in tilted coordinates to image steeply dipping reflectors and overturned waves using one-way wave equation. In this paper, we develop 3D full plane-wave migration in tilted coordinates.

This paper is organized as follows: we begin with a brief review of plane-wave migration, then describe the theory of plane-wave migration in tilted coordinates, and finally demonstrate our technique with a real dataset example.

3D PLANE-WAVE MIGRATION

The original surface seismic data are usually shot gathers. A typical seismic shot gather (the receiver wavefield of a shot at the surface) is a five dimensional object: $R(s_y, s_x, r_y, r_x, z = 0, t)$, where (s_y, s_x) is the source location, (r_x, r_y) is the receiver location and t is the travel time. After a Fourier transformation in t , we have the receiver wavefield in the frequency domain $R(s_y, s_x, r_y, r_x, z = 0, \omega)$, where ω is the angular frequency.

Each shot represents a real physical experiment. The most straight forward way to obtain the image of the subsurface is shot-profile migration, in which we obtain the local image of each experiment independently and form the final image of the subsurface by stacking all the local images. A typical shot-profile migration algorithm includes two steps. First, source and receiver wavefields are extrapolated into the subsurface using one-way wave equations. In isotropic media they are defined as follows:

$$\frac{\partial S}{\partial z} = -\frac{i\omega}{v} \sqrt{1 + \frac{v^2}{\omega^2} \left(\frac{\partial^2}{\partial x^2} + \frac{\partial^2}{\partial y^2} \right)} S, \quad (1)$$

$$\frac{\partial R}{\partial z} = +\frac{i\omega}{v} \sqrt{1 + \frac{v^2}{\omega^2} \left(\frac{\partial^2}{\partial x^2} + \frac{\partial^2}{\partial y^2} \right)} R, \quad (2)$$

where $v = v(x, y, z)$ is the velocity of the media, $S = S(s_y, s_x; x, y, z, \omega)$ is the source wavefield, which is an impulse at the surface and $R = R(s_y, s_x; r_y, r_x, z, \omega)$ is the receiver wavefield.

Second, the image is formed by cross-correlating the source and receiver wavefields:

$$I(x, y, z) = \int \int \int \bar{S}(s_x, s_y; x, y, z, \omega) R(s_x, s_y; x, y, z, \omega) d\omega ds_x ds_y. \quad (3)$$

Plane-wave source migration

Shot gathers can also be synthesized to a new dataset to represent a physical experiment that does not occur in reality. One of the most important examples is to synthesize shot gathers to plane-wave source gathers. The plane-wave source gathers represent experiments that planar sources originate from all angles at the surface. They can also be regarded as the accurate phase-encoding of the shot gathers (Liu et al., 2006). The plane-wave source dataset can be generated by delaying the shot in shot gathers or slant-stacking in receiver gathers as follows:

$$R_p(p_x, p_y; r_x, r_y, z = 0, \omega) = \int \int R(s_x, s_y; r_x, r_y, z = 0, \omega) e^{i\omega(s_x p_x + s_y p_y)} ds_x ds_y, \quad (4)$$

where p_x and p_y are ray parameters in the in-line and cross-line directions respectively. Its corresponding plane-wave source wavefield at the surface is

$$S_p(p_x, p_y; r_x, r_y, z = 0, \omega) = \int \int e^{i\omega(s_x p_x + s_y p_y)} ds_x ds_y. \quad (5)$$

Similar to the Fourier transformation, we can transform the plane-wave source data back to shot gathers by the inverse slant-stacking (Claerbout, 1985) as follows

$$R(s_x, s_y; r_x, r_y, z = 0, \omega) = \int \int \omega^2 R_p(p_x, p_y; r_x, r_y, z = 0, \omega) e^{-i\omega(s_x p_x + s_y p_y)} dp_x dp_y \quad (6)$$

In contrast to the inverse Fourier transformation, the kernel of the integral is weighted by the square of the frequency ω .

The source wavefield S_p and receiver wavefield R_p are extrapolated into the subsurface independently using the one-way wave equations 1 and 2. The image of a plane-wave source with a ray parameter pair (p_x, p_y) is formed by cross-correlating the source and receiver wavefields weighted with the square of the frequency ω :

$$I_{p_x, p_y}(x, y, z) = \int \omega^2 \bar{S}_p(p_x, p_y; x, y, z, \omega) R_p(p_x, p_y; x, y, z, \omega) d\omega. \quad (7)$$

The final image is generated by stacking the images of all possible plane-wave sources:

$$I_p = \int \int I_{p_x, p_y}(x, y, z) dp_x dp_y. \quad (8)$$

Because both slant-stacking and migration are linear operators, the image of the plane-wave migration I_p is equivalent to the image obtained by shot-profile migration (Liu et al., 2002; Zhang et al., 2005).

Conical-wave source migration

For narrow azimuth data, conical-wave source migration has been demonstrated as an efficient way to image the subsurface (Whitmore, 1995; Duquet et al., 2001; Zhang et al., 2005). The conical-wave source data are generated as follows

$$R_c(p_x, s_y; r_x, r_y, z = 0, \omega) = \int R(s_x, s_y; r_x, r_y, z = 0, \omega) e^{i\omega(s_x p_x)} ds_x. \quad (9)$$

And the corresponding conical source at the surface is

$$S_c(p_x, s_y; r_x, r_y, z = 0, \omega) = \int e^{i\omega(s_x p_x)} ds_x. \quad (10)$$

Similar to the plane-wave source migration, the image of a conical-wave source can be obtained by cross-correlating the source and receiver wavefields weighted with the frequency ω :

$$I_{p_x, s_y}(x, y, z) = \int \omega \bar{S}_c(p_x, s_y; x, y, z, \omega) R_c(p_x, s_y; x, y, z, \omega) d\omega, \quad (11)$$

where $S_c(p_x, s_y; x, y, z, \omega)$ and $R_c(p_x, s_y; x, y, z, \omega)$ are the conical-wave source and receiver wavefields extrapolated from the surface using equation 1 and 2. The final image is generated by stacking images of all possible conical-wave sources of all sail lines:

$$I_c = \int \int I_{p_x, s_y}(x, y, z) dp_x ds_y. \quad (12)$$

Similar to the 3D plane-wave migration, the image of conical-wave migration is equivalent to the shot-profile migration.

3D PLANE-WAVE MIGRATION IN TILTED COORDINATES

A 3D plane-wave source is specified by two ray-parameters, p_x and p_y . Given the velocity at the surface v_{z_0} , we can calculate the propagation direction of the plane-wave source at the surface from the two ray-parameters. For each plane-wave source, we rotate the Cartesian coordinates, so that the extrapolation direction of the new coordinates is close to the propagation direction of the plane-wave. In 3D, the propagation direction of a plane-wave source is defined by two angles: the azimuth angle α and the take-off angle θ . Given the velocity at the surface v_{z_0} and a plane-wave source with a ray parameter pair (p_x, p_y) , its propagation direction at the surface is defined by the vector (q_x, q_y, q_z) , where

$$q_x = p_x v_{z_0}, \quad (13)$$

$$q_y = p_y v_{z_0}, \quad (14)$$

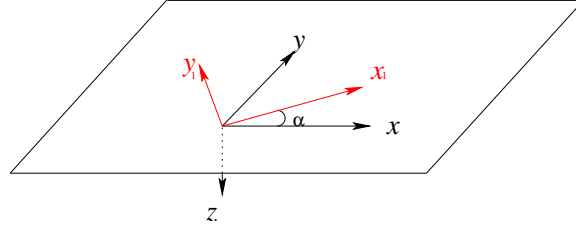
$$q_z = \sqrt{1 - (q_x^2 + q_y^2)}. \quad (15)$$

The azimuth angle and take-off angle of the plane-wave source are calculated from the vector (q_x, q_y, q_z) as follows:

$$\alpha = \arcsin(q_y/q_x), \quad (16)$$

$$\theta = \arccos(q_z). \quad (17)$$

Figure 1: Rotation about the axis z by α `guojian1-rotazimuth` [NR]

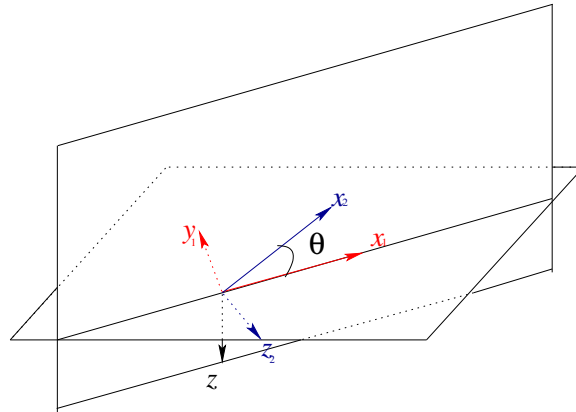


Rotations in 3D are specified by the axis of rotation and rotation angle. They can be described by a rotation matrix. For example, a rotation about the z -axis by an angle α (Figure 1) is

$$\begin{pmatrix} x_1 \\ y_1 \\ z_1 \end{pmatrix} = R_z(\alpha) \begin{pmatrix} x \\ y \\ z \end{pmatrix} = \begin{pmatrix} \cos\alpha & \sin\alpha & 0 \\ -\sin\alpha & \cos\alpha & 0 \\ 0 & 0 & 1 \end{pmatrix} \begin{pmatrix} x \\ y \\ z \end{pmatrix}. \quad (18)$$

To design a coordinate system with an extrapolation direction parallel the propagation direction of the plane-wave source (q_x, q_y, q_z) , we rotate the coordinates in two steps. First we rotate about the z -axis by an angle α (equation 18) shown in Figure 1. Second we rotate about the y_1 -axis by an angle θ (Figure 2) as follow:

Figure 2: Rotation about the axis y_1 by θ `guojian1-rottilt` [NR]



$$\begin{pmatrix} x_2 \\ y_2 \\ z_2 \end{pmatrix} = R_{y_1}(\theta) \begin{pmatrix} x_1 \\ y_1 \\ z_1 \end{pmatrix} = \begin{pmatrix} \cos\theta & 0 & \sin\theta \\ 0 & 1 & 0 \\ -\sin\theta & 0 & \cos\theta \end{pmatrix} \begin{pmatrix} x_1 \\ y_1 \\ z_1 \end{pmatrix}. \quad (19)$$

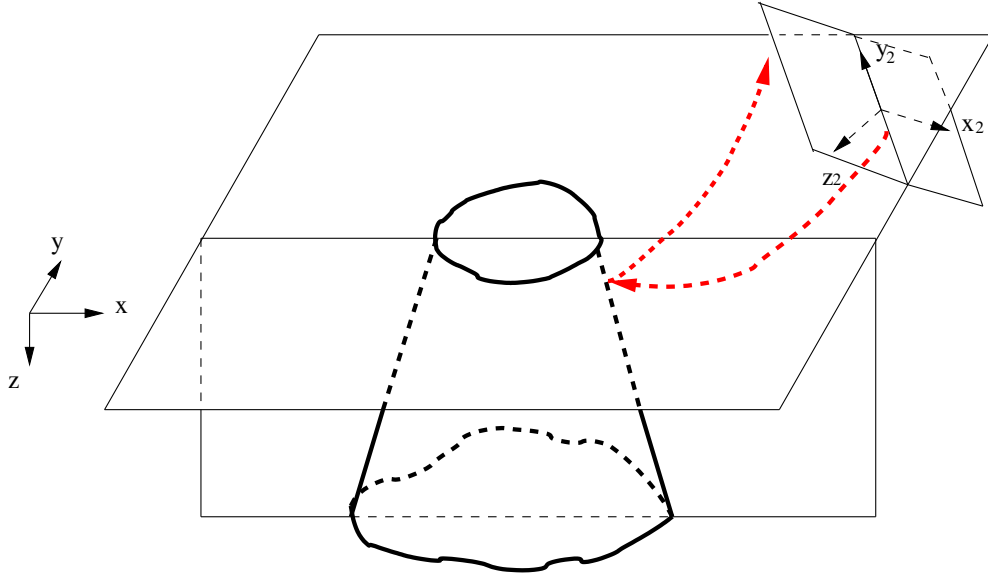


Figure 3: A plane-wave source and its coordinates to image the salt body. (x, y, z) is the original Cartesian coordinates. (x_2, y_2, z_2) is the new tilted coordinates. The dashed line with arrows are the source and receiver rays of the plane-wave source. The extrapolation direction of the new coordinates z_2 axis is closer to the propagation direction of the plane-wave source. guojian1-coordinates [NR]

Combining the two rotations, we have the rotation from original coordinates to the new tilted coordinates as follows,

$$\begin{pmatrix} x_2 \\ y_2 \\ z_2 \end{pmatrix} = \begin{pmatrix} \cos\theta \cos\alpha & \cos\theta \sin\alpha & \sin\theta \\ -\sin\alpha & \cos\alpha & 0 \\ -\sin\theta \cos\alpha & -\sin\theta \sin\alpha & \cos\theta \end{pmatrix} \begin{pmatrix} x \\ y \\ z \end{pmatrix}. \quad (20)$$

It is easy to verify that the depth axis of the new coordinates parallels the propagation direction (q_x, q_y, q_z) . In practice, we do not use the direction exactly paralleling the propagation of the plane-wave source at the surface. Considering that the velocity usually increases with the depth, the propagation direction of a plane-wave source becomes increasingly horizontal. So we usually choose a tilting angle θ that is a little bigger than $\arccos(q_z)$.

Figure 3 shows a typical coordinate system used for a plane-wave source to image a salt dome. The dashed lines with arrows show the propagation direction of the source and receiver waves for the plane-wave source. (x, y, z) is the Cartesian coordinate system, and (x_2, y_2, z_2) is the tilted coordinates for the plane-wave source. The extrapolation direction of the new coordinates, which parallels z_2 -axis, is much closer to the propagation direction of the plane-wave source than the conventional vertical extrapolation direction.

For conical-wave source migration, we can similarly design tilted coordinates for each conical source. In contrast to the 3D plane-wave source migration, we apply the second rotation directly without rotating the azimuth of the data. Given the conical-wave source with a ray parameter p_x and the surface velocity v_{z0} , we rotate the velocity and the surface data

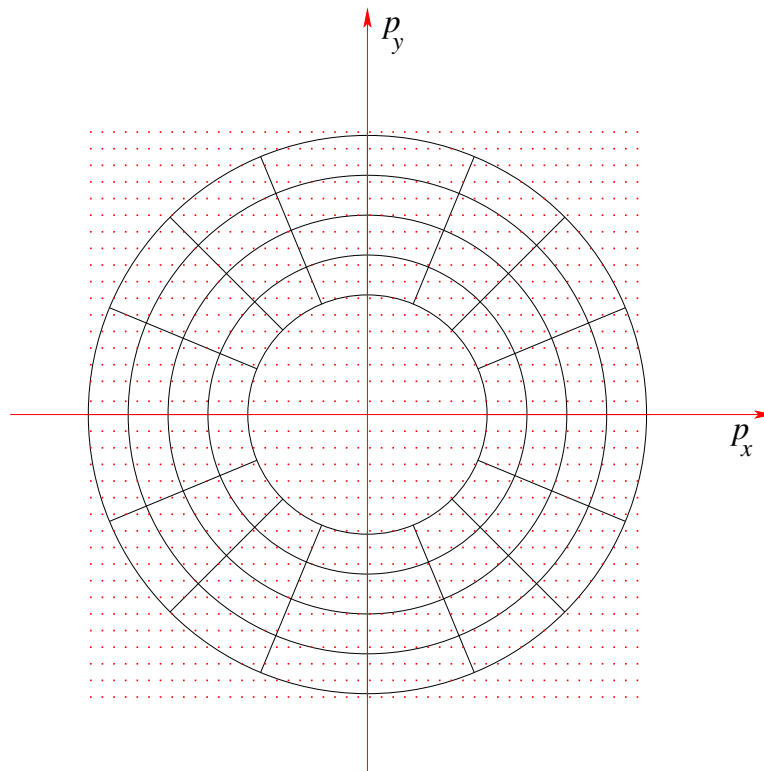


Figure 4: The dots represent all possible plane-wave sources. The circles are the contour of their take-off angles and the smallest circle represents plane-wave sources with a take-off angle of 15° . The radial lines show the contour of azimuth angles. All possible plane-wave sources are divided into small cells. The plane-wave sources in a cell have a similar take-off and azimuth angle and share a coordinate system. `guojian1-ppanel` [NR]

along y -axis by a angle of $\theta = \arcsin(p_x v_{z0})$ and migrate the data in the new coordinates. This usually works when the in-line direction is the predominant dip direction in the subsurface. When there are steep dips in the cross-line direction, it is still difficult to image these dips with conical-wave migration in tilted coordinates. In contrast, 3D plane-wave migration in tilted coordinates rotate the data and model into a general direction dependent on the propagation direction and it can image these cross-line direction dips.

PRACTICE CONSIDERATIONS

There are three steps to implement plane-wave migration in tilted coordinates for one plane-wave source. First, the source and receiver wavefields are rotated to the new coordinates. Second, for each frequency, source and receiver wavefields are extrapolated into the subsurface and the image is generated by cross-correlating the two wavefields in the new coordinates. Third, the image is rotated back to the original Cartesian coordinates after stacking the images of all the frequencies. In the first step, we rotate a 2D dataset for each frequency, this cost is

trivial compared to the wavefield extrapolation. In the third step, we rotate the 3D image back to Cartesian coordinates after stacking all frequencies, the cost is also very small.

To further reduce the cost of rotations, the plane-wave sources with similar propagation directions share the same tilted coordinate system. This reduces the rotation number in the third step. Figure 4 illustrates how to sample the ray parameters p_x and p_y and how to put plane-wave sources together to share a coordinate system. In Figure 4 we sample (p_x, p_y) in Cartesian coordinates, where p_x, p_y are defined as:

$$p_x = -p_{max}, -p_{max} + dp_x, \dots, p_{max} - dp_x, p_{max}, \quad (21)$$

$$p_y = -p_{max}, -p_{max} + dp_y, \dots, p_{max} - dp_y, p_{max}, \quad (22)$$

where p_{max} is defined by the maximum take-off angle and dp_x, dp_y are the sampling of the ray parameters. In Figure 4, each dot represents a plane-wave source with a ray parameter pair (p_x, p_y) . Given the surface velocity, we calculate the azimuth angle α and take-off angle θ from (p_x, p_y) and vice versa using equations 16 and 17. Therefore, we can divide the whole area into cells using (α, θ) as the coordinate system. Figure 4 shows the cells in the coordinates (α, θ) . All the plane-wave sources whose ray parameter pair (p_x, p_y) fall in a cell share the same coordinate system. The dots in the smallest circle in Figure 4 represent plane-wave sources whose take-off angle θ is smaller than 15° . For those plane-wave sources, we extrapolate its source and receiver wavefields in Cartesian coordinates. For all plane-wave sources whose ray parameter pair (p_x, p_y) is in a cell, we use their average take-off angle and azimuth angle to design the coordinate system for the migration.

ANISOTROPIC MEDIA IN TILTED COORDINATES

It is well known that a VTI (transversely isotropic with a vertical symmetry axis) medium is circularly symmetric in the horizontal plane. Therefore, the medium is still VTI after rotating the azimuth of the model (equation 18). In the second rotation step (equation 19), a VTI medium in Cartesian coordinates changes to a TTI (tilted TI) medium with a constant tilting angle θ in the new coordinates. We keep the y_2 -axis in (x, y) plane when we rotate the coordinates. This guarantees the symmetry axis of the new TTI media in the new plane (x_2, z_2) . For this kind of TTI media, the dispersion relation is not symmetric in the in-line direction but it is symmetric in the cross-line direction in the new coordinates. The extrapolation operator for this kind of TTI media is simpler than the general TTI media. We need a wavefield-extrapolation operator for TTI media to apply plane-wave migration in tilted coordinates in VTI media. We use optimized implicit finite-difference methods for TTI media (Shan, 2006a). The coefficients for the finite-difference scheme are obtained by fitting the dispersion relation with rational functions.

NUMERICAL EXAMPLES

We test the methodology on a real 3D dataset from the Gulf of Mexico. Figure 5 shows the vertical velocity model with a typical salt body. The salt body is not very complex, but its

flank in both the in-line and cross-line directions are very steep. We obtained the dataset with the velocity and anisotropy parameter models from Exxonmobil. The vertical velocity and anisotropy parameters were estimated by the integrated velocity model estimation (Bear et al., 2005), which incorporates the surface seismic data with all other data available. For this dataset, in addition to vertical check shots and a substantial number of sonic logs, there is an offset check shot survey that serve to constrain the estimation of the velocity and anisotropy parameters. The maximum value of the anisotropy parameters ε and δ are 0.20 and 0.10, respectively.

Figure 6 shows the velocity model we used for migration. We replace the velocity in the salt body with the sediment velocity around it. We migrate 2700 plane-waves in total. The sampling of ray parameter in both in-line and cross-line directions are 0.000013 s/m. And the maximum take-off angle θ is 38° . The samplings for the cells used for sharing tilted coordinates in Figure 4 are $d\theta = 5^\circ$ and $d\alpha = 22.5^\circ$.

For comparison, we did two migrations: anisotropic plane-wave migration in Cartesian coordinates (Shan, 2006b) and anisotropic plane-wave migration in tilted coordinates. Figures 7-10 compare the images of these two migrations at different locations. In these figures, the top panels are the images obtained by anisotropic plane-wave migration in Cartesian coordinates and the bottom ones are the images obtained by anisotropic plane-wave migration in tilted coordinates.

In Figure 7, at "A" in the cross-line section, the top of the salt energy is dim in Figure 7(a) while it is strong and continuous in Figure 7(b). At "B" in the in-line section, the salt flank is well imaged in Figure 7(b) while it is absent in Figure 7(a). At "C" in the depth section, we see the continuous salt boundary from the sediment in Figure 7(b), while we can only see half of it in Figure 7(a).

In Figure 8, at "B" in the in-line section, the salt flank, which is not visible in 8(a) become very evident in Figure 8(b). At "B" in the cross-line section, the salt flank is not imaged at the right position due to the limit of the accuracy of the operator in Figure 8(a) while it is well imaged in Figure 8(b). The salt flank at "D" is strong and continuous in Figure 8(b) but it almost disappears in 8(a). At "C" in the depth section, the salt body can be picked out easily from the sediments in 8(b) but it is not visible in 8(a).

In Figure 9, at "B" in the in-line section, the salt flank, which is not visible in Figure 9(a), is visible in Figure 9(b). The top of the salt in the in-line section in Figure 9(b) is sharper than that in Figure 9(a). In the cross-line section of Figure 9, the plane-wave migration in tilted coordinates images the salt flank at "A" and "D" (Figure 9(b)), which are very weak and not at the right position in Figure 9(a). In the depth section, we can see the salt boundary clearly in 9(b) while they are not visible in Figure 9(a).

In Figure 10 we can see similar improvements of the salt flanks at "A" and "B". At "C", we can also see the steeply dipping faults in Figure 10(b) are much better imaged than that in Figure 10(a).

From these comparisons, we find that plane-wave migration in tilted coordinates greatly improves the images of the salt body and steeply dipping faults.

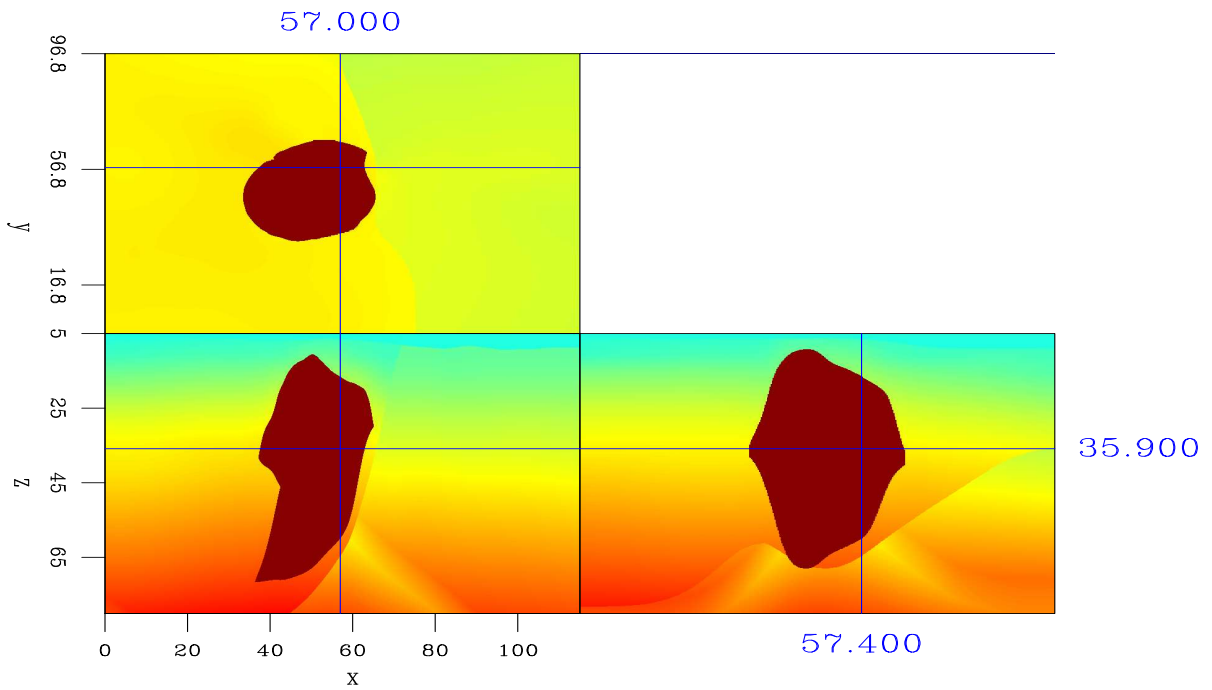


Figure 5: The vertical velocity model of the real dataset. The salt body is not complex but its flanks are steep. `guojian1-vel` [ER]

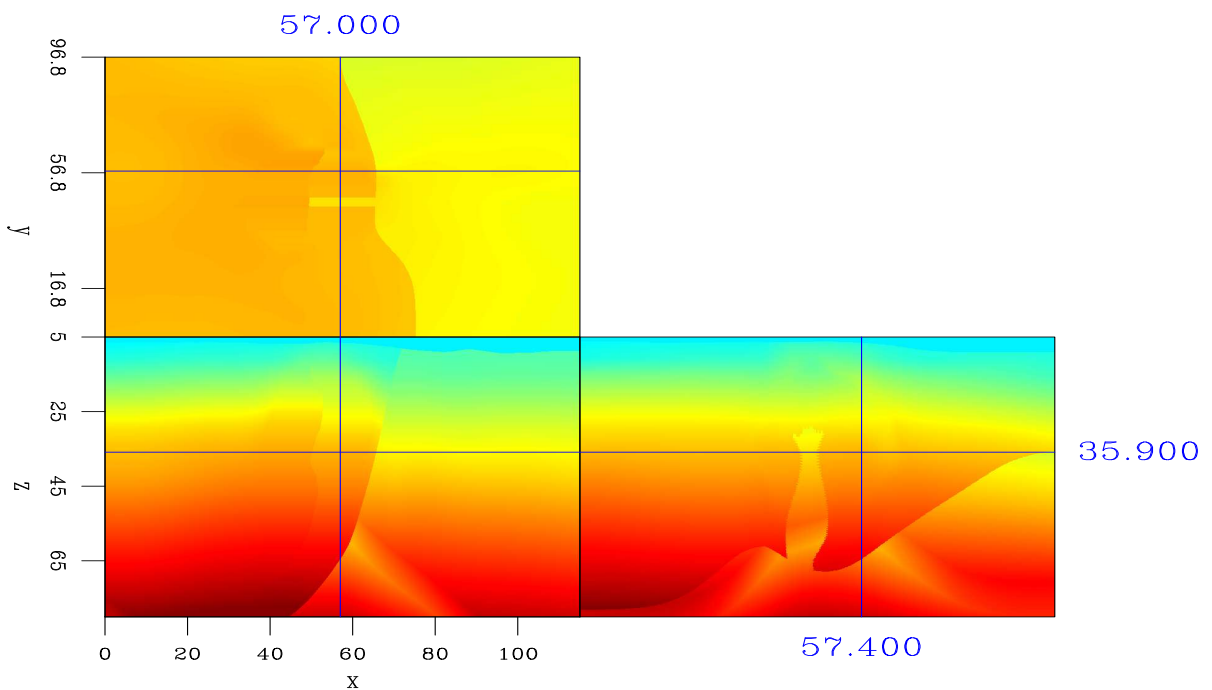


Figure 6: The vertical velocity model used for migration. The salt body is filled with the sediment velocity. `guojian1-velnosalt` [CR]

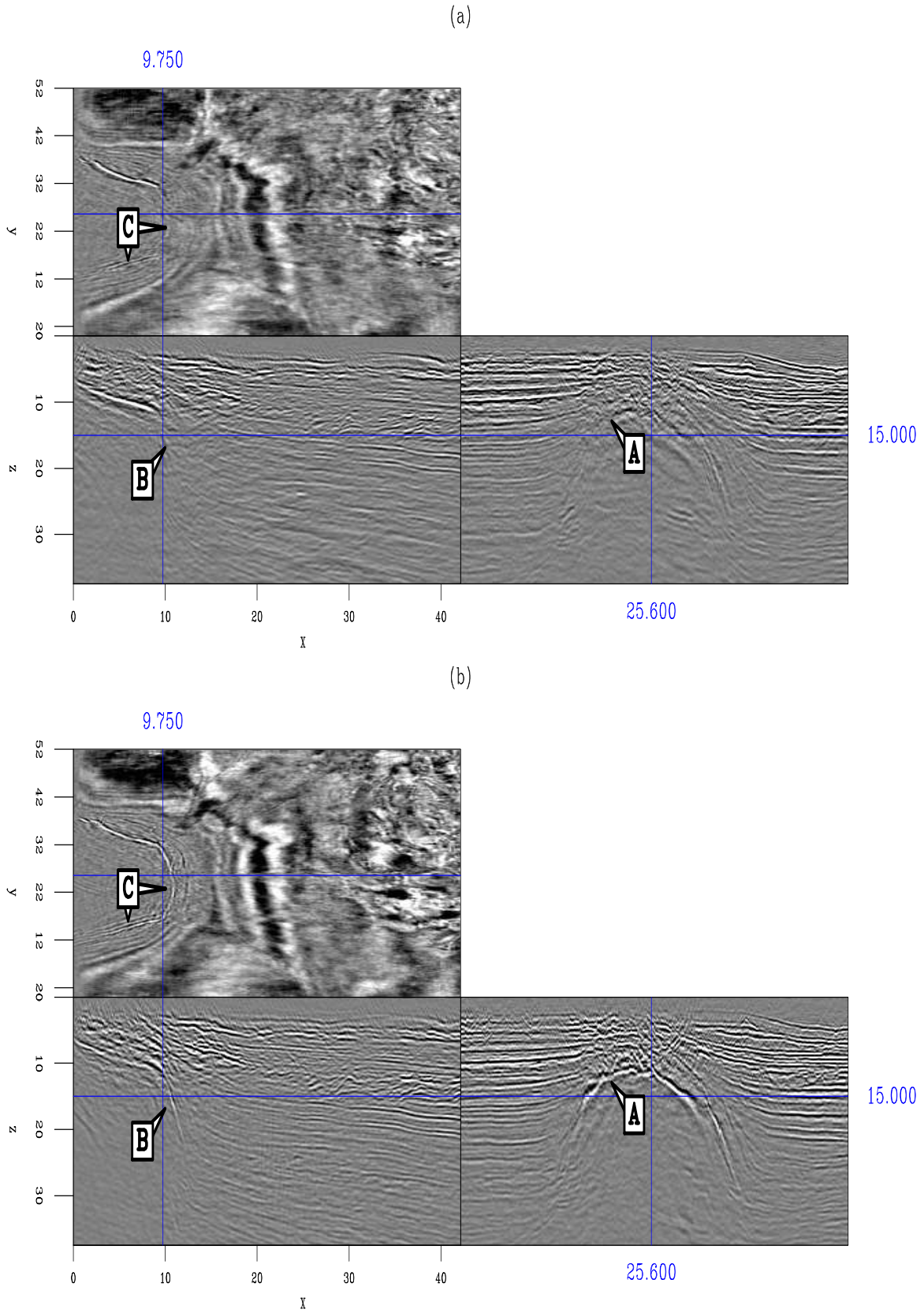


Figure 7: Image comparison: (a) Anisotropic plane-wave migration in Cartesian coordinates; (b) Anisotropic plane-wave migration in tilted coordinates. `guojian1-imgcompare1` [CR]

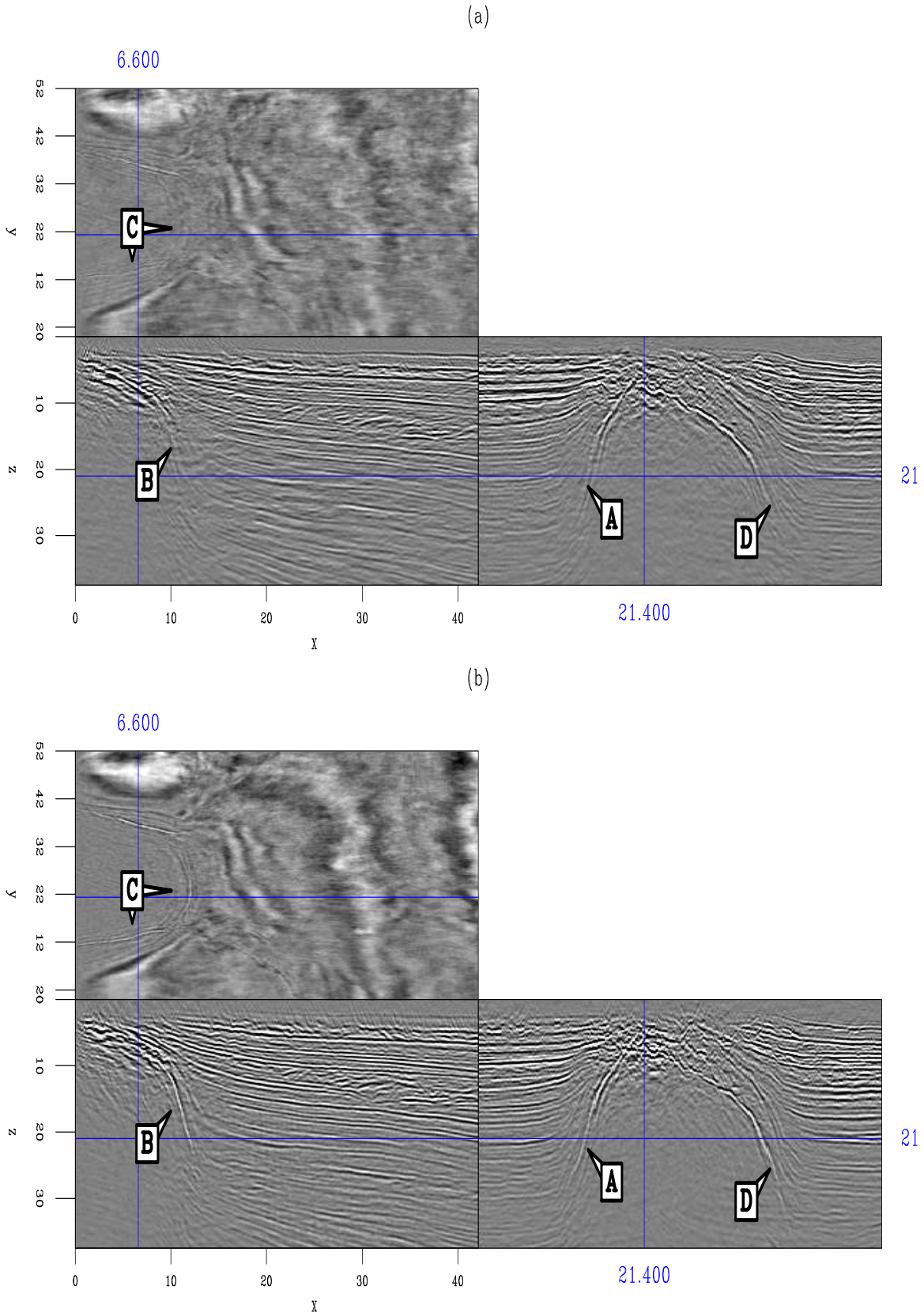


Figure 8: Image comparison: (a) Anisotropic plane-wave migration in Cartesian coordinates; (b) Anisotropic plane-wave migration in tilted coordinates. `guojian1-imgcompare2` [CR]

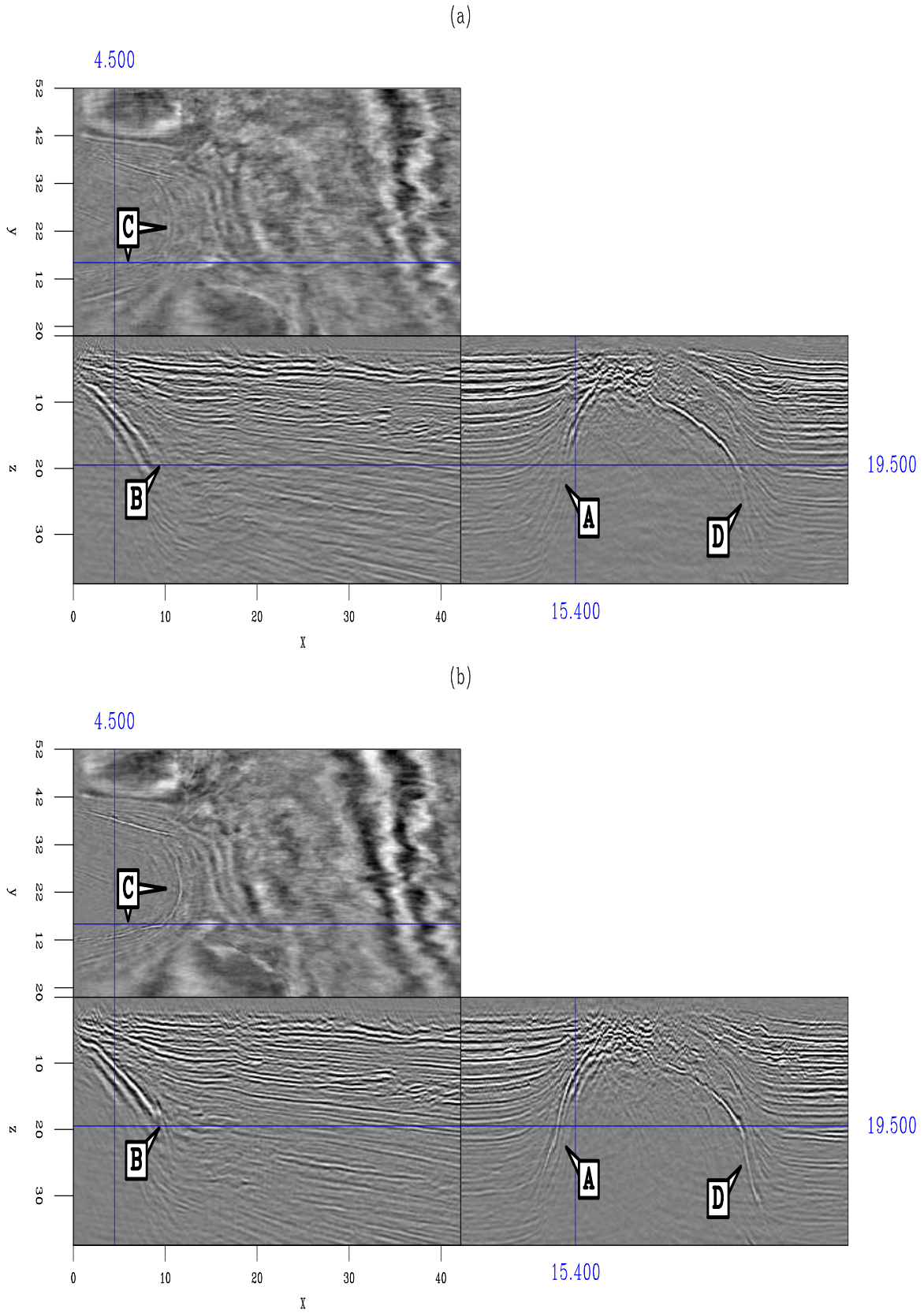


Figure 9: Image comparison: (a) Anisotropic plane-wave migration in Cartesian coordinates; (b) Anisotropic plane-wave migration in tilted coordinates. guojian1-imgcompare3 [CR]

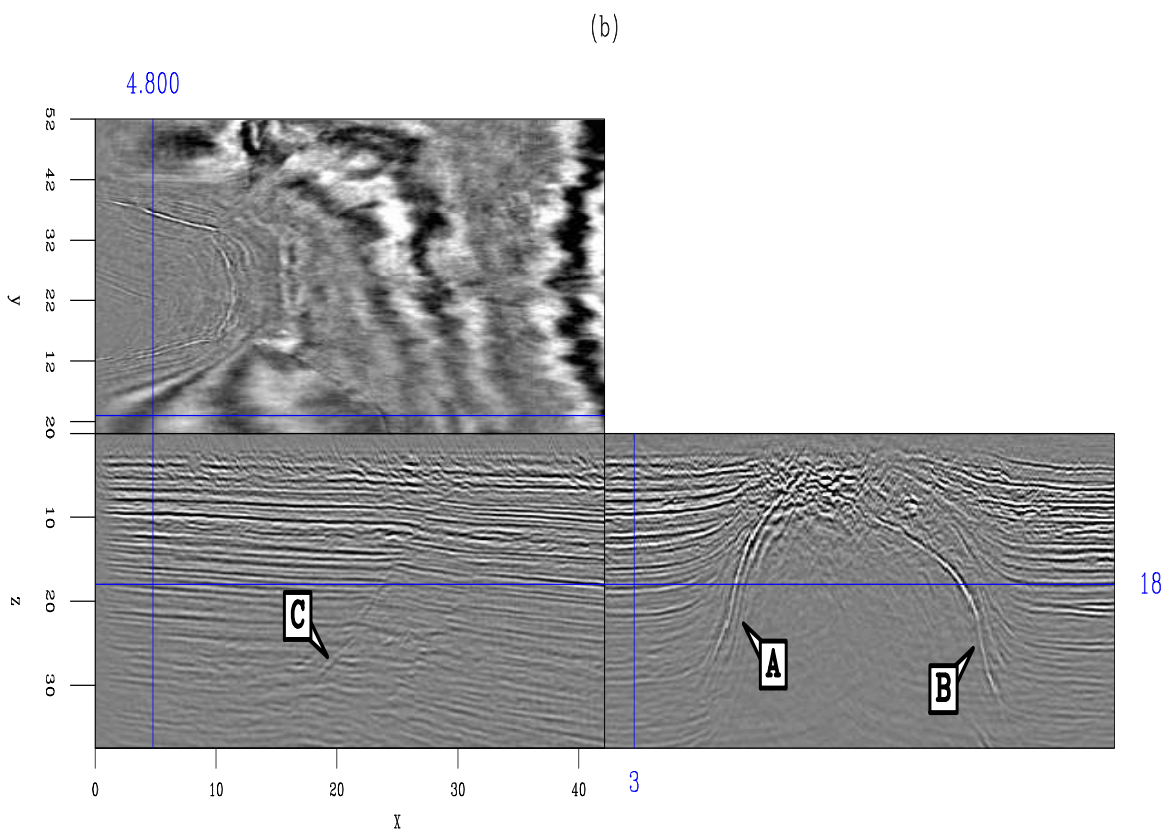
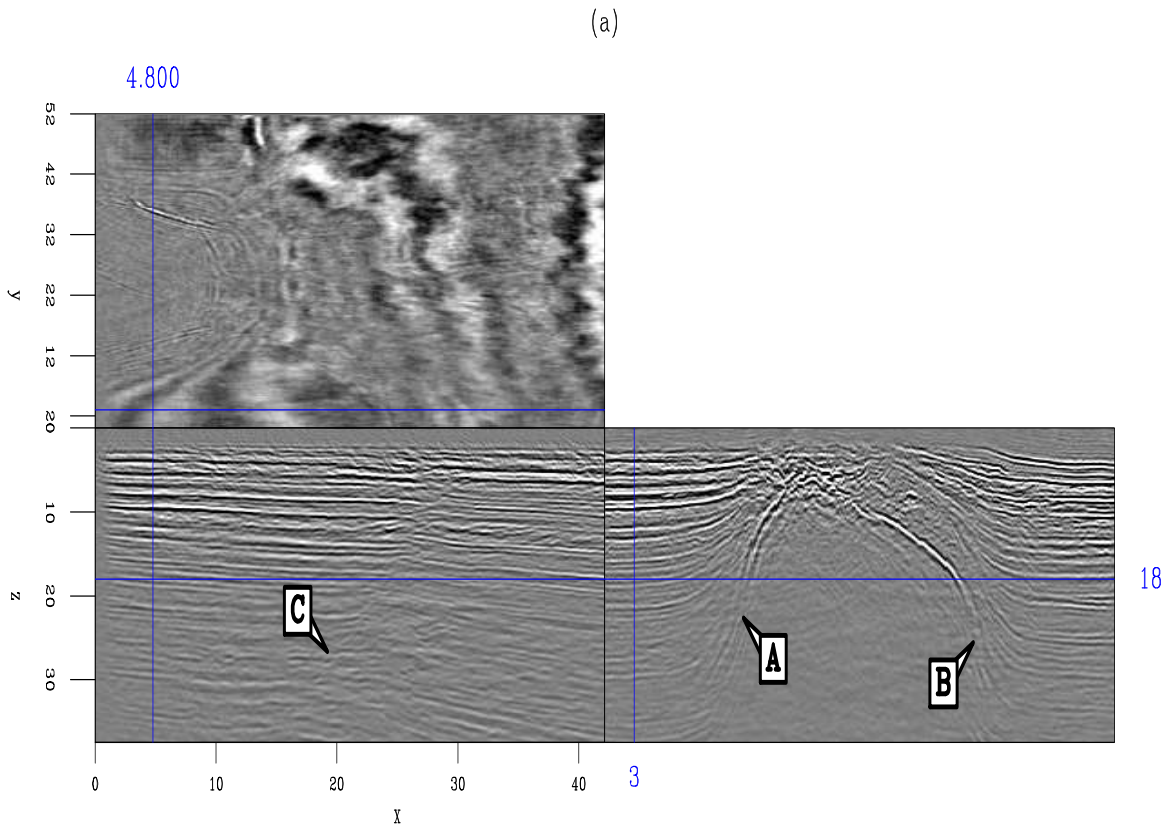


Figure 10: Image comparison: (a) Anisotropic plane-wave migration in Cartesian coordinates; (b) Anisotropic plane-wave migration in tilted coordinates. `guojian1-imgcompare4` [CR]

CONCLUSION

We present an efficient way to image steeply dipping reflectors and overturned waves using one-way wavefield extrapolation. We decompose the recorded data into plane-wave source data and migrate them using one-way wave equation operator in tilted coordinates. The real dataset examples show that this algorithm effectively images steeply dipping reflectors such as salt body flanks and faults.

ACKNOWLEDGMENTS

We thank ExxonMobil for making the dataset available.

REFERENCES

- Baysal, E., Kosloff, D. D., and Sherwood, J. W. C., 1983, Reverse time migration: *Geophysics*, **48**, 1514–1524.
- Bear, L., Dickens, T., Krebs, J., Liu, J., and Traynin, P., 2005, Integrated velocity model estimation for improved positioning with anisotropic PsDm: *The Leading Edge*, **24**, 622–634.
- Biondi, B., 2002, Stable wide-angle Fourier finite-difference downward extrapolation of 3-D wavefields: *Geophysics*, **67**, 872–882.
- Biondi, B., and Shan, G., 2002, Prestack imaging of overturned reflections by reverse time migration: Prestack imaging of overturned reflections by reverse time migration, *Soc. of Expl. Geophys.*, 72nd Ann. Internat. Mtg, 1284–1287.
- Claerbout, J. F., 1985, *Imaging the Earth's Interior*: Blackwell Scientific Publications.
- Duquet, B., Lailly, P., and Ehinger, A., 2001, 3D plane wave migration of streamer data: 3D plane wave migration of streamer data, *Soc. of Expl. Geophys.*, 71st Ann. Internat. Mtg, 1033–1036.
- Etgen, J., 2002, Waves, beams and dimensions: an illuminating if incoherent view of the future of migration: 72nd Ann. Internat. Mtg, *Soc. of Expl. Geophys.*, invited presentation.
- Gazdag, J., 1978, Wave equation migration with the phase-shift method: *Geophysics*, **43**, 1342–1351.
- Higginbotham, J. H., Shin, Y., and Sukup, D. V., 1985, Directional depth migration (short note): *Geophysics*, **50**, 1784–1796.
- de Hoop, M. V., 1996, Generalization of the Bremmer coupling series *in J. Math. Phys.* 3246–3282.

- Huang, L. Y., and Wu, R. S., 1996, Prestack depth migration with acoustic screen propagators: Prestack depth migration with acoustic screen propagators, Soc. of Expl. Geophys., 66th Ann. Internat. Mtg, 415–418.
- Lee, M. W., and Suh, S. Y., 1985, Optimization of one-way wave-equations (short note): Geophysics, **50**, 1634–1637.
- Li, Z., 1991, Compensating finite-difference errors in 3-D migration and modeling: Geophysics, **56**, 1650–1660.
- Liu, F., Hanson, D. W., Whitmore, N. D., and Robert H. Stolt, R. S. D., 2006, Toward a unified analysis for source plane-wave migration *in* Geophysics. S129–S139.
- Liu, F., Stolt, R., Hanson, D., and Day, R., 2002, Plane wave source composition: An accurate phase encoding scheme for prestack migration: Plane wave source composition: An accurate phase encoding scheme for prestack migration, Soc. of Expl. Geophys., 72nd Ann. Internat. Mtg, 1156–1159.
- Nichols, D., 1994, Imaging in complex structures using band-limited green's function *in* Ph.D. thesis. Stanford University.
- Rietveld, W. E. A., 1995, Controlled illumination of prestack seismic migration *in* Ph.D. thesis. Delft University of Technology.
- Ristow, D., and Ruhl, T., 1994, Fourier finite-difference migration: Geophysics, **59**, 1882–1893.
- Sava, P., and Fomel, S., 2005, Riemannian wavefield extrapolation: Geophysics, **70**, T45–T56.
- Shan, G., 2006a, Optimized implicit finite-difference migration for TTI media: SEP- **125**.
- , 2006b, Optimized implicit finite-difference migration for vti media: 76th Ann. Internat. Mtg., Soc. of Expl. Geophys., Expanded Abstracts.
- Shan, G., and Biondi, B., 2004, Imaging overturned waves by plane-wave migration in tilted coordinates: 74th Ann. Internat. Mtg., Soc. of Expl. Geophys., Expanded Abstracts, 969–972.
- Shragge, J., 2006, Non-orthogonal Riemannian wavefield extrapolation *in* Expanded Abstracts. 75th SEG Ann. Gen. Meeting and Exhibition, 2236–2240.
- Whitmore, N. D., 1983, Iterative depth migration by backward time propagation: Iterative depth migration by backward time propagation, Soc. of Expl. Geophys., 53rd Ann. Internat. Mtg, Session:S10.1.
- , 1995, An imaging hierarchy for common angle plane wave seismograms *in* Ph.D. thesis. University of Tulsa.

Zhang, J., and McMechan, G. A., 1997, Turning wave migration by horizontal extrapolation: *Geophysics*, **62**, 291–297.

Zhang, Y., Sun, J., Notfors, C., Gray, S., Chernis, L., and Young, J., 2005, Delayed-shot 3D depth migration: *Geophysics*, **70**, E21–E28.

Prestack depth migration in elliptic coordinates

Jeff Shragge and Guojian Shan

ABSTRACT

We extend Riemannian wavefield extrapolation (RWE) to prestack migration using 2D elliptic coordinate systems. The corresponding 2D elliptic extrapolation wavenumber introduces only a slowness model stretch to the single-square-root operator, enabling the use of existing Cartesian implicit finite-difference extrapolators for propagating wavefields. A zero-offset migration example illustrates the advantages of elliptic coordinates in imaging overturning wavefields. Imaging tests of the SMAART JV Pluto 1.5 and BP velocity benchmark data sets illustrate that the RWE migration algorithm generates high-quality prestack migration images equal to, or better than, the corresponding Cartesian coordinate systems. We still require higher-order extrapolators for accurate propagation and imaging using one-way wave equations, even in situations where RWE geometries are employed.

INTRODUCTION

Wave-equation migration techniques based on one-way extrapolators are often used to accurately image structure in complex geologic environments. Most conventional downward continuation approaches, though, are unable to handle the steeply propagating or overturning wavefield components often important for imaging areas of interest. A number of novel imaging approaches address these issues through a judicious decomposition of recorded wavefields (e.g. plane-wave migration (Whitmore, 1995)), partial or complete propagation domain decomposition (e.g. Gaussian beam (Hill, 2001) or Riemannian wavefield extrapolation (Sava and Fomel, 2005), respectively), or a combination thereof (e.g. plane-wave migration in tilted coordinates (Shan and Biondi, 2004)). Importantly, these techniques have overcome many, though not all, issues in the practical application of one-way extrapolation operators.

Riemannian wavefield extrapolation is a method for propagating wavefields on generalized coordinate meshes. The central idea behind RWE is transforming the geometry of the full domain to one where the extrapolation axis is oriented in the general wavefield propagation direction. Solving the corresponding one-way extrapolation equations propagates the bulk of wavefield energy at angles relatively close to the extrapolation axis, thus improving wavefield extrapolation accuracy. One obvious application is generating high-quality Green's functions for point-sources, where a ray-based coordinate system is first generated by ray-tracing through the velocity model and then used as the skeleton on which to propagate wavefields.

Although the full-domain decomposition approach naturally adapts to propagation in a point-source ray-coordinate system, two unresolved issues make it difficult to apply RWE

efficiently in the prestack domain. First, receiver wavefields are usually broadband in plane-wave dip spectrum and cannot be easily represented by a single coordinate system (i.e. opposing dips propagate in opposing directions). Second, optimal source and receiver meshes usually do not share a common geometry. This factor is detrimental to algorithmic efficiency where generating images by correlating source and receiver wavefields: by existing on different grids they must both be interpolated to a common Cartesian reference frame prior to imaging. This leads to a significant number of interpolations that leaves the algorithm computationally unattractive.

The main goal of this paper is to specify a single coordinate system that enables the accurate propagation of high-angle and overturning components of both the source and receiver wavefields. To these ends, we demonstrate that an elliptic coordinate system is a “natural” prestack shot-profile migration coordinate system exhibiting nice geometric properties. An elliptic coordinate system originates on the surficial plane and steps outward as a series of ellipses. Thus, the coordinate system expands in a radial-like manner appropriate for computing accurate point-source Green’s functions, while allowing the receiver wavefield to propagate at steep (and overturning) angles to either side of the acquisition array where required. One consequence of using a 2D elliptic coordinate system is that the corresponding extrapolation wavenumber is specified by only a slowness model stretch. Thus, high-order implicit finite-difference (FD) extrapolators with accuracy up to 80° from the extrapolation axis (Lee and Suh, 1985) can be used to propagate wavefields, readily enabling accurate imaging of overturning waves at a cost competitive with Cartesian downward continuation.

This paper begins with a discussion as to why elliptic meshes are a natural coordinate system choice for shot-profile PSDM. We then develop an extrapolation wavenumber appropriate for propagating wavefields on 2D elliptic coordinate systems. We present a zero-offset example illustrating the ability of the scheme to image overturning wavefields. We then present prestack migration examples for the SMAART JV Pluto 1.5 and BP velocity benchmark data set and conclude with a brief discussion on the advantage of elliptic over more dynamic coordinate systems. Finally, Appendix A presents the wavenumbers for two 3D elliptic coordinate systems.

WHY ELLIPTIC COORDINATES?

Generating a good coordinate system for RWE prestack migration requires appropriately linking mesh geometry with the dynamics of propagating wavefields. Figure 1 illustrates this for an idealized shot-profile imaging experiment where source and receiver wavefields (S and R) are point sources defined at $[\mathbf{s}, \tau_s = 0]$ and $[\mathbf{r}, \tau_r = \tau]$ in a constant velocity medium $v(\mathbf{x})$. In this experimental setup, the wavefields expand outward as spherical wavefronts (dashed lines) described by

$$S(\mathbf{s}, \mathbf{x}; t) = \delta \left(t - \frac{\|\mathbf{x} - \mathbf{s}\|}{v(\mathbf{x})} \right) \quad \text{and} \quad R(\mathbf{r}, \mathbf{x}; t) = \delta \left(t - \tau - \frac{\|\mathbf{x} - \mathbf{r}\|}{v(\mathbf{x})} \right). \quad (1)$$

An image is generated by applying a correlation imaging condition at $t = 0$,

$$I(\mathbf{x}) = \sum_s \sum_r \delta \left[\tau - \left(\frac{\|\mathbf{x} - \mathbf{r}\| + \|\mathbf{x} - \mathbf{s}\|}{v} \right) \right], \quad (2)$$

which is the equation of ellipse (solid line). This suggests a natural link between elliptic coordinate systems and prestack migration, which is illustrated in Figure 1 by the similarity of the drawn isochron and the coordinate mesh.

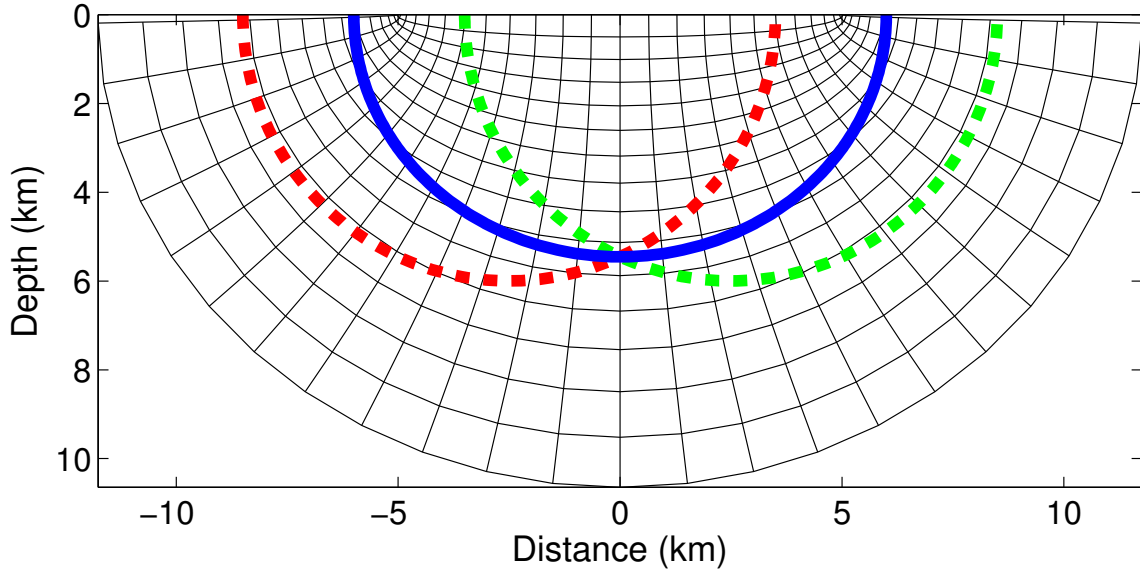


Figure 1: Idealized imaging experiment in a constant medium. Source and receiver wavefields (dashed lines) are expanding point sources described by fields $S(\mathbf{s}, \mathbf{x}; t)$ and $R(\mathbf{r}, \mathbf{x}; t)$. The corresponding image is an elliptic isochron surface $I(\mathbf{x})$ derived by cross-correlating the source and receiver wavefields (solid line). Note that the overlain elliptic coordinate system closely matches (though not identically) the isochron surface suggesting that this is a good coordinate system for RWE prestack shot-profile migration. jeff1-WhyEC [NR]

The keen observer will note that the foci of the elliptic coordinate system in Figure 1 were not specified relative to \mathbf{s} and \mathbf{r} . Shifting these points around alters both the mesh and how well it matches the isochrons. However, this represents two degrees of freedom that allow us to optimally match mesh geometry to the wavefield propagation dynamics.

ELLIPTIC COORDINATE EXTRAPOLATION

Propagating wavefields on elliptic meshes using RWE requires incorporating the geometry of the coordinate system directly in the extrapolation equations. This section derives the equations for propagation in the elliptic direction using the non-orthogonal RWE theory developed in Shragge (2006).

The analytic transformation between elliptic and Cartesian coordinate systems (see example in figure 1) is specified by,

$$\begin{bmatrix} x_1 \\ x_3 \end{bmatrix} = \begin{bmatrix} a \cosh \xi_3 \cos \xi_1 \\ a \sinh \xi_3 \sin \xi_1 \end{bmatrix}, \quad (3)$$

where $[x_1, x_3]$ are the underlying Cartesian coordinate variables, $[\xi_1, \xi_3]$ are the RWE elliptic coordinates, and a is a stretch parameter controlling the breadth of the coordinate system.

The metric tensor ($g_{ij} = \frac{\partial x_k}{\partial \xi_i} \frac{\partial x_k}{\partial \xi_j}$ with an implicit sum over index k) describing the geometry of the elliptic coordinate system is given by,

$$[g_{ij}] = \begin{bmatrix} A^2 & 0 \\ 0 & A^2 \end{bmatrix}, \quad (4)$$

where $A = a\sqrt{\sinh^2 \xi_3 + \sin^2 \xi_1}$. The determinant of the metric tensor is $|\mathbf{g}| = A^4$, leading to an associated (inverse) metric tensor given by,

$$[g^{ij}] = \begin{bmatrix} A^{-2} & 0 \\ 0 & A^{-2} \end{bmatrix}. \quad (5)$$

The weighted metric tensor (the product of the metric tensor and the determinant: $m^{ij} = \sqrt{|\mathbf{g}|} g^{ij}$) is given by,

$$[m^{ij}] = \begin{bmatrix} 1 & 0 \\ 0 & 1 \end{bmatrix}. \quad (6)$$

The corresponding extrapolation wavenumber is generated by using tensors g^{ij} and m^{ij} in the wavenumber expression for general 3D non-orthogonal coordinate systems (equations 13 and 14 in Shragge (2006)). Note that even though the elliptic coordinate system varies spatially, the local curvature parameters in the weighted metric tensor are constant. Thus, the extrapolation wavenumber, k_{ξ_3} , for recursive wavefield extrapolation stepping outward in concentric ellipses is,

$$k_{\xi_3} = \pm \sqrt{A^2 s^2 \omega^2 - k_{\xi_1}^2}, \quad (7)$$

where $A = a\sqrt{\sinh^2 \xi_3 + \sin^2 \xi_1}$, s is slowness (inverse of velocity), and k_{ξ_1} is the orthogonal wavenumber. Equation 7 is an exact representation of the extrapolation wavenumber and does not contain any kinematic approximations. The most striking observation about this expression is that the sole difference between propagation in elliptic and Cartesian coordinate systems is a smooth multiplicative slowness model stretch. Otherwise, existing Cartesian extrapolators can be used for propagating wavefields.

2D SYNTHETIC TESTS

This section presents 2D test results for a zero-offset overturning wavefield and the prestack Pluto and BP velocity benchmark (Billette and Brandsberg-Dahl, 2005) data sets. We propagate all wavefields with the isotropic one-way extrapolator described in Lee and Suh (1985)

on a elliptic coordinate system defined by equation 3 assuming effective slowness fields of $A(\xi_1, \xi_3)s(\xi_1, \xi_3)$ where stretch factor A is defined above. We use generic zero-offset and shot profile migration algorithms employing the extrapolation wavenumber in equation 7 and then transform the results back to Cartesian using sinc-interpolation.

Poststack migration of overturning waves

The first elliptic coordinate migration example uses the zero-offset data set shown in the upper panel of Figure 2. The data were generated by Sava (2006) from an adapted Sigsbee model (lower panel) using exploding reflector (two-way time-domain FD) modeling from all salt body edges. Migrated multiples are present in the image below because we apply no multiple suppression prior to imaging. Note also that the time axis begins at 10 s and extends to 30 s. Figure 3 shows the migrated image obtained by wavefield extrapolation in elliptic coordinates.

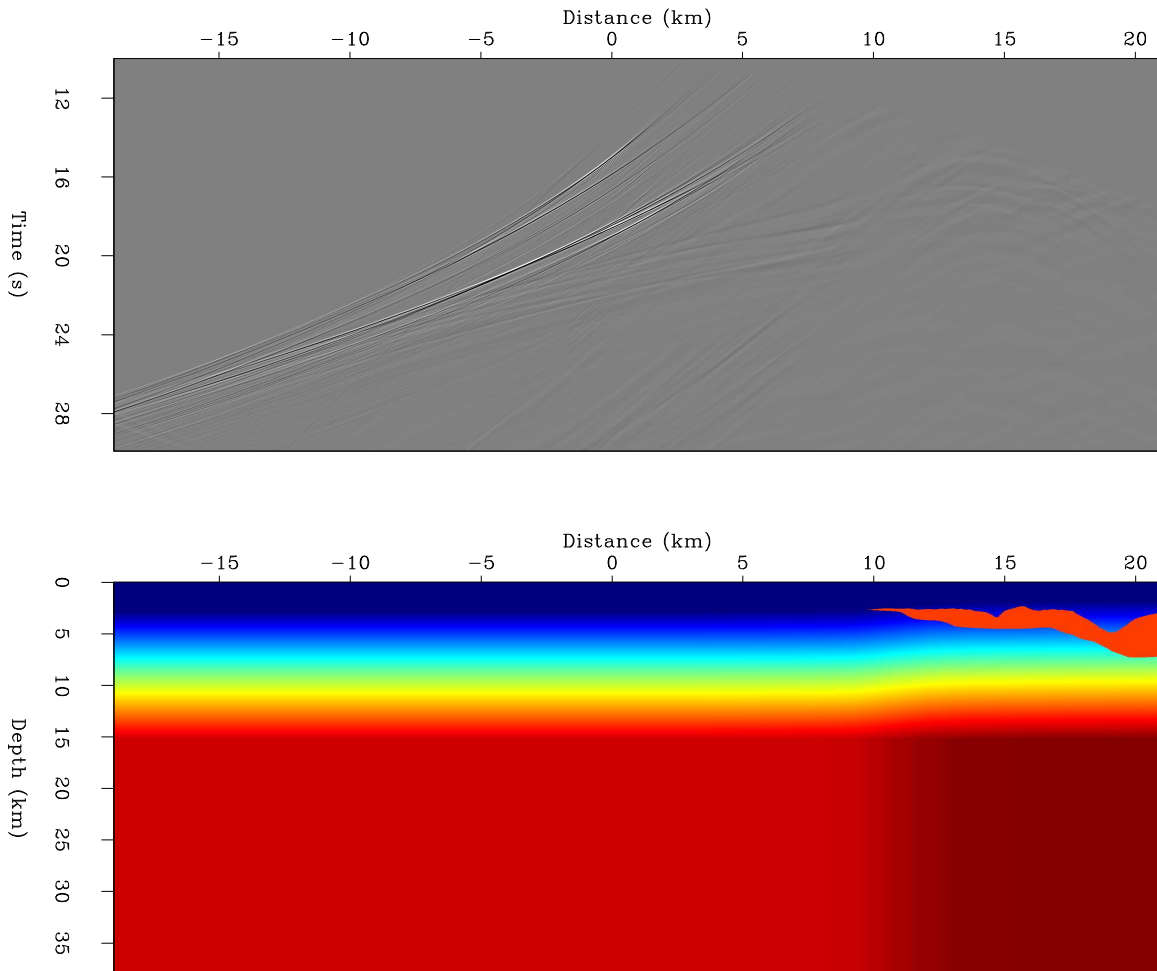


Figure 2: Overturning wavefield problem. Top: Exploding reflector data set generated through below model. Note that the time axis begins at 10s. Bottom: Migration velocity model.

jeff1-OverProb [ER]

The upper left panel shows the prestack migration result for a monochromatic wavefield with the elliptic coordinate system overlain. The monochromatic wavefield overturns and arrives at the dipping salt flank at normal incidence, as expected for exploding reflector modeling. Note also that the wavefield energy propagates at fairly steep angles to the extrapolation axis indicating that high-angle accuracy extrapolators are necessary for accurate imaging. The upper right panel shows the same image as the upper left, but in the elliptic coordinate system. This figure similarly depicts the monochromatic wavefield propagating at high angle to the coordinate system. The lower left and right panels show the broadband image results in Cartesian and elliptic coordinate systems, respectively. The steep salt flanks beneath the salt nose are accurately positioned, indicating that the potential for imaging overturning waves in elliptic coordinates with high-angle accuracy propagators.

Prestack Pluto 1.5

Figure 4 presents a 2D prestack RWE migration test for the Pluto model. The top and middle panels show the elliptic coordinate and Cartesian migration results using 80° FD extrapolators. The bottom panel presents another Cartesian migration, but generated with lower-order phase-shift plus interpolation (PSPI) extrapolators. Note that the steeply dipping flanks on the left-most salt body are well-imaged in the upper two panels, but not as well in the lower panel. This suggests that higher-order extrapolators, rather than a new coordinate system, are needed to accurately image this salt flank. The image of the multiples beneath this salt body is more accurately migrated in the elliptic coordinate system, suggesting improved extrapolation has occurred in elliptic coordinates.

Prestack BP Velocity Model

We performed a second prestack migration test in elliptic coordinates using the BP velocity benchmark model. The top panel presents the RWE shot-profile migration result in elliptic coordinates, while the bottom panel shows Cartesian plane-wave image constructed with the same FD operators. The salt body on the left is well-imaged in both the elliptic and Cartesian coordinate images. The flanks of the salt body on the right, known to be illuminated by overturning and prismatic waves, are better imaged in the elliptic system. We generated the RWE image using a code that included neither source compensation nor optimal placement of the foci of the coordinate system. Future work includes incorporating both of these factors, which should improve the image further.

Discussion

One question naturally arising when using RWE propagation in prestack migration is how does one obtain the optimal trade-off between: i) incorporating wave-propagation effects directly in a more dynamic coordinate system (e.g. through a ray-traced coordinate system); and ii) using higher-order extrapolators in coordinate systems not strictly conformal to the wavefield propa-

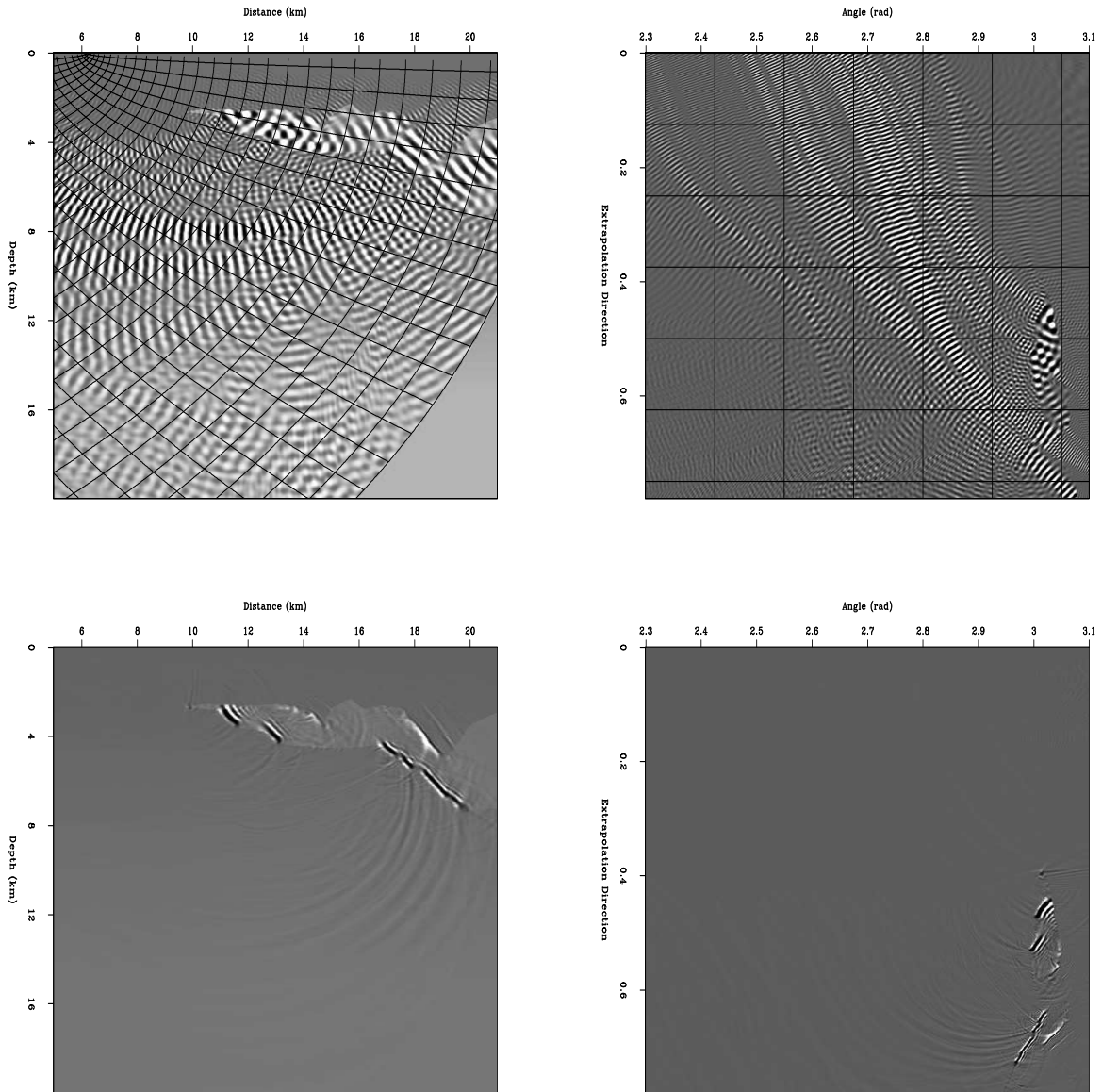


Figure 3: Post-stack migration of overturning waves. Upper left: Overturning monochromatic Cartesian wavefield with overlain elliptic coordinates. Top right: As in upper left panel, but for elliptic coordinates. Lower left: Broadband overturning wave image in Cartesian coordinates. Lower right: As in lower left panel, but for elliptic coordinates. [jeff1-XM](#) [CR]

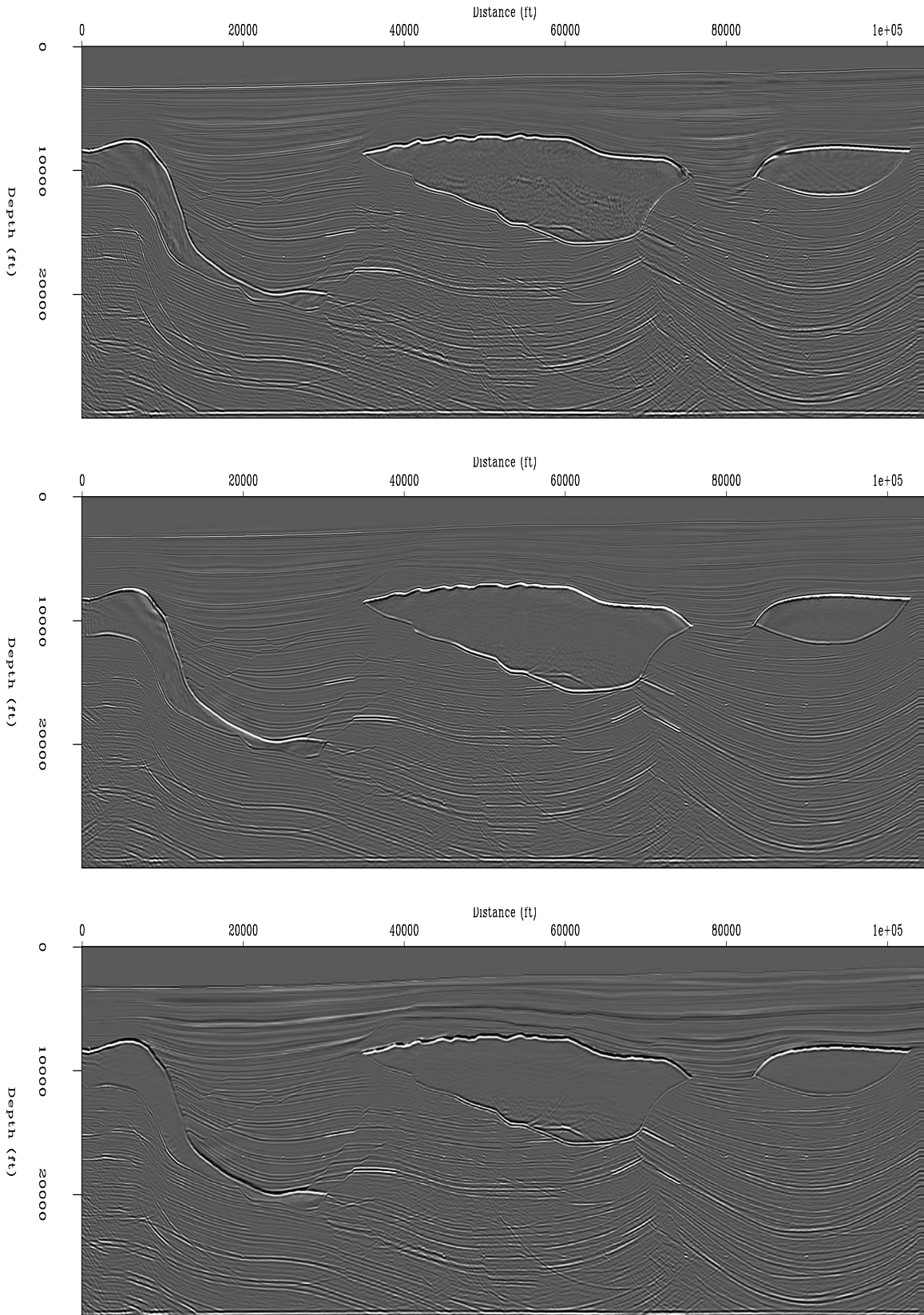


Figure 4: Pluto migration images for various coordinate systems and propagators. Top: Elliptic coordinates with FD propagators. Middle: Cartesian coordinates with FD propagators. Bottom: Cartesian coordinates with PSPI propagators. `jeff1-PLUTO` [CR]

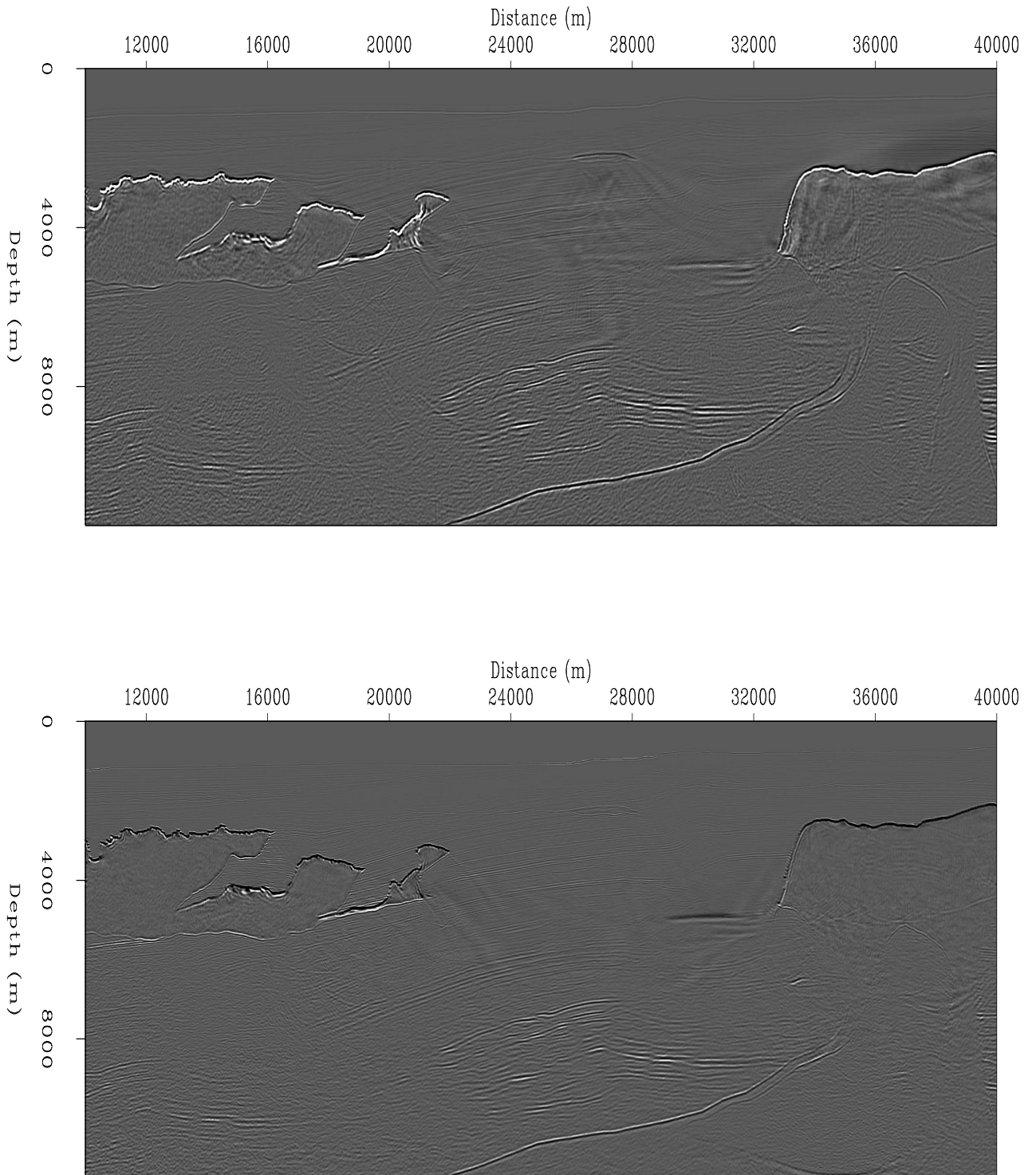


Figure 5: BP velocity synthetic migration results. Top panel: Elliptic coordinate migration result using FD propagators. Bottom panel: Cartesian migration result using FD propagators.
jeff1-BPM [CR]

gation direction. Based on our experience, we argue that a parametric coordinate system (such as tilted Cartesian or elliptic meshes) offers the advantage of being able to develop analytic extrapolation operators that readily lend themselves to accurate, high-order, finite-difference schemes. Importantly, while coordinate systems based on ray-tracing better conform to the direction of wavefield extrapolation, numerically generated meshes do not lend themselves as easily to high-order extrapolators due to the greater number, and spatially variability of, the mixed-domain coefficients.

A second question worth addressing is how can the elliptic coordinate approach be extended to 3D prestack shot-profile migration. Appendix A presents two candidate coordinate systems. The elliptic cylindrical system extends the 2D elliptic by constant factor in the third dimension and realizes a fairly basic expression for the extrapolation wavenumber. This coordinate system, though, does not propagate overturning waves in the cross-line direction. The second coordinate system, oblate spheroidal, incorporates more spherical geometry and enables overturning wave propagation in the cross-line direction, but yields a more complicated extrapolation wavenumber. As expected, both of these coordinate systems reduce to the above 2D elliptic expression for a zero cross-line wavenumber.

CONCLUDING REMARKS

This paper extends the theory of Riemannian wavefield extrapolation to prestack shot-profile migration. An elliptic coordinate system is chosen because it generally conforms to the direction of propagation and allows high-angle propagation of source and receiver wavefields. Post-stack migration results of an overturning wavefield data set validate the approach, while the 2D prestack imaging results show that the RWE migration algorithm generates high-quality migration images equal to, or better than, the corresponding Cartesian domain. Finally, because one can develop analytic extrapolation wavenumbers, we argue that parametric coordinate systems are an optimal trade-off between the competing constraints of dynamic constraints and simplicity in coordinate system design.

ACKNOWLEDGMENTS

We thank Biondo Biondi, Ben Witten and Brad Artman for enlightening discussions. We thank the SEP sponsors for their continuing support. We acknowledge the SMAART JV consortium for the Pluto data and BP for the synthetic velocity data set.

REFERENCES

- Billette, F. and S. Brandsberg-Dahl, 2005, The 2004 BP velocity benchmark: 67th meeting, Eur. Assn. Geosci. Eng., B035.
- Hill, N. R., 2001, Prestack Gaussian-beam depth migration: *Geophysics*, **66**, 1240–1250.
- Lee, M. W. and S. Y. Suh, 1985, Optimization of one-way wave-equations (short note): *Geophysics*, **50**, no. 10, 1634–1637.
- Sava, P. C. and S. Fomel, 2005, Riemannian wavefield extrapolation: *Geophysics*, **70**, T45–T56.
- Sava, P., 2006, Imaging overturning reflections by Riemannian Wavefield Extrapolation: *Journal of Seismic Exploration*, **15**, 209–223.
- Shan, G. and B. Biondi, 2004, Imaging overturned waves by plane-wave migration in tilted coordinates: 74th Ann. Internat. Mtg., Soc. of Expl. Geophys., Expanded Abstracts, 969–972.
- Shragge, J., 2006, Non-orthogonal Riemannian wavefield extrapolation: 75th SEG Ann. Gen. Meeting and Exhibition, Expanded Abstracts, 2236–2240.
- Whitmore, N. D., 1995, An imaging hierarchy for common angle plane wave seismograms: University of Tulsa, Ph.D. thesis.

APPENDIX A - 3D ELLIPTIC COORDINATE SYSTEMS

This appendix develops the dispersion relationship for extrapolating waves for two 3D elliptic coordinate systems: elliptic cylindrical and oblate spheroidal.

Elliptic Cylindrical Coordinates

The analytic transformation between the elliptic cylindrical and Cartesian coordinate systems (see example in figure A-1). A elliptical coordinate system is specified by,

$$\begin{bmatrix} x_1 \\ x_2 \\ x_3 \end{bmatrix} = \begin{bmatrix} a \cosh \xi_3 \cos \xi_1 \\ \xi_2 \\ a \sinh \xi_3 \sin \xi_1 \end{bmatrix}, \quad (\text{A-1})$$

where $[x_1, x_2, x_3]$ are the underlying Cartesian coordinate variables, $[\xi_1, \xi_2, \xi_3]$ the RWE elliptic cylindrical coordinates, and parameter a a stretch parameter controlling the breadth of the coordinate system. The metric tensor describing the geometry of the elliptic coordinate system

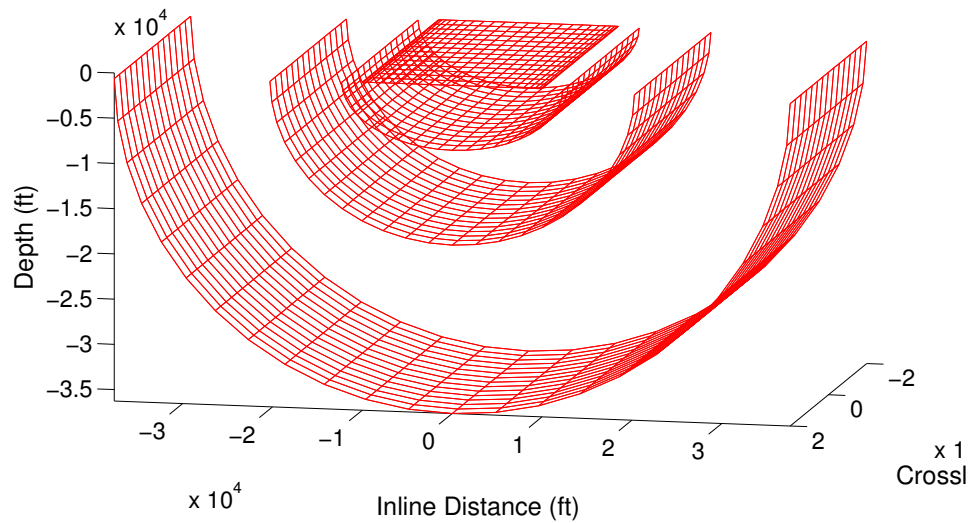


Figure A-1: Four sample extrapolation steps of an elliptic cylindrical coordinate system.

jeff1-ECC [NR]

is given by,

$$[g_{ij}] = \begin{bmatrix} A^2 & 0 & 0 \\ 0 & 1 & 0 \\ 0 & 0 & A^2 \end{bmatrix}, \quad (\text{A-2})$$

where $A = a\sqrt{\sinh^2 \xi_3 + \sin^2 \xi_1}$. The determinant of the metric tensor is: $|\mathbf{g}| = A^4$. The associated (inverse) metric tensor is given by,

$$[g^{ij}] = \begin{bmatrix} A^{-2} & 0 & 0 \\ 0 & 1 & 0 \\ 0 & 0 & A^{-2} \end{bmatrix}, \quad (\text{A-3})$$

and weighted metric tensor ($m^{ij} = \sqrt{|\mathbf{g}|} g^{ij}$) is given by,

$$[m^{ij}] = \begin{bmatrix} 1 & 0 & 0 \\ 0 & A^2 & 0 \\ 0 & 0 & 1 \end{bmatrix}. \quad (\text{A-4})$$

The corresponding extrapolation wavenumber is generated by using tensors g^{ij} and m^{ij} in the general wavenumber expression for 3D non-orthogonal coordinate system Shragge (2006). Note that even though the elliptic coordinate system varies spatially, the local curvature parameters remain constant: $n_1 = n_2 = n_3 = 0$. Thus, inserting the values of g^{ij} , m^{ij} and n_j leads to the following extrapolation wavenumber for stepping outward in concentric ellipses k_{ξ_3} ,

$$k_{\xi_3} = \pm \sqrt{A^2 s^2 \omega^2 - k_{\xi_1}^2 - A k_{\xi_2}^2}. \quad (\text{A-5})$$

The wavenumber for 2D extrapolation in elliptic coordinates reduces to

$$k_{\xi_3} \Big|_{k_{\xi_2}=0} = \pm \sqrt{A^2 s^2 \omega^2 - k_{\xi_1}^2}. \quad (\text{A-6})$$

Note that equation A-5 does not contain a kinematic approximation of the extrapolation wavenumber.

Oblate Spheroidal Coordinates

The analytic transformation between the oblate spheroidal and Cartesian coordinate systems (see example in figure A-2). A elliptical coordinate system is specified by,

$$\begin{bmatrix} x_1 \\ x_2 \\ x_3 \end{bmatrix} = \begin{bmatrix} a \cosh \xi_3 \cos \xi_1 \cos \xi_2 \\ a \cosh \xi_3 \cos \xi_1 \sin \xi_2 \\ a \sinh \xi_3 \sin \xi_1 \end{bmatrix}. \quad (\text{A-7})$$

where, again, a is a stretch parameter controlling the breadth of the coordinate system. The metric tensor g_{ij} describing the geometry of oblate spheroidal coordinates is given by,

$$[g_{ij}] = \begin{bmatrix} A^2 & 0 & 0 \\ 0 & B^2 & 0 \\ 0 & 0 & A^2 \end{bmatrix}, \quad (\text{A-8})$$

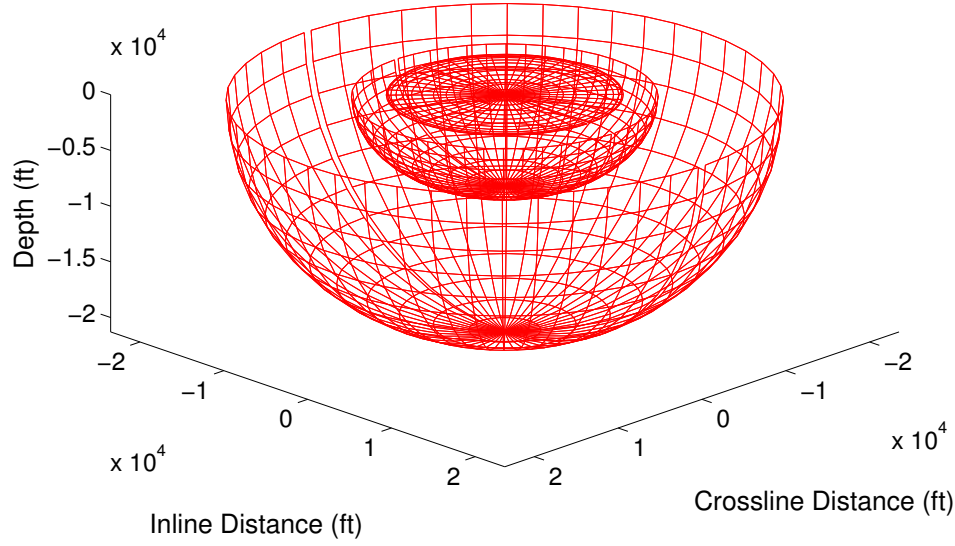


Figure A-2: Three sample extrapolation steps of an oblate spheroidal coordinate system. jeff1-OSC [NR]

where $A = a\sqrt{\sinh^2 \xi_3 + \sin^2 \xi_1}$ and $B = a \cosh \xi_3 \cos \xi_1$. The determinant of the metric tensor is: $|\mathbf{g}| = A^4 B^2$. The associated (inverse) metric tensor is given by,

$$[g^{ij}] = \begin{bmatrix} A^{-2} & 0 & 0 \\ 0 & B^{-2} & 0 \\ 0 & 0 & A^{-2} \end{bmatrix}. \quad (\text{A-9})$$

and weighted metric tensor is given by,

$$[m^{ij}] = \begin{bmatrix} B & 0 & 0 \\ 0 & \frac{A^2}{B} & 0 \\ 0 & 0 & B \end{bmatrix}. \quad (\text{A-10})$$

The corresponding extrapolation wavenumber is generated by inputting tensors g^{ij} and m^{ij} into the generalized wavenumber expression for 3D non-orthogonal coordinate systems (Shragge, 2006). Unlike in elliptic cylindrical coordinates, though, the oblate spheroidal system has non-stationary n^i coefficients: $n^1 = a \cosh \xi_3 \sin \xi_1$, $n^2 = 0$ and $n^3 = a \sinh \xi_3$. The resulting extrapolation wavenumber is

$$k_{\xi_3} = \frac{i \tanh \xi_3}{2} \pm \sqrt{A^2 s^2 \omega^2 - k_{\xi_1}^2 - \frac{\sqrt{\sinh^2 \xi_3 + \sin^2 \xi_1}}{\cosh \xi_3 \cos \xi_1} k_{\xi_2}^2 + i k_{\xi_1} \tan \xi_1 - \tanh^2 \xi_3}. \quad (\text{A-11})$$

The wavenumber for 2D extrapolation in elliptic coordinates reduces to

$$k_{\xi_3}|_{k_{\xi_2}=0} = \pm \sqrt{A^2 s^2 \omega^2 - k_{\xi_1}^2}. \quad (\text{A-12})$$

A tutorial on optimizing time domain finite-difference schemes: "Beyond Holberg"

John T. Etgen

ABSTRACT

Time-domain finite-difference solutions to the wave equation are a standard method for modeling seismic wave propagation, but they see limited use in data processing because they are expensive to compute. Given the resurgence of interest in reverse-time migration, anything that improves the performance and accuracy of the finite-difference method may be worthwhile. Additionally, the design problem for optimal finite-difference operators is a "simple and approachable" problem for teaching non-linear least squares. The standard solution for improving the finite-difference method is to use long spatial difference operators. However, there are computational reasons why it might be preferable to use spatially compact stencils, assuming they can be made accurate enough.

INTRODUCTION

All finite-difference solutions to wave equations in media with more than one spatial dimension have numerical phase and group velocities that differ from the desired phase and group velocities of the "true" solution. The errors manifest themselves as "dispersion"; different frequencies propagate at different speeds. This leads to progressively greater distortion of the propagating waveforms with increasing time and propagation distance. For example, the standard second-order in time, second-order in space finite-difference approximation to the 2D or 3D acoustic wave equation needs a large degree of oversampling of the spatial axes (ten points per wavelength or more) to achieve remotely reasonable accuracy. Thus, despite its simplicity, it's almost never used in practice. Finite difference methods that use spatial difference operators with more points, so called high-order finite-difference methods (Dablain, 1986; Etgen, 1986, 1988), are commonly used to improve the accuracy and efficiency of the method, as well as reduce its memory requirements, which is particularly important in 3D (Wu et al., 1996). Most original high-order finite-difference methods used a Taylor-series approach to derive spatial difference coefficients, while employing second-order differences in time to preserve the simplicity of a 3-point time marching scheme. Dablain (1986) is probably the earliest, most thorough description of this method. In the same paper, Dablain showed how to create a time marching algorithm that has fourth-order accuracy in time by applying the spatial difference operator in a two-term cascade and weighting the terms of the cascade appropriately to cancel the leading order error of the time discretization. The ultimate quest for accuracy often combines higher-order time expansion with the Fourier pseudo-spectral method (Reshef

et al., 1988) for the spatial derivatives. That approach can be generalized to many terms, ultimately leading to orthogonal-polynomial series solutions that have spectral accuracy (Tal-Ezer et al., 1987). The complexity involved in implementing these "very accurate" methods means that they don't see much large-scale practical application, particularly for reverse-time migration. They are also difficult to implement as "out-of-core" solutions or on a cluster of machines using message passing; techniques that are often necessary for large 3D problems. So, we return to the finite-difference method in the hope of creating an accurate scheme that is computationally flexible and efficient. Difference operators derived from Taylor-series expansion are "conservative" in that they have very high accuracy for low wavenumbers, but in achieving that, they waste some potential accuracy improvements at higher wavenumbers. In a classic paper, Holberg (1987) shows how to find improved spatial difference operators using optimization techniques. Most modern high-order finite-difference techniques use his method to create spatial-difference coefficients. But I believe there are a couple of fundamental shortcomings in Holberg's design; so I revisited the design problem for optimum finite-difference schemes. In one space dimension, the accuracy of the second-order in time, second-order in space finite-difference method improves the closer the time step size is to the stability limit, $v \Delta t / \Delta x = 1$. It's an interesting curiosity that the two sources of error cancel exactly when taking the time-step size at exactly the stability limit. While this exact cancellation does not exist for the second-order finite-difference method in any higher number of spatial dimensions, it does point out that there is an opportunity to "tune" the spatial-difference coefficient design by trading it off against the errors generated by the time discretization. I also felt that the classical "equiripple" filter design technique that Holberg used leads to unacceptably large errors at low and moderate wavenumbers, particularly when using relatively compact difference operators.

FINITE DIFFERENCE STENCILS BY LEAST SQUARES

The approach I take here begins in the same vein as Holberg; I set up an optimization problem to find spatial difference coefficients that minimize the dispersion of the resulting finite-difference scheme. First we need an expression for the numerical "velocity" of the finite-difference scheme as a function of frequency and propagation direction expressed in terms of the finite-difference coefficients. There are 2 commonly used (and ultimately equivalent) approaches to accomplish this. The first approach is to substitute the expression for a trial plane-wave solution into the difference expression. The second approach, which I follow here, is to take a few liberties with Fourier transforms and compute the multi-dimensional Fourier transform of the difference scheme directly. To illustrate this, let's take the 2D acoustic wave equation discretized with second-order finite-differences.

$$\begin{aligned} \frac{1}{\Delta t^2}(U(x, z, t + \Delta t) - 2U(x, z, t) + U(x, z, t - \Delta t)) = \\ \frac{v^2}{\Delta x^2}(U(x + \Delta x, z, t) - 2U(x, z, t) + U(x - \Delta x, z, t)) + \\ \frac{v^2}{\Delta z^2}(U(x, z + \Delta z, t) - 2U(x, z, t) + U(x, z - \Delta z, t)). \end{aligned}$$

Moving Δt and recalling how to transform a series of impulses, write the Fourier transform of the difference equation as:

$$(2 \cos(\omega \Delta t) - 2)U(\omega, k_x, k_z) = \frac{v^2 \Delta t^2}{\Delta x^2} (2 \cos(k_x \Delta x) - 2)U(\omega, k_x, k_z) + \frac{v^2 \Delta t^2}{\Delta z^2} (2 \cos(k_z \Delta z) - 2)U(\omega, k_x, k_z).$$

The numerical phase velocity is given simply by the ratio:

$$V_{phase} = \frac{\omega(k_x, k_z, v, \Delta x, \Delta z, \Delta t)}{\sqrt{k_x^2 + k_z^2}} \quad (1)$$

where I have left the dependence on all possible variables in the expression. At this point, I make my first deviation from the method that Holberg used. Holberg used group velocity in his expressions and ultimately matched the numerical group velocity of the difference scheme to the desired velocity. In the method here, I use phase velocity. One of the nice things about using phase velocity is that it is straight-forward to make simulated "far field signatures" of your finite-difference method without going to the trouble of coding the actual finite-difference algorithm. One possible criticism of using phase velocities is that they tend to show less variability than group velocities, that is, you might think that phase velocities understate the dispersion. Since phase velocities are computed from the ratio of ω and $|\mathbf{k}|$, phase velocities are more sensitive to the lower wavenumbers (and thus the lower frequencies) than group velocities which are computed from the slope of ω as a function of \mathbf{k} . I'll leave it as an exercise for the reader to show whether weighting functions would make the two approaches equivalent. The second and more important difference from Holberg's derivation is that I do not consider the error of the time discretization to be negligible. Near the beginning of his paper, Holberg assumes that computational time step sizes will be small enough to not contribute to the error of the scheme. For long (hence hopefully accurate) spatial difference operators, the error from time discretization is often the *largest* error at moderate frequencies/wavenumbers. Better still, the error from the time discretization is usually opposite in sense from that of the space discretization, so the two can be balanced against each other for improved accuracy. Making time steps coarser tends to lead to phase velocities that are too fast while inaccuracy in the spatial difference operator leads to phase velocities that are too slow. It's that fact that leads to the curious situation in 1D where the two sources of error can be balanced exactly. Although there's no way to balance the errors exactly in 2D or 3D, we should use an error expression that captures the contributions from both the time and space discretizations and balances them against each other to the best possible effect. I begin by creating an expression for the sum over the wavenumber domain of the squared differences between the numerical phase velocity of the difference scheme and the desired phase velocity;

$$Err = \sum_{\mathbf{k}} W(\mathbf{k}) [V_{phase}(\mathbf{k}) - V_{true}]^2. \quad (2)$$

Then we need the expression for V_{phase} as a function of the coefficients we wish to find. I express the difference operator for a second spatial derivative with respect to x as:

$$\frac{\partial^2 U}{\partial x^2} \approx \frac{1}{\Delta x^2} \sum_{i=1}^n a_i [U(x + i \Delta x) - 2U(x) + U(x - i \Delta x)]. \quad (3)$$

You'll notice that the difference operator, chosen this way, is essentially a series of weighted and gapped standard second difference operators. I did this to preserve the correct behavior of the approximate second derivative at zero wavenumber. Using the corresponding expressions for the differences in z (and in 3D y), Fourier transforming them, and using the expression from equation 2 for the Fourier transform of the time difference expression write:

$$2 \cos(\omega \Delta t) - 2 = \frac{v^2 \Delta t^2}{\Delta x^2} \sum_{i=1}^n a_i [2 \cos(ik_x \Delta x) - 2] + \frac{v^2 \Delta t^2}{\Delta z^2} \sum_{i=1}^n b_i [2 \cos(ik_z \Delta z) - 2] . \quad (4)$$

To compress the notation a bit, introduce:

$$\begin{aligned} F_x(\mathbf{a}) &= \sum_{i=1}^n a_i [2 \cos(ik_x \Delta x) - 2] \\ F_z(\mathbf{b}) &= \sum_{i=1}^n b_i [2 \cos(ik_z \Delta z) - 2] . \end{aligned}$$

Finally I arrive at a reasonably compact expression for V_{phase} as a function of the coefficients I seek and other parameters such as velocity, time step size and grid spacing.

$$V_{phase}(\mathbf{a}, \mathbf{b}) = \frac{\arccos \left[\frac{v^2 \Delta t^2}{2 \Delta x^2} F_x(\mathbf{a}) + \frac{v^2 \Delta t^2}{2 \Delta z^2} F_z(\mathbf{b}) + 1 \right]}{\Delta t |\mathbf{k}|} . \quad (5)$$

To find the coefficient vectors \mathbf{a} and \mathbf{b} , differentiate the sum squared error (equation 4) with respect to each a_i and b_i and set each of those equations equal to zero. Of course if Δx and Δz are the same, we can use the same coefficients for each, but for now I'll keep the expressions general because we want the method to work when $\Delta x \neq \Delta z$.

$$\begin{aligned} \frac{\partial Err}{\partial a_1} &= 0 \\ \frac{\partial Err}{\partial a_2} &= 0 \\ &\vdots \\ \frac{\partial Err}{\partial a_n} &= 0 \\ \frac{\partial Err}{\partial b_1} &= 0 \\ \frac{\partial Err}{\partial b_2} &= 0 \\ &\vdots \\ \frac{\partial Err}{\partial b_n} &= 0 \end{aligned}$$

This is a system of non-linear equations in the unknowns a_i and b_i . To solve them, I use a Gauss Newton iterative method which leads to the following system of linear equations (notation compressed a bit further):

$$\begin{aligned} \frac{\partial^2 Err}{\partial a_1^2} \Delta a_1 & \quad \frac{\partial^2 Err}{\partial a_1 \partial a_2} \Delta a_2 & \cdots & \quad \frac{\partial^2 Err}{\partial a_1 \partial b_n} \Delta b_n & = & -\frac{\partial Err}{\partial a_1} \\ \frac{\partial^2 Err}{\partial a_1 \partial a_2} \Delta a_1 & \quad \frac{\partial^2 Err}{\partial a_2^2} \Delta a_2 & \cdots & \quad \frac{\partial^2 Err}{\partial a_2 \partial b_n} \Delta b_n & = & -\frac{\partial Err}{\partial a_2} \\ & \vdots & & \vdots & = & \vdots \\ \frac{\partial^2 Err}{\partial a_1 \partial b_n} \Delta a_1 & \quad \frac{\partial^2 Err}{\partial a_2 \partial b_n} \Delta a_2 & \cdots & \quad \frac{\partial^2 Err}{\partial b_n^2} \Delta b_n & = & -\frac{\partial Err}{\partial b_n} . \end{aligned}$$

I solve these equations using the conjugate gradient method, and perform outer iterations until the gradient of the sum squared error doesn't decrease, which usually takes 3 or 4 iterations.

APPLICATION

We use finite-difference methods to propagate waves in heterogeneous media, so the spatial and temporal grid sizes are determined by the range of velocities in the model and the frequency content of the waves we wish to propagate. The maximum frequency and the minimum velocity combine with the accuracy of our scheme to limit the maximum spatial grid size that can be used. Then, given the spatial grid sizes, the maximum velocity in the model sets the maximum time step size that we can use for stability reasons. Because of all this, each model (each unique combination of v_{min} , v_{max} , Δx , Δz , and Δt) will have it's own set of optimum coefficients. In practice I just compute a table of coefficients for the case at hand and build precomputed "updating stencils". This wastes memory somewhat (maybe more than somewhat), but in principle can lead to a highly efficient code.

Right answer to the wrong question

Figure 1 shows the relative phase velocity error, clipped at 1%, for a Taylor-coefficient, sixth-order in space, second-order in time scheme for the 2D acoustic wave equation operating for the case $v = .33$, $dt = 0.3$, $\Delta x = 1.0$, $\Delta z = 1.0$. The spatial stencil for this scheme occupies the central point and 3 points to the sides on each spatial axis. I chose this particular combination of v and Δt to simulate the situation where waves are propagating in the low-velocity portion of a model that has a $v_{max}:v_{min}$ ratio of 3:1. This is where dispersion tends to be the greatest, so we want as much accuracy from our stencil as possible. In some sense, models with a large $v_{max}:v_{min}$ ratio are the most aggravating for the finite-difference method. Fine spatial sampling has to be used because of the low velocities, but then *really* small time steps have to be used because of the high velocities. As you might recall, accuracy tends to be better when you can run larger time steps since the error from the time differencing will partially cancel the error from the spatial differences. White areas of the wavenumber plane in Figure 1 have numerical phase velocities less than .99 times the correct phase velocity. Grey-colored areas have phase velocities within +/- 1% of the correct value, with neutral grey "perfect". Black areas (which there are none in this figure), would be wavenumbers that have phase velocities more than 1% greater than the correct value. This scheme is only accurate (to 1% anyway) out to about 45% of spatial Nyquist, requiring a sammple rate of about 4.4 points per shortest wavelength. This plot shows you the behavior of a finite-difference scheme with Taylor-series derived coefficients quite well; excellent accuracy at zero wavenumber and a flatish response out to some cutoff, then rapidly increasing error.

So, the hope is to use the optimization method described above to create a set of spatial differencing coefficients that will push the 1% error cutoff (or whatever error cutoff you wish) to higher wavenumbers, which enables the scheme to propagate higher frequencies on the same grid for the same cost. Figure 2 shows the relative phase velocity error for just such an "opti-

mized" 7 point second-difference operator that occupies the same stencil as the Taylor method shown in Figure 1, for the same velocity, time-step and spatial sample rates. The weight term used in the objective function (equation 4) was $1/|\mathbf{k}|$ for \mathbf{k} out to 80% of Nyquist with a superimposed taper down to zero weight at 90% of Nyquist. This is a pretty good illustration of "trying to do too much" and least squares methods doing exactly what you told them to do, not necessarily what you *really* want them to do. It's probably important to state that the least squares method is not failing per se. Figure 3 shows a graph of the relative phase velocity error along the k_z axis and we can see the approximate "equiripple" behavior of the error, typical of a least squares solution over the wavenumber band we allowed in the specification of the error function. This behavior arises because the error at the high wavenumbers is naturally larger than at low wavenumbers. With only a few coefficients, there's no way to correct that error without compromising the behavior at low wavenumbers. But in fact, if we were only going to propagate a short distance, this scheme has less than 1% phase velocity error out to almost 80% of Nyquist.

Asking a better question

We need a little more "intelligence" in what we ask least squares to do. In the expression for the sum squared error, the standard approach is to fit a perfectly flat V_{phase} . Even though I took some care, as described above, to weight the objective function appropriately over wavenumbers, and restrict the fit to a range of \mathbf{k} ; I found that trying to fit a "perfect" V_{phase} leads to difficulties. Rather than fit a flat V_{phase} , I fit my "low-order" compact stencil response to the response of a higher-order method. In what follows and in practice, I fit to the response of a much higher-order method with a small time-step size, and Taylor-series derived spatial difference coefficients. In addition to fitting a higher-order Taylor response, I also weight the error at each individual wavenumber by $1/|\mathbf{k}|^{1+\epsilon}$, where $0 < \epsilon \leq .5$, just to bias the fit to the low wavenumbers a bit. Now, I admit this is a somewhat "personal" choice, biased by my desire to preserve tight error bounds on low and mid-range wavenumbers. I purposefully do not want an equiripple phase velocity response, because a compact stencil just has too few degrees of freedom to keep the ripples to an acceptable level.

Figure 4 shows a plot of relative phase velocity error for a new set of "optimum" coefficients designed to preserve "good" behavior at low and moderate wavenumbers while improving the response at higher wavenumbers compared to Taylor coefficients. This scheme is very accurate out to 55% of Nyquist, requiring about 3.6 points per shortest wavelength. This phase velocity spectrum looks reminiscent of the phase velocity spectrum from a higher-order Taylor method, more of a "pseudo-maxi-flat" response than an "equiripple response", which is exactly what I wanted. Whether this particular scheme is acceptable or not depends on the amount of oversampling we can tolerate which depends on the architecture of the computer we plan to use. The method can design larger (or down to two degrees of freedom smaller, since this one only has three) stencils, giving me the ability to adapt to whatever size stencil works best on any particular machine.

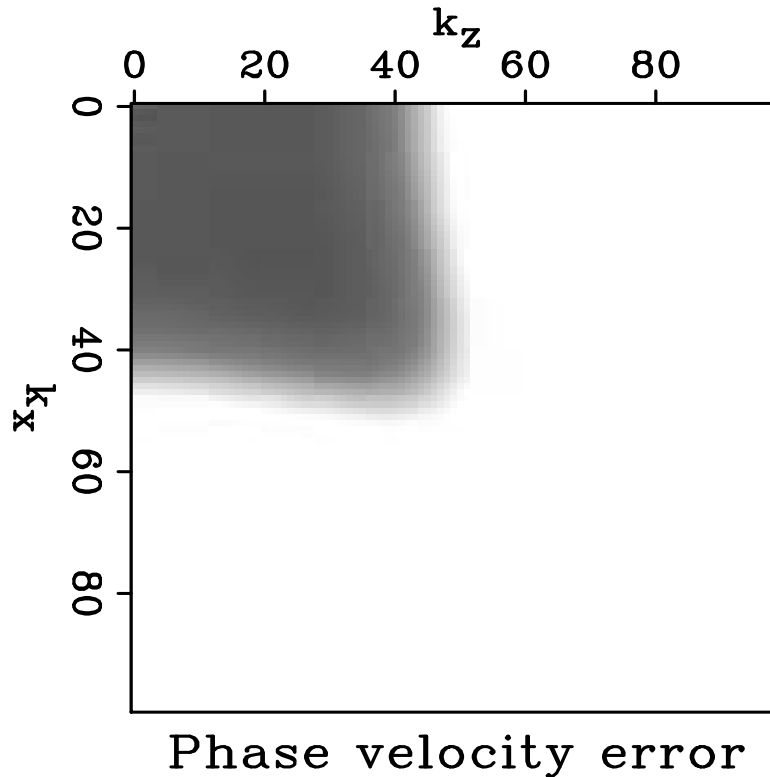
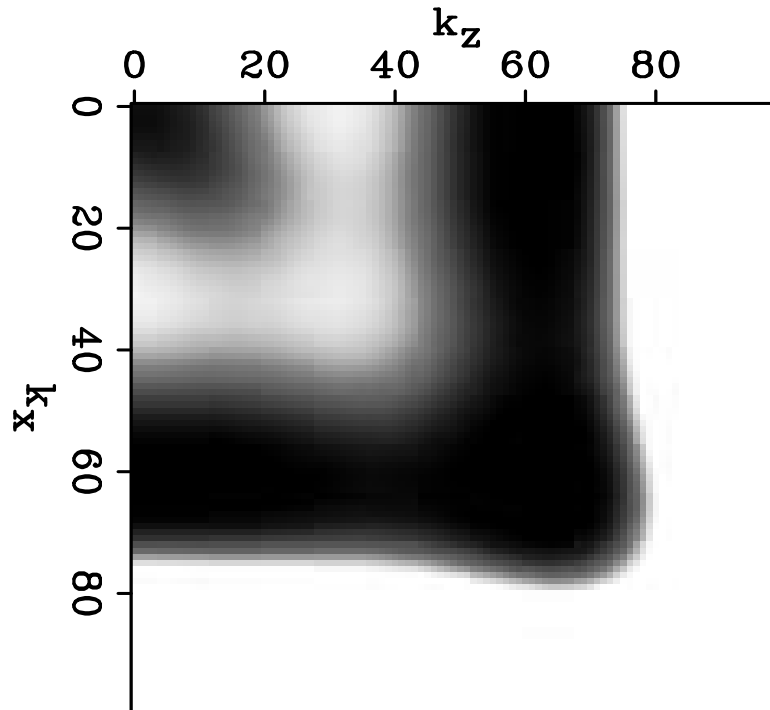


Figure 1: Relative phase velocity error clipped at 1% for the standard sixth-order in space, second-order in time finite-difference solution to the 2D acoustic wave equation. Grey areas of the plot have phase velocity close to the desired phase velocity. White areas have relative phase velocity error $> 1\%$ slow. `john1-Vphase_taylor6` [ER]

CONCLUSION

In principle, one shouldn't ignore the error caused by the time discretization of a finite-difference method; instead, use it to trade against the error from the spatial difference operator. Designing spatial finite-difference operators this way leads to spatially compact finite-difference stencils that achieve higher accuracy than schemes based on Taylor-series expansion (obviously). I think it's still an open question as to whether this method is better than a method that uses optimized spatial finite-difference coefficients that are not a function of the local velocity (Holberg's method). For spatially compact operators I think it's important to include the effect of the time discretization, and in this case the method presented here is the method of choice. For long spatial operators, which are used when one needs to use as few points per shortest wavelength as possible, the amount of storage required would probably be discouraging, but in principle, the method presented here is more accurate.



Phase velocity error

Figure 2: Relative phase velocity error clipped at 1% for an optimized finite-difference stencil with seven points on each spatial axis. Grey areas of the plot have nearly correct phase velocity. White areas of the plot have phase velocity too slow by >1%; Black areas of the plot have phase velocity >1% too fast. The optimization criterion was "too aggressive", resulting in an unacceptable fit. `john1-Vphase_opt_7pt_naive` [ER]

ACKNOWLEDGMENTS

I thank BP for permission to publish this material.

REFERENCES

- Dablain, M. A., 1986, The application of high-order differencing to the scalar wave equation: *Geophysics*, **51**, 54–66.
- Etgen, J., 1986, High order finite-difference reverse time migration with the two way nonreflecting wave equation: *SEP-48*, 133–146.
- , 1988, Evaluating finite difference operators applied to wave simulation: *SEP-57*, 243–258.
- Holberg, O., 1987, Computational aspects of the choice of operator and sampling interval for

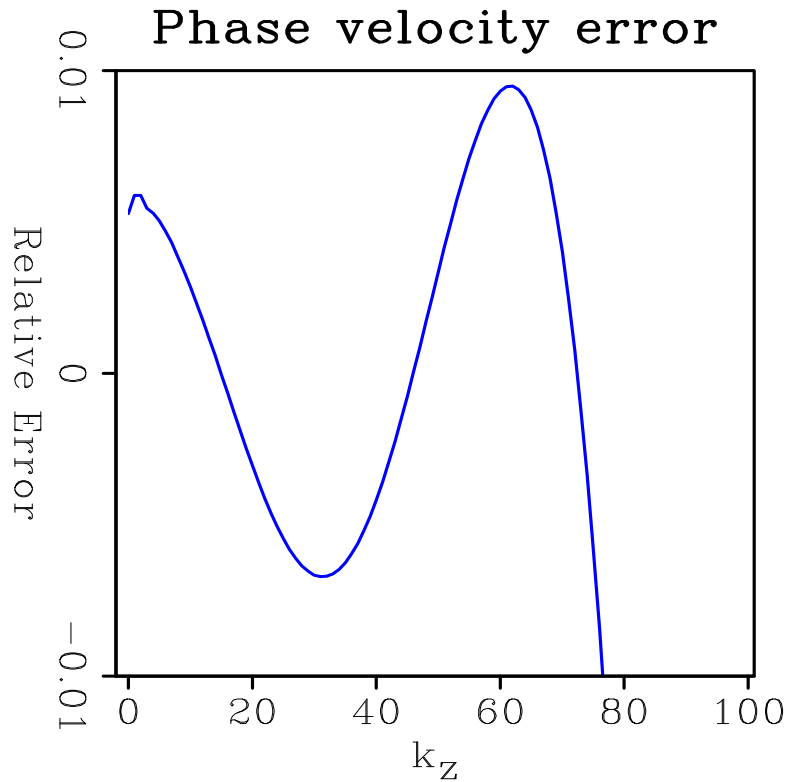


Figure 3: Graph of relative phase velocity error along the k_z axis showing approximate equiripple error. This amount of error is probably too large, although the fitting range is quite high, out to almost 80% of Nyquist. `john1-Vphase_opt_7pt_naive_graph` [ER]

numerical differentiation in large-scale simulation of wave phenomena: *Geophys. Prosp.*, **35**, 629–655.

Reshef, M., Kosloff, D., Edwards, M., and Hsiung, C., 1988, Three-dimensional acoustic modeling by the Fourier method: *Geophysics*, **53**, 1175–1183.

Tal-Ezer, H., Kosloff, D., and Koren, Z., 1987, An accurate scheme for seismic forward modelling: *Geophys. Prosp.*, **35**, 479–490.

Wu, W. J., Lines, L. R., and Lu, H. X., 1996, Analysis of higher-order, finite-difference schemes in 3-D reverse-time migration: *Geophysics*, **61**, 845–856.

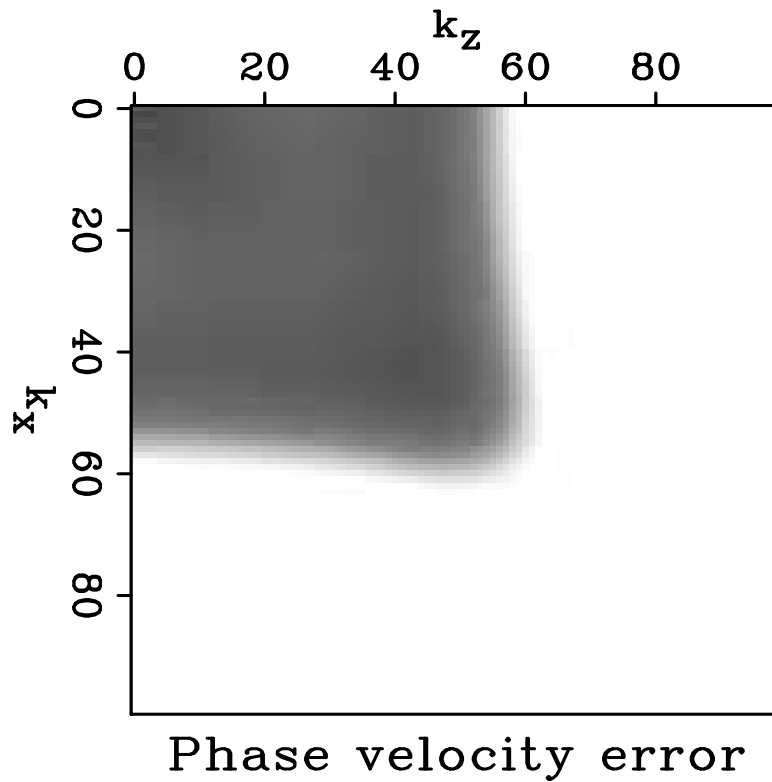


Figure 4: Relative phase velocity error clipped at 1% for an optimized finite-difference stencil with seven points on each spatial axis. Although the range of wavenumbers fit is smaller than in Figure 2, this set of difference coefficients can propagate accurately waves that are sampled at about 3.6 points per wavelength. `john1-Vphase_opt_7pt_improved` [ER]

Two-way vs. one-way: Understanding the approximations

Alejandro A. Valenciano

ABSTRACT

The one-way wave-equation approximation has a big impact on migration, modeling, and wave-equation inversion. That is why Amplitude vs. subsurface-offset (AVO), and amplitude vs. reflection angle (AVA) responses of the migration of a two-way and a one-way modeled datasets show different illumination patterns. Deconvolution by the one-way wave-equation Hessian can be use to account for the illumination problem. But the approximations used to compute the Hessian have an impact on how effectively the medium AVO and AVA is recover by the inversion.

INTRODUCTION

The dream of an explorationist is to be able to carry on AVO or AVA attributes analysis in areas with poor illumination. But the quality of the images that a state of the art migration can produce is not good enough for that purpose. One way to improve the image is to use an inversion formalism introduced by Tarantola (1987) to solve geophysical imaging problems. This procedure computes an image by convolving the migration result with the inverse of the Hessian matrix.

When the dimensions of the problem get large, the explicit calculation of the Hessian matrix and its inverse becomes unfeasible. That is why Valenciano and Biondi (2004) and Valenciano et al. (2006) proposed the following approximations: (1) to compute the one way wave equation Green functions from the surface to the target (or vice versa), to reduce the size of the problem; (2) to compute the Hessian, exploiting its sparse structure; and (3) to compute the inverse image following an iterative inversion scheme. The last item renders unnecessary an explicit computation of the inverse of the Hessian matrix. For efficiency reasons the Green's functions necessary to compute the Hessian are computed by means of a one-way wave-equation extrapolator.

In this paper I study the impact of the one-way wave-equation approximation to the wave propagation in: migration, modeling, and wave-equation inversion. I illustrate the differences between two-way and one-way data modeling, and the migration of two-way and one-way modeled data.

I also show how the approximations used to compute the Hessian have an impact on the recovery of the medium AVO and AVA response. This is done by comparing the inversion of

the two-way modeled TRIP data, a one-way modeled data (equivalent to the use of the full Hessian), and a one-way modeled data using an approximated Hessian.

LINEAR LEAST-SQUARES INVERSION

Tarantola (1987) formalizes the geophysical inverse problem by providing a theoretical approach to compensate for experimental deficiencies (e.g., acquisition geometry, complex overburden), while being consistent with the acquired data. His approach can be summarized as follows: given a linear modeling operator \mathbf{L} , compute synthetic data \mathbf{d} using $\mathbf{d} = \mathbf{L}\mathbf{m}$ where \mathbf{m} is a reflectivity model. Given the recorded data \mathbf{d}_{obs} , a quadratic cost function,

$$S(\mathbf{m}) = \|\mathbf{d} - \mathbf{d}_{obs}\|^2 = \|\mathbf{L}\mathbf{m} - \mathbf{d}_{obs}\|^2, \quad (1)$$

is formed. The reflectivity model $\hat{\mathbf{m}}$ that minimizes $S(\mathbf{m})$ is given by the following:

$$\hat{\mathbf{m}} = (\mathbf{L}'\mathbf{L})^{-1}\mathbf{L}'\mathbf{d}_{obs} = \mathbf{H}^{-1}\mathbf{m}_{mig}, \quad (2)$$

where \mathbf{L}' (migration operator) is the adjoint of the linear modeling operator \mathbf{L} , \mathbf{m}_{mig} is the migration image, and $\mathbf{H} = \mathbf{L}'\mathbf{L}$ is the Hessian of $S(\mathbf{m})$.

The main difficulty with this approach is the explicit calculation of the inverse Hessian. In practice, it is more feasible to compute the least-squares inverse image as the solution of the linear system,

$$\mathbf{H}\hat{\mathbf{m}} = \mathbf{m}_{mig}, \quad (3)$$

by using an iterative inversion algorithm.

Equation 3 states that if we convolve the Hessian matrix \mathbf{H} with a perfect model we should obtain the migration result ("Hessian impulse response"). In the next section we will study the approximations involved in the computation of the Hessian matrix, and will try to understand how far the "Hessian impulse response" computed using the approximated Hessian (from equation 3) is from the real migration result.

Subsurface-offset Hessian

Valenciano et al. (2006) define the zero subsurface-offset domain Hessian by using the adjoint of the zero subsurface-offset domain migration as the modeling operator \mathbf{L} . Then the zero-subsurface-offset inverse image can be estimated as the solution of a non-stationary least-squares filtering problem, using an iterative inversion algorithm (Valenciano et al., 2006).

The subsurface-offset Hessian was defined by Valenciano and Biondi (2006). The definition can be summarized as follows.

The prestack migration image (subsurface-offset domain) for a group of shots positioned at $\mathbf{x}_s = (x_s, y_s, 0)$ and a group of receivers positioned at $\mathbf{x}_r = (x_r, y_r, 0)$ can be given by the

adjoint of a linear operator \mathbf{L} acting on the data-space $\mathbf{d}(\mathbf{x}_s, \mathbf{x}_r; \omega)$ as

$$\begin{aligned} \mathbf{m}(\mathbf{x}, \mathbf{h}) &= \mathbf{L}' \mathbf{d}(\mathbf{x}_s, \mathbf{x}_r; \omega) \\ &= \sum_{\omega} \sum_{\mathbf{x}_s} \sum_{\mathbf{x}_r} \mathbf{f}(\omega) \mathbf{G}'(\mathbf{x} - \mathbf{h}, \mathbf{x}_s; \omega) \mathbf{G}'(\mathbf{x} + \mathbf{h}, \mathbf{x}_r; \omega) \sum_{\mathbf{h}}' \sum_{\mathbf{x}}' \mathbf{d}(\mathbf{x}_s, \mathbf{x}_r; \omega), \end{aligned} \quad (4)$$

where $\mathbf{G}(\mathbf{x}, \mathbf{x}_s; \omega)$ and $\mathbf{G}(\mathbf{x}, \mathbf{x}_r; \omega)$ are respectively the Green's functions from the shot position \mathbf{x}_s and from the receiver position \mathbf{x}_r to a point in the model space \mathbf{x} , $\mathbf{f}(\omega)$ is the source wavelet, and $\mathbf{h} = (h_x, h_y)$ is the subsurface-offset. The symbols $\sum_{\mathbf{h}}'$ and $\sum_{\mathbf{x}}'$ are spray operators (adjoint of the sum) in the subsurface-offset and physical space dimensions $\mathbf{x} = (x, y, z)$, respectively. The Green's functions are computed by means of the one-way wave-equation.

The synthetic data can be modeled (as the adjoint of equation 4) by the linear operator \mathbf{L} acting on the model space $\mathbf{m}(\mathbf{x}, \mathbf{h})$

$$\begin{aligned} \mathbf{d}(\mathbf{x}_s, \mathbf{x}_r; \omega) &= \mathbf{L} \mathbf{m}(\mathbf{x}, \mathbf{h}) \\ &= \sum_{\mathbf{x}} \sum_{\mathbf{h}} \mathbf{G}(\mathbf{x} + \mathbf{h}, \mathbf{x}_r; \omega) \mathbf{f}(\omega) \mathbf{G}(\mathbf{x} - \mathbf{h}, \mathbf{x}_s; \omega) \sum_{\mathbf{x}_r}' \sum_{\mathbf{x}_s}' \sum_{\omega}' \mathbf{m}(\mathbf{x}, \mathbf{h}), \end{aligned} \quad (5)$$

where the symbols $\sum_{\mathbf{x}_r}'$, $\sum_{\mathbf{x}_s}'$, and \sum_{ω}' are spray operators in the shot, receiver, and frequency dimensions, respectively.

The second derivative of the quadratic cost function with respect to the model parameters is the subsurface-offset Hessian:

$$\begin{aligned} \mathbf{H}(\mathbf{x}, \mathbf{h}; \mathbf{x}', \mathbf{h}') &= \sum_{\omega} \mathbf{f}(\omega)^2 \sum_{\mathbf{x}_s} \mathbf{G}'(\mathbf{x} - \mathbf{h}, \mathbf{x}_s; \omega) \mathbf{G}'(\mathbf{x}' - \mathbf{h}', \mathbf{x}_s; \omega) \\ &\quad \times \sum_{\mathbf{x}_r} \mathbf{G}'(\mathbf{x} + \mathbf{h}, \mathbf{x}_r; \omega) \mathbf{G}'(\mathbf{x}' + \mathbf{h}', \mathbf{x}_r; \omega), \end{aligned} \quad (6)$$

where $(\mathbf{x}', \mathbf{h}')$ are the off-diagonal terms of the Hessian matrix.

An approximation to the full subsurface-offset Hessian involves computing only the off-diagonal terms at close to the diagonal (Valenciano and Biondi, 2006).

$$\begin{aligned} \mathbf{H}(\mathbf{x}, \mathbf{h}; \mathbf{x} + \mathbf{a}, \mathbf{h}') &= \sum_{\omega} \mathbf{f}(\omega)^2 \sum_{\mathbf{x}_s} \mathbf{G}'(\mathbf{x} - \mathbf{h}, \mathbf{x}_s; \omega) \mathbf{G}'(\mathbf{x} + \mathbf{a} - \mathbf{h}', \mathbf{x}_s; \omega) \\ &\quad \times \sum_{\mathbf{x}_r} \mathbf{G}'(\mathbf{x} + \mathbf{h}, \mathbf{x}_r; \omega) \mathbf{G}'(\mathbf{x} + \mathbf{a} + \mathbf{h}', \mathbf{x}_r; \omega), \end{aligned} \quad (7)$$

where $\mathbf{a} = (a_x, a_y, a_z)$ are the off-diagonal coefficients. The impact of this approximation will be evaluated in the following sections.

Data fitting goal

In this paper I do not use any regularization to solve the linear system in equation 3, since the objective of the study was to find out how well the Hessian operator could fit the different

kind of data. Having regularization could obscure the results. However, in areas of poor illumination, this problem will have a large null space. The null space is partially caused by the fact that our survey can not have infinite extents and infinitely dense source and receiver grids. Any noise that exists within the null space can grow with each iteration until the problem becomes unstable.

The inversion was carried out in the subsurface-offset domain. The fitting goal used was

$$\mathbf{H}(\mathbf{x}, \mathbf{h}; \mathbf{x}', \mathbf{h}') \hat{\mathbf{m}}(\mathbf{x}, \mathbf{h}) - \mathbf{m}_{mig}(\mathbf{x}, \mathbf{h}) \approx 0, \quad (8)$$

In the next sections I compare the numerical solution of the inversion problems stated in equation 8 in the imaging of the TRIP synthetic dataset.

TWO-WAY VS. ONE-WAY MODELING

For efficiency reasons the Green's functions in equations 4, 5, and 6 are computed by means of a one-way wave-equation extrapolator. No upgoing energy can be modeled by following this approach, since the evanescent energy is usually damped (Claerbout, 1985). This makes the one-way propagator act as a dip filter depending on the velocity model (from the dispersion relation, $\frac{\omega^2}{v^2} < \mathbf{k}^2$). Also, the conventional one-way wave-equation does not model accurately the the amplitude behavior with the angle of propagation (Zhang et al., 2005). Another problem arises when the velocity varies laterally, then getting energy to accurately propagate close to 90° is a big challenge.

The previous limitations of the one-way modeling can be mitigated by getting sophisticated when implementing the extrapolator. The dip filter effect should be reduced by including the Jacobian of the change of variable from ω to k_z (Sava and Biondi, 2001), thus making \mathbf{L} closer to be unitary. To properly model the amplitude behavior with the angle of propagation, Zhang et al. (2005) proposed using a modified one-way wave-equation whose solution match the Kirchhoff inversion solution. The effect caused by the lateral variation of the velocity can also be mitigated by using better approximations of the square root operator.

For the example presented in this paper I used the conventional one-way wave equation (Claerbout, 1985). I did not include the Jacobian, and approximated the square root operator with Split Step Fourier plus interpolation (PSPI).

NUMERICAL RESULTS

Modeling

The TRIP synthetic dataset was created from a model with a constant-reflectivity flat reflector lying beneath a Gaussian low velocity anomaly (Figure 1). The data was modeled with the following acquisition geometry: the shots and receivers were positioned every 10 m on the interval $\mathbf{x} = [-2.0, 2.0]$ km .

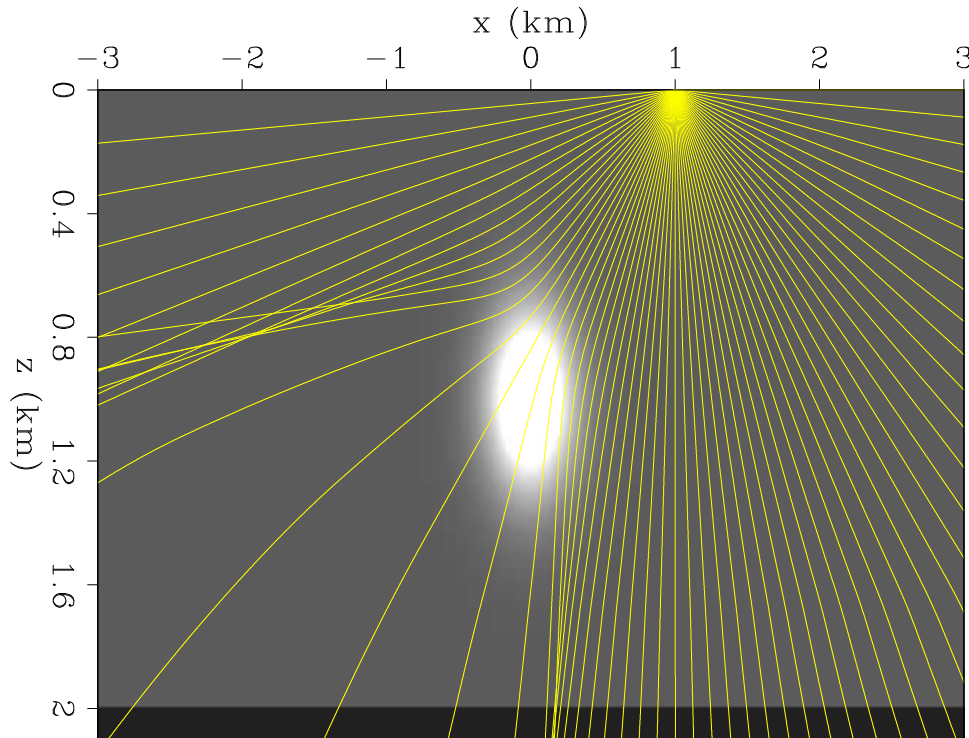


Figure 1: Gaussian anomaly velocity model with overlay rays showing the uneven illumination of the reflector. [alejandro1-rays](#) [ER]

The Gaussian anomaly distorts the direction in which the energy is propagated (from small to high angles) and it also makes the velocity change with x position, thus the effect of using one-way vs. two-way modeling should be noticeable. One important difference between these two data sets is the assumed AVA of the flat reflector. I assumed a constant AVA when modeling the one-way data with equation 5. Conversely, a AVA corresponding to a constant density is implicit in the TRIP two-way finite-differences modeling code.

Figure 2 shows a comparison of the two-way (Figures 2a, 2c) modeled data provided by TRIP vs. the one-way (Figures 2b, 2d) modeled using equation 5. The first row correspond to a shot located at $x = -2$ km, and the bottom row corresponds to a shot located at $x = 1$ km.

The main differences (besides the artifact in the two-way modeling with linear moveout) can be spotted in the top row. The one-way modeled data (Figure 2a) shows a decay of the amplitude with offset (compare with Figure 2b) that could be related to the errors in the amplitude (absence of the Jacobian) in the one-way extrapolator. There is also an overturning event arriving at far offset (Figure 2b), which is impossible to model with the one-way extrapolator. Besides the AVO differences (dynamic) a very good agreement of the kinematics can be observed.

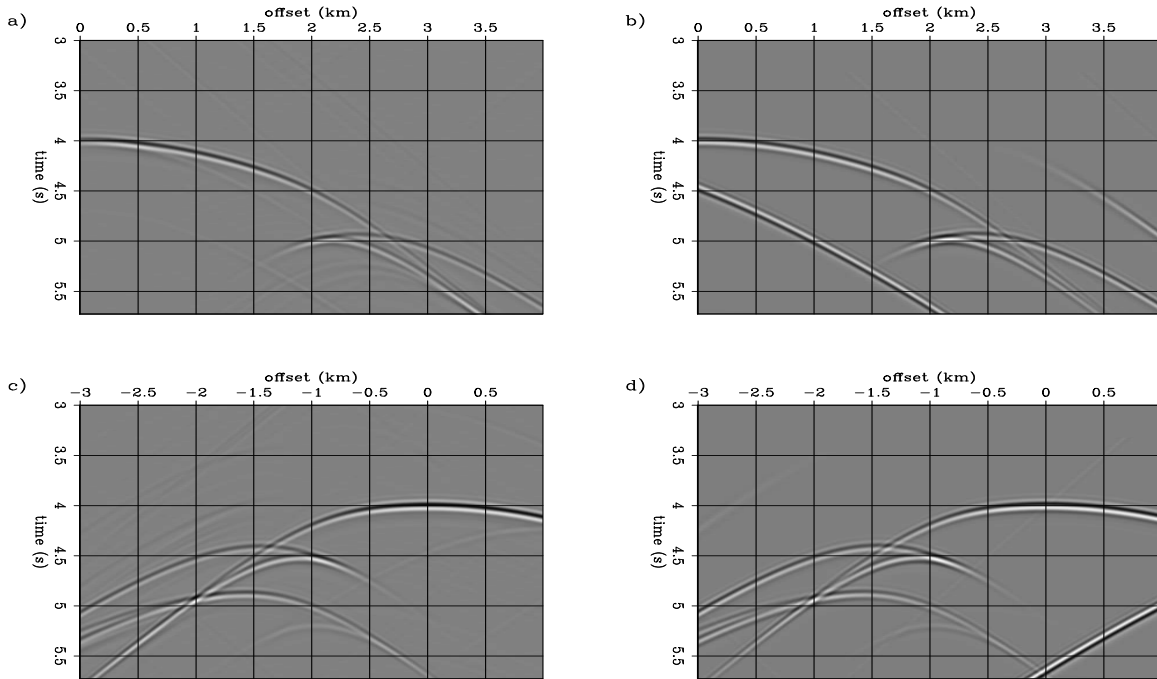


Figure 2: Comparison of the two-way (b,d) modeled data provided by TRIP vs. the one-way (a,c) modeled using equation 5. The top row shows the data from a shot located at $x = -2$ km, and the bottom row corresponds to a shot located at $x = 1$ km. `alejandrol-compare` [CR,M]

Migration

The next step is to compare the subsurface-offset migration results from the two different data sets. Figure 3 shows a comparison the two-way (3a) vs. the one-way modeled data (3b) migrations in the subsurface-offset domain. The results are comparable in terms of resolution, but the amplitudes show a different behavior. This is something to expect from the data differences in AVO behavior (Figure 2). Even though the images shown in Figure 3 are in the sub-surface offset domain, we can see how different they are going to be when transformed to reflection angle by using Sava and Fomel (2003) transformation.

Figure 4 shows a comparison the two-way (Figure 4a) vs. the one-way modeled data (Figure 4b) migrations in the reflection angle domain. This result is obtained after applying an offset to angle transformation to the images in Figure 3. Notice the difference between the illumination patterns in the images. As we discussed in the modeling subsection the images in Figure 4a and Figure 4b should have different AVA responses. But, from inspecting the figures we can see that they are not that far apart. For most of the x positions the angle range illumination is the same, being different in intensity. I will discuss the impact of this on the recovery of the AVA in the Inversion subsection.

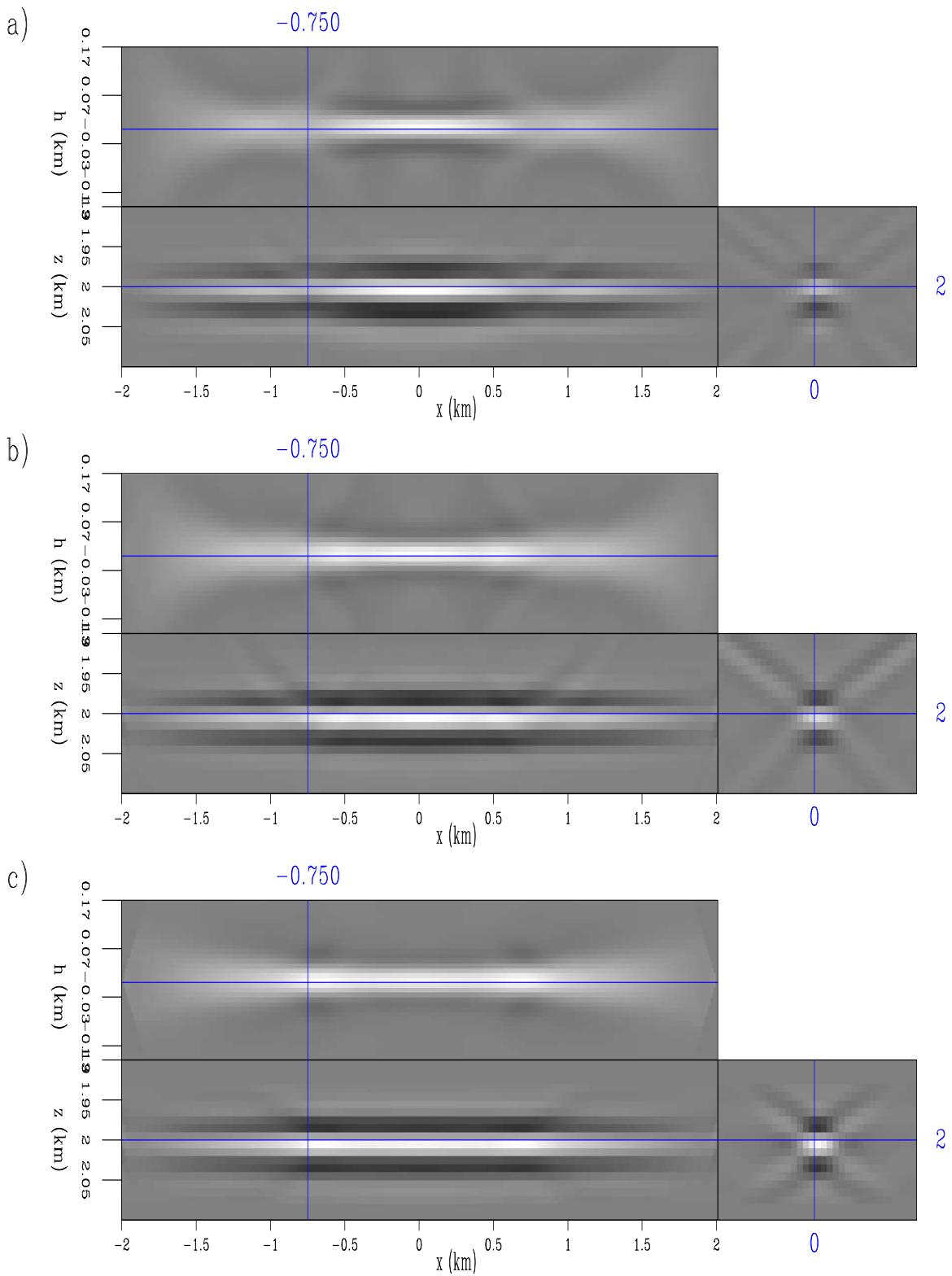


Figure 3: Comparison of the migration results in subsurface-offset domain of the two-way (a) vs. the one-way modeled data (b), and vs. the migration "Hessian impulse response" (c) (from equation 3) `alejandro1-compare_mig1` [CR,M]

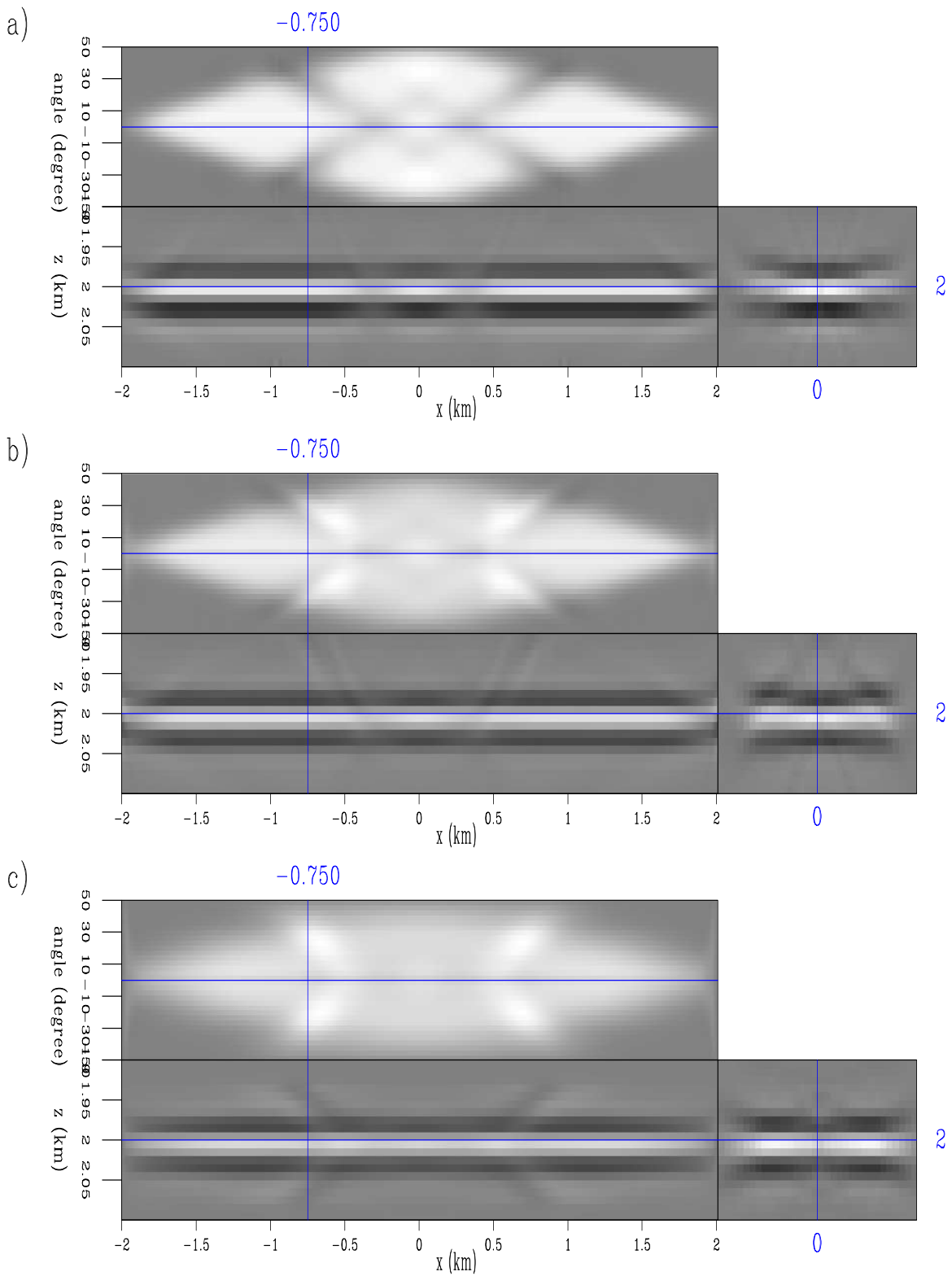


Figure 4: Comparison of the migration results in reflection angle of the two-way (a) vs. the one-way modeled data (b), and vs. the migration "Hessian impulse response" (c) (from equation 3) `alejandro1-compare_mig2` [CR,M]

Migration vs. "Hessian impulse response"

Another important comparison is the between the the one-way modeled data migration (Figures 3b and 4b) and the migration "Hessian impulse response" (Figures 3c and 4c). This two results should have been identical if all the off-diagonal terms of the Hessian matrix would have been computed (equation 7) to obtain Figures 3c. In the modeling of the one-way data all the off-diagonal elements of the Hessian matrix are implicitly computed. To obtain Figure 3c only ($a_x = 15 \times a_z = 15 \times h' = 32$) off-diagonal elements of the Hessian matrix were computed.

The two results are very similar at small offsets, but at far subsurface-offset the migration "Hessian impulse response" (Figure 3c) amplitudes are washed out. That might indicate the need of computing more off-diagonal coefficients in the (x, z) dimensions (a_x, a_z) , probably the same number off subsurface-offsets. The angle migration "Hessian impulse response" differs at higher angles to the angle one-way modeled data migration, a result that is the consequence of the washed out amplitudes at far subsurface-offset "Hessian impulse response".

An important feature to notice when comparing Figures 4a, 4b, and 4c is that some places with low illumination in Figure 4a, have high illumination in Figure 4b, and Figure 4c. In those places the deconvolution by the one-way wave-equation Hessian will not recover the correct amplitudes. Thus the AVA signature will be affected.

Inversion

Deconvolution by the one-way wave-equation Hessian can be use to account for the illumination problem caused by the low velocity Gaussian anomaly (Figure 4). To understand the effect of using one-way wave-equation Green functions in the Hessian computation, I compare the inversion of the: two-way modeled data (Figures 5a, and 6a), the one-way modeled data (Figures 5b, and 6b), and the migration "Hessian impulse response" (Figures 5c, and 6c). The images in Figure 6 are the result of applying an offset to angle transformation to the images in Figure 5.

The first thing to notice is that in the case in that the same operator was used for the modeling and for the inversion ("Hessian impulse response", Figures 5c, and 6c) the deconvolution by the Hessian gives a almost perfect result. See how the energy in the subsurface-offset dimension concentrates around zero subsurface-offset (Figure 5c), and by consequence the more uniform angle coverage (Figure 6c) compare to the migration results in Figures 3c and 4c.

The second best result is obtained for the one-way modeled data inversion (Figures 5b, and 6b). Here the operators used for the modeling (implicitly) and the operator used for the inversion (explicitly) differ, since not all the of off-diagonal elements of the Hessian were computed. Nevertheless, there is an improvement in the AVA uniformity (expected from modeling) in most of the x positions. Especially at the center of the model.

The result of the two-way modeled data inversion (Figures 5a, and 6a) is the one showing less improvements. Nevertheless, there are several x positions where the AVA looks less

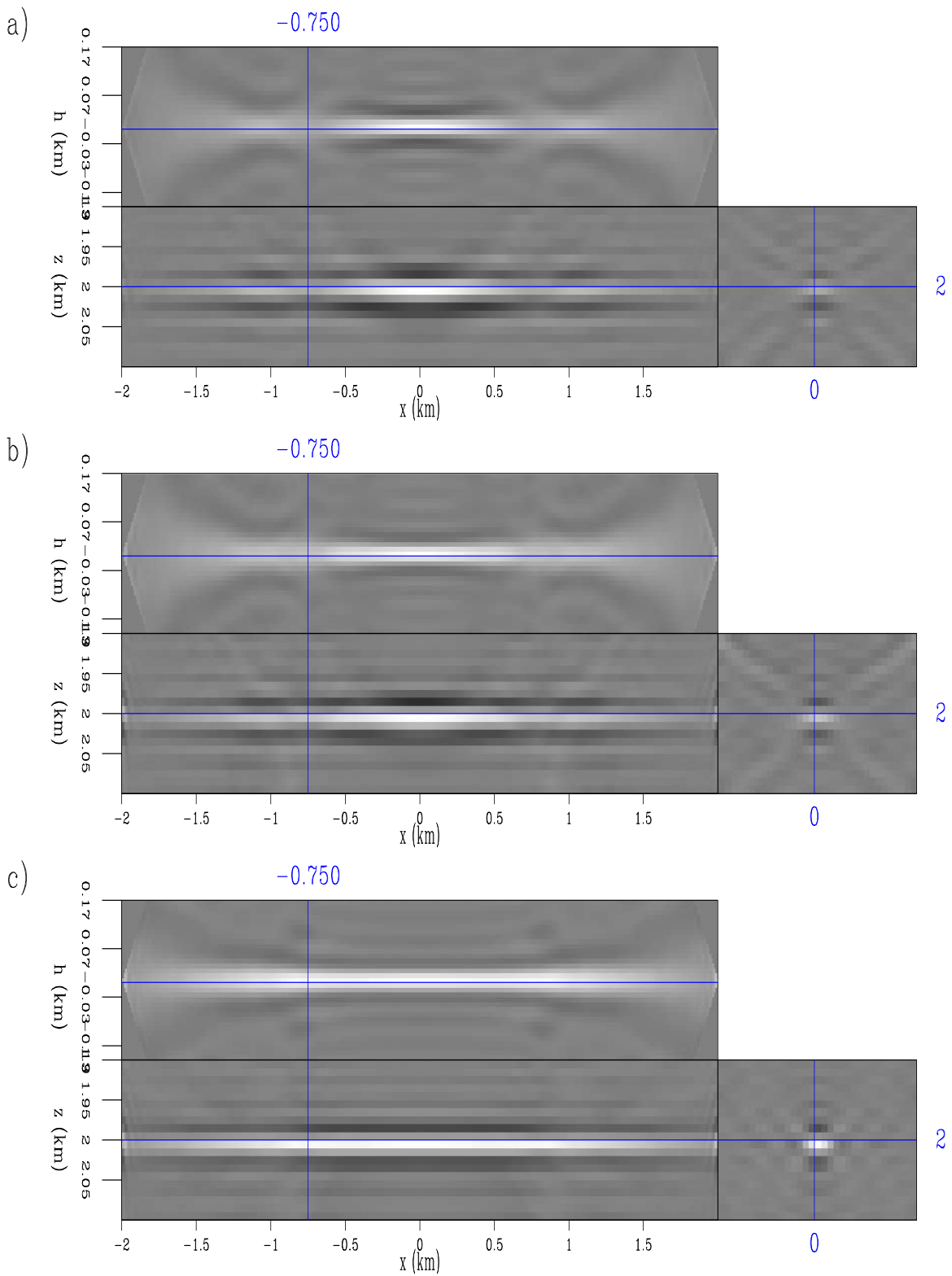


Figure 5: Comparison of the inversion results in reflection angle of the two-way (a) vs. the one-way modeled data (b), and vs. the migration "Hessian impulse response" (c) (from equation 3) `alejandrol-compare_inv1` [CR,M]

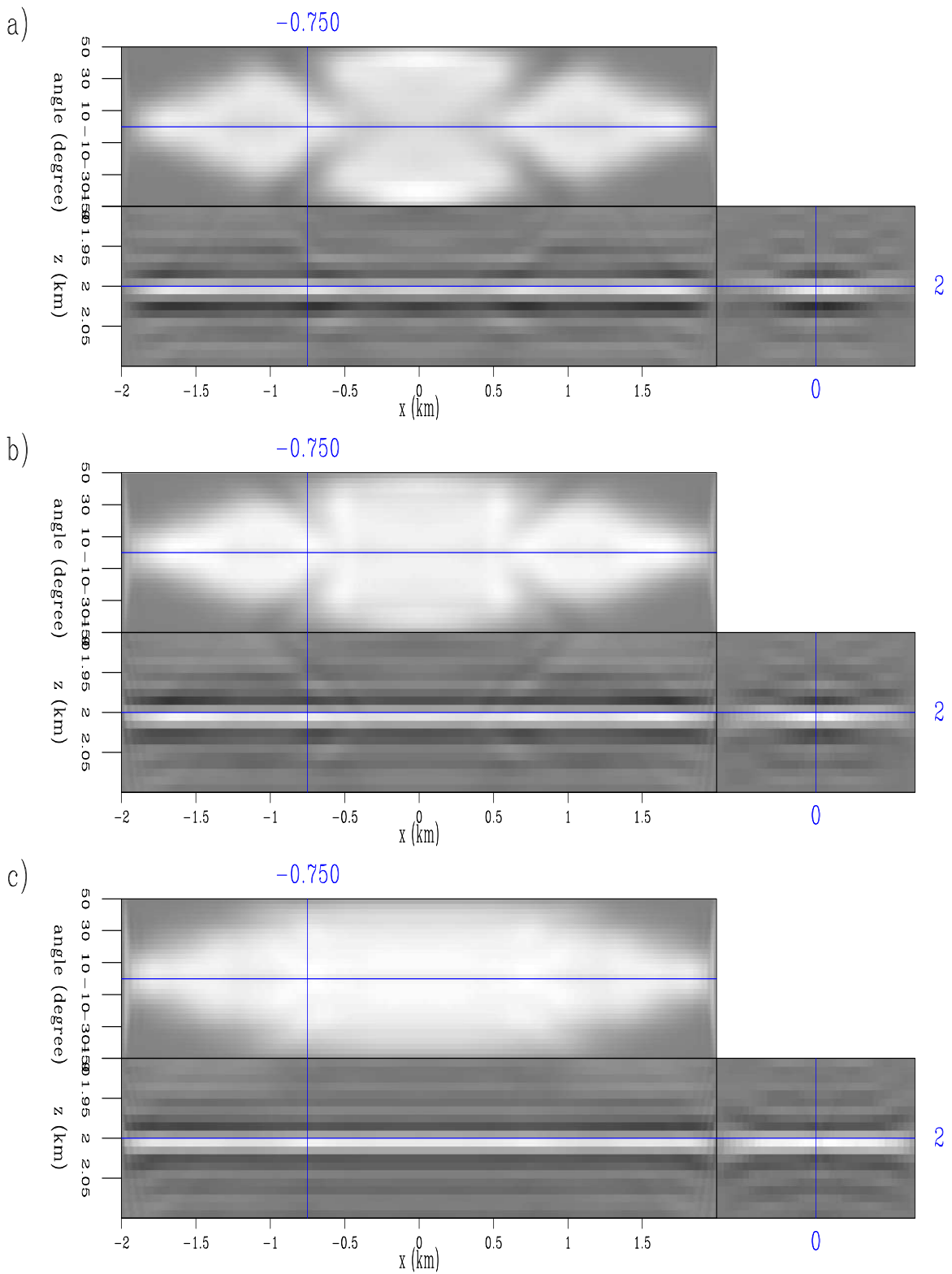


Figure 6: Comparison of the inversion results in reflection angle of the two-way (a) vs. the one-way modeled data (b), and vs. the migration "Hessian impulse response" (c) (from equation 3) `alejandrol-compare_inv4` [CR,M]

affected by the velocity anomaly. Especially at the center of the model.

The results indicate that if the modeling and the inversion operators differ there is little chance to recover the correct AVA in poorly illuminated areas. This is because, in areas of poor illumination, this problem will have a large null space. The proper strategy appears to be the use of regularization. Three different regularization schemes for wave-equation inversion have been discussed in the literature. First, an identity operator (damping) which is customary in many scientific applications. Second, a geophysical regularization which penalizes the roughness of the image in the offset ray parameter dimension (which is equivalent the reflection angle dimension) (Prucha et al., 2000; Kuehl and Sacchi, 2001). Third, a differential semblance operator to penalize the energy in the image not focused at zero subsurface-offset (Shen et al., 2003).

CONCLUSIONS

Modeling and migration of a data set with a Gaussian velocity anomaly shows that the main differences between the two-way vs. one-way modeled data are at far offsets. The one-way modeled data amplitudes decay with offset, because of the many approximations used (PSPI to handle variable horizontal velocities) and the absence of the Jacobian of the change of variable from ω to k_z .

An important fact derived from the numerical experiments is that the one-way modeled data migration vs. migration "Hessian impulse response" show differences. Those differences are attributed to the computed number of off-diagonal terms of the Hessian matrix. An added value of this comparison is that it corroborates the approximations used to compute the Hessian.

The results indicate that if the modeling and the inversion operators differ there is little chance to recover the correct AVA in poor illumination areas. Because, in areas of poor illumination, this problem will have a large null space. The proper strategy to recover the AVA in those areas is the use of regularization, where previous knowledge about the model can be introduced to reduce the model null space.

ACKNOWLEDGMENTS

I would like to thank Bill Symes and TRIP for the Gaussian anomaly velocity model used in this paper.

REFERENCES

- Claerbout, J. F., 1985, *Imaging the earth's interior*: Blackwell Scientific Publications.
- Kuehl, H. and M. Sacchi, 2001, Generalized least-squares DsR migration using a common angle imaging condition: Generalized least-squares DsR migration using a common angle imaging condition:, *Soc. of Expl. Geophys.*, 71st Ann. Internat. Mtg, 1025–1028.
- Prucha, M. L., R. G. Clapp, and B. Biondi, 2000, Seismic image regularization in the reflection angle domain: *SEP-103*, 109–119.
- Sava, P. and B. Biondi, 2001, Amplitude-preserved wave-equation migration: *SEP-108*, 1–26.
- Sava, P. and S. Fomel, 2003, Angle-domain common-image gathers by wavefield continuation methods: *Geophysics*, **68**, 1065–1074.
- Shen, P., W. Symes, and C. C. Stolk, 2003, Differential semblance velocity analysis by wave-equation migration: 73st Annual International Meeting, SEG, Expanded Abstracts, 2132–2135.
- Tarantola, A., 1987, *Inverse problem theory: Methods for data fitting and model parameter estimation*: Elsevier Science Publication Company, Inc.
- Valenciano, A. A. and B. Biondi, 2004, Target-oriented computation of the wave-equation imaging Hessian: *SEP-117*, 63–76.
- Valenciano, A. A. and B. Biondi, 2006, Wave-equation angle-domain hessian: EAGE 68th Annual Conference, Expanded Abstracts.
- Valenciano, A. A., B. Biondi, and A. Guitton, 2006, Target-oriented wave-equation inversion: *Geophysics*, **71**, no. 4, A35–A38.
- Zhang, Y., G. Zhang, and N. Bleistein, 2005, Theory of true-amplitude one-way wave equations and true-amplitude common-shot migration: *Geophysics*, **70**, no. 4, E1–E10.

Optimized implicit finite-difference migration for TTI media: A 2D synthetic dataset

Guojian Shan

ABSTRACT

I review optimized implicit finite-difference migration for tilted TI media. The implicit finite-difference scheme is designed by fitting the dispersion relation with rational functions using least-squares optimization. I apply the method to a synthetic dataset. The result shows that the algorithm can handle laterally varying tilted TI media.

INTRODUCTION

Implicit finite-difference methods that are adapted to strongly laterally varying media and guarantee stability, have been one of the most attractive methods for isotropic media. Traditional implicit finite-difference migration methods are based on the truncation of the Taylor series of the dispersion relation. For anisotropic media, phase-shift plus interpolation (PSPI) methods (Rousseau, 1997; Ferguson and Margrave, 1998) or explicit finite-difference methods (Uzcategui, 1995; Zhang et al., 2001a,b; Baumstein and Anderson, 2003; Shan and Biondi, 2005; Ren et al., 2005) are usually chosen for migration because the dispersion relation of anisotropic media is very complex and it is difficult to derive a Taylor series for the implicit finite-difference scheme with high accuracy. However, TTI (tilted TI) media are not circularly symmetric and a 2D convolution operator is required instead of the McClellan transformations (Hale, 1991) to implement the explicit finite-difference scheme (Shan and Biondi, 2005). Although Lloyd's algorithm can be used to reduce the number of reference velocity and anisotropy parameters in PSPI (Tang and Clapp, 2006), too many reference wavefields are required to achieve decent accuracy in a strongly laterally varying TTI medium.

Lee and Suh (1985) approximate the square-root operator with rational functions and optimize the coefficients by least-squares function fitting. This method improves the accuracy of the finite-difference scheme without increasing the computational cost. Under the weak anisotropy assumption, Ristow and Ruhl (1997) design an implicit finite-difference scheme for VTI (transversely isotropic with a vertical symmetry axis) media. Liu et al. (2005) apply a phase-correction operator (Li, 1991) in the Fourier domain in addition to the implicit finite-difference operator for VTI media and improve the accuracy. Shan (2006b) approximates the dispersion relation of VTI media with rational functions and obtains the coefficients for the finite-difference scheme by using the weighted least-squares optimization. Similarly, Shan (2006a) designs implicit-finite difference scheme for TTI media by fitting the dispersion relation with rational functions and shows impulse responses in a homogeneous medium.

In this paper, I review the optimized implicit finite-difference method for TTI media and apply it to a 2D synthetic dataset to verify the methodology in laterally varying media.

OPTIMIZED FINITE-DIFFERENCE FOR TTI MEDIA

The dispersion relation of TTI media can be characterized by a quartic equation as follows:

$$d_4 S_z^4 + d_3 S_z^3 + d_2 S_z^2 + d_1 S_z + d_0 = 0, \quad (1)$$

where the coefficients d_0, d_1, d_2, d_3 , and d_4 are defined as follows:

$$\begin{aligned} d_0 &= (2 + 2\varepsilon \cos^2 \varphi - f) S_x^2 - 1 - \left[(1 - f)(1 + 2\varepsilon \cos^2 \varphi) + \frac{f}{2}(\varepsilon - \delta) \sin^2 2\varphi \right] S_x^4, \\ d_1 &= [2\varepsilon(1 - f) \sin 2\varphi - f(\varepsilon - \delta) \sin 4\varphi] S_x^3 - 2\varepsilon \sin 2\varphi S_x, \\ d_2 &= [f(\varepsilon - \delta) \sin^2 2\varphi - 2(1 - f)(1 + \varepsilon) - 2f(\varepsilon - \delta) \cos^2 2\varphi] S_x^2 + (2 + 2\varepsilon \sin^2 \varphi - f), \\ d_3 &= [f(\varepsilon - \delta) \sin 4\varphi + 2\varepsilon(1 - f) \sin 2\varphi] S_x, \\ d_4 &= f - 1 + 2\varepsilon(f - 1) \sin^2 \varphi - \frac{f}{2}(\varepsilon - \delta) \sin^2 2\varphi, \end{aligned}$$

where ε and δ are Thomsen anisotropy parameters (Thomsen, 1986) and φ is the tilting angle of the media. Theoretically, equation 1 can be solved analytically, but there is no explicit analytical expression for its solution. The solid line in Figure 1 shows how the dispersion relation looks, given the anisotropy parameters $\varepsilon = 0.4$, $\delta = 0.2$ and the tilting angle $\varphi = 30^\circ$. Note that S_z is not a symmetric function of S_x . And S_z has two branches when $S_x > 0.8$. One of them represents the up-going waves and the other one represents the down going waves. Therefore, in a TTI medium waves may overturn even though it is homogeneous.

Conventional implicit finite-difference methods are designed by truncating the Taylor series of the dispersion relation. The dispersion relation for TTI media is so complex that it is difficult to derive an analytical Taylor series used for an implicit finite-difference scheme.

Generally, the Padé approximation suggests that if the function $S_z(S_x) \in C^{n+m}$, then $S_z(S_x)$ can be approximated by a rational function $R_{n,m}(S_x)$:

$$R_{n,m}(S_x) = \frac{P_n(S_x)}{Q_m(S_x)}, \quad (2)$$

where

$$P_n(S_x) = \sum_{i=0}^n a_i S_x^i$$

and

$$Q_m(x) = \sum_{i=0}^m b_i S_x^i$$

are polynomials of degree n and m , respectively. The coefficients a_i and b_i can be obtained either analytically by Taylor-series analysis or numerically by least-squares fitting.

S_z is an even function of S_x for isotropic and VTI media. In contrast, S_z is not an symmetric function of S_x for TTI media. It's well known that an general function can be decomposed into an even function and an odd function. We approximate the even part of the dispersion with the even rational functions, such as S_x^2, S_x^4 and approximate the odd part with odd rational functions, such as S_x, S_x^3 .

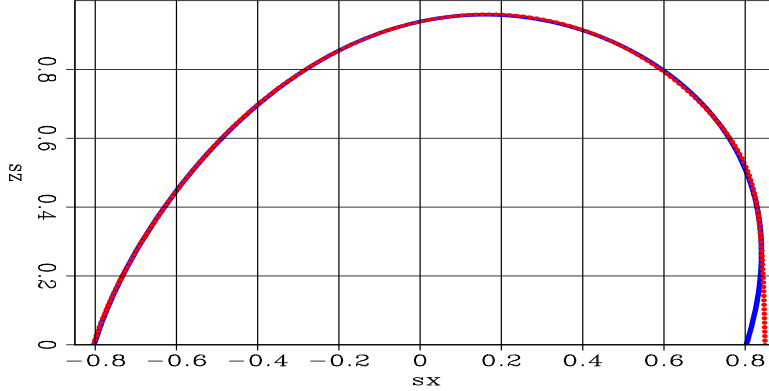


Figure 1: Comparison of the true and approximate dispersion relations for a TTI medium with $\varepsilon = 0.4$, $\delta = 0.2$ and $\varphi = 30^\circ$: the solid line is the true dispersion relation for TTI media; the dashed line is the approximate dispersion relation for finite-difference scheme. The dispersion relation for the finite-difference scheme is very close to the true one for negative S_x . When the phase-angle is close to 90° or more than 90° for the positive S_x , the dispersion for the finite-difference scheme diverge from the true one. guojian2-dispersion [ER]

Considering the stability of the finite-difference scheme, I approximate the dispersion relation of TTI media with rational functions as follows:

$$S_z(S_x) \approx S_{z0} + \frac{a_1 S_x^2 + c_1 S_x}{1 + b_1 S_x^2} + \frac{a_2 S_x^2 + c_2 S_x}{1 + b_2 S_x^2}, \quad (3)$$

where $S_{z0} = S_z(0)$ and the coefficients $a_1, b_1, c_1, a_2, b_2, c_2$ are estimated by least-squares optimization. They are functions of the anisotropy parameters ε, δ and the tilting angle φ . Figure 1 compares the true dispersion relation with the approximate dispersion relation. The solid line is the true dispersion relation (equation 1) and the dashed line is the approximate dispersion relation for the finite-difference scheme (equation 3). The dispersion relation for the finite-difference scheme is very close to the true one for the negative S_x . When the phase-angle is close to 90° or more than 90° for positive S_x , the dispersion for the finite-difference scheme diverges from the true one. Figure 2 shows the relative dispersion error defined as follows:

$$E(S_x) = \frac{S_z^{fd}(S_x) - S_z^{true}(S_x)}{S_z^{true}(S_x)}, \quad (4)$$

where $S_z^{true}(S_x)$ is the value of S_z calculated from equation 1 and $S_z^{fd}(S_x)$ is the value of S_z from equation 3 using the coefficients from the least-squares estimation.

For a laterally varying medium, the anisotropy parameters vary laterally. As a consequence, the coefficients for the finite-difference scheme vary laterally. It is too expensive to

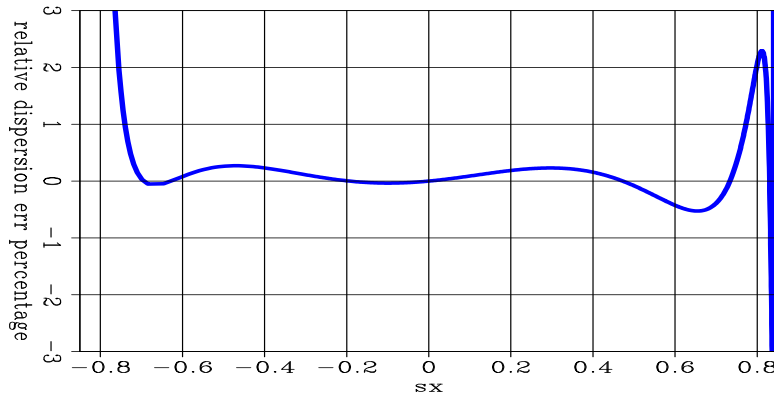


Figure 2: Relative dispersion relation error of finite-difference approximation for a TTI medium with $\varepsilon = 0.4$, $\delta = 0.2$ and $\varphi = 30^\circ$. `guojian2-err` [ER]

estimate these coefficients for each discrete grid during the wavefield extrapolation. After estimating the minimum and maximum value of the anisotropy parameters and the tilting angle, I compute the coefficients for the anisotropy parameters and the tilting angle in these ranges and store them in a table before the migration. During the wavefield extrapolation, given the anisotropy parameters ε , δ , and the tilting angle φ , I search the coefficients in the table and put them into the finite-difference scheme. Given the coefficients found from the table, the finite difference algorithm in TTI media is the same as the isotropic media. The table of coefficients is small, and the computation cost for table-searching is trivial compared to that of solving the finite-difference equation. Therefore, the cost of the optimized implicit finite-difference for TTI media is similar to that of the conventional finite-difference methods for isotropic media.

2D SYNTHETIC DATA EXAMPLE

Figure 3 shows an anisotropic model with a thrust sheet embedded in the isotropic background (Fei et al., 1998). Figure 3(a) shows the tilting angle of the thrust, Figure 3(b)-(d) show the velocity, the anisotropy parameters ε and δ of the model, respectively. This model represents the thrust shale layer usually seen in the Canadian Foothills. In the thrust sheet, the anisotropy parameter ε is 0.224, the anisotropy parameter δ is 0.10, and the velocity (in the direction paralleling to the symmetry axis) is 2925m/s. The background velocity is 2740m/s. The tilting angles of the anisotropic layer are 0° , 30° , 45° and 60° . There are 86 shots recorded with a split-spread geometry.

Figure 4 compares images of the synthetic dataset. Figure 4(a) is the image migrated by using an isotropic migration, Figure 4(b) is the image obtained by an anisotropic migration regarding the model as VTI media (Shan, 2006b), and Figure 4(c) is the image obtained by an anisotropic migration for TTI media. In Figure 4(a) and (b), the low boundary of the thrust sheet are not at the right position and the flat reflector does not focus at the right position in the area below the thrust sheet (at "A"). These features are imaged well in Figure 4(c) by the anisotropic migration for TTI media.

At "B", the low boundary of the 60° thrust sheet is better imaged in the isotropic migration (Figure 4(a)), compared to the migration for VTI media (Figure 4(b)). For the high-angle energy in a TTI medium with a large tilting angle, the velocity of the waves is close to the velocity in the symmetry-axis direction. When we regard the medium as a VTI medium, for the high-angle energy we use the velocity close to the velocity in the direction normal to the symmetry axis. In contrast, we use the velocity paralleling the symmetry axis in the isotropic migration. That is why the low boundary of the 60° thrust sheet at "B" is better imaged by the isotropic migration compared to the anisotropic migration for VTI media.

CONCLUSION

I present the optimized implicit finite-difference method for wavefield extrapolation in TTI media. The 2D synthetic dataset shows that the algorithm is stable and works for laterally varying media.

ACKNOWLEDGMENTS

I thank BP for making the synthetic dataset available. I also thank Sam Gray for sending me the dataset.

REFERENCES

- Baumstein, A., and Anderson, J., 2003, Wavefield extrapolation in laterally varying VTI media: Wavefield extrapolation in laterally varying VTI media, Soc. of Expl. Geophys., 73rd Ann. Internat. Mtg., 945–948.
- Fei, T., Dellinger, J. A., Murphy, G. E., Hensley, J. L., and Gray, S. H., 1998, Anisotropic true-amplitude migration: Anisotropic true-amplitude migration, Soc. of Expl. Geophys., 68th Ann. Internat. Mtg, 1677–1679.
- Ferguson, R. J., and Margrave, G. F., 1998, Depth migration in Ti media by nonstationary phase shift: Depth migration in Ti media by nonstationary phase shift, Soc. of Expl. Geophys., 68th Ann. Internat. Mtg, 1831–1834.
- Hale, D., 1991, 3-D depth migration via McClellan transformations: Geophysics, **56**, 1778–1785. Erratum in GEO-57-2-370.
- Lee, M. W., and Suh, S. Y., 1985, Optimization of one-way wave-equations (short note): Geophysics, **50**, 1634–1637.
- Li, Z., 1991, Compensating finite-difference errors in 3-D migration and modeling: Geophysics, **56**, 1650–1660.

- Liu, F., Day, R., Hanson, D., Whitmore, D., Mosher, C., and Sinton, J., 2005, A stable wave equation migration method in 3D VTI media: 67th Ann. Internat. Mtg., EAGE, Expanded Abstracts, P002.
- Ren, J., Gerrard, C., McClean, J., and Orlovich, M., 2005, Wave equation prestack depth migration in laterally varying VTI media: 75th Ann. Internat. Mtg., Soc. of Expl. Geophys., Expanded Abstracts, 104–107.
- Ristow, D., and Ruhl, T., 1997, Migration in transversely isotropic media using implicit operators: Migration in transversely isotropic media using implicit operators, Soc. of Expl. Geophys., 67th Ann. Internat. Mtg, 1699–1702.
- Rousseau, J. H. L., 1997, Depth migration in heterogeneous, transversely isotropic media with the phase-shift-plus-interpolation method: Depth migration in heterogeneous, transversely isotropic media with the phase-shift-plus-interpolation method, Soc. of Expl. Geophys., 67th Ann. Internat. Mtg, 1703–1706.
- Shan, G., 2006a, Optimized implicit finite-difference migration for tti media: SEP- **125**.
- , 2006b, Optimized implicit finite-difference migration for vti media: 76th Ann. Internat. Mtg., Soc. of Expl. Geophys., Expanded Abstracts.
- Shan, G., and Biondi, B., 2005, 3D wavefield extrapolation in laterally-varying tilted TI media: 75th Ann. Internat. Mtg., Soc. of Expl. Geophys., Expanded Abstracts, 104–107.
- Tang, Y., and Clapp, R., 2006, Selection of reference-anisotropy parameters for wavefield extrapolation by Lloyd's algorithm: 76th Ann. Internat. Mtg., Soc. of Expl. Geophys., Expanded Abstracts, 189–193.
- Thomsen, L., 1986, Weak elastic anisotropy: *Geophysics*, **51**, 1954–1966. Discussion in GEO-53-04-0558-0560 with reply by author.
- Uzcategui, O., 1995, 2-D depth migration in transversely isotropic media using explicit operators: *Geophysics*, **60**, 1819–1829.
- Zhang, J., Verschuur, D. J., and Wapenaar, C. P. A., 2001a, Depth migration of shot records in heterogeneous, transversely isotropic media using optimum explicit operators: *Geophys. Prosp.*, **49**, 287–299.
- Zhang, J., Wapenaar, C., and Verschuur, D., 2001b, 3D depth migration in VtI media with explicit extrapolation operators: 3D depth migration in VtI media with explicit extrapolation operators, Soc. of Expl. Geophys., 71st Ann. Internat. Mtg, 1085–1088.

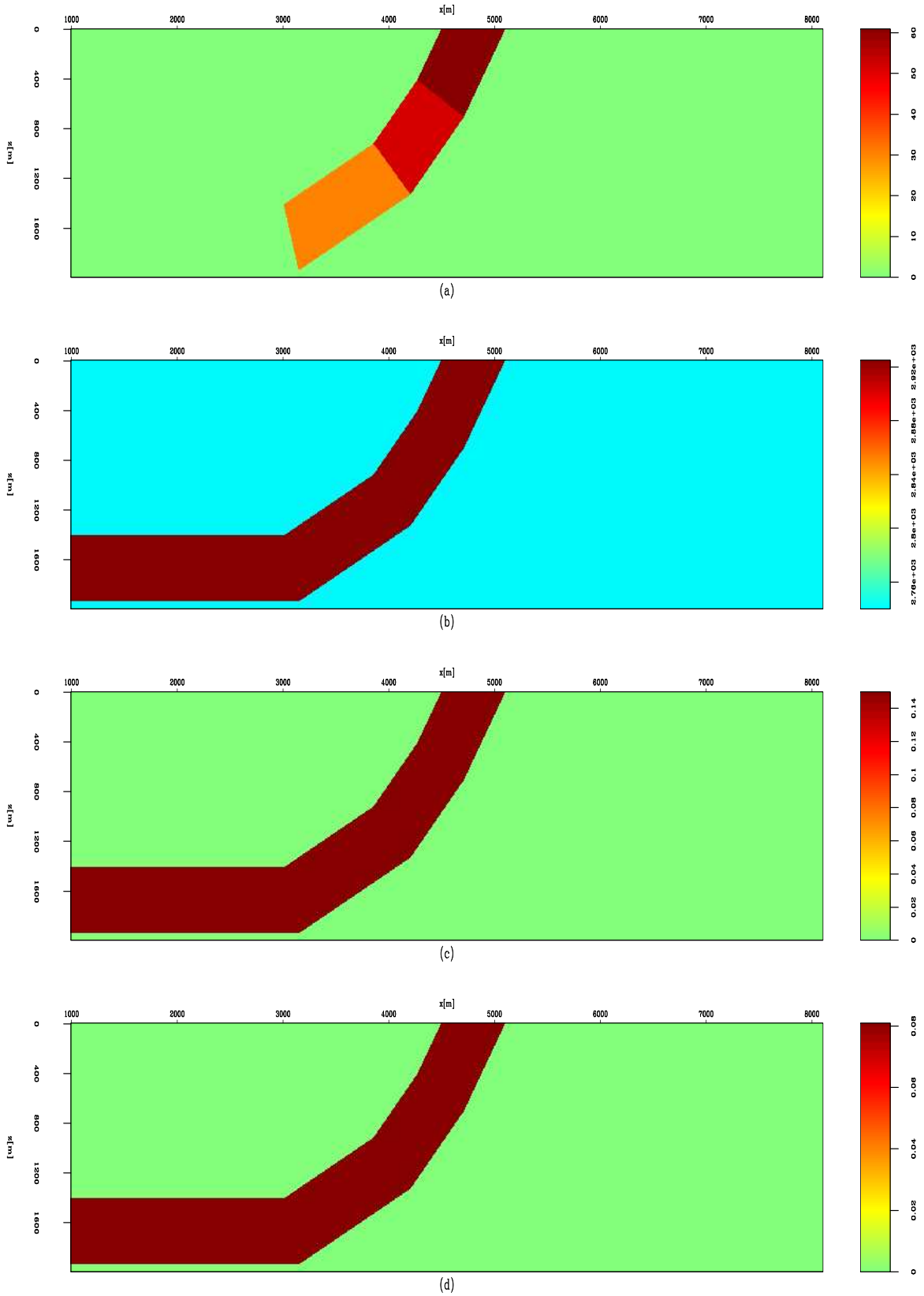


Figure 3: The velocity model and anisotropy parameters: (a) the tilting angle of the TTI medium; (b) the velocity paralleling the symmetry axis; (c) the anisotropy parameter ε ; (d) the anisotropy parameter δ . `guojian2-model` [ER]

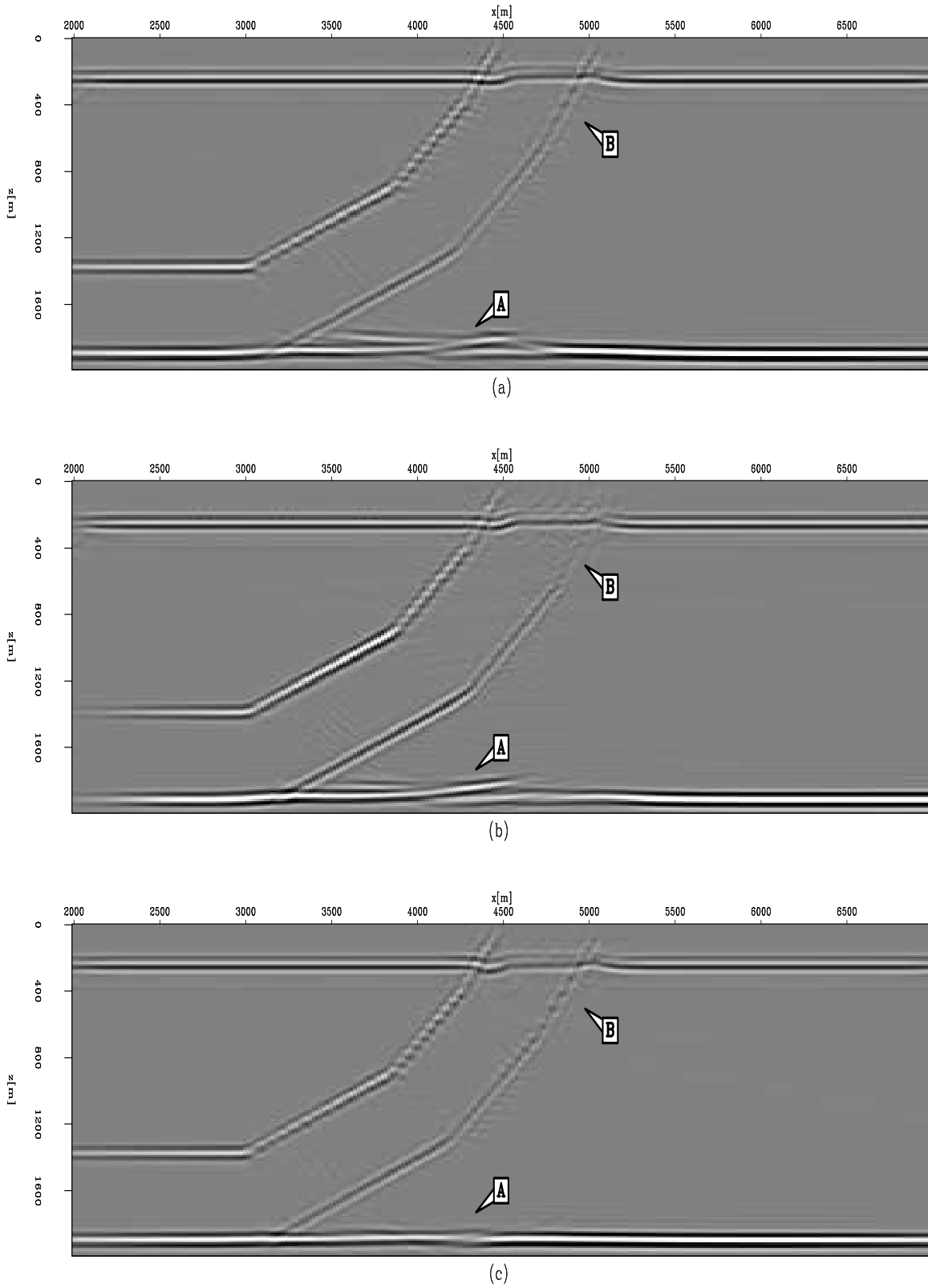


Figure 4: Image comparisons: (a) the image obtained by the isotropic migration; (b) the image obtained by anisotropic migration for VTI media; (c) the image obtained by anisotropic migration for TTI media. `guojian2-image` [CR]

Target-oriented wave-equation inversion: Sigsbee model

Alejandro A. Valenciano

ABSTRACT

A complex velocity model can cause shadow zones in an image computed by migration due to poor illumination. These shadow zones may contain weak signals masked by artifacts. To reduce artifacts and recover the real signal, a target-oriented wave-equation inversion scheme can be developed that uses an explicitly computed least squares inversion Hessian. To solve the otherwise ill-conditioned inversion problem a model regularization needs to be added. One choice for regularization is to use the customary damping in the image space, another is to penalize the energy in the image not focused at zero subsurface-offset. To apply the second, the subsurface-offset Hessian needs to be computed by using the adjoint of migration as the modeling operator. Results on Sigsbee model show encouraging results.

INTRODUCTION

Conventional imaging techniques such as migration cannot provide an accurate picture of poorly illuminated areas (Clapp, 2005). In such areas, migration artifacts can easily obscure the small amount of signal that exists. One way to solve this problem is to use an inversion formalism introduced by Tarantola (1987) to solve geophysical imaging problems. This procedure computes an image by weighting the migration result with the inverse of the Hessian matrix.

However, when the dimensions of the problem get large, the explicit calculation of the Hessian matrix and its inverse becomes unfeasible. That is why the following approximation to the wave-equation inversion must be performed: (1) to compute the Hessian in a target-oriented fashion to reduce the size of the problem; (2) to exploit the sparse structure of the Hessian matrix; and (3) to compute the inverse image following an iterative inversion scheme. The last item renders unnecessary an explicit computation of inverse of the Hessian matrix.

In this paper, I apply the target-oriented wave-equation inversion to the Sigsbee data set. I show poststack (zero subsurface-offset) and prestack (subsurface-offset) image space inversion results. I use a customary damping model regularization to make the poststack inversion stable. By the other hand, the prestack inversion is stabilized by using a regularization that penalizes energy not focused at zero subsurface-offset (Shen et al., 2003).

LINEAR LEAST-SQUARES INVERSION

Tarantola (1987) formalizes the geophysical inverse problem by giving a theoretical approach to compensate for experimental deficiency (e.g., acquisition geometry, complex overburden), while being consistent with the acquired data. His approach can be summarized as follows: given a linear modeling operator \mathbf{L} , compute synthetic data \mathbf{d} using $\mathbf{d} = \mathbf{L}\mathbf{m}$ where \mathbf{m} is a reflectivity model. Given the recorded data \mathbf{d}_{obs} , a quadratic cost function,

$$S(\mathbf{m}) = \|\mathbf{d} - \mathbf{d}_{obs}\|^2 = \|\mathbf{L}\mathbf{m} - \mathbf{d}_{obs}\|^2, \quad (1)$$

is formed. The reflectivity model $\hat{\mathbf{m}}$ that minimizes $S(\mathbf{m})$ is given by the following:

$$\hat{\mathbf{m}} = (\mathbf{L}'\mathbf{L})^{-1}\mathbf{L}'\mathbf{d}_{obs} = \mathbf{H}^{-1}\mathbf{m}_{mig}, \quad (2)$$

where \mathbf{L}' (migration operator) is the adjoint of the linear modeling operator \mathbf{L} , \mathbf{m}_{mig} is the migration image, and $\mathbf{H} = \mathbf{L}'\mathbf{L}$ is the Hessian of $S(\mathbf{m})$.

The main difficulty with this approach is the explicit calculation of the Hessian inverse. In practice, it is more feasible to compute the least-squares inverse image as the solution of the linear system of equations,

$$\mathbf{H}\hat{\mathbf{m}} = \mathbf{m}_{mig}, \quad (3)$$

by using an iterative inversion algorithm.

Regularization in the poststack image space

The condition number of the target-oriented Hessian matrix can be high, making the solution of the non-stationary least-squares filtering problem in equation (3) unstable. One solution is adding a smoothing regularization operator to equation (3):

$$\begin{aligned} \mathbf{H}\hat{\mathbf{m}} - \mathbf{m}_{mig} &\approx 0, \\ \epsilon\mathbf{I}\hat{\mathbf{m}} &\approx 0, \end{aligned} \quad (4)$$

where the choice of the identity operator (\mathbf{I}) as regularization operator is customary. A more sophisticated regularization scheme could involve applying a smoothing operator in the reflection angle (or offset ray-parameter) dimension (Prucha et al., 2000; Kuehl and Sacchi, 2001) or, more generally, in the reflection and azimuth angles.

Regularization in the prestack image space

The previous subsection solve equation 3 in a poststack image domain (zero subsurface-offset). But a prestack regularization is necessary to reduce the noise in the inversion result. If subsurface offset is included in the computation of the Hessian, a generalization to the prestack image domain of equation 4 is possible.

Three different regularization schemes for wave-equation inversion have been discussed in the literature. First, an identity operator which is customary in many scientific applications (damping). Second, a geophysical regularization which penalizes the roughness of the image in the offset ray parameter dimension (which is equivalent the reflection angle dimension) (Prucha et al., 2000; Kuehl and Sacchi, 2001). Third, a differential semblance operator to penalize the energy in the image not focused at zero subsurface-offset (Shen et al., 2003). In this paper I use the third regularization scheme, the regularization in the reflection angle domain.

A generalization to the prestack image domain of equation 3 needs regularization to obtain a stable solution. The first option for regularization is a customary damping that can be stated as follows:

$$\begin{aligned}\mathbf{H}(\mathbf{x}, \mathbf{h}; \mathbf{x}', \mathbf{h}')\hat{\mathbf{m}}(\mathbf{x}, \mathbf{h}) - \mathbf{m}_{mig}(\mathbf{x}, \mathbf{h}) &\approx 0, \\ \varepsilon \mathbf{I}\hat{\mathbf{m}}(\mathbf{x}, \mathbf{h}) &\approx 0,\end{aligned}\quad (5)$$

where $\mathbf{x} = (z, x, y)$ is a point in the image, and $\mathbf{h} = (h_x, h_y, h_z)$ is the half subsurface-offset. The subsurface-offset Hessian $\mathbf{H}(\mathbf{x}, \mathbf{h}; \mathbf{x}', \mathbf{h}')$ is

$$\begin{aligned}\mathbf{H}(\mathbf{x}, \mathbf{h}; \mathbf{x}', \mathbf{h}') = &\sum_{\omega} \sum_{\mathbf{x}_s} \mathbf{G}'(\mathbf{x} - \mathbf{h}, \mathbf{x}_s; \omega) \mathbf{G}(\mathbf{x}' + \mathbf{h}', \mathbf{x}_s; \omega) \\ &\sum_{\mathbf{x}_r} \mathbf{G}'(\mathbf{x} + \mathbf{h}, \mathbf{x}_r; \omega) \mathbf{G}(\mathbf{x}' - \mathbf{h}', \mathbf{x}_r; \omega),\end{aligned}$$

where $\mathbf{G}(\mathbf{x}, \mathbf{x}_s; \omega)$ and $\mathbf{G}(\mathbf{x}, \mathbf{x}_r; \omega)$ are the Green functions from shot position \mathbf{x}_s and receiver position \mathbf{x}_r to a model space point \mathbf{x} .

The third regularization option for the prestack generalization of equation 3, is penalizing the energy in the image not focused at zero subsurface-offset. This is obtained using the fitting goals,

$$\begin{aligned}\mathbf{H}(\mathbf{x}, \mathbf{h}; \mathbf{x}', \mathbf{h}')\hat{\mathbf{m}}(\mathbf{x}, \mathbf{h}) - \mathbf{m}_{mig}(\mathbf{x}, \mathbf{h}) &\approx 0, \\ \varepsilon \mathbf{P}_h \hat{\mathbf{m}}(\mathbf{x}, \mathbf{h}) &\approx 0,\end{aligned}\quad (6)$$

where $\mathbf{P}_h = |\mathbf{h}|$ is the differential semblance operator (Shen et al., 2003). The only difference between equations 5 and 6 is in the regularization operator.

In the next section I compare the numerical solution of the inversion problems stated in equations 5 and 6 to the imaging of Sigsbee model.

NUMERICAL RESULTS: SIGSBEE MODEL

The Sigsbee data set was modeled by simulating the geological setting found on the Sigsbee escarpment in the deep-water Gulf of Mexico. The model exhibits the illumination problems due to the complex salt shape, characterized by a rugose salt top (see Figure 1). We choose a target zone (see Figure 4) to see the effects of illumination on imaging close to the salt.

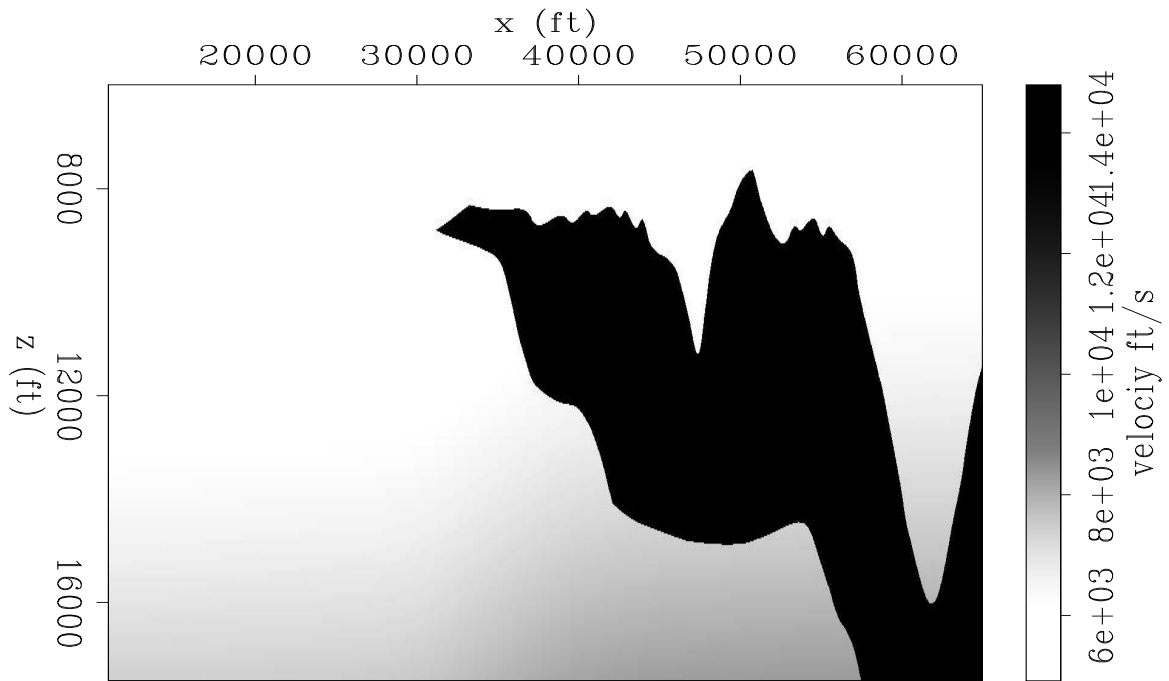


Figure 1: Sigsbee velocity model. `alejandro2-Sis_vel` [ER]

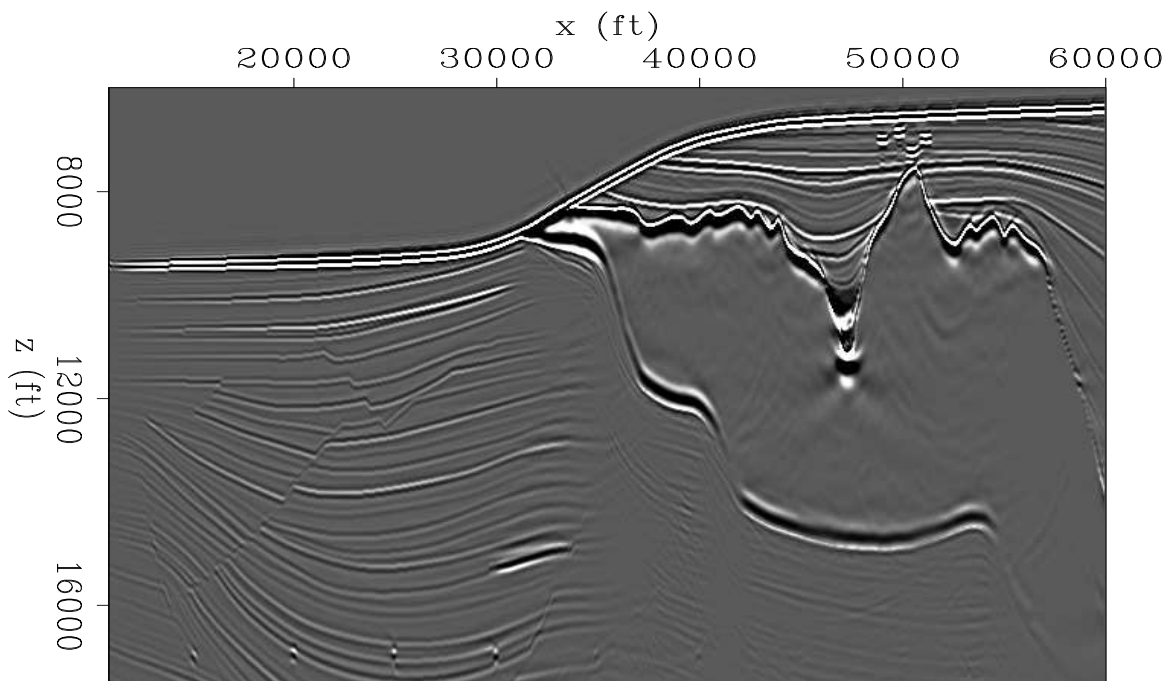


Figure 2: Sigsbee shot-profile migration image using cross-correlation imaging condition. `alejandro2-mig_Sis` [CR]

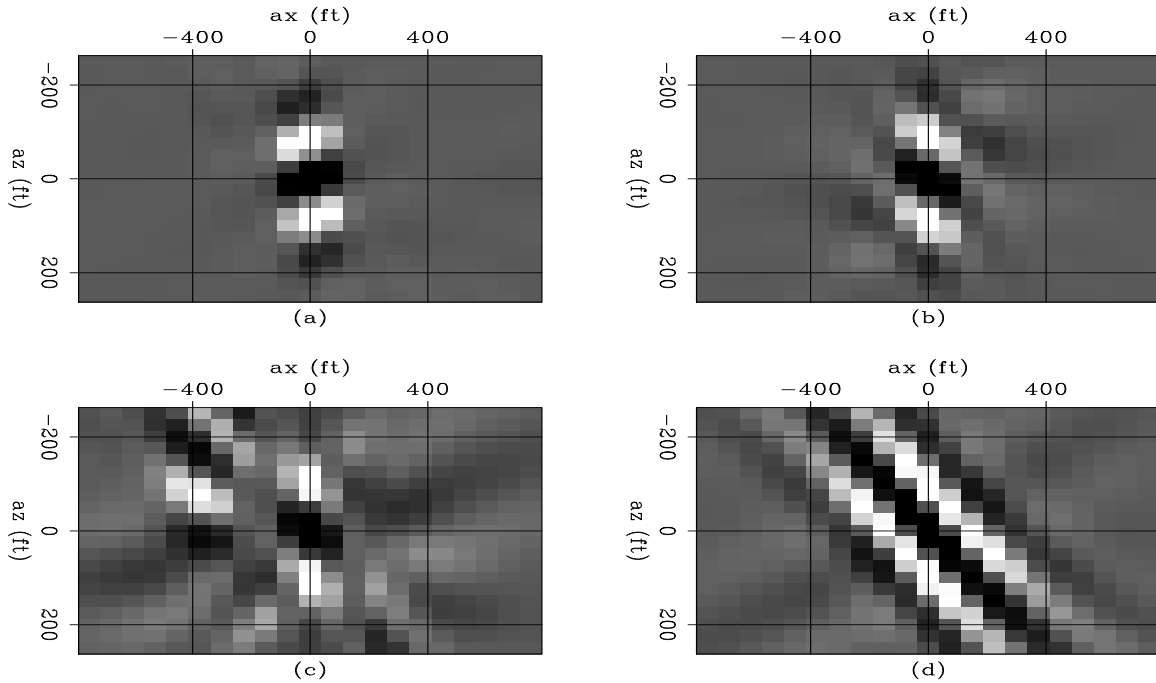


Figure 3: Hessian of the Sigsbee model, (a) point 1 $\mathbf{x} = (12000, 32000) ft$, (b) point 2 $\mathbf{x} = (12000, 33500) ft$, (c) point 3 $\mathbf{x} = (12000, 35000) ft$, and (d) point 4 $\mathbf{x} = (12000, 36500) ft$.
[alejandro2-hessian_phase_Sis](#) [CR]

Figure 2 shows the shot-profile migration image (using cross-correlation imaging condition) corresponding to the portion of Sigsbee model shown in figure 1. Notice how the amplitudes of the reflectors fade away as they get closer to the salt.

Figure 3 shows a 21×21 coefficient filter (target-oriented Hessian) at constant depth as the x coordinate moves from the sediments to the salt boundary. Figure 3a shows point 1, with coordinates $\mathbf{x} = (12000, 32000) ft$ (far from the salt). Figure 3b shows point 2, with coordinates $\mathbf{x} = (12000, 33500) ft$. Figure 3c shows point 3, with coordinates $\mathbf{x} = (12000, 35000) ft$. Figure 3d shows point 4, with coordinates $\mathbf{x} = (12000, 36500) ft$.

The shape of the filter is not dependent only on the acquisition geometry but the subsurface geometry (presence of the salt body). In the area unaffected by the salt the filter looks the same as is the constant velocity case, but as we get closer to the salt the illumination varies (in intensity and angle) and the filter behaves differently. This is due to a focusing and defocusing effect created by the salt. To correct this effect we computed the least-squares inverse image.

Figure 5 shows a comparison between the migration and the poststack inversion images in the target area. The reflection coefficients are shown in Figure 4a. Notice the position of the faults. Figure 4b shows the illumination, which is the diagonal of the Hessian matrix. Notice the decrease in the illumination as it gets closer to the salt with the exception of a narrow strip where energy focuses close to the salt. The migration result is shown in Figure 5a. The reflectors dim out as they get closer to the salt. In contrast, Figure 5b shows the poststack

inversion result, the resolution increases and the section looks more balanced. The fault can be followed and interpreted closer to the salt body.

The salt, in the inversion image looks distorted. This is due to the fact that data values (migration) in the salt boundary are bigger than everywhere else (Figure 5a), and so are the data residuals. Thus, the solver expends most of the time decreasing the residuals in that area. A residual weight designed to decrease the salt contribution should improve the image. Figures 6 and 7 compare the migration and the prestack inversion images in the reduced target area. The resolution increases, and the section looks more balanced in the prestack inversion result. The fault can be followed and interpreted closer to the salt body in the inversion image.

CONCLUSIONS

A generalization of the wave-equation target-oriented inversion to the prestack image domain needs regularization, since the condition number of the target-oriented Hessian matrix can be high. In general, inversion gives more balanced sections and higher resolution images. However, it also increases the noise that is not modeled by the one-way Green functions.

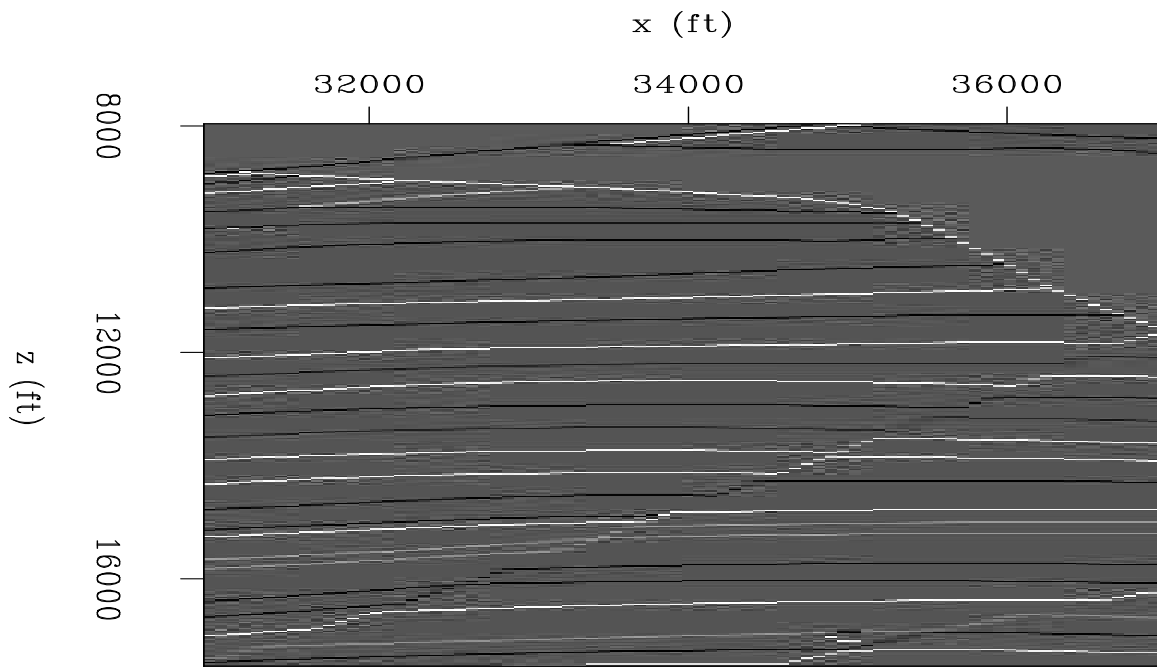
While imaging the Sigsbee model, both poststack and prestack inversion methods obtained better zero subsurface-offset images than migration, increasing the resolution and the continuity of the events into the shadow zones.

ACKNOWLEDGMENTS

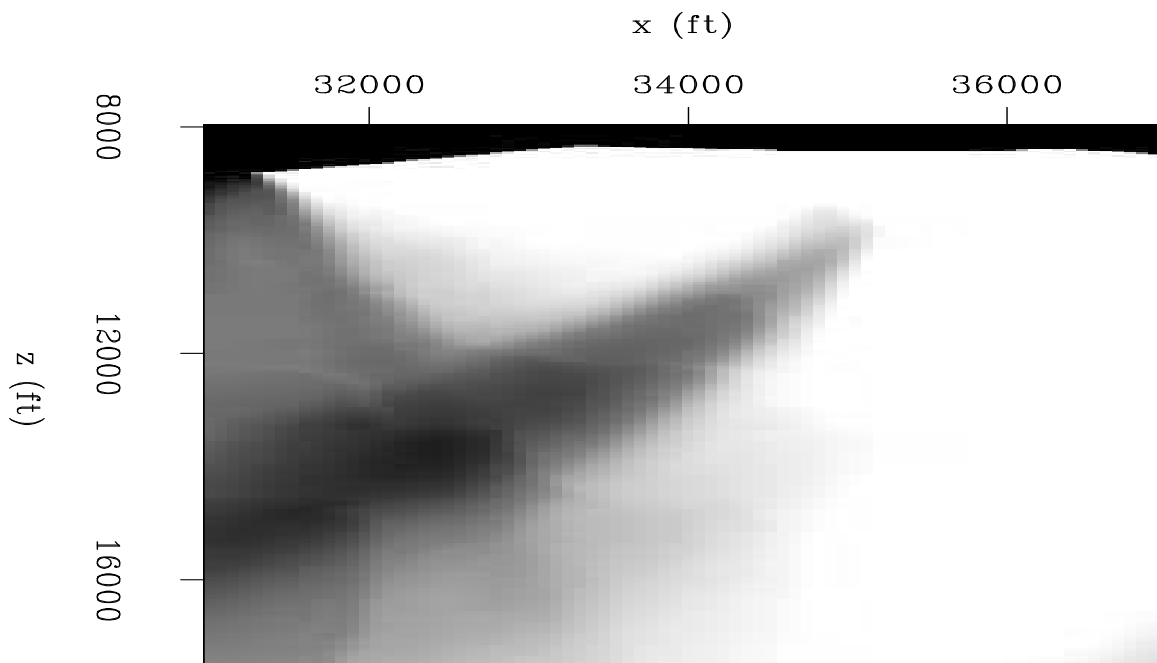
I would like to thank the SMAART JV for the synthetic data used in the experiments, as well as the Stanford Exploration Project sponsors for financial and technical support.

REFERENCES

- Clapp, M. L., 2005, Imaging under salt: illumination compensation by regularized inversion: Ph.D. thesis, Stanford University.
- Kuehl, H. and M. Sacchi, 2001, Generalized least-squares DsR migration using a common angle imaging condition: Generalized least-squares DsR migration using a common angle imaging condition:, Soc. of Expl. Geophys., 71st Ann. Internat. Mtg, 1025–1028.
- Prucha, M. L., R. G. Clapp, and B. Biondi, 2000, Seismic image regularization in the reflection angle domain: SEP-103, 109–119.
- Shen, P., W. Symes, and C. C. Stolk, 2003, Differential semblance velocity analysis by wave-equation migration: 73rd Annual International Meeting, SEG, Expanded Abstracts, 2132–2135.



(a)



(b)

Figure 4: Target area comparison. (a) reflection coefficients, and (b) illumination (dark is high and light is low) [alejandro2-comp_Sis_full1](#) [CR]

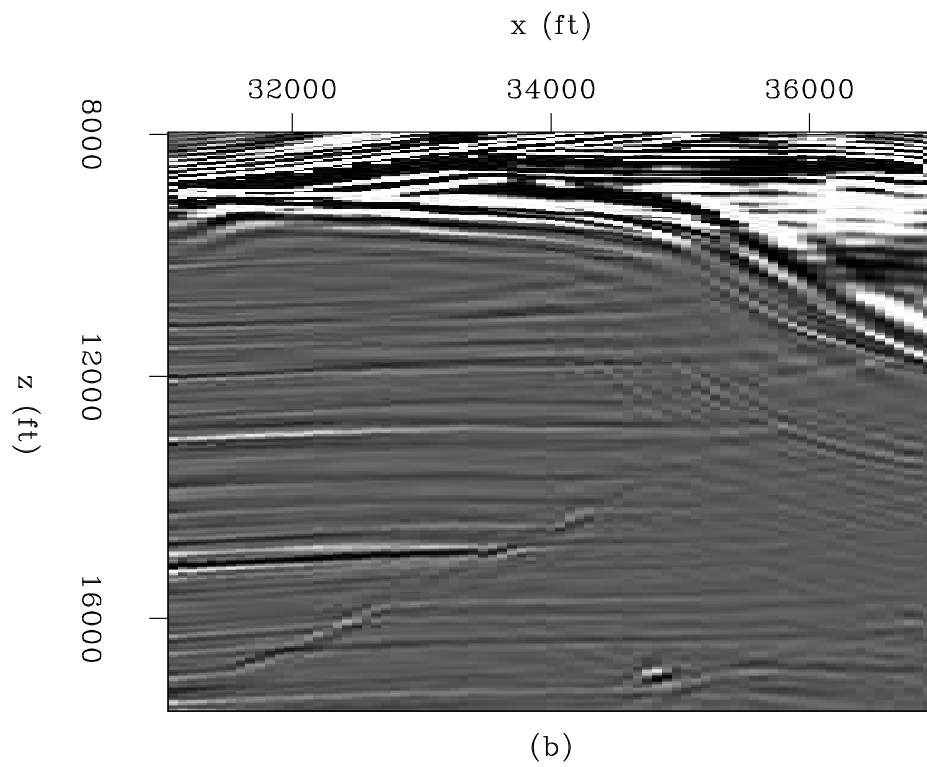
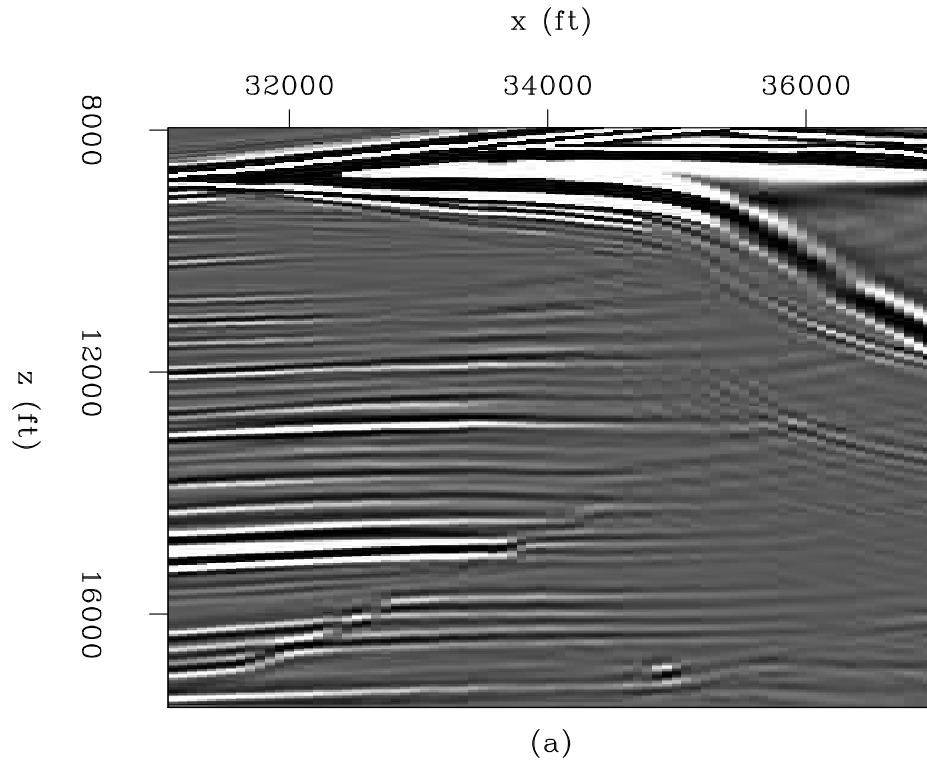


Figure 5: Target area comparison. (a) zero subsurface-offset migration, and (b) inversion. [alejandro2-comp_Sis_full2](#) [CR]

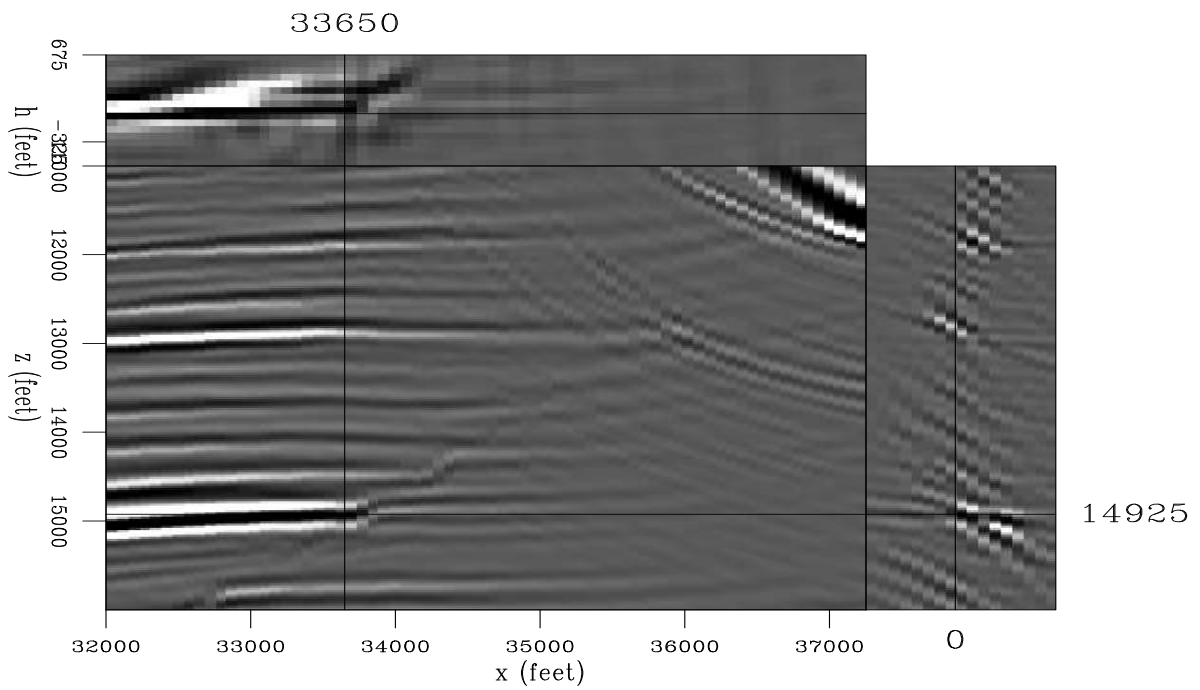


Figure 6: Sigsbee shot-profile migration prestack image using cross-correlation imaging condition. `alejandros2-mig_off` [CR]

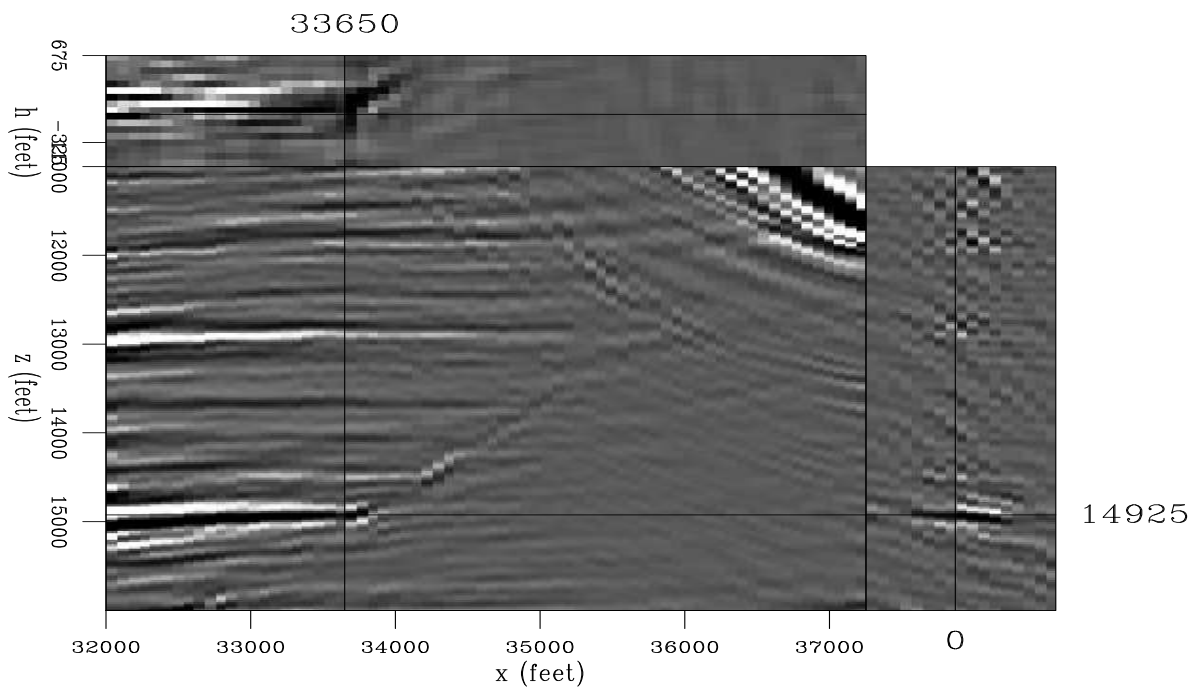


Figure 7: Sigsbee shot-profile inversion prestack image. `alejandros2-mig_inv1` [CR]

Tarantola, A., 1987, Inverse problem theory: Methods for data fitting and model parameter estimation: Elsevier Science Publication Company, Inc.

Non-stationary interpolation in the f-x domain

William Curry

ABSTRACT

Interpolation of seismic data has previously been performed using non-stationary prediction-error filters in the t-x domain. This methodology is applied in the f-x domain, and is tested on synthetic data as well as 3D pre-stack marine data in various domains. Benefits include a reduced memory footprint and computational cost, which leads to the ability to interpolate in higher dimensions than with t-x domain interpolation. However, one severe drawback is the assumption of stationarity in time.

INTRODUCTION

Interpolation of seismic data can be performed in many different domains. A simple band-limited interpolation is achieved by padding in the f-k domain. Other methods in the f-k domain involve a sparse inversion of a non-uniform (or uniform) Fourier transform (Duijndam and Schonewille, 1999; Liu and Sacchi, 2004; Xu et al., 2005).

Interpolation beyond aliasing can be performed using prediction filters in the f-x domain (Spitz, 1991) as well as prediction-error filters in the t-x domain (Claerbout, 1999; Crawley, 2000). Interpolating in the t-x domain involves estimating a single filter for the entire dataset while the f-x domain method involves estimating an independent filter for each frequency and separately interpolating each frequency. Interpolation in f-x appears to be much faster than t-x and requires a much smaller memory footprint, while the t-x approach allows for the introduction of a time-variable weighting function and is also less sensitive to noise.

Interpolation in t-x can also be performed using non-stationary filters (Crawley, 2000). These prediction-error filters vary in space and time, and solve a global problem instead of the more traditional approach of breaking the problem up into stationary regions and solving those problems independently. Interpolation in the f-x domain can also be performed using non-stationary filters, but due to the Fourier transform these filters do not vary as a function of time. This can lead to some issues when dealing with non-stationarity in time.

Non-stationary interpolation in the f-x domain provides a much less expensive alternative to the t-x domain. With this method it is now possible to perform higher-dimensional interpolation for large-scale applications such as surface-related multiple prediction. The drawbacks include acausal energy appearing in the result as well as the inability to weight in time.

PEF-BASED INTERPOLATION

A prediction-error filter (PEF) can be estimated by minimizing the following residual,

$$\mathbf{0} \approx \mathbf{r} = \begin{bmatrix} d_2 & d_1 & d_0 \\ d_3 & d_2 & d_1 \\ d_4 & d_3 & d_2 \\ d_5 & d_4 & d_3 \\ d_6 & d_5 & d_4 \end{bmatrix} \begin{bmatrix} 0 & \cdot & \cdot \\ \cdot & 1 & \cdot \\ \cdot & \cdot & 1 \end{bmatrix} \begin{bmatrix} 1 \\ f_1 \\ f_2 \end{bmatrix} + \begin{bmatrix} d_2 \\ d_3 \\ d_4 \\ d_5 \\ d_6 \end{bmatrix}, \quad (1)$$

where f_i are unknown filter values and d_i are known data values. In this case the filter has two free coefficients and there are seven data points. In practice, the PEF is multi-dimensional and contains many more coefficients. Once the PEF has been estimated it can be used in a second least-squares problem

$$\begin{aligned} \mathbf{S}(\mathbf{m} - \mathbf{d}) &= \mathbf{0} \\ \mathbf{F}\mathbf{m} &\approx \mathbf{0}, \end{aligned} \quad (2)$$

where \mathbf{S} is a selector matrix which is 1 where data is present and 0 where it is not, \mathbf{F} represents convolution with the PEF and \mathbf{m} is the desired model. The first line in equation 2 is a hard constraint while the second line is not.

In order for this method to work, the data used as input to equation 1 needs to be similar to the desired output model in equation 2. The slightly different approximations used in t-x and f-x PEFs are discussed next.

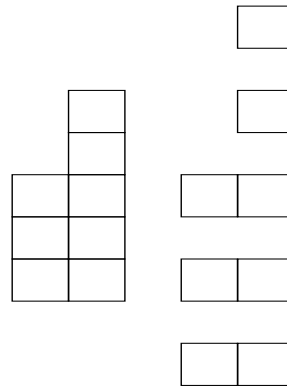
T-X VERSUS F-X METHOD

Interpolation in the time domain is accomplished by first estimating the PEF on the input data with a spaced version of the PEF, as shown in Figure 1. The amount of spacing corresponds to the factor of interpolation. Once the PEF has been estimated on the input data, it is returned to the original spacing and then the second step of the interpolation takes place, where the interpolated model space is regularized by the PEF. This PEF is estimated on the entire input dataset and is applied on the entire output dataset as two global problems.

Interpolation in the f-x domain is performed by estimating a PEF for a single frequency; for a two-dimensional f-x scenario this would be a one-dimensional PEF along x. A unique PEF is estimated at each frequency of the input data, and this PEF is then used to regularize the output data at a higher frequency equal to the original frequency multiplied by the interpolation factor. In practice, the data used to create the PEF is padded in time before being transformed to frequency so that the frequencies after multiplication by the scale factor correspond to the output frequencies that are desired.

Because the f-x domain approach interpolates each frequency independently, the input data can be broken along the frequency axis and interpolated in parallel or sequentially. This means that the memory footprint of the f-x method is smaller by a factor corresponding to the size of

Figure 1: Left: PEF on output data; right: PEF spaced by a factor of two on input data with half the sampling in space. `bill1-space` [NR]



the time (or frequency) axis. Since this is typically the largest axis, this can mean a reduction in the memory use by two to three orders of magnitude. This savings of memory means that more input data can be held in memory, and simultaneous interpolation of more dimensions is possible with the f - x approach. For example, Figure 2 was quickly created on a laptop in a few minutes, whereas the same interpolation in t - x would strain a larger workstation. The result

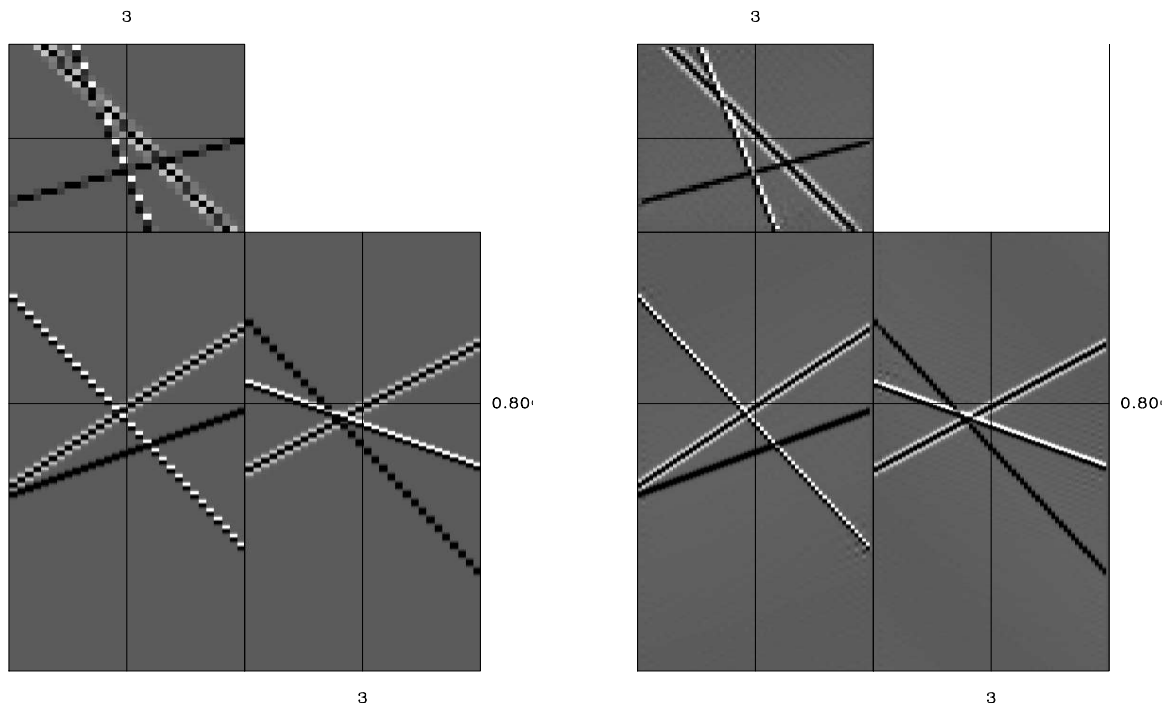


Figure 2: Left: one cube from 4D input data; right: cube interpolated by a factor of eight. The PEF used was 3D with $4 \times 4 \times 4$ coefficients. `bill1-fxpef` [ER]

shown in Figure 2 is interpolated by a factor of two on three of the four axes. This type of approach not only provides a better prediction by increasing the amount of input information but also speeds up the interpolation process by simultaneously interpolating more dimensions, which would require a cascade of lower-dimension interpolations with a t - x approach.

One reason why this f - x interpolation is much faster than t - x interpolation is that the t - x

approach captures spectral information from the data which is not used during the interpolation. F-x PEFs are a much more compact and efficient way to capture the dip information in the training data. Also, the parameterization on the PEF in t-x is less intuitive than in f-x. In f-x, the size of the PEF roughly corresponds to the number of dips that it would be able to predict. In the t-x case, the length of the PEF in time also comes in to play as it relates to the maximum dip that could be predicted by the filter. Also, the spacing of the PEF assumes that the data are very oversampled in time, so if the data are not high-cut filtered before the PEF estimation the filter could be time-aliased. Since in f-x PEFs the lower frequencies are explicitly used to interpolate the higher frequencies this problem does not happen, although it also relies upon oversampling in time.

NON-STATIONARY F-X INTERPOLATION

Since seismic data has dips that vary in space and time, the stationary methodology shown in the previous section cannot be blindly applied to entire data sets. Instead the data are either broken up into regions that are assumed to be stationary or the PEF that is estimated on the data is non-stationary. Non-stationary PEFs estimated in the t-x domain have been used to interpolate data with dips varying in both space and time. Non-stationary PEFs that are estimated in f-x can also be used to interpolate data, but since the dimensionality of the filter is less (with no time/frequency component) and the data are Fourier transformed prior to interpolation, the dip spectrum is assumed to be stationary in time.

In addition to the issue with time non-stationarity, a time-variable weighting function which could be implemented in t-x could not be implemented in f-x as the frequencies are solved independently. Figure 3 shows the qdome synthetic that is both non-stationary in space and time being interpolated by a factor of 16, 4 in each spatial dimension. The issue of non-stationarity in time in Figure 3 does not appear to be a very large problem. While the flat layers at the top and bottom of the interpolated result do contain some erroneous dips, their amplitude is quite weak compared to the dominant dips in that location.

REAL DATA EXAMPLES

Figure 4 shows various interpolations of a common-offset section from a sail line from a 3D marine survey. Figure 4(a) shows the original common-offset section, 4(b) is a 2D interpolation where the only input to the interpolation is what is shown in Figure 4(a). Figure 4(c) shows the result of a 3D interpolation where a single receiver cable as well as the common-offset section from the sail line in (a) were used. Figure 4(d) is the result of a 4D interpolation, where all four receiver cables were used as well as what was used in 4(c). The most obvious issue with all of the interpolations is the introduction of noise before the water bottom reflection. This is a result of the assumption of stationarity in time, putting all dips at all times. This noise is much more prevalent in the 2D interpolation than in the 3D and 4D interpolations. The quality of the 3D interpolation on the whole is much higher than the 2D interpolation, whereas the 4D interpolation is almost identical to the 3D case. This is not overly surprising

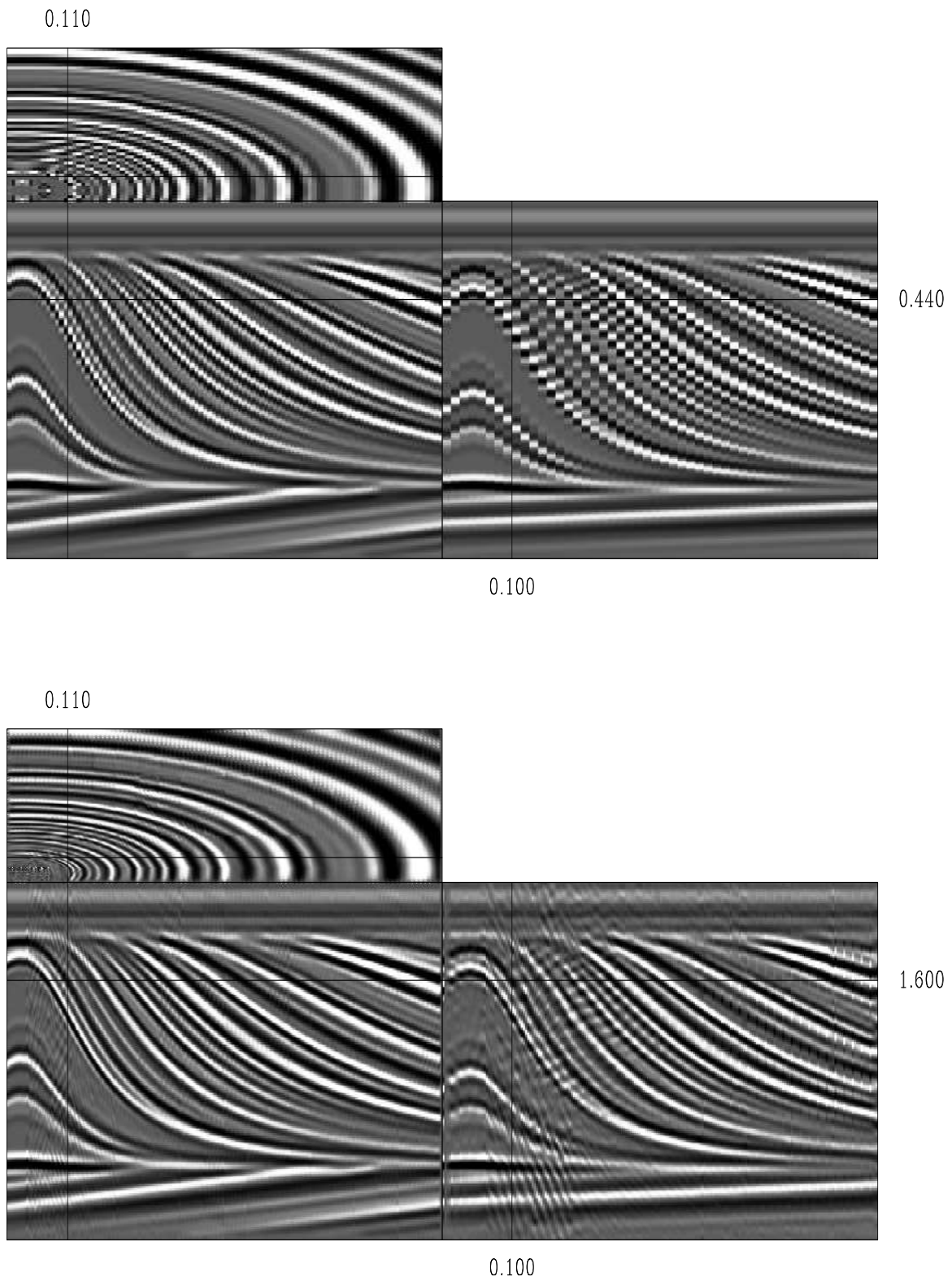


Figure 3: Top: qdome input data; bottom: qdome interpolated by a factor of 4 in each direction. PEF size is 5x5. `bill1-nspef` [ER]

since there are only 4 points in the 4th dimension (cross-line offset) which do not contribute much to the result.

Next, I compare the interpolation of receiver cables using a 3D and a 4D interpolation for a single shot. Figure 5 shows a 3D shot with the front panel as a recorded receiver cable, interpolated by a factor of 2. The number of cables is also interpolated from 4 to 8. There is an obvious improvement associated with moving from a 3D to 4D interpolation. In Figure 6 the same shot is interpolated in 3D and 4D, but the front panel of the cubes now show an interpolated receiver cable. This result looks poor in both cases, although noticeably better for the 4D interpolation. The issue of non-stationarity in time is crippling, although the overall trend of the water-bottom arrival is captured in both cases. In combination with the previous Figure shows how the length of the axis being added to the interpolation has a profound effect on the result. The interpolated cables are of much worse quality than the interpolated inline receivers, which is due to both the larger distance between the cables and the small number of receiver cables in the acquisition.

CONCLUSIONS AND FUTURE WORK

Non-stationary f-x domain interpolation appears to be a promising route to generate the vast quantities of data needed for surface-related multiple elimination. The process is embarrassingly parallel and leaves the data in a similar state as would be needed by subsequent processing algorithms. The process is also much faster than a t-x approach, and needs orders of magnitude less memory to run. However, the issue of non-stationarity in time is large, and impossible to ignore. This problem is more pronounced on the poorest-sampled axes, such as cross-line offset. Applying this non-stationary f-x methodology in time windows should hopefully address this problem.

One important thing to note is that while higher-dimensionality of the interpolation could improve the end result, this was only the case when the axis that was added was well-sampled, such as the in line source or inline offset axis. The addition of the 4 points on the cross-line offset axis did little to the end result.

In order to combine this approach with an extrapolator to quickly generate input data for a 3D surface-related multiple prediction, the next steps will be to apply this method in time-windows to address the time-non-stationarity issue as well as attempt to apply this method in the log-stretch frequency domain so that an efficient AMO operator could be applied.

ACKNOWLEDGMENTS

I would like to thank VeritasDGC for providing the dataset and Dr. Jan Pajchel of Norsk Hydro for his help in securing permission to use the dataset.

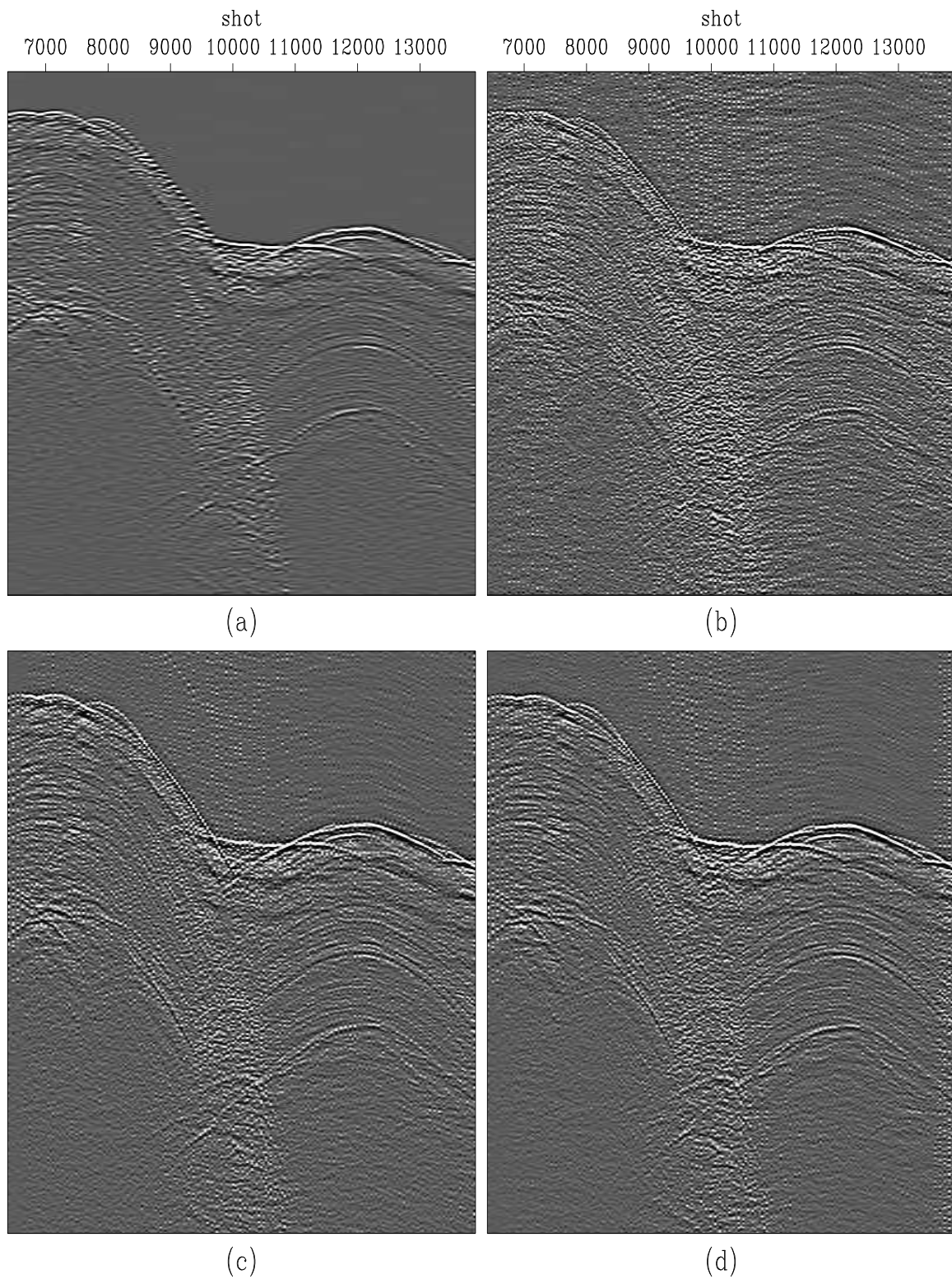


Figure 4: Interpolation of a common-offset section. (a) Input data. (b) 2D interpolation in shot, frequency. (c) 3D interpolation in shot, $offset_x$, frequency. (d) 4D interpolation in shot, $offset_x$, $offset_y$, frequency. `bill1-coffsetcomp` [CR]

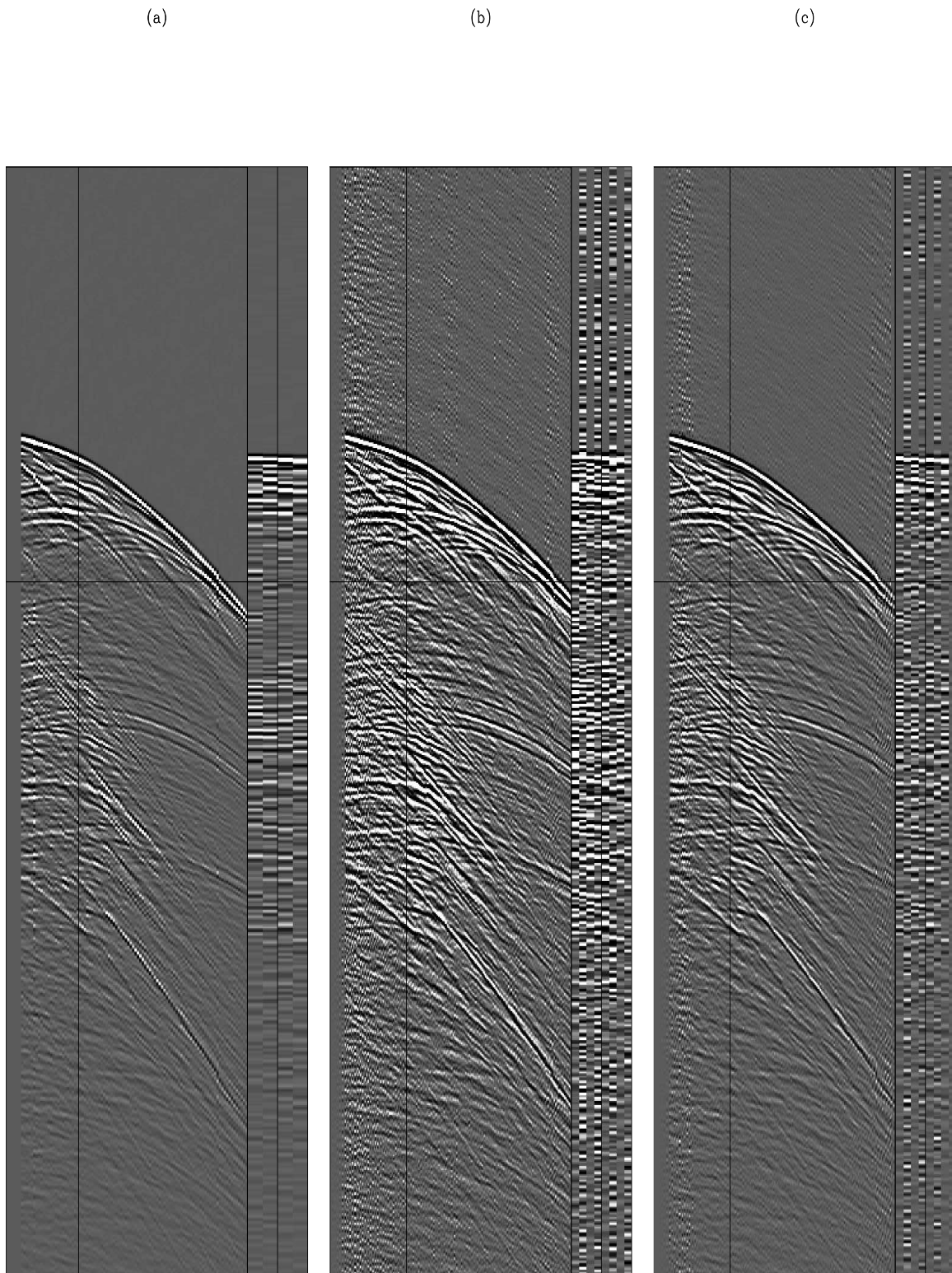


Figure 5: Interpolation of a single shot. The front panel is a recorded cable. (a) Input data with 4 streamers. (b) 3D interpolation of receivers along a cable. (c) 4D interpolation in shot, offset_x , offset_y , frequency of same shot as in (a). `bill1-shotcomp1` [CR]

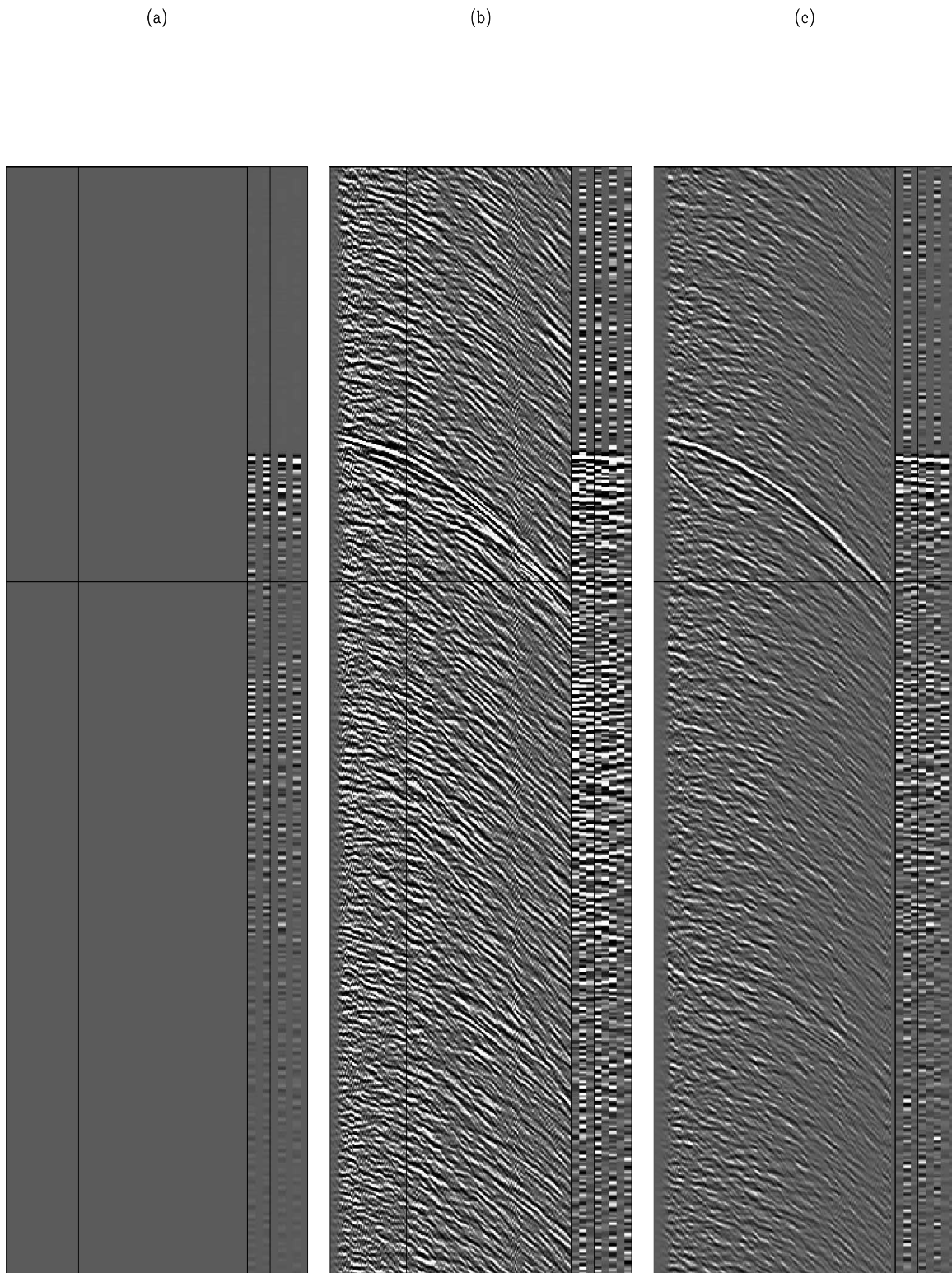


Figure 6: Interpolation of a single shot. The front panel is an interpolated cable (a) Input data. (b) 3D interpolation of a streamer using a single shot. (c) 4D interpolation in shot, offset_x, and offset_y, using multiple shots. `bill1-shotcomp2` [CR]

REFERENCES

- Claerbout, J., 1999, Geophysical estimation by example: Environmental soundings image enhancement: Stanford Exploration Project, <http://sepwww.stanford.edu/sep/pro f/>.
- Crawley, S., 2000, Seismic trace interpolation with nonstationary prediction-error filters: **SEP-104**.
- Duijndam, A. J. W. and M. A. Schonewille, 1999, Nonuniform fast Fourier transform: Geophysics, **64**, no. 2, 539–551.
- Liu, B. and M. D. Sacchi, 2004, Minimum weighted norm interpolation of seismic records: Geophysics, **69**, no. 6, 1560–1568.
- Spitz, S., 1991, Seismic trace interpolation in the F-X domain: Geophysics, **56**, no. 06, 785–794.
- Xu, S., Y. Zhang, D. Pham, and G. Lambare, 2005, Antileakage Fourier transform for seismic data regularization: Geophysics, **70**, no. 04, V87–V95.

Interpolation with pseudo-primaries: revisited

William Curry

ABSTRACT

Large gaps may exist in marine data at near offsets. I generate pseudo-primaries by auto-correlating data containing both primary and multiple reflections. These pseudo-primaries are used as training data for a non-stationary prediction-error filter, which is then used to interpolate the missing near offsets. This method yields good results using filters in the t-x domain, whereas f-x domain filters do not fare well at eliminating the crosstalk in the pseudo-primaries.

INTRODUCTION

Interpolation has become more important recently, largely due to increased reliance on algorithms that require dense and regular data sampling, such as wave-equation migration and 3D surface-related multiple elimination (SRME) (Dedem and Verschuur, 2005). Examples of current interpolation methods include Fourier (Duijndam and Schonewille, 1999; Liu and Sacchi, 2004; Xu et al., 2005), Radon transform (Trad, 2003), and prediction-error filter (PEF) based methods (Spitz, 1991). Other methods that rely on the underlying physics (and typically also a velocity model) include migration/demigration (Pica et al., 2005), DMO-based methods (Biondi and Vlad, 2001), and the focal transform (Berkhout et al., 2004), which requires an input focal operator instead of velocity.

In this paper, I further examine a hybrid approach that combines both non-stationary PEFs (Crawley, 2000) and pseudo-primaries generated from surface-related multiples (Shan and Guitton, 2004) in order to interpolate missing near offsets. I generate pseudo-primaries by auto-correlation of the input data, which gives a similar result to the cross-correlation of the input data with a multiple model described in a previous paper (Curry, 2006). Once the pseudo-primaries have been generated, I estimate a non-stationary PEF on the pseudo-primaries by solving a least-squares problem. I then solve a second least-squares problem where the newly found PEF is used to interpolate the missing data (Claerbout, 1999). This is done in both the t-x and f-x domains.

The data used in this example is the Sigsbee2B synthetic dataset where the first 2000 feet of offset were removed. Near-offset data is typically missing from marine data, and large near-offset gaps can exist when undershooting obstacles such as drilling platforms. Estimating a PEF on the pseudo-primaries, which are generated without the near offset data, gives promising results using t-x filters but f-x filters do not eliminate the crosstalk.

GENERATION OF PSEUDO-PRIMARIES

Pseudo-primaries can be generated by computing a slightly modified version of cross-correlation of primaries and a multiple model (Shan and Guitton, 2004)

$$W(x_p, x_m, \omega) = \sum_{x_s} D(x_s, x_m, \omega) \bar{D}(x_s, x_p, \omega), \quad (1)$$

where W is the pseudo-primary data, ω is frequency, x_s is the shot location, x_p and x_m are receiver locations, $\bar{D}(x_s, x_p, \omega)$ is the complex conjugate of the original trace at (x_s, x_p) and $D(x_s, x_p, \omega)$ is that same data at x_m . In this equation, the result of the cross-correlation of primaries, first-order multiples and second-order multiples in D are outlined in the table below, with the first and second columns corresponding to the inputs to the cross-correlation and the third column corresponding to the output.

Input 1	Input 2	Output
first-order multiples	first-order multiples	zero-lag
second-order multiples	second-order multiples	zero-lag
first-order multiples	primaries	pseudo-primaries
second-order multiples	first-order multiples	pseudo-primaries
second-order multiples	primaries	pseudo-first-order multiples

With higher order multiples the trend in this table continues. This produces similar results to cross-correlating primaries with a multiple model (Shan and Guitton, 2004), as the additional correlation of the primaries on one term is already taking place with the identical primaries on the other term of the autocorrelation.

Pseudo-primaries generated in this fashion contain subsurface information that would not be recorded with a non-zero minimum offset. One example of this is a first-order multiple that reflects at the free surface within the recording array, resulting in near offsets being recorded when that wave returns to the surface. This is shown in Figures 1 and 2, where Figure 1 is a cube of the input Sigsbee2B shots (including the negative offsets predicted by reciprocity) but with offsets less than 2000 feet removed, and Figure 2 is the corresponding cube of pseudo-primaries for the same area. Put briefly, the source coverage of the pseudo-primary data is much greater than that of the input data because all receivers in the original data become sources for the pseudo-primaries.

Figure 2 contains a lot of near-offset information present in the pseudo-primaries that is not present in the recorded primaries. However, simply replacing the missing near offsets of the primaries with the corresponding pseudo-primaries would not yield a satisfactory result due to the crosstalk and noise in the pseudo-primaries.

The crosstalk in the pseudoprimaries is largely a function of the number of shots that are summed over in the input data. Figure 3 shows the shot on the right panel of Figure 2, but without the summing over shots in equation 1 where instead of summing over shots each shot is plotted along the front face of the cube. It shows how the stacking procedure greatly increases the signal-to-noise ratio.

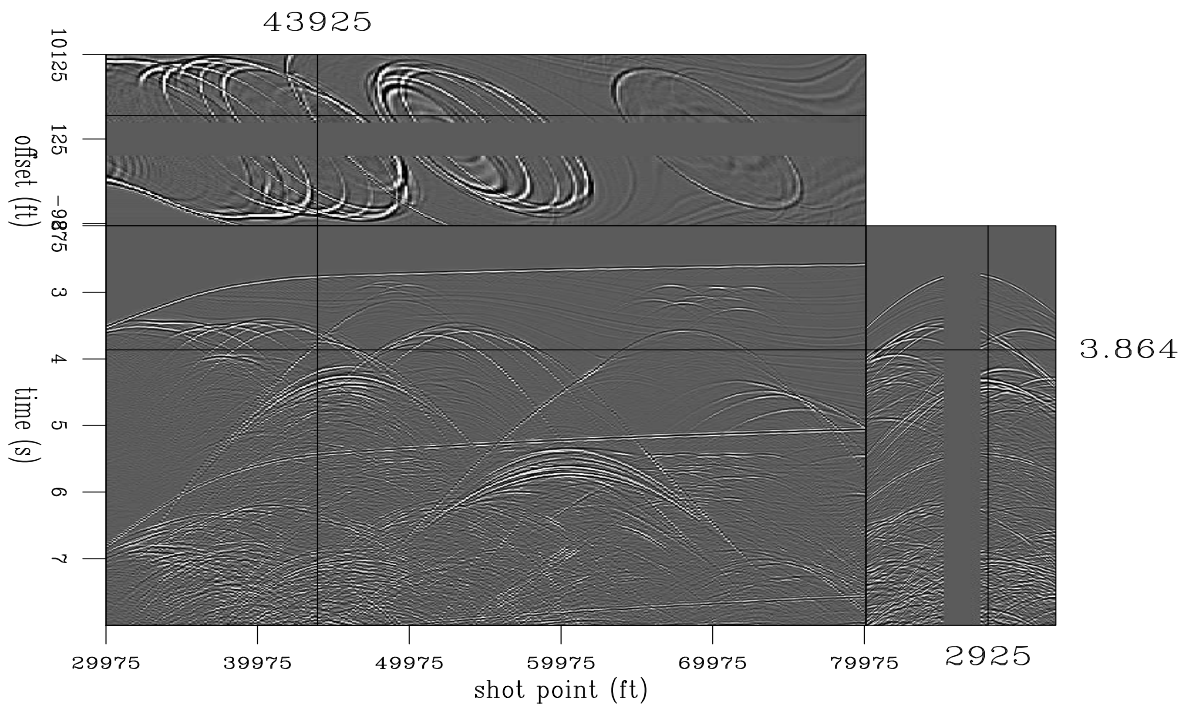


Figure 1: Input dataset missing the nearest 2000' of offsets on either side. bill2-input [ER]

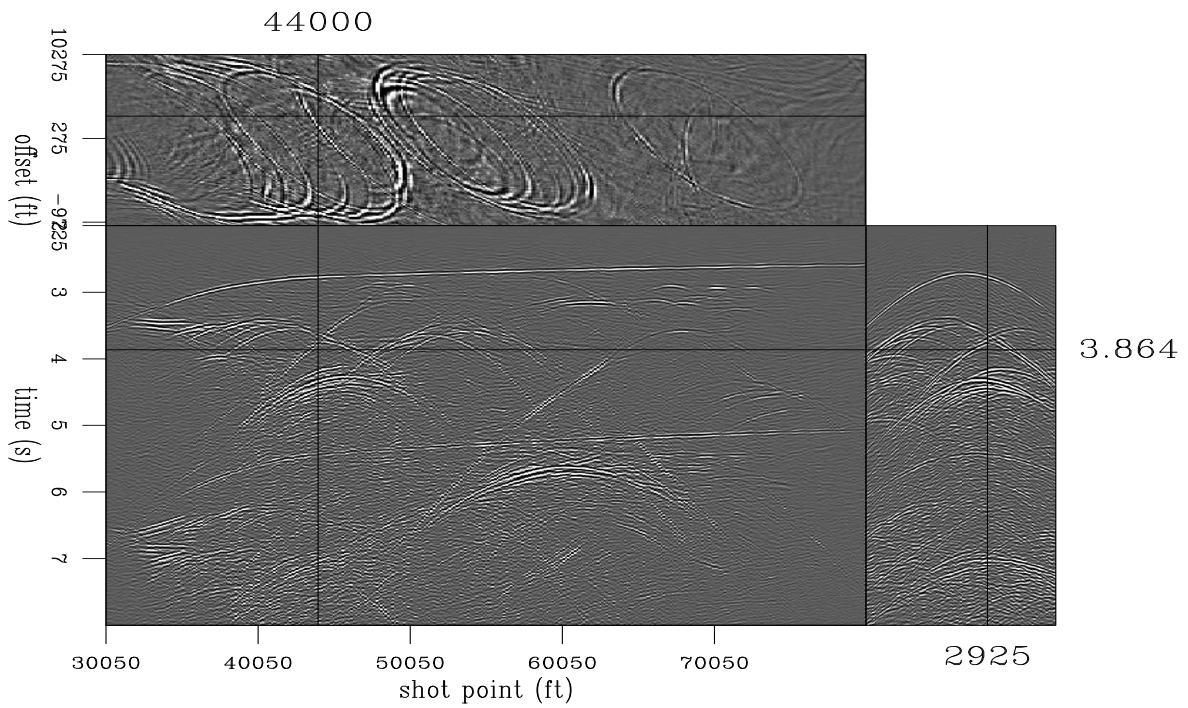


Figure 2: Pseudo-primaries created by autocorrelation and summation of Figure 1. Note that the near offsets have been filled in. bill2-pseudo [CR]

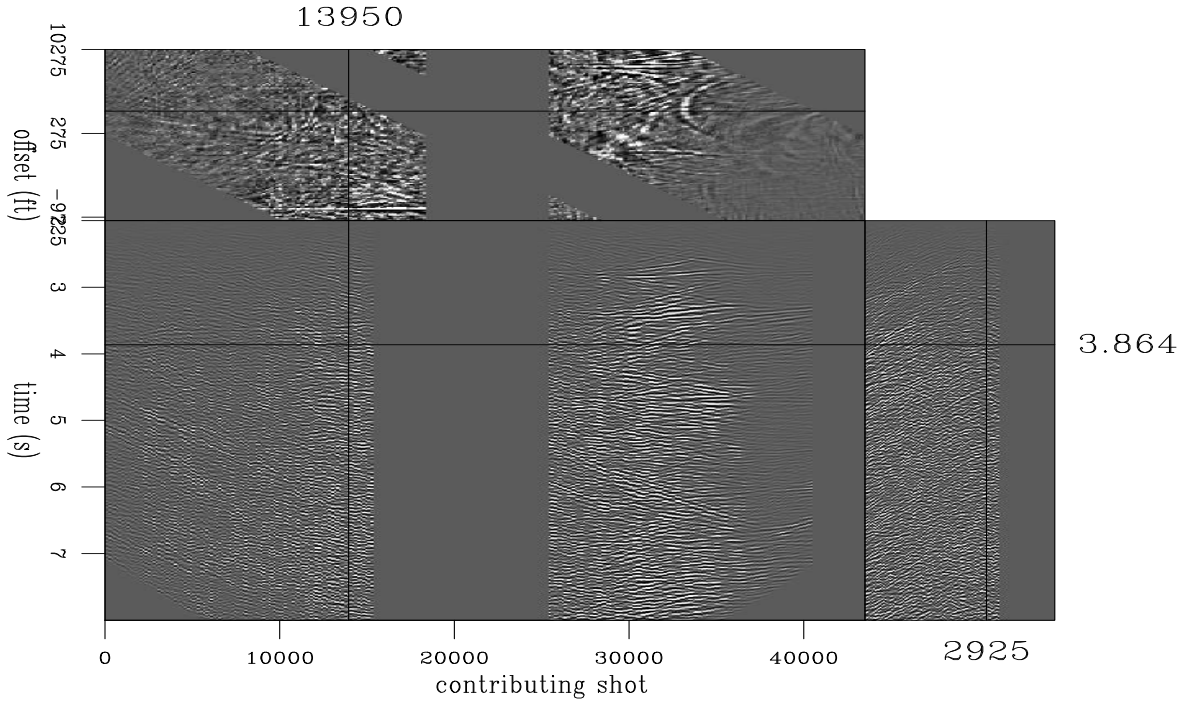


Figure 3: A single virtual shot from figure 2 that has been expanded over the input shot axis.
bill2-pseudoex [CR]

INTERPOLATION WITH NON-STATIONARY PEFs

Interpolation can be cast as a series of two inverse problems where a prediction-error filter is estimated on known data and is then used to interpolate missing data. A prediction-error filter (PEF) can be estimated by minimizing the output of convolution of known data with an unknown filter (except for the leading 1), which can be written in matrix form as

$$\mathbf{0} \approx \mathbf{r} = \begin{bmatrix} d_2 & d_1 & d_0 \\ d_3 & d_2 & d_1 \\ d_4 & d_3 & d_2 \\ d_5 & d_4 & d_3 \\ d_6 & d_5 & d_4 \end{bmatrix} \begin{bmatrix} 0 & \cdot & \cdot \\ \cdot & 1 & \cdot \\ \cdot & \cdot & 1 \end{bmatrix} \begin{bmatrix} 1 \\ f_1 \\ f_2 \end{bmatrix} + \begin{bmatrix} d_2 \\ d_3 \\ d_4 \\ d_5 \\ d_6 \end{bmatrix}, \quad (2)$$

where f_i are unknown filter values and d_i are known data values.

The filters used in this paper are all multidimensional, which are computed with the helical coordinate. In the case of a stationary multidimensional PEF, this is an over-determined least-squares problem with a unique solution.

Seismic data is non-stationary in nature, so a single stationary PEF is not adequate for changing dips. I estimate a single spatially-variable non-stationary PEF and solve a global optimization problem (Guitton, 2003). In that case the problem is under-determined, and a

regularization term is added to the least-squares problem so that (in matrix notation),

$$\begin{aligned} \mathbf{DKf} + \mathbf{d} &\approx \mathbf{0} \\ \epsilon \mathbf{Af} &\approx \mathbf{0}, \end{aligned} \quad (3)$$

where \mathbf{D} represents non-stationary convolution with the data, \mathbf{f} is now a non-stationary PEF, \mathbf{K} (a selector matrix) and \mathbf{d} (a copy of the data) both constrain the value of the first filter coefficient to 1, \mathbf{A} is a regularization operator (a Laplacian operating over space) and ϵ is a trade-off parameter for the regularization. Solving this system will create a smoothly variable PEF.

Once the PEF has been estimated, it can be used in a second least squares problem that matches the output model to the known data while simultaneously regularizing the model with the newly found PEF,

$$\begin{aligned} \mathbf{S}(\mathbf{m} - \mathbf{d}) &= \mathbf{0} \\ \mathbf{Fm} &\approx \mathbf{0}, \end{aligned} \quad (4)$$

where \mathbf{S} is a selector matrix which is 1 where data is present and 0 where it is not, \mathbf{F} represents convolution with the non-stationary PEF, and \mathbf{m} is the desired model.

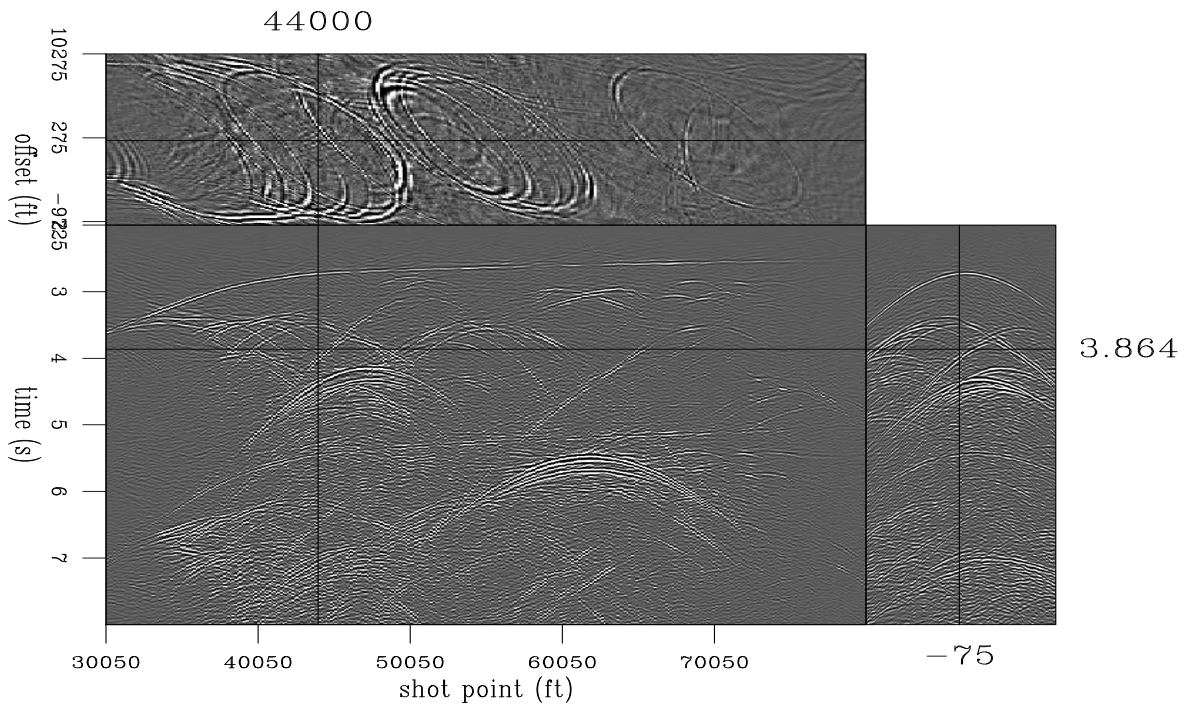


Figure 4: Pseudo primaries located on a missing common-offset section from the input data set. `bill2-pseudo2` [CR]

RESULTS

To increase the sampling by an integer factor, a PEF is typically estimated on the input data with some sort of change in sampling. In this example with a large gap this will not suffice. Instead, we estimate the PEF on the pseudo primaries generated by equation 1 using equation 3 and then use that PEF to interpolate the recorded data with equation 4. The results of this experiment (using a non-stationary t-x filter) are shown in Figure 5.

The near offset gap is 4000 feet or 26 traces, as shown in Figure 1. A non-stationary PEF in the t-x domain is then independently estimated on each shot in Figure 4, and that PEF is then used to fill in the missing data in the input and the result is shown in Figure 5.

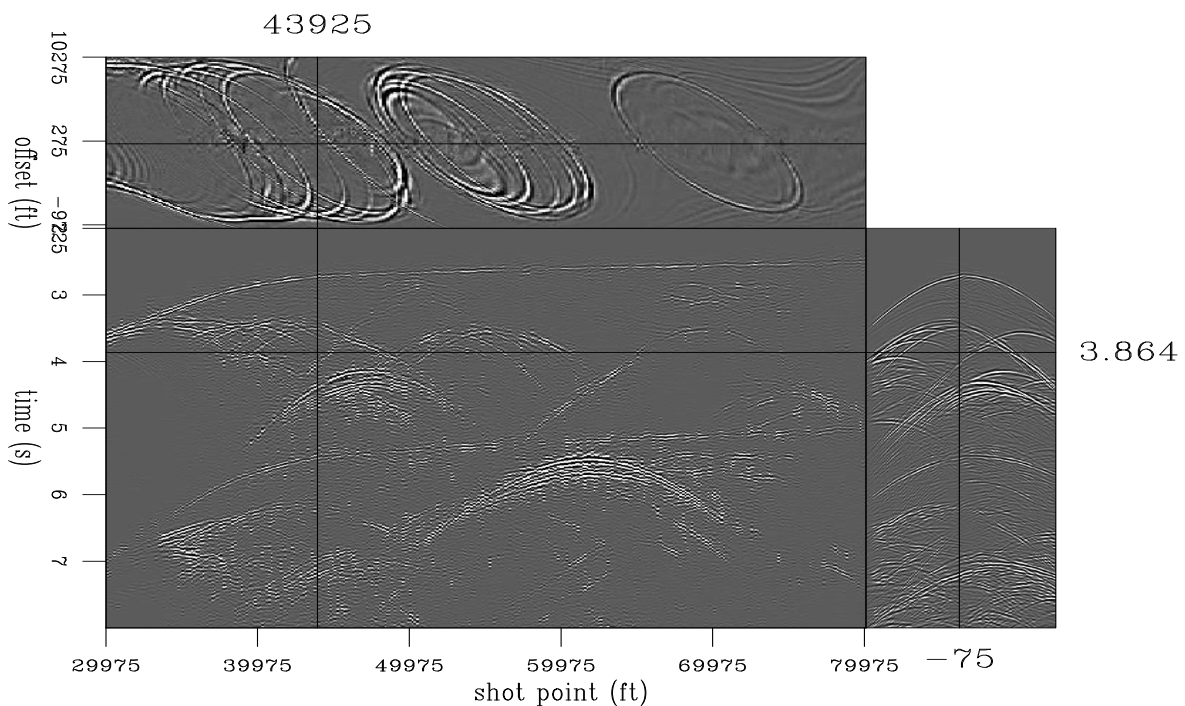


Figure 5: Near offsets interpolated with a non-stationary PEF trained on the pseudo primaries in the t,offset domain. `bill2-txinterp` [CR]

The result in Figure 5 looks very good. The interpolated portion of the shot on the right side of Figure 5 looks very good, with diffractions and crossing events correctly interpolated. Most of the crosstalk present in the pseudo primaries in Figure 4 is gone. However, there is a slight change in the wavelet, which can be explained by the squaring of the wavelet in the cross-correlation and the t-x domain PEF capturing spectral information.

Now looking at the front panel of Figure 5 that corresponds to a constant-offset section, another problem becomes more apparent. The section looks somewhat jagged from one shot to the next. This is largely because this problem was solved on a shot-by-shot basis so that there is no guarantee of lateral continuity between shots. This could be remedied by using a 3D PEF in t,offset, and shot so that correlations between shots would be taken into account.

Another less expensive method would be to use a non-stationary f-x-y domain PEF (Curry, 2007), described next.

Instead of interpolating in t-x, we can transform the data into the frequency domain and perform the interpolation individually for each frequency. This approach would largely use the same machinery as the t-x approach, except that all numbers are now complex and the filter would be 2D in shot and offset space. Since this filter does not operate along time or frequency no spectral information is captured, which should eliminate the wavelet issue in the t-x example and the added shot axis (due to the much lower memory requirements of the method) should reduce the jitteriness across the shot axis in the result.

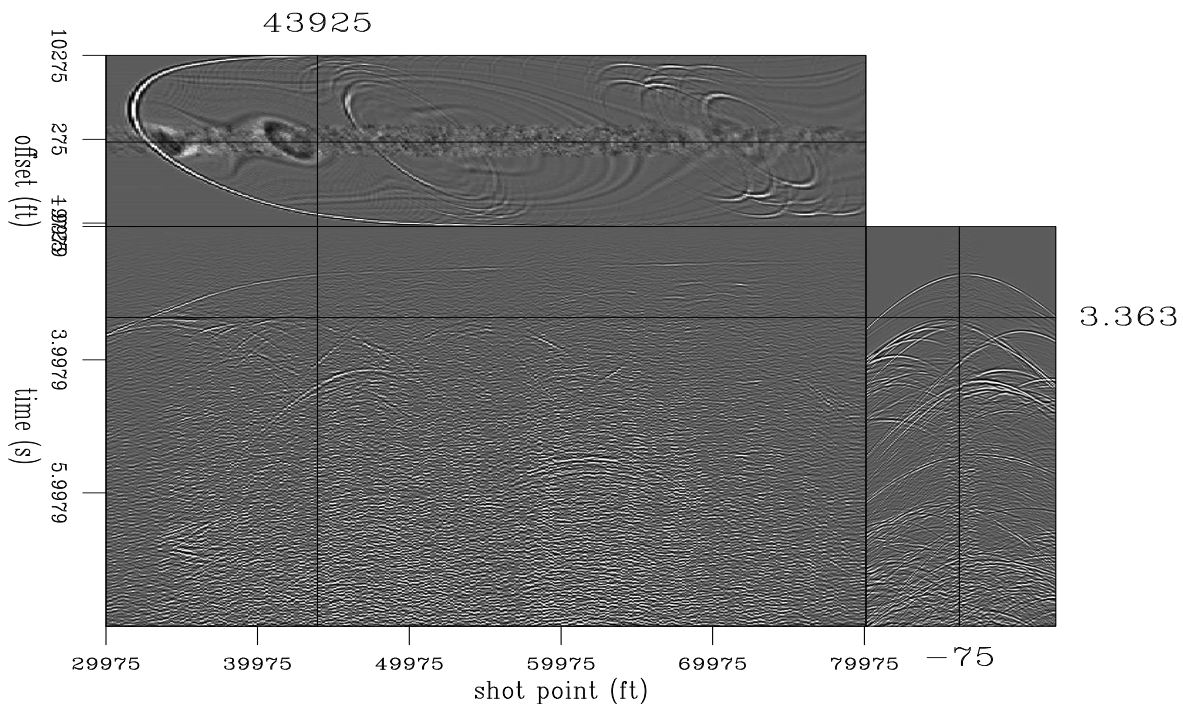


Figure 6: Near offsets interpolated with a non-stationary PEF trained on the pseudo-primaries in the f,offset,and shot domain. `bill2-fxinterp` [CR]

The f-x-y interpolation result, shown in Figure 6 does reduce both of these problems. The wavelet now remains consistent between the recorded data and the interpolated data. The interpolation result also seems less jagged along the shot axis as the PEF is also estimated along this axis. However, the problem of what appears to be crosstalk is much worse. This is due to assumed stationarity in time. Since the data were Fourier Transformed as a whole and the problem is solved in the frequency domain, all dips for a given spatial location appear to be present at all times. This problem could hopefully be addressed by breaking the input data into small time windows that are more stationary in time.

CONCLUSIONS AND FUTURE WORK

Incorporating pseudo-primary data into a non-stationary prediction-error filter based interpolation method gives promising results for large gaps in the near offset. This problem would be very difficult to solve without the additional information provided by the pseudo-primaries, and the prediction-error filter approach eliminates a lot of the crosstalk that a simple cut-and-paste approach would have. T-x filters give a much nicer result than f-x, even with the greater dimensionality of the f-x filters. This is largely due to the issue of non-stationarity in time, which may be addressed by using the f-x approach in small time windows.

This method has been attempted on real data, and would initially appear to have the most benefit in the cross-line direction by creating pseudo-source lines where the receiver cables are, but the signal-to-noise ratio of initial attempts is very poor and not useful to show here. This would be equivalent to reducing the number of samples along the shot axis in Figure 3, which would clearly present problems. Also, the issues of cable feathering, swerving sail lines, 3D geometry and coherent noise all present problems with using this approach with real data.

ACKNOWLEDGMENTS

The author would like to thank the SMAART JV for the Sigsbee2B dataset, and Guojian Shan for assistance with the pseudo-primaries.

REFERENCES

- Berkhout, A. J., D. J. Verschuur, and R. Romijn, 2004, Reconstruction of seismic data using the focal transformation: Reconstruction of seismic data using the focal transformation:, Soc. of Expl. Geophys., 74th Ann. Internat. Mtg., 1993-1996.
- Biondi, B. and I. Vlad, 2001, Amplitude preserving prestack imaging of irregularly sampled 3-D data: SEP-110, 1-18.
- Claerbout, J., 1999, Geophysical estimation by example: Environmental soundings image enhancement: Stanford Exploration Project, <http://sepwww.stanford.edu/sep/pro/f/>.
- Crawley, S., 2000, Seismic trace interpolation with nonstationary prediction-error filters: SEP-104.
- Curry, W., 2006, Interpolation with pseudo-primaries: SEP-124.
- Curry, W., 2007, Non-stationary interpolation in the f-x domain: SEP-129.
- Dedem, E. V. and D. Verschuur, 2005, 3D surface-related multiple prediction: A sparse inversion approach: Geophysics, 70, no. 03, V31-V43.

- Duijndam, A. J. W. and M. A. Schonewille, 1999, Nonuniform fast Fourier transform: *Geophysics*, **64**, no. 2, 539–551.
- Guitton, A., 2003, Multiple attenuation with multidimensional prediction-error filters: *SEP-113*, 57–74.
- Liu, B. and M. D. Sacchi, 2004, Minimum weighted norm interpolation of seismic records: *Geophysics*, **69**, no. 6, 1560–1568.
- Pica, A., G. Poulain, et al., 2005, 3D surface-related multiple modeling: *The Leading Edge*, **24**, no. 3, 292–296.
- Shan, G. and A. Guitton, 2004, Migration of surface-related multiples: Tests on Sigsbee2B data sets: Migration of surface-related multiples: Tests on Sigsbee2B data sets., *Soc. of Expl. Geophys.*, 74th Ann. Internat. Mtg., 1285–1288.
- Spitz, S., 1991, Seismic trace interpolation in the F-X domain: *Geophysics*, **56**, no. 06, 785–794.
- Trad, D. O., 2003, Interpolation and multiple attenuation with migration operators: *Geophysics*, **68**, no. 6, 2043–2054.
- Xu, S., Y. Zhang, D. Pham, and G. Lambare, 2005, Antileakage Fourier transform for seismic data regularization: *Geophysics*, **70**, no. 04, V87–V95.

Seismic monitoring of sub-salt reservoirs: Time-lapse wave-equation inversion

Gboyega Ayeni and Biondo Biondi

ABSTRACT

Time-lapse seismic is now a core technology for reservoir monitoring and characterization. However, many challenges continue to exist in its application in complex geology (e.g. sub-salt reservoirs). Differences in acquisition geometry (non-repeatability) and poor illumination are examples of factors that cause contamination of the desired time-lapse effects (i.e. changes due to production). By computing the time-lapse response as a difference between least-squares inverse images or posing time-lapse imaging as a least-squares inverse problem, we hope to attenuate geometry and other unwanted effects.

INTRODUCTION

Time-lapse (or 4D) seismic monitoring of hydrocarbon reservoirs has seen tremendous growth throughout the 1990s and during this decade. In general, 4D seismic is based on the premise that changes in fluid content (e.g. due to production) cause changes in the acoustic properties of rocks which are detectable in recorded seismic data. A detailed review of the seismic properties of reservoir pore-fluids is given by Batzle and Wang (1992). Lumley (1995) gives a comprehensive review of the theory, caveats and applications of time-lapse seismic in reservoir monitoring. Also, in his review of methods and current applications of 4D seismic, Calvert (2005) outlined many of the acquisition, processing modeling and integration requirements for successful application of the technology. Since its adoption as a monitoring tool, many successful applications of time-lapse seismic monitoring have been published (Biondi et al., 1998; Lefeuvre et al., 2003; Whitcombe et al., 2004; Zou et al., 2006).

Repeatability is a major consideration for successful application of 4D seismic monitoring, especially in reservoirs with very low seismic responses. Non-repeatability may result from differences in survey acquisition geometry and binning, cable feathering, tides, source-wavelet bandwidth and phase variability, differential static time-shifts, ambient noise, residual multiple energy, and relative mispositioning of imaged reflection events (Rickett and Lumley, 2001; Johnston, 2005). Laws and Kragh (2000) and Eiken et al. (2003) discuss acquisition techniques that may reduce some of these uncertainties. Recent advances in time-lapse processing have improved the success rate in 4D seismic monitoring. Some of the common processing issues are discussed by Ross and Altan (1997) and Eastwood et al. (1994). Rickett and Lumley (2001) outline a cross-equalization scheme involving spatial re-alignment, matched filtering,

amplitude balancing and warping. Co-processing or parallel processing (involving controlled amplitude and phase, early geometry equalization, and application of the same algorithms and parameters) of the different seismic datasets is now common practice (Johnston, 2005).

Although some of the best practices in time-lapse reservoir monitoring help improve the the reliability of time-lapse responses and confidence in their interpretations, many loopholes still exist. Most of these shortcomings may not be important in reservoirs with large seismic responses — where such unwanted effects are submerged by the much stronger time-lapse response. However, in many scenarios (e.g. sub-salt reservoirs), slight inaccuracies may cause considerable spurious 4D effects. We envisage that with the gradual increase in demand for more optimal reservoir management (hence the need for more accurate amplitudes), and current changes in acquisition patterns (hence the need to utilize surveys with potentially widely varying geometries), circumventing the shortcomings in current time-lapse imaging practice will be necessary.

We briefly discuss some of the challenges in sub-salt reservoir monitoring and show preliminary (raw) 2D synthetic time-lapse images in the presence and absence of salt. Our goal is to attenuate contamination by artifacts caused by differences in acquisition geometries and also to correct for the weakened time-lapse response due to limited illumination. We discuss two target-oriented least-squares inversion approaches that may overcome some of these challenges.

In the first approach, based on previous work by Valenciano et al. (2006), the time-lapse image is given as the difference between two least-squares inverse images. In the second approach, we pose time-lapse imaging as an inverse problem and propose to directly solve for the time-lapse image by least-squares inversion. By solving for the time-lapse image through inversion rather than as a difference between migrated seismic surveys, we believe many undesired effects in seismic monitoring of sub-salt reservoirs — and reservoirs with very complex overburdens — could be removed.

SUBSALT RESERVOIR MONITORING

The large velocity contrast at salt boundaries, complexity of seismic travel paths, lack of amplitude reciprocity, and effects from peaks and pits (Muerdter and Ratcliff, 2001) are some of the causes of illumination problems in sub-salt reservoirs. Several acquisition techniques (wide-, rich-, and full-azimuth surveys, ocean-bottom surveys and VSPs) now help improve illumination of subsalt reservoirs (Sava, 2006). Also, 3D prestack depth migration (PSDM) has been shown to be an important processing tool for sub-salt imaging (Ratcliff et al., 1994; Biondi et al., 1999; Malaguti et al., 2001).

Although many advanced acquisition and processing techniques help to correctly image reflectors beneath most complex/detached and/or steeply dipping salt bodies, the seismic amplitudes recovered from most of these techniques are not usually reliable. Rickett (2003) suggested weighting functions derived from reference images to correct for amplitude distortions caused by illumination problems. While amplitudes recovered from such normalization

schemes meet many imaging requirements, their reliability may be considerably lower in scenarios such as sub-salt reservoir monitoring where slight inaccuracies could be very important. As shown in Figure 1, slight changes in shot/image position (and/or acquisition geometry) could result in widely different (and complex) travel paths of sub-salt reflections. Also, artifacts from the migration process tend to obscure the weak signals from these reflectors (Clapp, 2005) and even small differences between these artifacts may considerably contaminate the time-lapse response. In many cases, there is no guarantee that the cross-equalization process would leave the desired time-lapse effect intact. These factors, coupled with the original illumination problem, make subsalt reservoir monitoring a difficult task.

2D NUMERICAL EXAMPLE

2D synthetic data were generated for the two sets of simple velocity models (Figure 2) using by acoustic finite difference modeling. Changes in fluid content due to production are modeled as an increasing Gaussian velocity anomaly located at ($x = 0$ m, $z = 600$ m). In each case, we modeled end-on surveys consisting of 201 shots (range: -2000 m to 2000 m, shot spacing: 20 m, receiver spacing: 20 m, maximum offset: 1200 m) in opposite directions.

The datasets were migrated using a shot-profile migration algorithm (an adjoint to the forward-modeling operation). By using exactly the same processing parameters, we preclude frequency, bandwidth and phase differences. Migrated images — using the correct model velocities — are shown in Figures 3 and 4. Since the actual velocity models are not usually known, it is common practice to migrate the datasets with the same velocity (e.g. baseline) model. Raw difference images obtained using different velocity fields are shown in Figures 5 and 6. For exactly the same acquisition geometry, the time-lapse response in the presence of the salt wedge (Figure 5b) is relatively weaker and much more complicated than when no salt is present (Figure 5a). Also, as seen in Figures 5c and d, a change in the acquisition geometry introduces more artifacts into time-lapse image when the salt wedge is present. These effects result partly from the poor illumination close to the salt flank, unequal illumination of the salt flank (due to the difference in survey direction) and contamination by differences in the relatively much stronger migration artifacts. As shown in Figure 6, using an incorrect velocity field introduces a different pattern of artifacts when the salt wedge is present. Thus, since exact velocities are not used in practice, any assumptions made with regards to the migration velocities may be difficult to account for. In the absence of the salt wedge, the results are much less complicated and simple cross-equalization of the surveys should suffice. While opposite acquisition directions may be an extreme, surveys over very complex salt bodies acquired with slightly different geometries may result in highly deteriorated time-lapse images even after careful cross-equalization.

TIME-LAPSE IMAGING AS AN INVERSE PROBLEM

(Tarantola, 1987; Claerbout, 2004) discuss the use of geophysical inversion as an imaging tool. In recent applications, inverted seismic images are computed by weighting the migra-

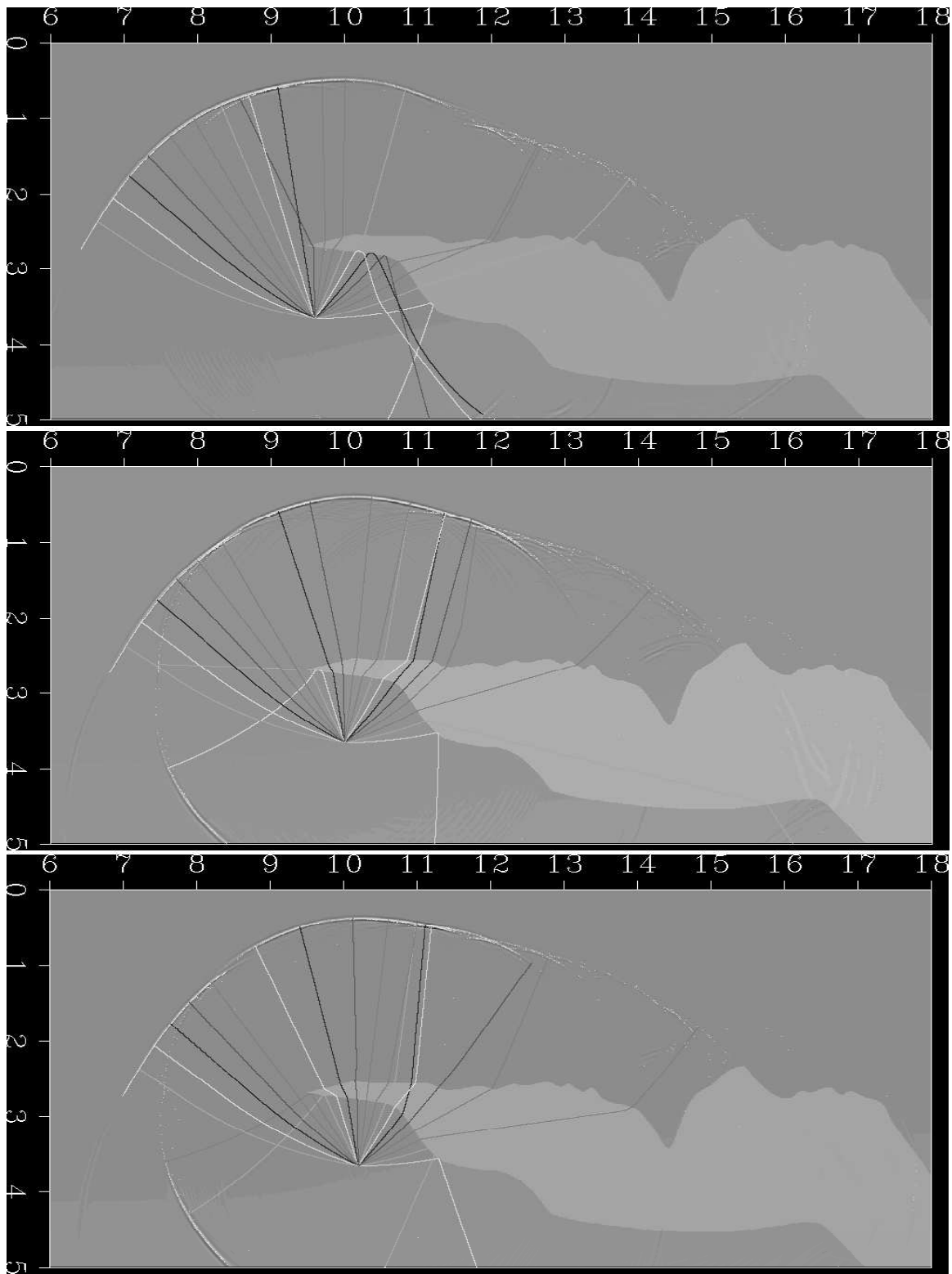


Figure 1: Subsalt Illumination effects: wave-field/ray-tracing modeling. Notice the dramatic changes in raypaths as the image point shifts from left (top) to right (bottom).
`gayeni1-Biond_Ray` [NR]

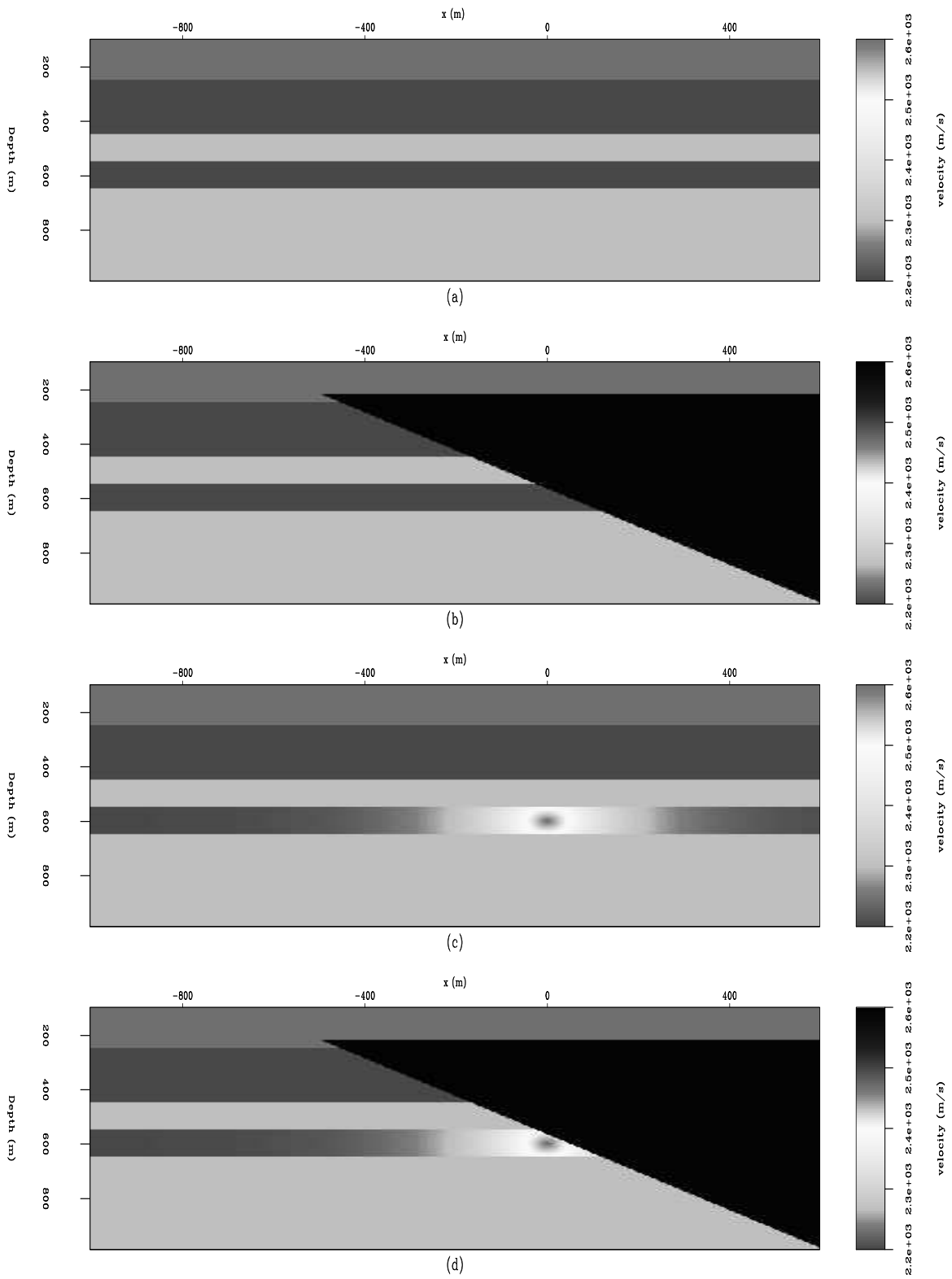


Figure 2: Velocity models for (a) and (b) Baseline, (c) and (d) Monitor surveys. Velocity from top: 2500, 2350, 2300, 2350, 2300m/s; salt velocity: 4500 m/s. Velocity change between surveys: +200m/s. [gayeni1-Gboye_2DVel](#) [ER]

tion result with the inverse of the Hessian matrix. The associated large computational cost and complexity makes the explicit computation of the Hessian matrix and its inverse impracticable. Valenciano et al. (2006) demonstrate that by taking the sparsity of the Hessian into account, the inverse of the Hessian matrix may be computed cheaply and applied in a target-oriented manner. This approach appears to yield better results than simple migration in subsalt reservoirs. For the time-lapse problem, one approach would be to compute the time-lapse image as a difference between inverse images computed as described above. Another approach would be to solve for the time-lapse image through inversion rather a difference between images.

Given a linear modeling operator \mathbf{L} , the synthetic data \mathbf{d} is computed using $\mathbf{d} = \mathbf{L}\mathbf{m}$, where \mathbf{m} is a reflectivity model. Two different surveys (say a baseline and monitor) may be represented as follows:

$$\begin{aligned}\mathbf{L}\mathbf{m}_0 &= \mathbf{d}_0, \\ \mathbf{L}\mathbf{m}_1 &= \mathbf{d}_1,\end{aligned}\tag{1}$$

where \mathbf{m}_0 and \mathbf{m}_1 are the reflectivity models at the time we acquire the datasets, (\mathbf{d}_0 and \mathbf{d}_1) respectively. Taking \mathbf{L}_0 and \mathbf{L}_1 to be the modeling operators for two different surveys, the quadratic cost functions are defined as

$$\begin{aligned}S(\mathbf{m}) &= \|\mathbf{L}_0\mathbf{m}_0 - \mathbf{d}_0\|^2, \\ S(\mathbf{m}) &= \|\mathbf{L}_1\mathbf{m}_1 - \mathbf{d}_1\|^2.\end{aligned}\tag{2}$$

The least-squares solutions to the problems are given as

$$\begin{aligned}\hat{\mathbf{m}}_0 &= (\mathbf{L}'_0\mathbf{L}_0)^{-1}\mathbf{L}'_0\mathbf{d}_0 = (\mathbf{L}'_0\mathbf{L}_0)^{-1}\tilde{\mathbf{m}}_0 = \mathbf{H}_0^{-1}\tilde{\mathbf{m}}_0, \\ \hat{\mathbf{m}}_1 &= (\mathbf{L}'_1\mathbf{L}_1)^{-1}\mathbf{L}'_1\mathbf{d}_1 = (\mathbf{L}'_1\mathbf{L}_1)^{-1}\tilde{\mathbf{m}}_1 = \mathbf{H}_1^{-1}\tilde{\mathbf{m}}_1,\end{aligned}\tag{3}$$

where $\tilde{\mathbf{m}}_0$ and $\tilde{\mathbf{m}}_1$ are the migrated images, $\hat{\mathbf{m}}_0$ and $\hat{\mathbf{m}}_1$ are the least-squares inverse images, \mathbf{L}'_0 and \mathbf{L}'_1 are the migration operators, while $\mathbf{H}_0 = \mathbf{L}'_0\mathbf{L}_0$ and $\mathbf{H}_1 = \mathbf{L}'_1\mathbf{L}_1$ are the Hessian matrices.

In the first approach, the inverse time-lapse image ($\Delta\hat{\mathbf{m}}$) is given by

$$\Delta\hat{\mathbf{m}} = \hat{\mathbf{m}}_1 - \hat{\mathbf{m}}_0.\tag{4}$$

In the second approach, we express the modeling of operation for the two surveys as follows:

$$\begin{aligned}\mathbf{L}_0\mathbf{m}_0 &= \mathbf{d}_0, \\ \mathbf{L}_1(\mathbf{m}_0 + \Delta\mathbf{m}) &= \mathbf{d}_1.\end{aligned}\tag{5}$$

where $\mathbf{m}_0 + \Delta\mathbf{m} = \mathbf{m}_1$. In matrix form, we can write

$$\begin{bmatrix} \mathbf{L}_0 & 0 \\ \mathbf{L}_1 & \mathbf{L}'_1 \end{bmatrix} \begin{bmatrix} \mathbf{m}_0 \\ \Delta\mathbf{m} \end{bmatrix} = \begin{bmatrix} \mathbf{d}_0 \\ \mathbf{d}_1 \end{bmatrix}. \quad (6)$$

The least-squares solution to equation 6 is given as

$$\begin{bmatrix} \mathbf{L}'_0\mathbf{L}_0 + \mathbf{L}'_1\mathbf{L}_1 & \mathbf{L}'_1\mathbf{L}_1 \\ \mathbf{L}'_1\mathbf{L}_1 & \mathbf{L}'_1\mathbf{L}_1 \end{bmatrix} \begin{bmatrix} \hat{\mathbf{m}}_0 \\ \Delta\hat{\mathbf{m}} \end{bmatrix} = \begin{bmatrix} \mathbf{L}'_0 & \mathbf{L}'_1 \\ 0 & \mathbf{L}'_1 \end{bmatrix} \begin{bmatrix} \mathbf{d}_0 \\ \mathbf{d}_1 \end{bmatrix} = \begin{bmatrix} \tilde{\mathbf{m}}_0 + \tilde{\mathbf{m}}_1 \\ \tilde{\mathbf{m}}_1 \end{bmatrix}, \quad (7)$$

$$\begin{bmatrix} \mathbf{H}_0 + \mathbf{H}_1 & \mathbf{H}_1 \\ \mathbf{H}_1 & \mathbf{H}_1 \end{bmatrix} \begin{bmatrix} \hat{\mathbf{m}}_0 \\ \Delta\hat{\mathbf{m}} \end{bmatrix} = \begin{bmatrix} \tilde{\mathbf{m}}_0 + \tilde{\mathbf{m}}_1 \\ \tilde{\mathbf{m}}_1 \end{bmatrix}. \quad (8)$$

This, may be re-arranged as follows:

$$\begin{bmatrix} \hat{\mathbf{m}}_0 \\ \Delta\hat{\mathbf{m}} \end{bmatrix} = \begin{bmatrix} \mathbf{H}_0 + \mathbf{H}_1 & \mathbf{H}_1 \\ \mathbf{H}_1 & \mathbf{H}_1 \end{bmatrix}^{-1} \begin{bmatrix} \tilde{\mathbf{m}}_0 + \tilde{\mathbf{m}}_1 \\ \tilde{\mathbf{m}}_1 \end{bmatrix}. \quad (9)$$

DISCUSSION

Although it is not feasible to explicitly compute the inverse matrix in equation 9, an iterative least squares solution of equation 8 is expected to yield reasonably good results for $\hat{\mathbf{m}}_0$ and $\Delta\hat{\mathbf{m}}$. In the 2D case considered, for a given frequency ω and an image-point $i(x, z)$, the measured data $\mathbf{d}(i_s, i_r)$ in equation is given by

$$\mathbf{d}(i_s, i_r; \omega) = \mathbf{L}\mathbf{m}_{i_{xz}} = \sum_{i_{xz}} \mathbf{G}(i_{xz}, i_s; \omega) \mathbf{G}(i_{xz}, i_r; \omega) \mathbf{m}_{i_{xz}}, \quad (10)$$

where $\mathbf{G}(i_{xz}, i_s; \omega)$ and $\mathbf{G}(i_{xz}, i_r; \omega)$ are the Green's functions from the shot and receiver positions ($i_s(x_s, 0)$ and $i_r(x_r, 0)$) respectively.

The Hessian sub-matrices (\mathbf{H}_0 and \mathbf{H}_1), which are the second derivatives of the cost functions (equations 1 and 2) with respect to the model parameters $\mathbf{m}_{i_{xz}}$ and $\mathbf{m}_{j_{xz}}$ (where j_{xz} is some other point in the model space), may be computed as follows:

$$\mathbf{H}(i_{xz}, j_{xz}) = \sum_{\omega} \sum_{i_s} \mathbf{G}'(i_{xz}, i_s; \omega) \mathbf{G}(j_{xz}, i_s; \omega) \sum_{i_r} \mathbf{G}'(i_{xz}, i_r; \omega) \mathbf{G}(j_{xz}, i_r; \omega). \quad (11)$$

Using a target-oriented approach and limiting the computation to near-diagonal elements (Valenciano et al., 2006), equation 11 is reduced to

$$\mathbf{H}(i_T, i_T + a_i) = \sum_{\omega} \sum_{i_s} \mathbf{G}'(i_T, i_s; \omega) \mathbf{G}(i_T + a_i, i_s; \omega) \sum_{i_r} \mathbf{G}'(i_T, i_r; \omega) \mathbf{G}(i_T + a_i, i_r; \omega), \quad (12)$$

where a_i is the offset from the target image-point i_T .

Computation of the target-oriented wave-equation Hessian is discussed in detail by Valenciano and Biondi (2004). Hence, it is possible to compute the matrix of Hessian terms in equation 8 for specific targets of interest (e.g. regions around a sub-salt reservoir) and therefore compute the least-squares time-lapse image, $\Delta\hat{\mathbf{m}}$. Since the geometry (and other unwanted) information are contained in the Hessian terms, it should be possible to such effects from the time-lapse image by solving the inverse problem in equation 9 (or practically by solving equation 8 in a least-squares sense). The inversion technique is itself limited by the amount of good quality data from the sub-salt reflectors, but we expect that it provides better results than presently obtainable with migration. We intend to compare results from the inversion schemes with those from standard cross-equalization and to determine whether our techniques could make seismic monitoring of sub-salt reservoirs a reality.

CONCLUSIONS

Sub-salt reservoir monitoring of hydrocarbon reservoirs is a major challenge. We propose the computation of the time-lapse image either as a difference between inverse images or as a solution to a least-squares inverse problem. By solving for the time-lapse response through inversion (rather than a difference between two adjoint operations) it may be possible to obtain more reliable amplitude information and to correct for geometry and other effects which have heretofore limited seismic monitoring of sub-salt reservoirs. Suitable regularization and/or preconditioning may be used to better constrain the inversion result and to potentially reduce the required number of iterations in the inversion scheme. It may also be possible to structure the regularization operator to account for geomechanical and other changes outside the reservoir.

ACKNOWLEDGMENTS

Thanks to Alejandro Valenciano whose previous work and advice are helping get this research started and to Bob Clapp for many useful suggestions.

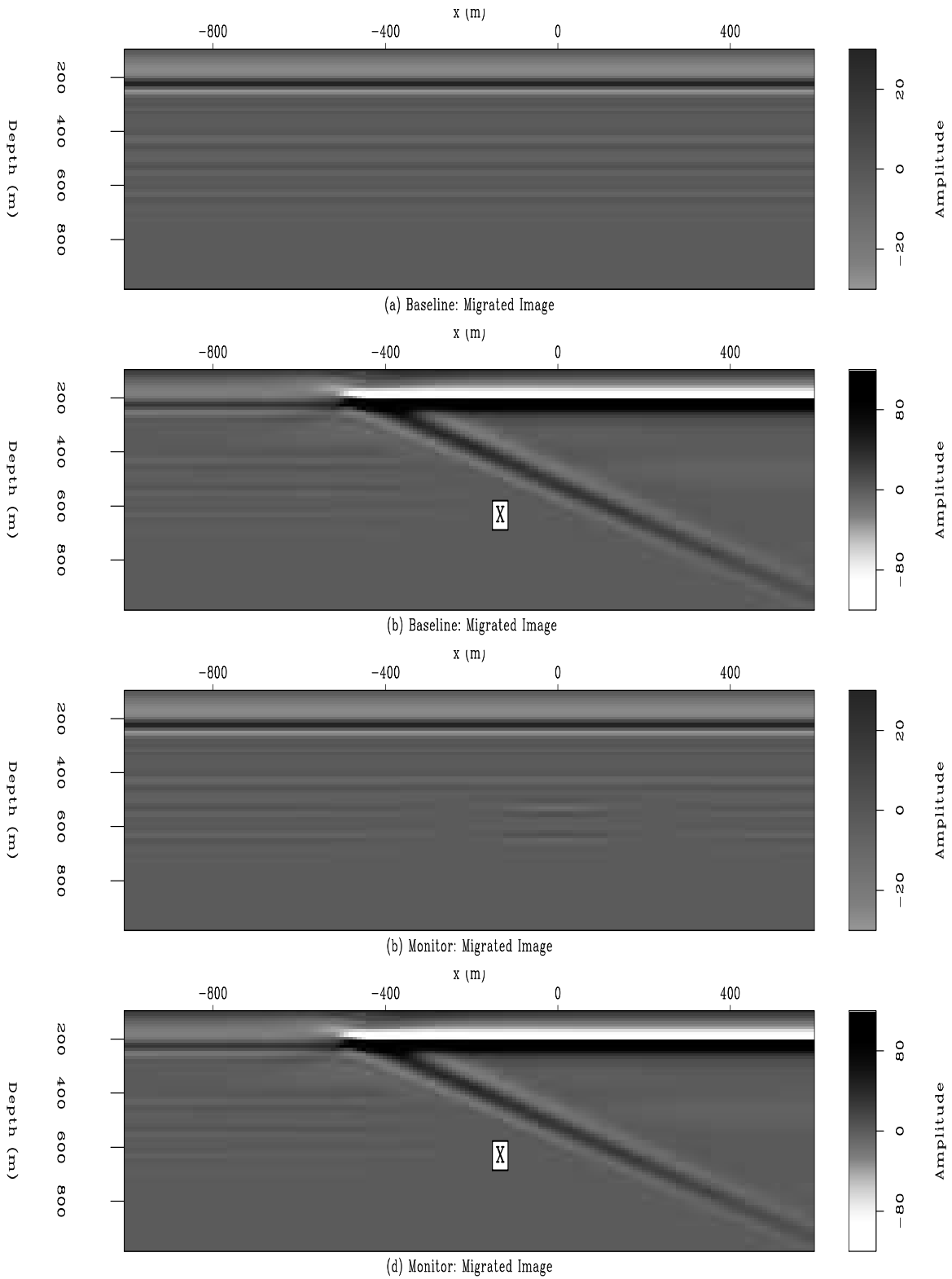


Figure 3: Migrated Images for velocity models in Figure 2. Survey direction: right to left. Data migrated using the correct (smoothed) velocity models. (a) and (b) Baseline; (c) and (d) Monitor. Notice the poor illumination of the reflectors close to the salt flank (region marked 'X' in (b) and (d)). gayeni1-GboyeImg [ER]

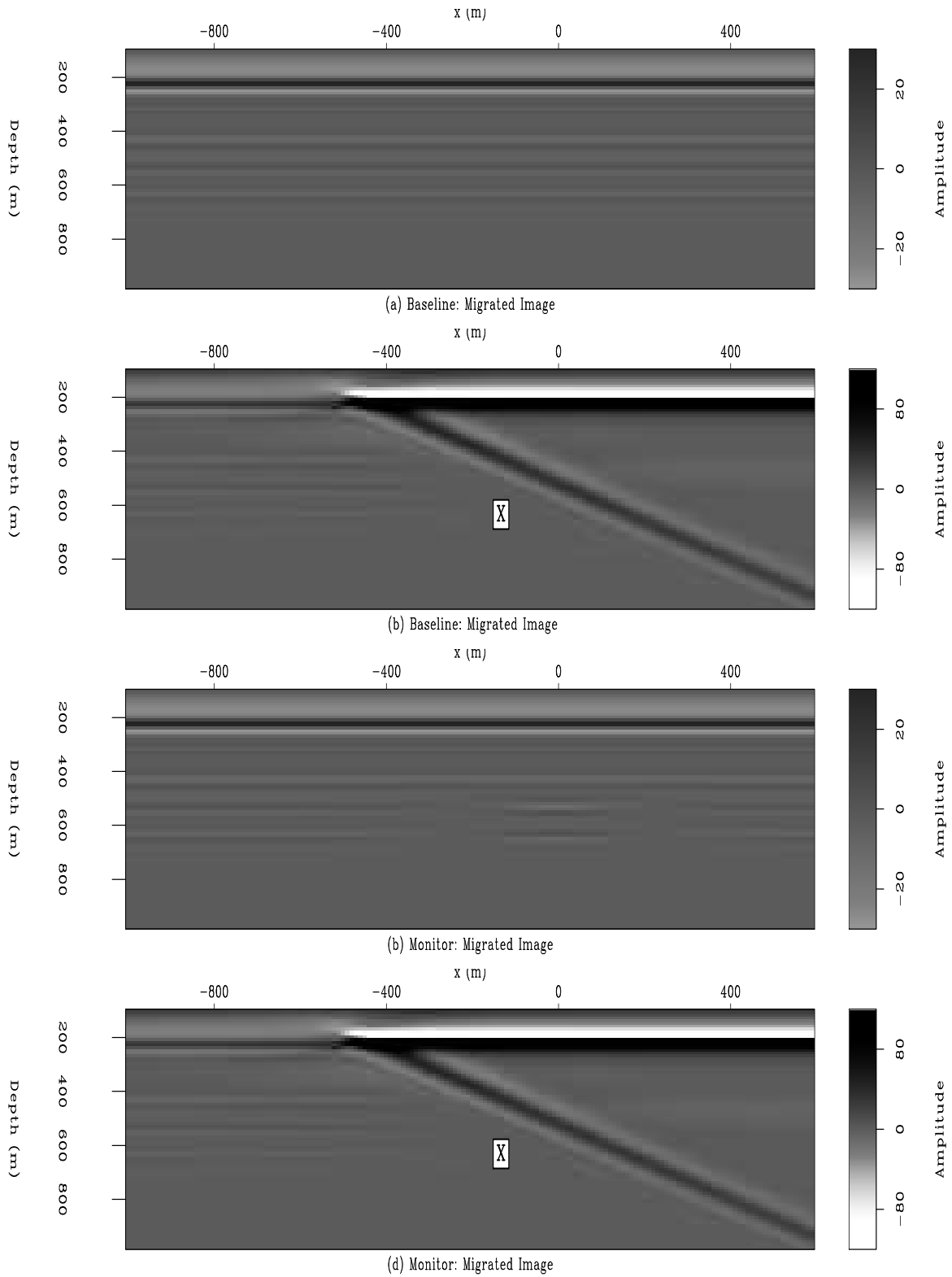


Figure 4: Migrated Images for velocity models in Figure 2. Survey direction: left to right. Data migrated using the correct (smoothed) velocity models. (a) and (b) Baseline; (c) and (d) Monitor. Note the poor illumination of the reflectors close to the salt flank (region marked 'X' in (b) and (d)). [gayeni1-GboyeImg2](#) [ER]

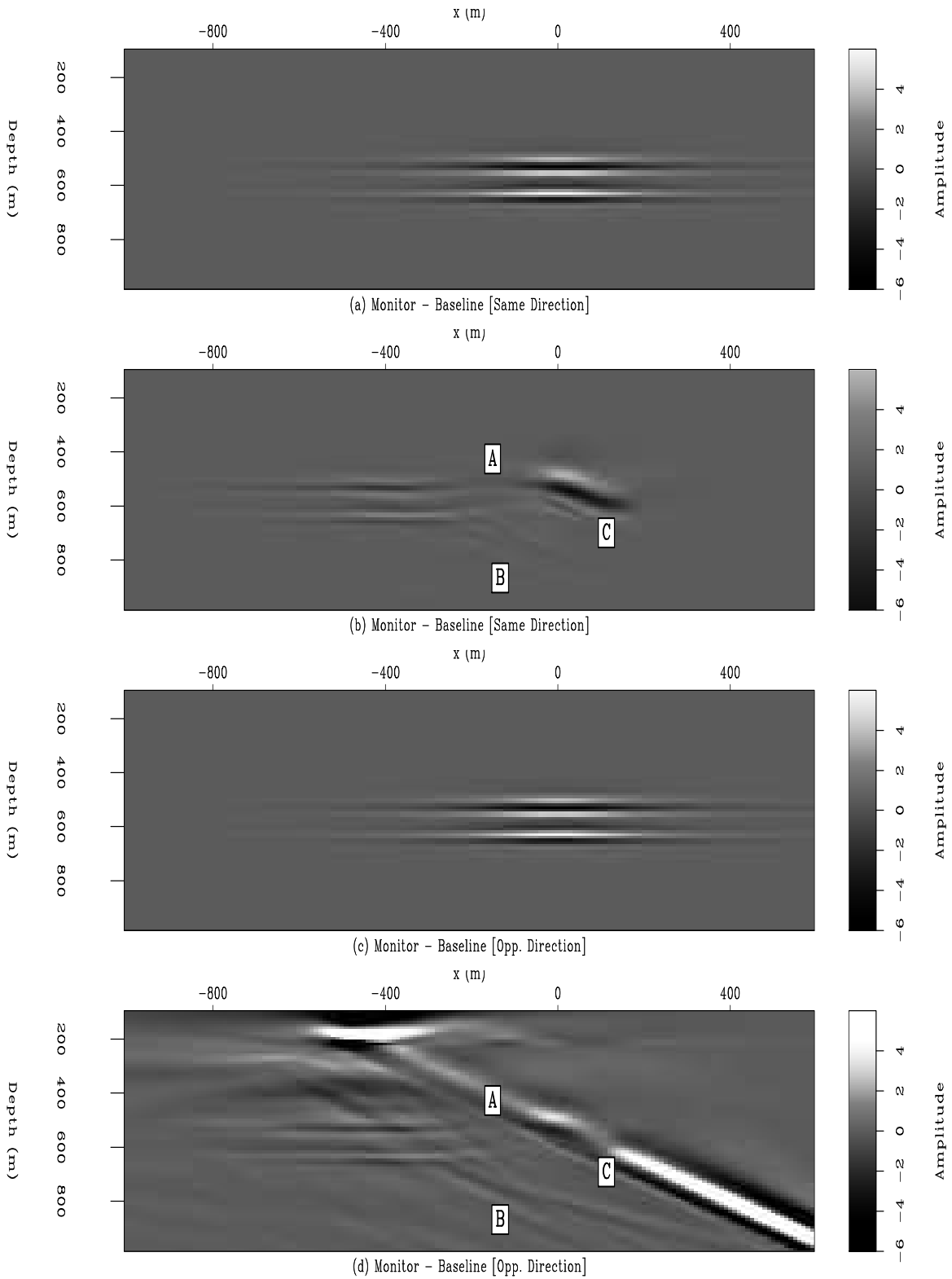


Figure 5: Raw difference Images (with and without the salt wedge) for same (a and b) and opposite (c and d) acquisition directions. Data migrated with the correct velocity models. Note the weak time-lapse response close to the reservoir (a result of the poor illumination) in the region marked 'A'. [gayeni1-GboyeFB](#) [ER]

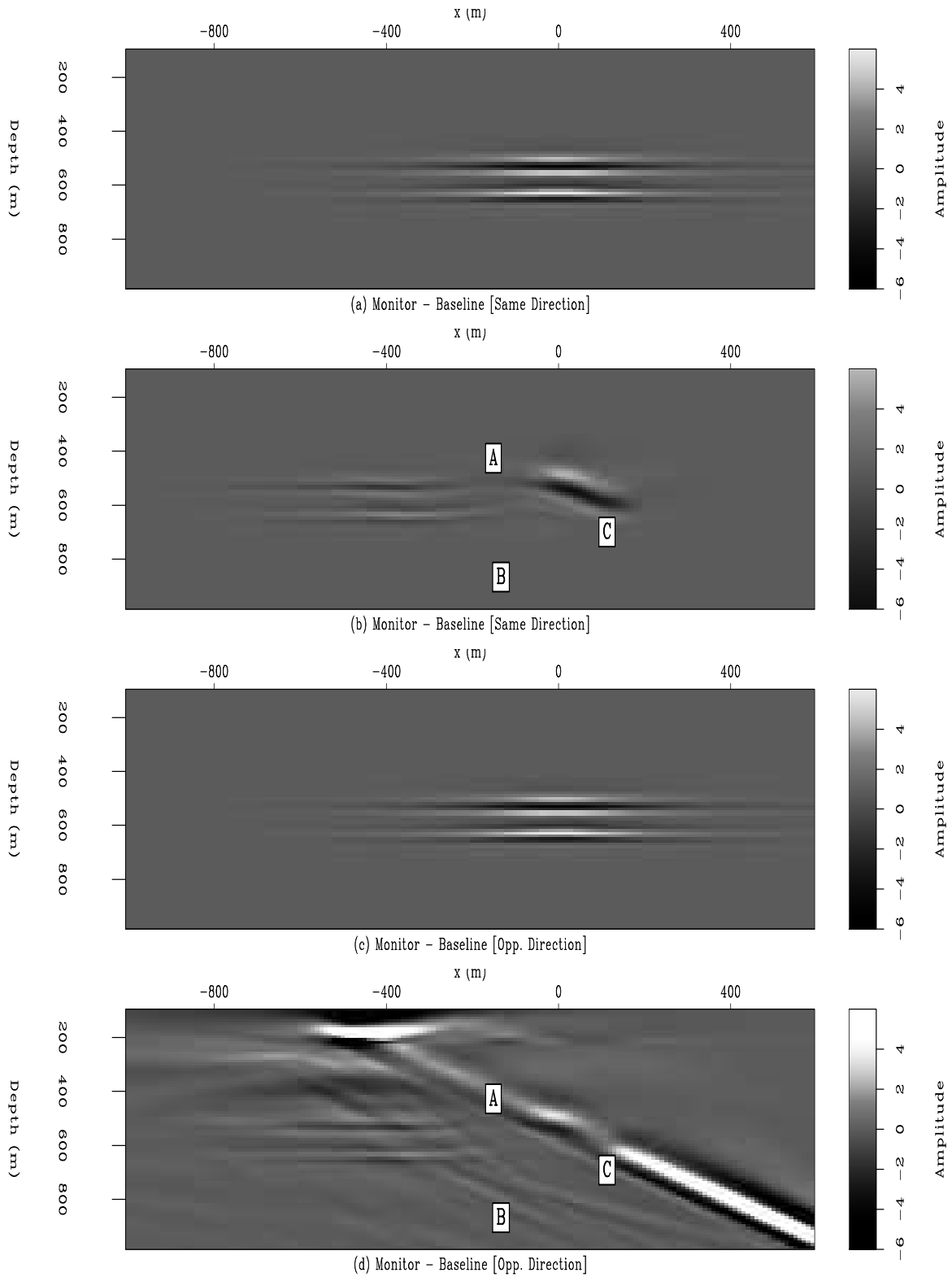


Figure 6: Raw difference Images (with and without the salt wedge) for same (a and b) and opposite (c and d) acquisition directions. Data migrated with the smoothed baseline velocity models. Note the differences in migration artifacts between Figures 5b and 6b in the regions marked 'B' and 'C'. [gayeni1-GboyeSFB](#) [ER]

REFERENCES

- Batzle, M. and Z. Wang, 1992, Seismic properties of pore fluids: *Geophysics*, **57**, no. 11, 1396–1408.
- Biondi, B., G. Mavko, et al., 1998, Reservoir monitoring: A multidisciplinary feasibility study: *The Leading Edge*, **17**, no. 10, 1404–1414.
- Biondi, B., M. Prucha, and P. C. Sava, 1999, 3D wave-equation prestack imaging under salt.: 6th International Congress, Brazilian Geophysical Society.
- Calvert, R., 2005, Insights and methods for 4D reservoir monitoring and characterization: SEG/EAGE DISC (Distinguished Instructor Lecture Course).
- Claerbout, J. F., 2004, Image estimation by example: Geophysical soundings image construction: multidimensional autoregression:, http://sepwww.stanford.edu/sep/prof/gee/toc_html/.
- Clapp, M. L., 2005, Imaging under salt: illumination compensation by regularized inversion: Ph.D. thesis, Stanford University, http://sepwww.stanford.edu/public/docs/sep122/paper_html/index.html.
- Eastwood, J., P. Lebel, A. Dilay, and S. Blakeslee, 1994, Seismic monitoring of steam-based recovery of bitumen: *The Leading Edge*, **13**, no. 04, 242–251.
- Eiken, O., G. U. Haugen, M. Schonewille, and A. Duijndam, 2003, A proven method for acquiring highly repeatable towed streamer seismic data: *Geophysics*, **68**, no. 4, 1303–1309.
- Johnston, D., 2005, Time-lapse 4D technology: Reservoir surveillance: AAPG Search and Discovery.
- Laws, R. and E. Kragh, 2000, Rough seas and time-lapse seismic: Rough seas and time-lapse seismic:, *Eur. Assn. Geosci. Eng.*, 62nd Mtg., Session:L0015.
- Lefevre, F., Y. Kerdraon, et al., 2003, Improved reservoir understanding through rapid and effective 4D: Girassol field, Angola, West Africa: SEG Technical Program Expanded Abstracts, **22**, no. 1, 1334–1337.
- Lumley, D. E., 1995, Imaging under salt: illumination compensation by regularized inversion: Ph.D. thesis, Stanford University, <http://sepwww.stanford.edu/public/docs/sep91/>.
- Malaguti, R., M. Allen, A. Litvin, and C. Gregory, 2001, Sub-salt imaging using 3D pre-stack depth migration in the UK Southern North Sea - a case history: *First Break*, **19**, no. 05, 253–258.
- Muerdter, D. and D. Ratcliff, 2001, Understanding subsalt illumination through ray-trace modeling, Part 3: Salt ridges and furrows, and the impact of acquisition orientation: *The Leading Edge*, **20**, no. 8, 803–816.

- Ratcliff, D. W., C. A. Jacewitz, and S. H. Gray, 1994, Subsalt imaging via target-oriented 3-D prestack depth migration: *The Leading Edge*, **13**, no. 03, 163–170.
- Rickett, J. and D. E. Lumley, 2001, Cross-equalization data processing for time-lapse seismic reservoir monitoring: A case study from the Gulf of Mexico: *Geophysics*, **66**, no. 4, 1015–1025.
- Rickett, J., 2003, Illumination-based normalization for wave-equation depth migration: *Geophysics*, **68**, 1371–1379.
- Ross, C. P. and M. S. Altan, 1997, Time-lapse seismic monitoring: Some shortcomings in nonuniform processing: *The Leading Edge*, **16**, no. 06, 931–937.
- Sava, P., 2006, Subsalt exploration and development: Imaging, interpretation, and drilling—What have we learned? 2006 SEG/EAGE summer research workshop: *The Leading Edge*, **25**, no. 11, 1370–1376.
- Tarantola, A., 1987, *Inverse problem theory: Methods for data fitting and model parameter estimation*: Elsevier Science Publication Company, Inc.
- Valenciano, A. A. and B. Biondi, 2004, Target-oriented computation of the wave-equation imaging Hessian: *SEP-117*, 63–76.
- Valenciano, A. A., B. Biondi, and A. Guitton, 2006, Target-oriented wave-equation inversion: *Geophysics*, **71**, A35–A38.
- Whitcombe, D. N., J. M. Marsh, et al., 2004, The systematic application of 4D in BP's North-West Europe operations — 5 years on: *SEG Technical Program Expanded Abstracts*, **23**, no. 1, 2251–2254.
- Zou, Y., L. R. Bentley, L. R. Lines, and D. Coombe, 2006, Integration of seismic methods with reservoir simulation, Pikes Peak heavy-oil field, Saskatchewan: *The Leading Edge*, **25**, no. 6, 764–781.

Short Note

Transmission wavefield velocity analysis

Jeff Shragge

INTRODUCTION

Transmission wavefields contain important information on subsurface velocity profiles. This is evident from the many tomography-based techniques that invert for perturbations on an assumed background velocity using the transmission wavefield response. One of the more successful approaches is waveform tomography (Pratt and Worthington, 1989; Woodward, 1992), an approach to non-linear velocity inversion problem that iteratively obtains an estimate of velocity perturbations by minimizing the difference between forward-modeled waveforms and acquired data through residual back-projection. A commonly used and accurate way to forward model synthetic data is using two-way finite-differences. Inversion of the correspondingly large matrices required for 2-D waveform inversion is typically done using a memory-intensive LU decomposition approach (Štekl and Pratt, 1998). Current computer memory limitations preclude the use of this approach on typical 3-D seismic volumes (Operto et al., 2006).

Wave-equation migration velocity analysis (WEMVA) is another velocity inversion technique (Sava and Biondi, 2004). This procedure back-projects wavefield perturbations derived from variations in migrated image volume (i.e. angle-gathers) to image velocity perturbations. Unlike typical waveform inversion approaches, this procedure is often implemented with one-way phase-only wavefield extrapolation for forward modeling, and is applied to the back-scattered reflection response. However, nothing precludes using a WEMVA-like formalism in inverting transmission wavefields for velocity perturbations. One potential benefit is that because the phase-only extrapolation operator is stated explicitly, one can represent scattering as a matrix operation that provides a direct link between a velocity perturbation and the gradient field.

In this paper, I derive a WEMVA-like framework for modeling transmission wavefields. I then use the waveform inversion objective function (Pratt and Worthington, 1989) to develop the equations appropriate for transmission wavefield waveform inversion using one-way extrapolation operators. Finally, I demonstrate that forward modeling in generalized coordinate systems (Sava and Fomel, 2005) does not pose any theoretical difficulties for the inversion process.

WEMVA FORWARD MODELING

Following Sava and Biondi (2004), I develop equations for imaging by wavefield extrapolation based on recursive continuation of the wavefields \mathcal{U} from a given depth level to the next by means of an extrapolator operator \mathbf{E}

$$\mathcal{U}_{z+\Delta z} = \mathbf{E}_z[\mathcal{U}_z], \quad (1)$$

where $\mathbf{E}_z[\cdot] = e^{ik_z \Delta z}$, k_z is extrapolation wavenumber, and Δz is the depth step. Throughout this paper, I use a notation where $\mathbf{A}[x]$ denotes that operator \mathbf{A} is applied to a field x . Subscripts z and $z + \Delta z$ correspond to quantities associated with depth levels z and $z + \Delta z$, respectively.

Using this operator notation, a data wavefield \mathcal{D} can be recursively extrapolated through a medium described by model parameters (i.e. slowness). This operation can be written explicitly in matrix form,

$$\begin{bmatrix} \mathbf{1} & 0 & 0 & \dots & 0 & 0 \\ -\mathbf{E}_0 & \mathbf{1} & 0 & \dots & 0 & 0 \\ 0 & -\mathbf{E}_1 & \mathbf{1} & \dots & 0 & 0 \\ \vdots & \vdots & \vdots & \vdots & \vdots & \vdots \\ 0 & 0 & 0 & \dots & -\mathbf{E}_{n-1} & \mathbf{1} \end{bmatrix} \begin{bmatrix} \mathcal{U}_0 \\ \mathcal{U}_1 \\ \mathcal{U}_2 \\ \vdots \\ \mathcal{U}_n \end{bmatrix} = \begin{bmatrix} \mathcal{D}_0 \\ 0 \\ 0 \\ \vdots \\ 0 \end{bmatrix}, \quad (2)$$

where $\mathbf{1}$ is an identity operator, and fields without subscripts (e.g. \mathcal{U} and \mathcal{D}) refer to complete wavefields. Equation 2 is written more compactly as

$$(\mathbf{1} - \mathbf{E}) \mathcal{U} = \mathcal{D}, \quad (3)$$

where $(\mathbf{1} - \mathbf{E})$ is a Green's function $\mathbf{G}_0(\mathbf{x}', \mathbf{x})$ between levels \mathbf{x} and \mathbf{x}' generated by wavefield extrapolation. The Green's function satisfies the following adjoint definitions,

$$(\mathbf{1} - \mathbf{E}) = \mathbf{G}_0(\mathbf{x}', \mathbf{x}) = \mathbf{G}_0^\dagger(\mathbf{x}, \mathbf{x}'), \quad (4)$$

$$(\mathbf{1} - \mathbf{E})^{-1} = \mathbf{G}_0^\dagger(\mathbf{x}', \mathbf{x}) = \mathbf{G}_0(\mathbf{x}, \mathbf{x}'), \quad (5)$$

where superscripts $^{-1}$ and † indicate the inverse and adjoint operation (i.e. complex transpose), respectively.

Source wavefields well-modeled by a delta function exhibit the following relationships,

$$\mathcal{U}(\mathbf{x}, \mathbf{s}) = (\mathbf{1} - \mathbf{E})^{-1} \mathcal{D} = \mathbf{G}_0(\mathbf{x}, \mathbf{x}') \delta(\mathbf{x}' - \mathbf{s}) = \mathbf{G}_0(\mathbf{x}, \mathbf{s}), \quad (6)$$

where $\mathbf{G}_0(\mathbf{x}, \mathbf{s})$ describes the propagation from source point \mathbf{s} throughout the domain denoted by \mathbf{x} . Note that the choice of \mathbf{s} is arbitrary and an equivalent development applies for a receiver Green's function $\mathbf{G}_0(\mathbf{x}, \mathbf{r})$,

$$\mathbf{G}_0(\mathbf{x}, \mathbf{r}) = \mathbf{G}_0(\mathbf{x}, \mathbf{x}') \delta(\mathbf{x}' - \mathbf{r}) = (\mathbf{1} - \mathbf{E})^{-1} \delta(\mathbf{x}' - \mathbf{r}), \quad (7)$$

where \mathbf{r} is receiver location.

Introducing velocity perturbations

If a velocity perturbation is applied at some depth level, a perturbed wavefield $\Delta\mathcal{U}$ can be derived from the background wavefield by application of the chain rule to equation 1,

$$\Delta\mathcal{U}_{z+\Delta z} = \mathbf{E}_z[\Delta\mathcal{U}_z] + \Delta\mathcal{V}_{z+\Delta z}, \quad (8)$$

where $\Delta\mathcal{V}_{z+\Delta z}$ represents the scattered wavefield generated at $z + \Delta z$ by the interaction of the velocity model at depth z . Field $\Delta\mathcal{U}_{z+\Delta z}$ is the accumulated wavefield perturbation corresponding to the slowness perturbations at all levels above. It is computed by extrapolating the wavefield perturbations from the level above $\Delta\mathcal{U}_z$, plus the scattered wavefield at this level, $\Delta\mathcal{V}_{z+\Delta z}$.

Equation 8 is also a recursive equation that can be written in matrix form

$$\begin{bmatrix} \mathbf{1} & 0 & 0 & \dots & 0 & 0 \\ -\mathbf{E}_0 & \mathbf{1} & 0 & \dots & 0 & 0 \\ 0 & -\mathbf{E}_1 & \mathbf{1} & \dots & 0 & 0 \\ \vdots & \vdots & \vdots & \vdots & \vdots & \vdots \\ 0 & 0 & 0 & \dots & -\mathbf{E}_{n-1} & \mathbf{1} \end{bmatrix} \begin{bmatrix} \Delta\mathcal{U}_0 \\ \Delta\mathcal{U}_1 \\ \Delta\mathcal{U}_2 \\ \vdots \\ \Delta\mathcal{U}_n \end{bmatrix} = \quad (9)$$

$$\begin{bmatrix} 0 & 0 & 0 & \dots & 0 & 0 \\ \Delta\mathbf{E}_0 & 0 & 0 & \dots & 0 & 0 \\ 0 & \Delta\mathbf{E}_1 & 0 & \dots & 0 & 0 \\ \vdots & \vdots & \vdots & \vdots & \vdots & \vdots \\ 0 & 0 & 0 & \dots & \Delta\mathbf{E}_{n-1} & 0 \end{bmatrix} \begin{bmatrix} \mathcal{U}_0 \\ \mathcal{U}_1 \\ \mathcal{U}_2 \\ \vdots \\ \mathcal{U}_n \end{bmatrix}, \quad (10)$$

or in more compact notation as,

$$(\mathbf{1} - \mathbf{E})\Delta\mathcal{U} = \Delta\mathbf{E}\mathcal{U}. \quad (11)$$

Operator $\Delta\mathbf{E}$ denotes a perturbation of the extrapolation operator \mathbf{E} , while quantity $\Delta\mathbf{E}\mathcal{U}$ represents a scattered wavefield and is a function of the medium perturbation given by the scattering relationship derived in Appendix A. For single scattering we write,

$$\Delta\mathcal{V}_{z+\Delta z} \equiv \Delta\mathbf{E}_z[\mathcal{U}_z] = \mathbf{E}_z[\mathbf{S}_z(\tilde{\mathcal{U}}_z)[\Delta s]], \quad (12)$$

where \mathbf{S}_z is the scattering operator, and Δs is slowness perturbation. This expression yields a recursive relationship that can be written in matrix form:

$$\begin{bmatrix} \mathbf{1} & 0 & 0 & \dots & 0 & 0 \\ -\mathbf{E}_0 & \mathbf{1} & 0 & \dots & 0 & 0 \\ 0 & -\mathbf{E}_1 & \mathbf{1} & \dots & 0 & 0 \\ \vdots & \vdots & \vdots & \vdots & \vdots & \vdots \\ 0 & 0 & 0 & \dots & -\mathbf{E}_{n-1} & \mathbf{1} \end{bmatrix} \begin{bmatrix} \Delta\mathcal{U}_0 \\ \Delta\mathcal{U}_1 \\ \Delta\mathcal{U}_2 \\ \vdots \\ \Delta\mathcal{U}_n \end{bmatrix} =$$

$$\begin{bmatrix} 0 & 0 & 0 & \dots & 0 & 0 \\ \mathbf{E}_0 & 0 & 0 & \dots & 0 & 0 \\ 0 & \mathbf{E}_1 & 0 & \dots & 0 & 0 \\ \vdots & \vdots & \vdots & \vdots & \vdots & \vdots \\ 0 & 0 & 0 & \dots & \mathbf{E}_{n-1} & 0 \end{bmatrix} \begin{bmatrix} 0 & 0 & 0 & \dots & 0 & 0 \\ \mathbf{S}_0 & 0 & 0 & \dots & 0 & 0 \\ 0 & \mathbf{S}_1 & 0 & \dots & 0 & 0 \\ \vdots & \vdots & \vdots & \vdots & \vdots & \vdots \\ 0 & 0 & 0 & \dots & \mathbf{S}_{n-1} & 0 \end{bmatrix} \begin{bmatrix} \Delta s_0 \\ \Delta s_1 \\ \Delta s_2 \\ \vdots \\ \Delta s_n \end{bmatrix}, \quad (13)$$

or in more compact notation

$$(\mathbf{1} - \mathbf{E}) \Delta \mathcal{U} = \mathbf{E} \mathbf{S} \Delta s, \quad (14)$$

where vector Δs denotes slowness perturbations at all depths.

Finally, introducing

$$\mathbf{L} = (\mathbf{1} - \mathbf{E})^{-1} \mathbf{E} \mathbf{S}, \quad (15)$$

we can write a simple relationship between slowness Δs and wavefield $\Delta \mathcal{U}$ perturbations:

$$\Delta \mathcal{U} = \mathbf{L} \Delta s. \quad (16)$$

This expression represents the wavefield scattering caused by the interaction of the background wavefield with the a medium perturbation. The total modeled field Ψ_m is defined as,

$$\Psi_m(\mathbf{r}, \mathbf{s}) = \tilde{\mathcal{U}}(\mathbf{r}, \mathbf{s}) + \Delta \mathcal{U}(\mathbf{r}, \mathbf{s}), \quad (17)$$

where $\tilde{\mathcal{U}}$ is the background wavefield modeled by equation 3.

WAVEFORM INVERSION PROBLEM

The goal of waveform inversion is to invert for the optimal set of velocity perturbations that minimize the difference between forward-modeled waveforms and acquired data. The first step in setting up the inverse problem is defining data residuals, $\Delta \Psi$,

$$\Delta \Psi(\mathbf{r}, \mathbf{s}; \omega) = \Psi_m(\mathbf{r}, \mathbf{s}; \omega) - \Psi_d(\mathbf{r}, \mathbf{s}; \omega), \quad (18)$$

where $\Psi_d(\mathbf{r}, \mathbf{s})$ is the recorded data. The L_2 residual norm is used to set up an objective function,

$$E = \frac{1}{2} \sum_{\mathbf{s}} \sum_{\mathbf{r}} \Delta \Psi^\dagger(\mathbf{r}, \mathbf{s}) \Delta \Psi(\mathbf{r}, \mathbf{s}), \quad (19)$$

that is minimized with respect to slowness perturbations Δs^\dagger

$$\frac{\partial E}{\partial \Delta s^\dagger} = \frac{1}{2} \sum_{\mathbf{s}} \sum_{\mathbf{r}} \frac{\partial}{\partial \Delta s^\dagger} (\Delta \Psi^\dagger + \Delta s^\dagger \mathbf{L}^\dagger) (\Delta \Psi + \mathbf{L} \Delta s) = 0. \quad (20)$$

This results in the following least-squares estimate of the slowness perturbations

$$\Delta s(\mathbf{x}) = - \left(\sum_{\mathbf{s}} \sum_{\mathbf{r}} \mathbf{L}^\dagger \mathbf{L} \right)^{-1} \sum_{\mathbf{s}} \sum_{\mathbf{r}} \mathbf{L}^\dagger \Delta \Psi. \quad (21)$$

From here on, the sum over all sources and receivers is implicitly assumed. Also, we discuss only the gradient vector and the filtering of the gradient by the inverse Hessian matrix $(\mathbf{L}^\dagger \mathbf{L})^{-1}$ is implicitly assumed.

The adjoint gradient operator \mathbf{L}^\dagger is a composite matrix consisting of a number of chained operators (from equation 15):

$$\mathbf{L}^\dagger = \mathbf{S}^\dagger \mathbf{E}^\dagger ((1 - \mathbf{E})^{-1})^\dagger, \quad (22)$$

where scattering operator or at each extrapolation interval, S_z is defined by (see Appendix A),

$$S_z = \omega^2 \tilde{\mathcal{U}}_z \frac{is_0}{\sqrt{\omega^2 s_0^2 - |\mathbf{k}|^2}} = \omega^2 \tilde{\mathcal{U}}_z F_z, \quad (23)$$

where F_z is considered a filter. This allows us to write composite operator \mathbf{L}^\dagger with scattering \mathbf{S}^\dagger and filter \mathbf{F}^\dagger matrices as,

$$\mathbf{L}^\dagger = \omega^2 \tilde{\mathcal{U}}^\dagger \mathbf{F}^\dagger \mathbf{E}^\dagger ((1 - \mathbf{E})^{-1})^\dagger \quad (24)$$

Inserting this expression into equation 21 yields,

$$\Delta s \approx -\omega^2 \tilde{\mathcal{U}}^\dagger \mathbf{F}^\dagger \mathbf{E}^\dagger ((1 - \mathbf{E})^{-1})^\dagger \Delta \Psi. \quad (25)$$

Thus, using the relationship in equations 6 and 7, leads to the following result,

$$\Delta s \approx -\omega^2 \mathbf{G}_0^\dagger(\mathbf{x}, \mathbf{s}) \mathbf{F}^\dagger(\mathbf{x}) \mathbf{E}^\dagger(\mathbf{x}) \mathbf{G}_0^\dagger(\mathbf{x}, \mathbf{r}) \Delta \Psi(\mathbf{r}, \mathbf{s}). \quad (26)$$

Relationship to Pratt's approach to waveform inversion

Equation 26 is a direct statement of the waveform inversion procedure of Pratt and Worthington (1989) and Sirgue and Pratt (2004). However, the use of one-way operators leads to the definition of an explicit scattering operator and a slightly different gradient operator:

$$g(\mathbf{x}) \approx -\omega^2 \sum_{\mathbf{s}} \sum_{\mathbf{r}} \Re [\mathbf{G}_0^*(\mathbf{x}, \mathbf{s}) \mathbf{G}_0^*(\mathbf{x}, \mathbf{r}) \Delta \Psi(\mathbf{r}, \mathbf{s})], \quad (\text{Pratt}) \quad (27)$$

$$\Delta s(\mathbf{x}) \approx -\omega^2 \sum_{\mathbf{s}} \sum_{\mathbf{r}} \Re [\mathbf{G}_0^\dagger(\mathbf{x}, \mathbf{s}) \mathbf{F}^\dagger(\mathbf{x}) \mathbf{E}^\dagger(\mathbf{x}) \mathbf{G}_0^\dagger(\mathbf{x}, \mathbf{r}) \Delta \Psi(\mathbf{r}, \mathbf{s})]. \quad (\text{WEMVA}) \quad (28)$$

Note that the two approaches are similar: the wavefield residuals are back-projected from the source point through the model and correlated with the source Green's function. This approach, though, has the scattering matrix chained between the source and receiver Green's functions. This derives from the application of a differential operator directly on the phase of the extrapolation operator.

CONCLUSION

This paper introduces an approach to waveform inversion that builds from the WEMVA theory developed by Sava and Biondi (2004). The main differences between this approach and that of Pratt and Worthington (1989) is that this formalism provides a scattering operator that permits a direct estimate of the slowness perturbation. Future work will implement this scheme into a transmission wavefield WEMVA scheme.

REFERENCES

- Operto, S., J. Virieux, et al., 2006, 3D frequency-domain finite-difference modeling of acoustic waves using a massively parallel direct solver: A feasibility study: 75th SEG Ann. Gen. Meeting Conference and Exhibition, Expanded Abstracts.
- Pratt, R. and M. Worthington, 1989, The application of diffraction tomography to cross-hole seismic data: *Geophysics*, **53**, 1284–1294.
- Sava, P. and B. Biondi, 2004, Wave-equation migration velocity analysis. I. Theory: *Geophysical Prospecting*, **52**, 593–606.
- Sava, P. and S. Fomel, 2005, Riemannian wavefield extrapolation: *Geophysics*, **70**, T45–T56.
- Shragge, J., 2006, Non-orthogonal Riemannian wavefield extrapolation: 75th SEG Ann. Gen. Meeting and Exhibition, Expanded Abstracts, 2236–2240.
- Sirgue, L. and R. Pratt, 2004, Efficient waveform inversion and imaging: A strategy for selecting temporal frequencies: *Geophysics*, **69**, 231–248.
- Štekl, I. and R. Pratt, 1998, Accurate visco-elastic modeling frequency-domain finite differences using rotated operators: *Geophysics*, **63**, 1779–1794.
- Woodward, M., 1992, Wave-equation tomography: *Geophysics*, **57**, 15–26.

APPENDIX A

This appendix develops a WEMVA scattering operator (Sava and Biondi, 2004) for use in transmission wavefield waveform inversion. The extrapolation operator, \mathbf{E} , is given by,

$$\mathbf{E}_z[\cdot] = e^{ik_z \Delta z}, \quad (\text{A-1})$$

where k_z is the depth wavenumber and Δz is the extrapolation depth step. The extrapolation wavenumber in depth is given by

$$k_z = \sqrt{\omega^2 s^2 - |\mathbf{k}|^2}, \quad (\text{A-2})$$

where ω is temporal frequency and $|\mathbf{k}|$ is the horizontal wavenumber magnitude.

The vertical wavenumber can be separated into two components, one corresponding to the background medium, \tilde{k}_z , and one corresponding to a perturbation, Δk_z , such that,

$$k_z = \tilde{k}_z + \Delta k_z. \quad (\text{A-3})$$

In a first-order approximation, we can relate these two extrapolation wavenumbers by a Taylor-series expansion,

$$\begin{aligned} k_z &\approx \tilde{k}_z + \left. \frac{dk_z}{ds} \right|_{s=\tilde{s}} (s - \tilde{s}) \\ &\approx \tilde{k}_z + \omega \frac{w\tilde{s}}{\sqrt{\omega^2 \tilde{s}^2 - |\mathbf{k}|^2}} (s - \tilde{s}), \end{aligned} \quad (\text{A-4})$$

where $s(x, z)$ is the slowness and $\tilde{s}(z)$ corresponds to a background slowness.

Within any depth slab we can extrapolate the wavefield from the top, either in the perturbed or in the background medium. The wavefields at the bottom of the slab, $\tilde{\mathcal{U}}_{z+\Delta z} = \mathcal{U}_z e^{i\tilde{k}_z \Delta z}$ and $\mathcal{U}_{z+\Delta z} = \mathcal{U}_z e^{ik_z \Delta z}$, related by,

$$\mathcal{U}_{z+\Delta z} \approx \tilde{\mathcal{U}}_{z+\Delta z} e^{i\Delta k_z \Delta z}. \quad (\text{A-5})$$

Equation A-5 is a direct statement of the Rytov approximation, because the wavefields at the bottom of the slab correspond to different phase shifts related by a linear equation. Thus, we obtain the wavefield perturbation $\Delta \mathcal{V}$ at the bottom of the slab by subtracting the background wavefield $\tilde{\mathcal{U}}$ from the perturbed wavefield \mathcal{U} :

$$\begin{aligned} \Delta \mathcal{V}_{z+\Delta z} &\approx \mathcal{U}_{z+\Delta z} - \tilde{\mathcal{U}}_{z+\Delta z} \\ &\approx (e^{i\Delta k_z \Delta z} - 1) \tilde{\mathcal{U}}_{z+\Delta z} \\ &\approx e^{i\tilde{k}_z \Delta z} \left(e^{i \left. \frac{dk_z}{ds} \right|_{s=\tilde{s}} \Delta s_z \Delta z} - 1 \right) \tilde{\mathcal{U}}_z. \end{aligned} \quad (\text{A-6})$$

For the Born approximation, we further assume that the wavefield differences are small so that we linearize the exponential function according to $e^{i\Delta\phi} \approx 1 + i\Delta\phi$. With this approximation we write the following downward continued scattered wavefield,

$$\Delta \mathcal{V}_{z+\Delta z} \approx e^{i\tilde{k}_z \Delta z} \left(i \left. \frac{dk_z}{ds} \right|_{s=\tilde{s}} \Delta s_z \Delta z \right) \tilde{\mathcal{U}}_z, \quad (\text{A-7})$$

which, in operator form is

$$\mathbf{S}_z(\tilde{\mathcal{U}}_z[\Delta s_z]) \approx i \left. \frac{dk_z}{ds} \right|_{s=\bar{s}} \Delta s_z \Delta z \tilde{\mathcal{U}}_z. \quad (\text{A-8})$$

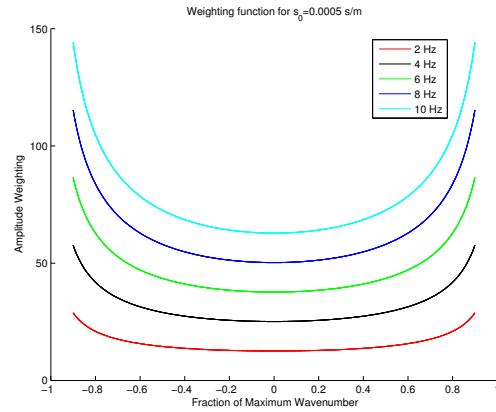
The Born operator may be implemented in the Fourier domain relative to a constant reference slowness in any individual slab. In this case,

$$\left. \frac{dk_z}{ds} \right|_{s=\bar{s}} \approx \omega \frac{\omega s_0}{\sqrt{\omega^2 s_0^2 - (1 - \eta^2) |\mathbf{k}|^2}}, \quad (\text{A-9})$$

where η is a damping parameter to avoid division by zero.

Figure A-1 shows the amplitude weighting demanded by the filter in equation A-9 for five different frequencies for slowness 0.5 s/km.

Figure A-1: Example of the Born amplitude weighting function demanded by the WEMVA theory for a slowness of 0.5 s/km and a damping factor of 0.001. `jeff2-KXfilter` [NR]



Waveform Inversion in Riemannian Space

Waveform extrapolation employing forward modeling in Riemannian coordinates (Sava and Fomel, 2005; Shragge, 2006) does not present a problem for general approach to waveform inversion developed herein because inversion does not take place in generalized coordinates. Rather, the calculated Green's functions are transformed back to global Cartesian grid through mapping pair

$$\mathbf{G}_0(\xi, \mathbf{s}) \approx \mathbf{T}(\mathbf{x}; \xi) \mathbf{G}_0(\mathbf{x}, \mathbf{s}) \quad (\text{A-10})$$

$$\mathbf{G}_0(\mathbf{x}, \mathbf{s}) \approx \mathbf{T}^\dagger(\mathbf{x}; \xi) \mathbf{G}_0(\xi, \mathbf{s}) \quad (\text{A-11})$$

where \mathbf{T} is a transformation matrix that interpolates from the Riemannian space defined by ξ to global Cartesian space \mathbf{x} that includes the transformation Jacobian. In practice, this is applied using weighted sinc interpolation. Thus, one may rewrite the adjoint of equation 26 in the following manner

$$\Delta s(\mathbf{x}) \approx -\omega^2 \sum_{\mathbf{s}} \sum_{\mathbf{r}} \mathbf{T}^\dagger(\mathbf{x}; \xi) \mathbf{G}_0^\dagger(\xi; \mathbf{s}) \mathbf{F}^\dagger(\xi) \mathbf{E}^\dagger(\xi) \mathbf{G}_0^\dagger(\xi; \mathbf{r}) \Delta \Psi(\mathbf{r}, \mathbf{s}). \quad (\text{A-12})$$

ℓ_1 Regularized Inversion

Ben Witten

ABSTRACT

Here an interior point inversion method is presented that solve a least squares problem with ℓ_1 regularization. Velocity inversion can benefit from ℓ_1 regularization because the sparse solution creates blocky velocity models. This is often more geologically accurate than smooth models. In this paper an efficient method is present for solving ℓ_1 regularized least squares problems. Its usefulness is shown through comparisons of previous methods on an example using a least squares formulation for Dix inversion.

INTRODUCTION

Interval velocity estimation is an fundamental problem in reflection seismology. An accurate velocity model is essential to creating an interpretable image from seismic data. There are many techniques for estimating velocity (Clapp, 2001; Sava, 2004) in complex geological settings, but these are often very expensive due to, not only, the operator but also the non-linear nature of the problem and coherent noise that can lead the linear problem to local minima. In this paper an inversion technique is presented for ℓ_1 regularized problems that could potentially decrease the computation time for velocity estimation.

Grid based techniques have an additional drawback, in that they tend to create smooth models even where sharp contrast exists. When considering velocity inversion problems, ℓ_1 regularization can be used to create a sparse solution, resulting in more “blocky” velocity models. The ℓ_1 regularization preserves sharp geologic boundaries, such as channel margins, salt bodies, or carbonate layers. Recently, a specialized interior point method has been presented for efficiently solving ℓ_1 regularized least squares problems (Kim et al., submitted).

A modified version of that algorithm is presented here. To exemplify its utility it will be used to solve the least squares Super Dix equations, originally presented by Clapp et al. (1998). Expanding on this work, Valenciano et al. (2003) introduced ℓ_1 regularization to the problem formulation using a nonlinear iterative approach that approximated an ℓ_1 regularization. Witten and Grant (2006) solved the same problem using a MATLAB based convex optimization solver. MATLAB, however, was pushed to its limits to solve even this small problem.

In this paper, the algorithm will be described. The method is first applied to a simple synthetic model. Then it is applied to a real data set from the Gulf of Mexico. It initial results compared to previous methods for this same dataset.

THE METHOD

The general form of the problem examined by Kim et al. (submitted) is

$$\text{minimize } |\mathbf{C}\mathbf{u} - \mathbf{d}|_2^2 + \sum_{i=1}^n \epsilon |\mathbf{u}_i|, \quad (1)$$

where \mathbf{u} is the model, \mathbf{C} is an operator relating the model to the data \mathbf{d} and \mathbf{u}_i is the model value at point i .

In this paper a very similar problem, of the form,

$$\text{minimize } |\mathbf{W}(\mathbf{C}\mathbf{u} - \mathbf{d})|_2^2 + \sum_{i=1}^n \epsilon_x |\mathbf{D}_x \mathbf{u}_i| + \sum_{i=1}^n \epsilon_\tau |\mathbf{D}_\tau \mathbf{u}_i|, \quad (2)$$

will be explored. Here \mathbf{u} is a vector whose components range over vertical travel time depth τ and whose values are the interval velocity squared v_{int}^2 and \mathbf{d} is the data vector which has the same range as \mathbf{u} , but whose values are the scaled root-mean squared (RMS) velocities squared, $\tau v_{RMS}^2 / \Delta\tau$, where $\tau / \Delta\tau$ is the index on the time axis. \mathbf{C} is the casual integration operator, and \mathbf{W} is a weight matrix which is proportional to our confidence in the RMS velocities. As well, \mathbf{D}_x and \mathbf{D}_τ are the first order finite-difference derivatives along the midpoint and travel-time axis, respectively, and ϵ_x and ϵ_τ are the regularization parameters that control the importance of the two model residuals, effectively controlling the smoothing.

This problem can be transformed to a convex quadratic problem with linear inequality constraints,

$$\begin{aligned} &\text{minimize } |\mathbf{W}(\mathbf{C}\mathbf{u} - \mathbf{d})|_2^2 + \sum_{i=1}^n \epsilon_x \mathbf{v}_i^x + \sum_{i=1}^n \epsilon_\tau \mathbf{v}_i^\tau \\ &\text{subject to } \quad -\mathbf{v}_i^x \leq \mathbf{D}_x \mathbf{u}_i \leq \mathbf{v}_i^x \quad i = 1, \dots, n \\ &\quad \quad \quad -\mathbf{v}_i^\tau \leq \mathbf{D}_\tau \mathbf{u}_i \leq \mathbf{v}_i^\tau \quad i = 1, \dots, n, \end{aligned} \quad (3)$$

where $v^{x,\tau}$ serve to remove the absolute value from the problem. The new problem (3) can be solved by interior point methods (e.g. (Ye, 1997; Wright, 1997)). With this goal in mind, we can now construct logarithmic barrier functions, which approximate an inequality constraint by increasing to infinity as the point approaches the constraint. For a simple problem,

$$\begin{aligned} &\text{minimize } f_0(x) \\ &\text{subject to } f_i(x) \leq 0, \quad i = 1, \dots, m, \end{aligned} \quad (4)$$

the logarithmic barrier function is

$$-\left(\frac{1}{t}\right) \log(-f_i(x)), \quad (5)$$

where $t > 0$ is a parameter the determines how closely you approximate the constraint (Boyd and Vandenberghe, 2004).

For the bound constraints in equation 3 the barrier functions are:

$$\Phi^x(\mathbf{u}, \mathbf{v}^x) = -\sum_{i=1}^n \log(\mathbf{v}_i^x + \mathbf{D}_x \mathbf{u}_i) - \sum_{i=1}^n \log(\mathbf{v}_i^x - \mathbf{D}_x \mathbf{u}_i) = -\sum_{i=1}^n \log(\mathbf{v}_i^{x2} - (\mathbf{D}_x \mathbf{u}_i)^2), \quad (6)$$

and

$$\Phi^\tau(\mathbf{u}, \mathbf{v}^\tau) = -\sum_{i=1}^n \log(\mathbf{v}_i^\tau + \mathbf{D}_\tau \mathbf{u}_i) - \sum_{i=1}^n \log(\mathbf{v}_i^\tau - \mathbf{D}_\tau \mathbf{u}_i) = -\sum_{i=1}^n \log(\mathbf{v}_i^{\tau 2} - (\mathbf{D}_\tau \mathbf{u}_i)^2), \quad (7)$$

Now we can define the centering problem as,

$$\text{minimize } \phi_t(\mathbf{u}, \mathbf{v}^x, \mathbf{v}^\tau) = t|\mathbf{W}(\mathbf{C}\mathbf{u} - \mathbf{d})|_2^2 + t\sum_{i=1}^n \epsilon_x \mathbf{v}_i^x + t\sum_{i=1}^n \epsilon_\tau \mathbf{v}_i^\tau + \Phi^x + \Phi^\tau. \quad (8)$$

The centering problem is an equivalent representation to problem (3) and has a unique solution parametrized by t , called the central path which leads to an optimal solution (Boyd and Vandenberghe, 2004). Newtons method can now be applied to the centering problem, which involves solving a system on linear equations,

$$H \begin{bmatrix} \Delta \mathbf{u} \\ \Delta \mathbf{v}^x \\ \Delta \mathbf{v}^\tau \end{bmatrix} = -g, \quad (9)$$

where $H = \nabla^2 \phi_t(\mathbf{u}, \mathbf{v}^x, \mathbf{v}^\tau)$ is the Hessian and $g = \nabla \phi_t(\mathbf{u}, \mathbf{v}^x, \mathbf{v}^\tau)$ is the gradient. Conjugate gradients is used to find an approximate solution to this system. We differ from Kim et al. (submitted) by choosing not to solve the whole system with conjugate gradients. Instead, \mathbf{v}^x and \mathbf{v}^τ will be solved analytically, decreasing the size of the system of equations needed to be solved solve from $3n$ to n , substantially reducing computational time.

‘To solve for \mathbf{v}^x analytically, take the derivative of $\phi_t(\mathbf{u}, \mathbf{v}^x, \mathbf{v}^\tau)$ with respect to \mathbf{v}^x , then solve for \mathbf{v}^x . This gives

$$\mathbf{v}_i^x = \frac{1}{t\epsilon_x} + \sqrt{\left(\frac{1}{t\epsilon_x}\right)^2 + (\mathbf{D}_x \mathbf{u}_i)^2}. \quad (10)$$

The same can be done for \mathbf{v}^τ . We can also write the Hessian and gradient succinctly as,

$$H = t\nabla^2 |\mathbf{W}(\mathbf{C}\mathbf{u} - \mathbf{d})|_2^2 + \nabla^2 \Phi^x(\mathbf{u}, \mathbf{v}^x) + \nabla^2 \Phi^\tau(\mathbf{u}, \mathbf{v}^\tau) = 2t\mathbf{W}\mathbf{C}^T\mathbf{C} + \mathbf{D}, \quad (11)$$

where

$$\mathbf{D} = \text{diag} \left(2 \left(\frac{\mathbf{v}_1^{x2} + (\mathbf{D}_x \mathbf{u}_1)^2}{\mathbf{v}_1^{x2} - (\mathbf{D}_x \mathbf{u}_1)^2} + \frac{\mathbf{v}_1^{\tau 2} + (\mathbf{D}_\tau \mathbf{u}_1)^2}{\mathbf{v}_1^{\tau 2} - (\mathbf{D}_\tau \mathbf{u}_1)^2} \right), \dots, 2 \left(\frac{\mathbf{v}_n^{x2} + (\mathbf{D}_x \mathbf{u}_n)^2}{\mathbf{v}_n^{x2} - (\mathbf{D}_x \mathbf{u}_n)^2} + \frac{\mathbf{v}_n^{\tau 2} + (\mathbf{D}_\tau \mathbf{u}_n)^2}{\mathbf{v}_n^{\tau 2} - (\mathbf{D}_\tau \mathbf{u}_n)^2} \right) \right) \quad (12)$$

where diag denotes a diagonal matrix with elements $2 \left(\frac{\mathbf{v}_1^{x2} + (\mathbf{D}_x \mathbf{u}_1)^2}{\mathbf{v}_1^{x2} - (\mathbf{D}_x \mathbf{u}_1)^2} + \frac{\mathbf{v}_1^{\tau 2} + (\mathbf{D}_\tau \mathbf{u}_1)^2}{\mathbf{v}_1^{\tau 2} - (\mathbf{D}_\tau \mathbf{u}_1)^2} \right)$. The gradient can be written as

$$\begin{aligned} g &= \nabla_{\mathbf{u}} \phi_t(\mathbf{u}, \mathbf{v}^x, \mathbf{v}^\tau) \\ &= t(2\mathbf{W}\mathbf{C}^T(\mathbf{C}\mathbf{u} - \mathbf{d}) + \left[\frac{2\mathbf{u}_1}{\mathbf{v}_1^{x2} - \mathbf{D}_x \mathbf{u}_1^2} + \frac{2\mathbf{u}_1}{\mathbf{v}_1^{\tau 2} - \mathbf{D}_\tau \mathbf{u}_1^2}, \dots, \frac{2\mathbf{u}_1}{\mathbf{v}_1^{x2} - \mathbf{D}_x \mathbf{u}_1^2} + \frac{2\mathbf{u}_1}{\mathbf{v}_1^{\tau 2} - \mathbf{D}_\tau \mathbf{u}_1^2} \right]^T). \end{aligned} \quad (13)$$

Since the Hessian is constructed from more than the linear operator (it incorporates the barrier functions), matrix multiplication is used to solve the system of equations in the Newton

system. Thus each step of the conjugate gradient is slow, but time is saved by reducing the overall number of conjugate gradient steps.

The final algorithm is:

given the update parameters for t , set the initial values $t = 1/\epsilon$, $\mathbf{u} = \mathbf{0}$, and $\mathbf{v}^{x,\tau} = \mathbf{1}$.

repeat

1. Calculate \mathbf{v}^x and \mathbf{v}^τ
2. Compute the search direction Δu using conjugate gradients
3. Compute the step size s by backtracking line search
4. Update $\mathbf{u} = \mathbf{u} + s(\Delta \mathbf{u})$
5. Calculate \mathbf{v}^x and \mathbf{v}^τ update
6. Evaluate the duality gap and quit if appropriate (see Boyd and Vandenberghe (2004) for more on Duality)
7. Update t

SYNTHETIC EXAMPLE

A synthetic data example is created to test the algorithm to make sure that it works properly. A simple layer-cake earth model is used, shown in Figure 1. RMS velocities are then created from this model as input data to the algorithm. If the inversion is run on this simple model, the result is almost perfect, as shown in Figure 2. The inversion is off by a maximum of 3%, which occurs at the bottom-most interface. This error could most likely be reduced further if we decrease the stopping criterion.

Now 1 and 5 percent Gaussian noise is added to the RMS velocities to simulate real data. The inversion of this noisy data with very little smoothness applied is shown in Figures 3 and 4. The noise introduced to the model shows up as block features. As more noise is added the layers become harder to distinguish from each other. If we increase the smoothing parameters on the ℓ_1 regularization, then much of the noise is smoothed out in the result (Figure 5 and Figure 6). If the regularization parameters, $\epsilon_{x,\tau}$ are increased further then the result will be even smoother (Figure 7 and Figure 8).

As seen in these examples, it is important to correctly choose the regularization parameter to get a good inversion result that is compromise between desired blockiness and introducing spurious elements into the model in the form high spatial frequency events. It can be seen that not all the noise is smoothed out in either Figure 7 or Figure 8. This is because if boundaries are sharp then the ℓ_1 regularization preserves them. The sharper the boundary, the higher the ϵ needs to be smooth them out. Much of the sharp contrast, however, is also smoothed away. From this test it became clear the smoothing along the midpoint is not currently working properly.

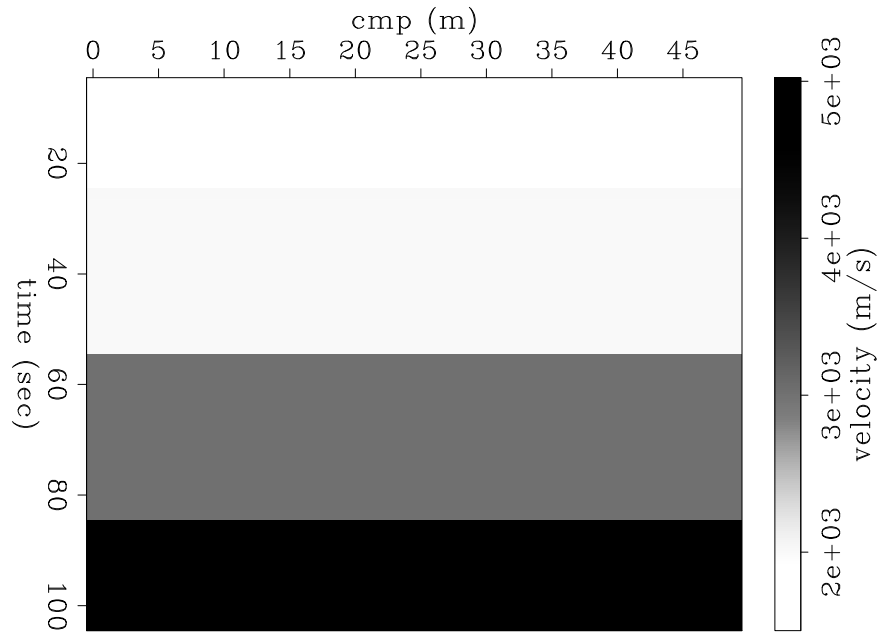


Figure 1: A simple layer cake earth model `ben2-model` [ER]

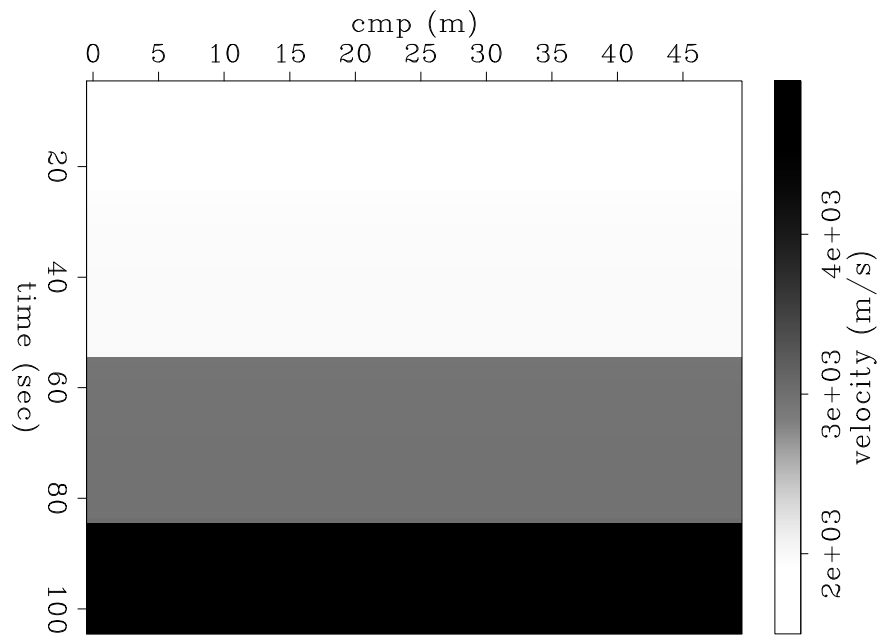


Figure 2: Inversion result for simple model using the algorithm above. For the simple model shown in Figure 1, the result is almost perfect. `ben2-Modvint` [ER]

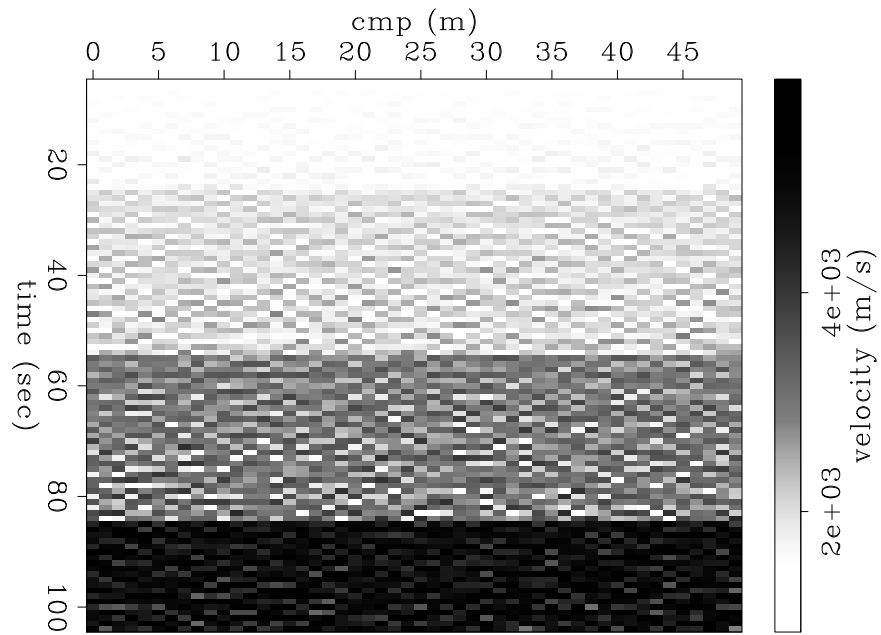


Figure 3: Inversion of the data with 1% noise. The layer boundaries are still visible, but the noise pollutes the results substantially. `ben2-ModvintNoise` [ER]

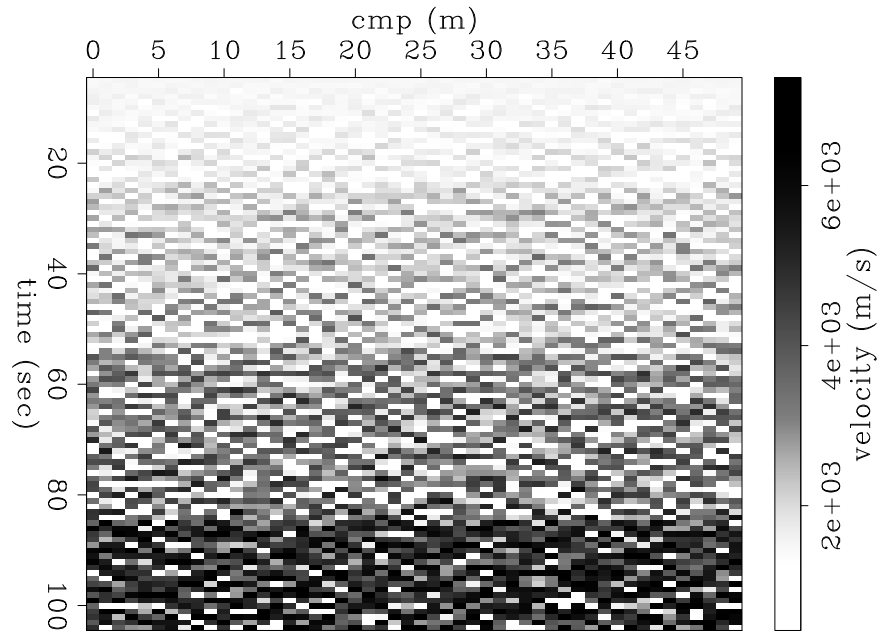


Figure 4: Inversion of noisy data with 5% noise. The noise is severe enough that the boundary layers are no longer discernible. `ben2-ModvintNoise5` [ER]

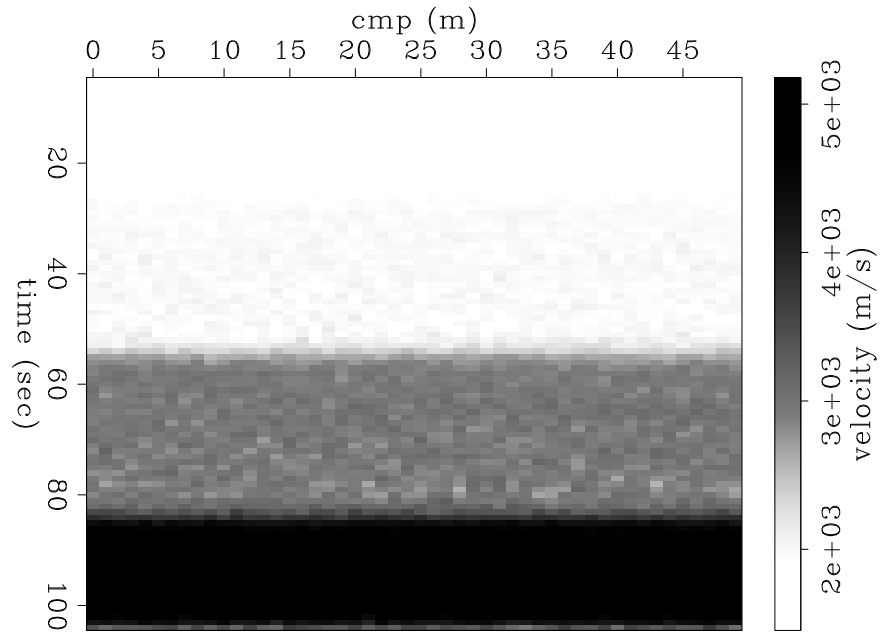


Figure 5: Smoothed version the data with 1% noise. Much of the noise has been smoothed out, but the sharp boundary contacts are still clear. `ben2-ModvintNoiseSmooth` [ER]

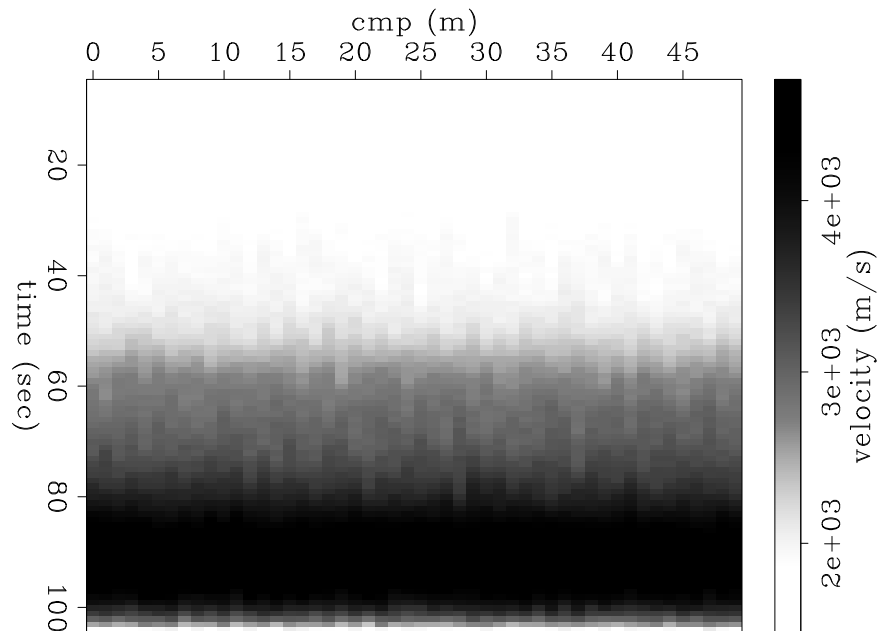


Figure 6: Smoothed version of the data with 5% noise. The smoothing parameter had to be increased to get rid of much of the noise. The boundaries are more evident here than in Figure 6, but the layer boundaries are smoothed out. `ben2-ModvintNoiseSmooth5` [ER]

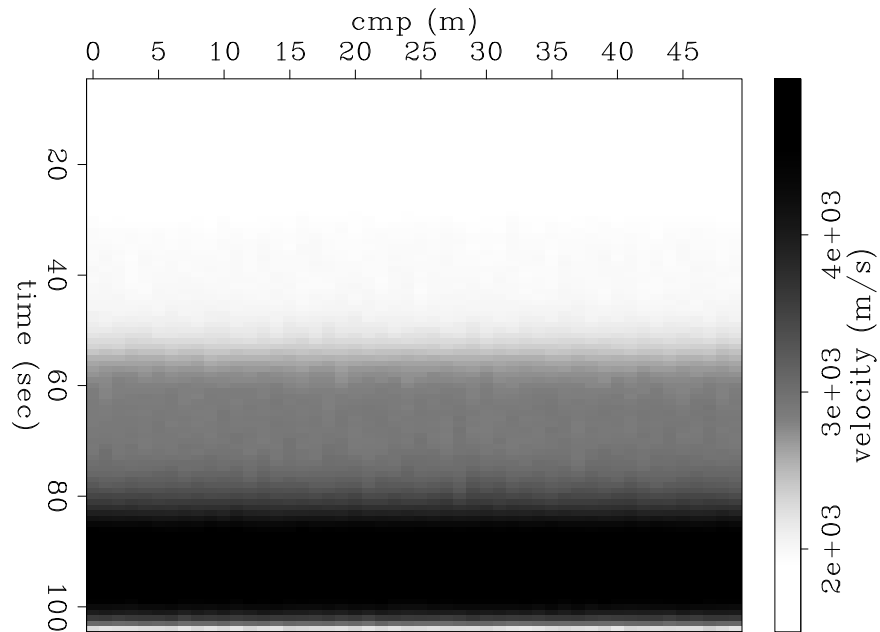


Figure 7: The smoothing parameters were increased further for the 1% noise. Most of the noise is no longer visible, but the layer boundaries are not as sharp. `ben2-ModvintNoiseSmooth2` [ER]

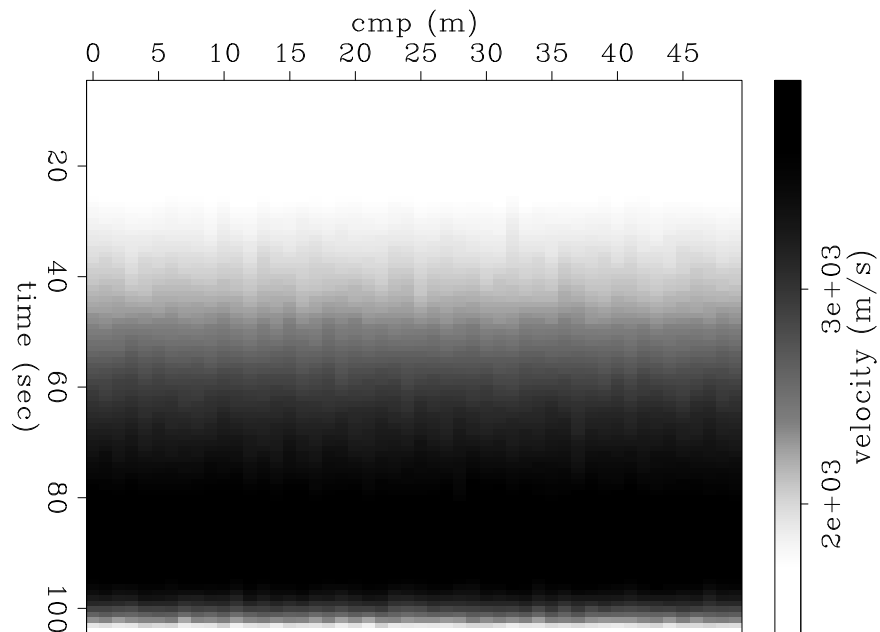


Figure 8: Smoothing parameters were increased for the 5% noise to the point that almost no noise is visible. Doing this, however, has smoothed out the entire result. `ben2-ModvintNoiseSmooth2-5` [ER]

REAL DATA EXAMPLE

Real data from the Gulf on Mexico will now be examined. Figure 9 shows the RMS velocity. Figures 10 and 11 show the previous inversion results done by Valenciano et al. (2003) and

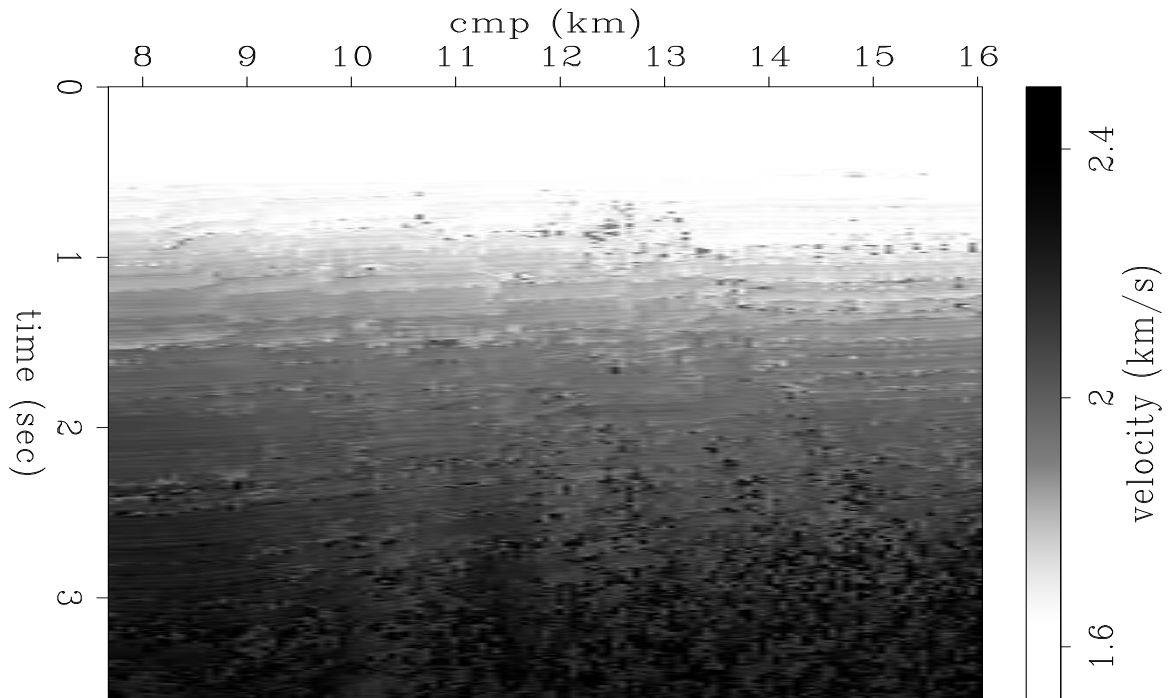


Figure 9: RMS velocity for Gulf of Mexico data. `ben2-vrms` [ER]

Witten and Grant (2006), respectively. Notice that Figure 10 is smoother than Figure 11. This is because Figure 10 uses an approximate ℓ_1 norm.

The results from both previous inversion schemes have limitations. Valenciano et al. (2003) uses an approximate ℓ_1 norm and has no stopping criterion. Thus it requires as many iterations as the user is willing to execute. For the result shown here, 800 conjugate gradient steps were taken. Witten and Grant (2006) is hampered by the use of the MATLAB based `icvx` software (Grant et al., 2006), limiting its use to small problems.

Although Figure 12 is not perfect, the inversion result for the method presented in this paper is close to the previous results. The result in Figure 12 took only 108 iterations. All of the major features are present in all three inversion results. The main difference is in the smoothness of the result.

CONCLUSIONS AND FUTURE WORK

The algorithm presented in this paper offers a fast and efficient method for ℓ_1 regularized inversion problems. By using ℓ_1 regularization the result is often more consistent geologically

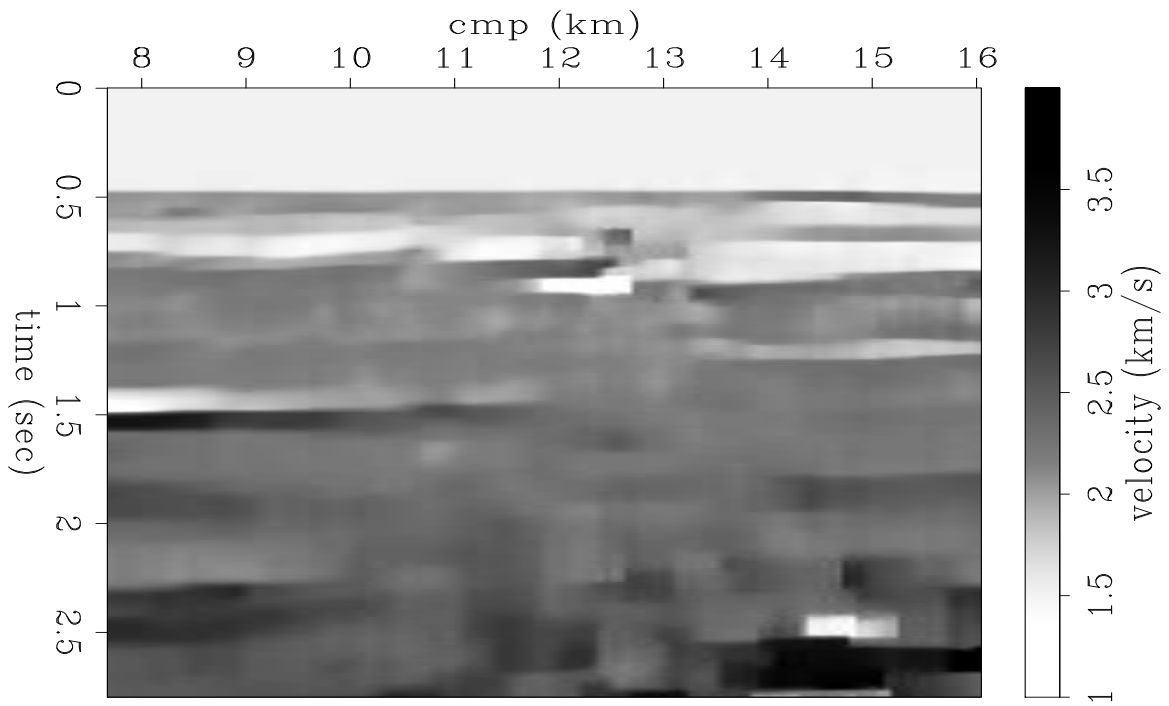


Figure 10: Inversion result from Valenciano et al. (2003). `ben2-vintOld` [ER]

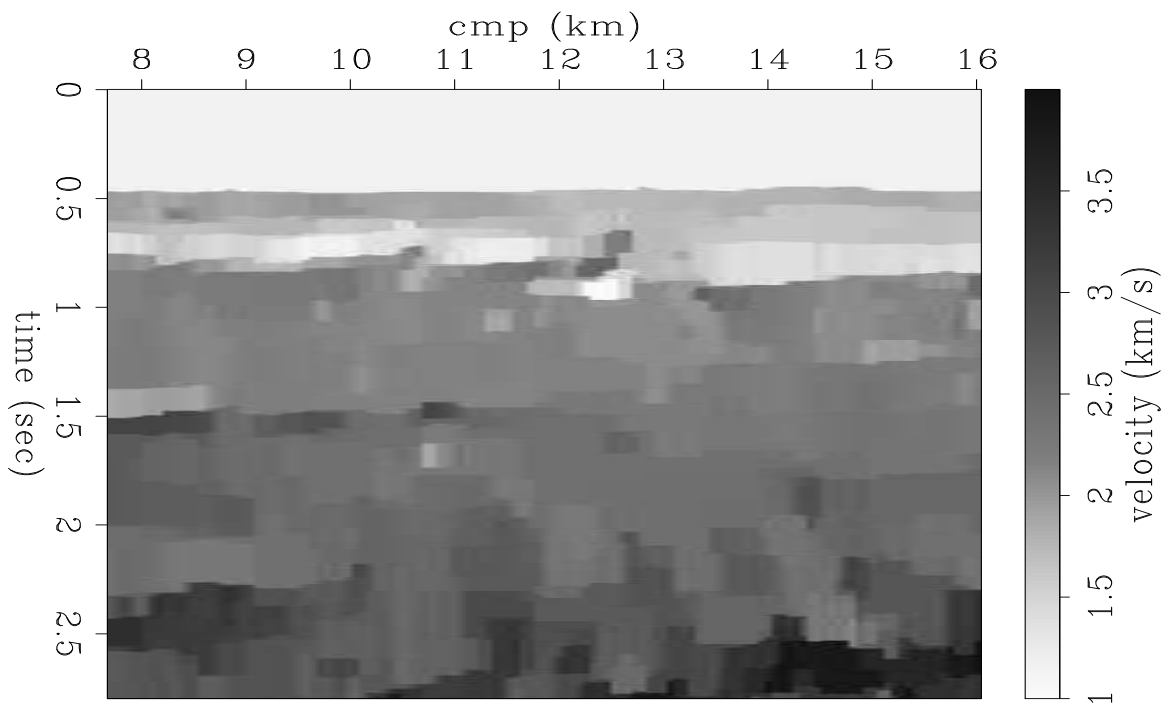


Figure 11: Inversion result from Witten and Grant (2006). `ben2-vintOldcvx` [CR]

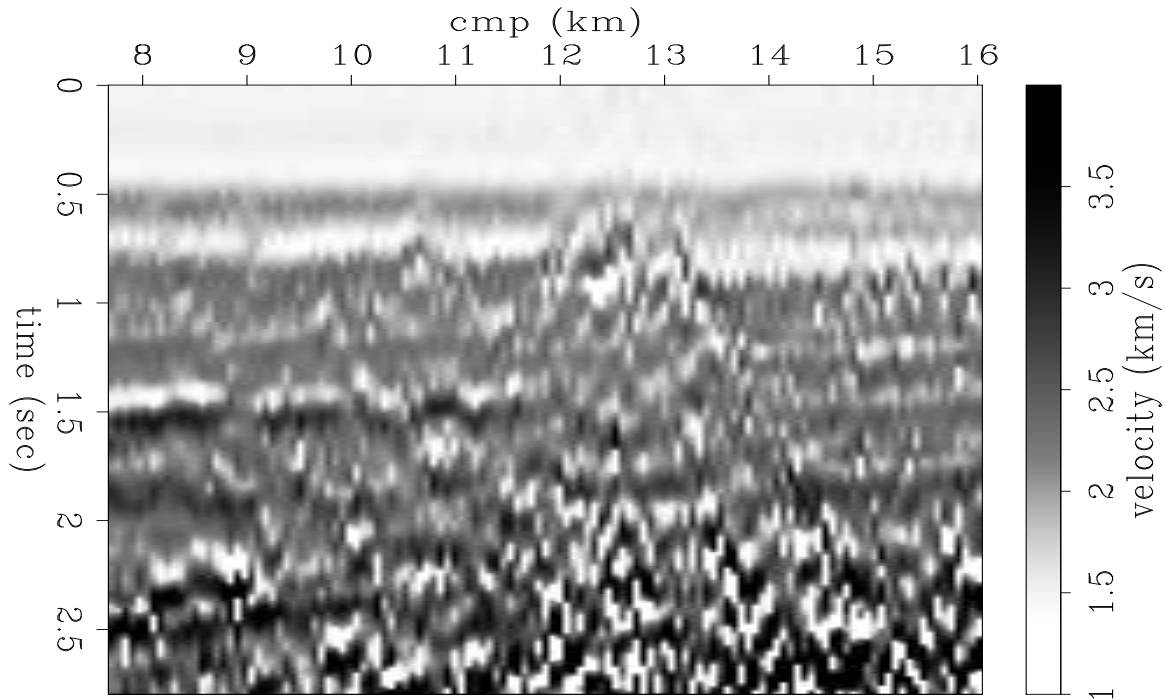


Figure 12: Inversion result from scheme presented in this paper. The inversion appears to be working properly as all of the main features seen in the Figures 10 and 11. The smoothing along the midpoint axis does not work. `ben2-vint` [ER]

because the sharp boundaries are preserved. Even though this method reduces the number of conjugate gradients steps, it could be slow since it must use matrix multiplication. This can be overcome, however, if we implement the matrix multiplication in a parallel fashion as presented by Lomask and Clapp (2006).

Further work involves applying the smoothness along the midpoint-axis and adding hard equality and inequality constraints to the inversion, limiting the range of velocities acceptable in different parts of the model. This would ensure that bad data did not put an impossible velocity in a particular area, such as an ultra-low velocity at great depths. It would also allow for other forms of data, especially ground truth through well logs, to be easily incorporated into the inversion.

ACKNOWLEDGMENTS

I would like to Michael Grant for his help throughout this project.

REFERENCES

- Boyd, S. and L. Vandenberghe, 2004, *Convex optimization*: Cambridge University Press.
- Clapp, R. G., P. Sava, and J. F. Claerbout, 1998, Interval velocity estimation with a null-space: SEP-97, 147–156.
- Clapp, R. G., 2001, *Geologically constrained migration velocity analysis*: Ph.D. thesis, Stanford University.
- Grant, M., S. Boyd, and Y. Ye, 2006, *cvx*: Matlab software for disciplined convex programming: <http://www.stanford.edu/boyd/cvx/>.
- Kim, S., a. L. M. Koh, H., S. Boyd, and D. Gorinevsky, submitted, A method for large-scale ℓ_1 -regularized least squares problems with applications in signal processing and statistics:.
- Lomask, J. and R. G. Clapp, 2006, Parallel implementation of image segmentation for tracking 3d salt boundaries: SEP-124.
- Sava, P., 2004, *Migration and velocity analysis by wavefield extrapolation*: Ph.D. thesis, Stanford University.
- Valenciano, A. A., M. Brown, M. D. Sacchi, and A. Guitton, 2003, Interval velocity estimation using edge-preserving regularization: SEP-114, 136–150.
- Witten, B. and M. Grant, 2006, Interval velocity estimation through convex optimization: SEP-125.
- Wright, S., 1997, *Primal-dual interior-point methods*: Society for Industrial and Applied Mathematics, Philadelphia, PA, USA.
- Ye, Y., 1997, *Interior point algorithms: theory and analysis*: John Wiley & Sons.

Full-volume dip corrections for velocity analysis and MVA

Roland Günther

ABSTRACT

Picking of stacking velocities and residual migration velocities can be difficult in noisy data. Common solutions involve the creation of super-gathers, stacking semblance panels, and flattening data along picked horizons. This report shows that full-volume dip corrections can be used for practical enhancements to velocity analysis workflows. The dip fields are computed both with a semblance method and plane-wave deconstruction filters. Following equations from common reflection surface (CRS) processing, the dip fields are used to extend the standard move-out equations to more precisely describe reflections in super-gathers. This correction improves the sharpness of semblance panels and makes it possible to use larger panels than would be possible without the corrections. The report shows 3D examples of using the full-volume dip information both for conventional stacking and pre-stack time migration.

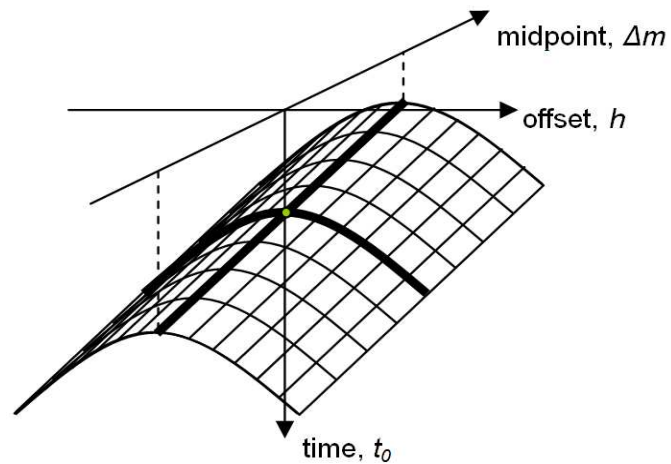
INTRODUCTION

In modern marine surveys with good signal quality, it is often easy to identify move-out curves for velocity analysis or migration velocity analysis (MVA), and automatic algorithms can pick semblance panels with little manual intervention. The main challenge becomes determining the depth migration velocity model that best fits the picked move-outs. But in other datasets, especially land datasets, it can be challenging even to hand-pick initial RMS velocity fields. A variety of practical solutions are used to overcome this challenge. One of the most common is the use of super-gathers, which are sets of adjacent common-midpoint (CMP) gathers treated as single larger CMP gathers. By including more traces in the computation of semblance panels, the signal-to-noise ratio (SNR) improves. However, the size of super-gathers must be limited in areas with steep dips because travel-time surfaces start to cut across reflections in the midpoint direction (Figure 1). A typical size for super-gathers is 3x3 or 3x5, with a larger size often used in the cross-line direction, which is likely to be flatter. When dips are so steep that the data is close to being spatially aliased, even 3x3 super-gathers can be problematic. To overcome this problem, it can be helpful to compute semblance panels on individual CMPs and then to stack adjacent semblance panels. This approach is unlikely to degrade the quality of the final panel, but stacking the all-positive semblance panels does not yield the same SNR improvements that are possible by including more data in a single semblance computation. For horizon-based velocity analysis, super-gathers are sometimes locally flattened using interpreted horizons. Because of the need for human interpretation, this approach is practical only for select horizons.

This report shows that full-volume dip fields can be used to make such corrections on the full volume of velocity panels. Dip fields can typically be computed automatically on stack sections. Because these sections, migrated or unmigrated, have higher SNR than prestack data, automatic dip scans are much more reliable than automatic velocity scans. The dip field is then used as input for a dip corrected velocity analysis. An example from a 3D land dataset shows that the quality of semblance panels improves, especially in the near surface, and that larger super-gathers can be used.

The dip corrections can be viewed either as extensions to standard move-out equations or as simplifications of common reflection surface (CRS) processing, which uses a series of searches for move-out curvature, dip, and reflection curvature to generate parametric descriptions of pre-stack data (e.g., Jäger and Hubral (2001)). CRS processing scans for semblance along travel-time surfaces in super-gathers similar to the surfaces described here, but searches in super-gathers are simultaneous searches for multiple parameters and are intended to be automatic. While convenient when they work, automatic searches may become instable in noisy data. The dip corrections in this report make use of a similar representation of move-out in super-gathers, but the application is changed to allow for manual picking and easier integration into standard processing workflows.

Figure 1: Semblance surface in a 2D super-gather. Uncorrected velocity analysis treats the top of hyperbolas as flat, but precomputed dips can be used to match the shape of reflections more accurately. This is also the surface for a 2D CRS stack. Note that stacking along this surface is equivalent to first summing along the hyperbolas (a conventional NMO stack), and then summing along the apexes (a post-stack slant-stack).



`rgunther1-supergather_moveout`
[NR]

EXTENSIONS TO THE MOVE-OUT FORMULAE

The move-out formulae used for both pre-migration velocity analysis and residual velocity analysis are typically simple hyperbolic equations which are functions of the time t_0 at the apex of the hyperbola and the half-offset h of a trace. For NMO velocity analysis, the travel-time t to a reflection is expressed by:

$$t^2 = t_0^2 + \frac{4h^2}{V_{RMS}^2}. \quad (1)$$

For residual velocity analysis, the equation is essentially the same. By convention, the use of a residual parameter r in the numerator rather than the denominator allows perfectly flat gathers to correspond to a residual of zero:

$$t^2 = t_0^2 + 4h^2r. \quad (2)$$

It is implicit in these equations that all of the data used for the analysis have the same midpoint. Bins are usually chosen to be small enough that post-stack reflections are not aliased. Unmigrated data with midpoints at opposite ends of a bin are not likely to have significantly different t_0 times for a single reflection. For migrated data, the midpoints of all traces in a bin are by definition identical. But when super-gathers are formed, it is likely that the apex of dipping reflections from a trace at one end of the super-gather may be shifted from the apex in a trace at the other end. To correct for this problem, the solution is to extend the hyperbolic move-out equation to move the apex of the reflection up or down along dip. In order to accomplish this, the equation becomes a function of the vector distance $\Delta\mathbf{m}$ of a trace midpoint from the center of the gather and the apparent vector dip σ as determined from dip estimation on the stack section. In the case of NMO velocities, dip is estimated on an unmigrated stack, and in the case of residual velocities, it is estimated on a migrated stack. With these extensions, the move-out formulae become:

$$t^2 = (t_0^2 + \sigma \cdot \Delta\mathbf{m}) + \frac{4h^2}{V_{RMS}^2} \quad (3)$$

for NMO velocity analysis and

$$t^2 = (t_0^2 + \sigma \cdot \Delta\mathbf{m}) + 4h^2r \quad (4)$$

for residual velocity analysis.

In this formulation, the only change to the equation is a shift in the apexes of travel-time hyperbolas. For the case of residual velocity analysis, this is the final form of the equation. For the NMO velocities, it is possible to use knowledge of the dips for an additional correction. The typical goal for pre-migration velocity analysis is to obtain velocities suitable for time migration. These velocities should be the zero-dip velocities obtained after dip move-out (DMO), not dip-dependant NMO velocities. DMO corrects the shape of reflections for all possible dips, but velocities are chosen from semblance panels, picks are typically made for strong individual reflections. Such reflections usually have well-defined dips that are identified by the dip scan. With knowledge of this dip, it is possible to make an explicit dip correction to the velocity term. It is convenient to convert the dip σ to azimuth α and dip angle β , where azimuth is the map-view angle and β is defined as:

$$\beta = \sin^{-1} \left(\frac{V \cdot \|\sigma\|}{2} \right) \quad (5)$$

The dip and azimuth variables extend the move-out formula with the familiar dip correction to velocity:

$$t^2 = (t_0 + \sigma \cdot \Delta\mathbf{m})^2 + \frac{4 \cdot \cos^2 \beta \cdot (\cos \alpha \cdot h_x + \sin \alpha \cdot h_y)^2 + (\sin \alpha \cdot h_x + \cos \alpha \cdot h_y)^2}{V_{RMS}^2}. \quad (6)$$

For offsets in the direction parallel to the dip, the velocities are decreased while the velocities for “strike” offsets remain unchanged. Because the same dip corrections can be achieved by applying DMO to the data prior to velocity analysis, this additional correction is neglected in the data examples, which instead focus on the affects of shifting t_0 up or down within super-gathers.

CRS Stack

The CRS move-out equations can be used not only for velocity analysis but also for stacking. By stacking along the CRS travel-time surface through super-gathers, it is possible to construct a stack with enhanced SNR. This so-called CRS stack can be constructed either by directly summing over the CRS travel-time surfaces or by first summing along individual hyperbolas—as implemented by a conventional NMO stack—and subsequently summing along the apexes of these hyperbolas—as implemented by a slant stack along a pre-computed dip field (see Figure 1). Thus, the SNR improvements of a CRS stack can be equivalently achieved with conventional stacking followed by a post-stack slant stack (Günther, 2006).

EXAMPLES

Stable estimate of dips in the stacked zero-offset or migrated section are required in order to make super-gather corrections. Typical results of such dip scans are shown for an inline of the SEG/EAGE Salt model (Figure 2). Claerbout (1992) introduces plane-wave deconstruction filters that locally decompose an image into plane waves, and Fomel (2002) extends the concept to a least-squares method for continuously decomposing an image into dips. Figure (3) shows the result of applying this algorithm to the 2D stack image. A semblance scan provides an alternative—and somewhat simpler—method for computing dips. This method is identical to CRS post-stack parameter estimation (Jäger and Hubral, 2001). At evenly spaced locations in the stack, a grid search maximizes semblance across circular slices through the volume for different values of the dip σ . For 3D data, the search iterates over both x- and y-components of the dip, so it can be expensive to finely sample the search space. A staged search strategy can help overcome this problem by first determining coarse dip estimates and then iteratively refining the results with finer search grids. Figure (4) shows the dip section from the semblance scan.

Figure (5) shows velocity spectra computed on a super-gather from the salt model. The gather contains data from 5 inlines and 5 crosslines, and the spectra are computed with NMO (left) and with the dip corrected move-out (right). While this example shows that dip corrections can improve the quality of semblance panels for super-gathers, it does not motivate the need for super-gathers. Since the salt model does not contain noise, a perfectly adequate velocity spectrum can be computed from a single CDP. But in real data, especially land datasets, noise is a major impediment for velocity analysis. The next example tests the correction on a 3D land dataset. The data were collected with 25m spacing in both the in-line and cross-line directions in a region with complex geology characterized by salt intrusions. With an average

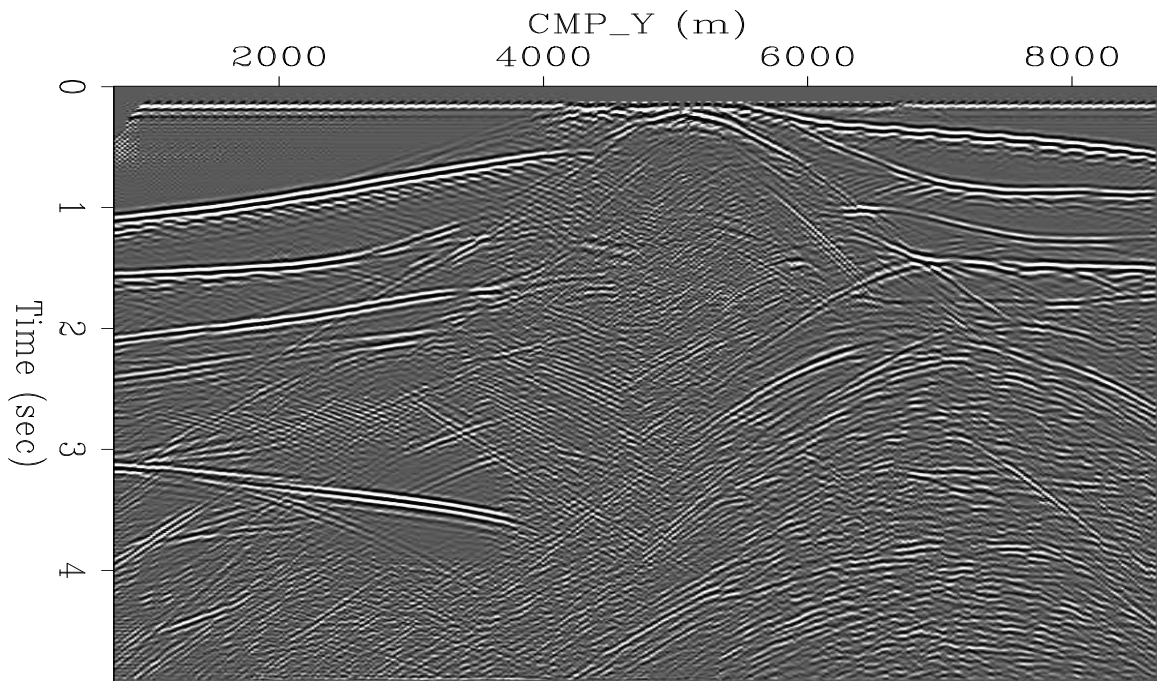


Figure 2: An inline from a zero-offset stack of the SEG/EAGE Salt model.
`rgunther1-seg_inline` [ER]

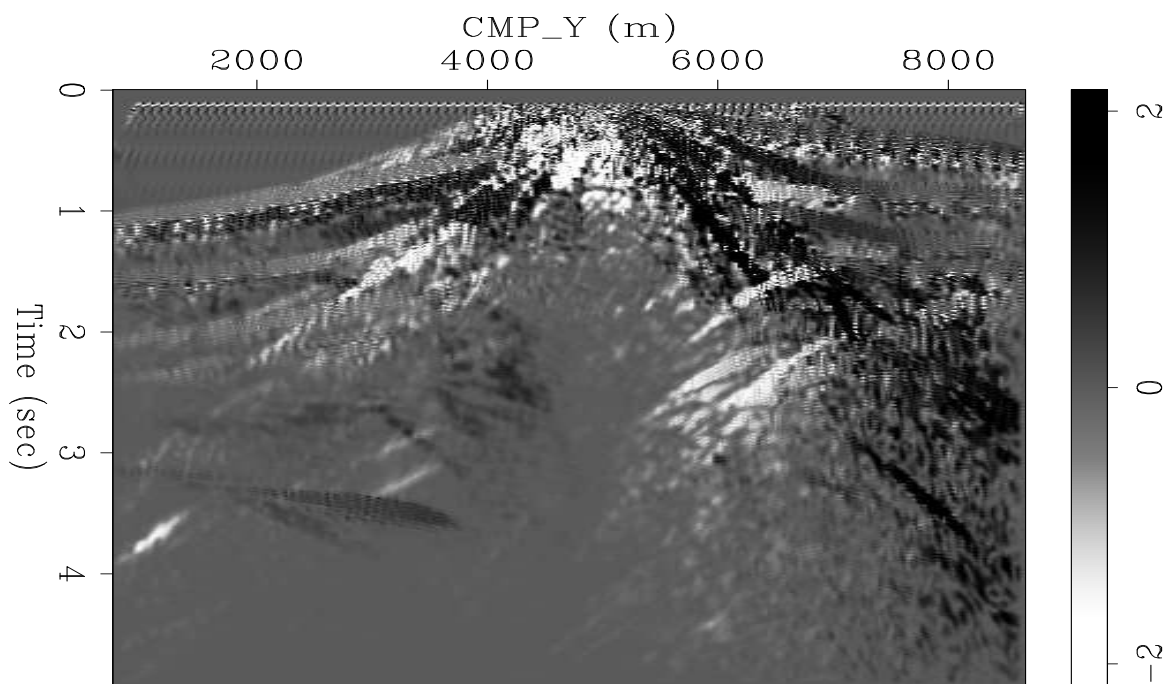


Figure 3: Dips computed for the SEG/EAGE Salt model after Fomel (2002).
`rgunther1-fomel_dips` [ER]

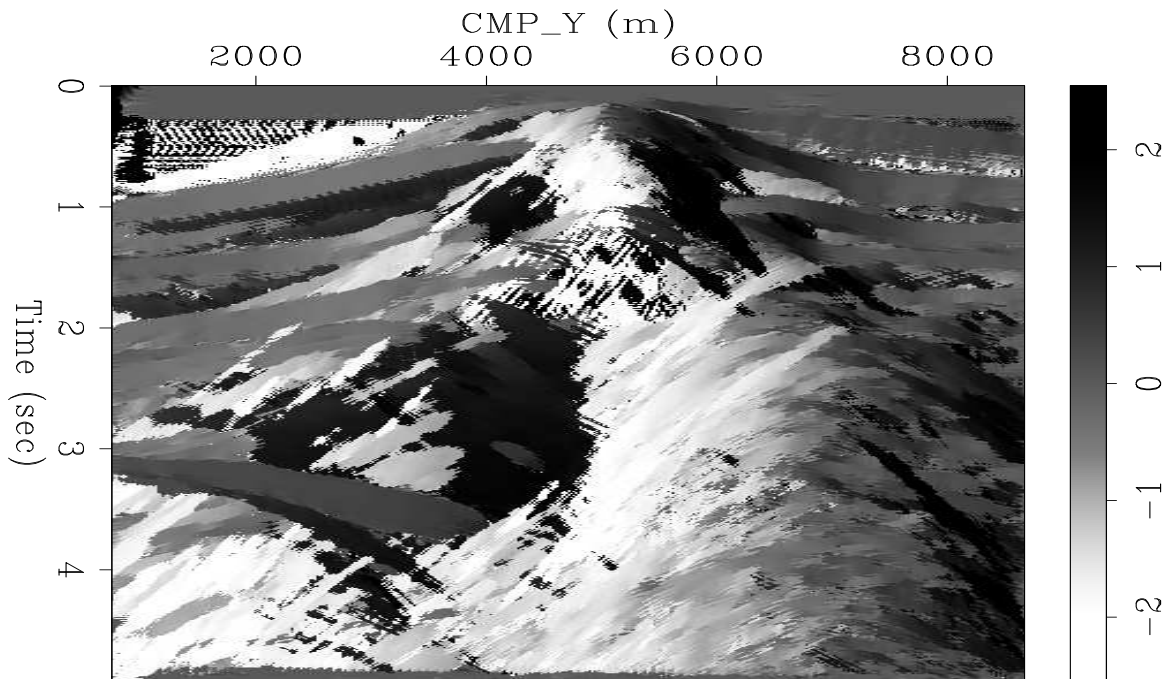


Figure 4: Dips computed for the SEG/EAGE Salt model using a semblance scan. `rgunther1-sem_b_dips` [ER]

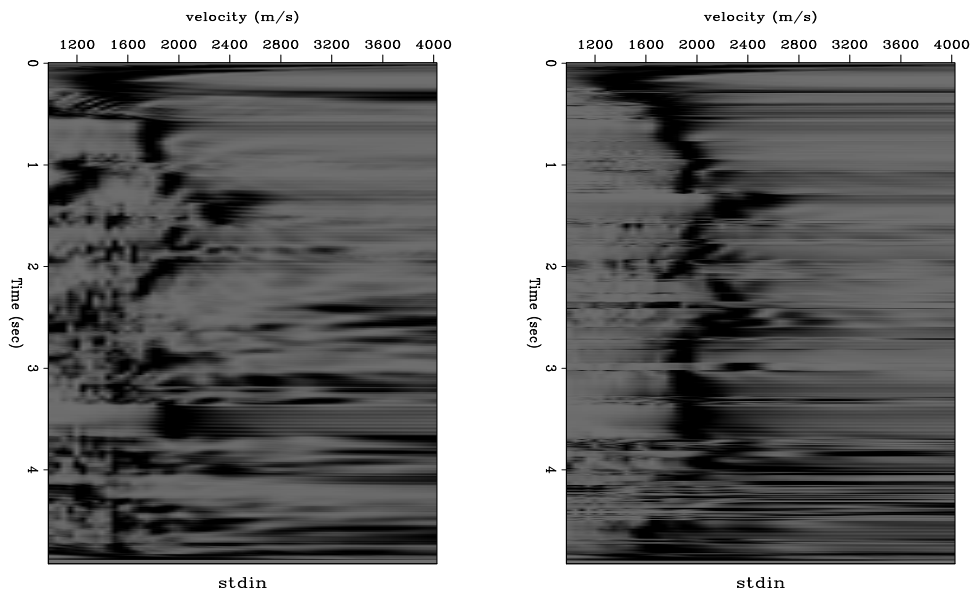


Figure 5: Velocity panel for a 5x5 super-gather computed without dip corrections (left) and with dip corrections (right). The dip corrections improve the coherence of the semblance peaks and make the panel easier to pick. `rgunther1-seg_vel_pan` [ER]

fold of 25, noise is a significant problem for velocity analysis.

Land example

Figure (6) shows dips estimated on a stacked section and semblance panels for both a small (3x3) and a large (11x11) super-gather, computed without (upper panels) and with dip corrections (lower panels). In the large super-gather, the results computed without dips are noisier than those from the small super-gather. For this reason, data processors often prefer to use small super-gathers in areas with significant structure. The best semblance panel is obtained when the large super-gather is combined with the dip correction. Note that the largest improvement is achieved in the near-surface. The higher frequency of the data in this region makes it more likely that the super-gathers cause degradation of the semblance peaks in uncorrected panels. The minimum dip that is spatially aliased is inversely proportional to the temporal frequency of the data, so higher frequencies make it more likely that uncorrected travel-time surfaces cut laterally across reflections.

Figure (7) shows RMO panels for 11x11 super-gathers of time-migrated CMPs at the same location as for the previous gathers. Where the data are migrated with the correct velocity, the semblance is centered on zero r in the middle of the panel. Semblance maxima at negative r indicate over-migrated data, while maxima at positive r indicate under-migrated data. The effect of the dip corrections is similar for the PSTM gathers as for the semblance panels.

CONCLUSIONS

With noise commonly plaguing the interpretation of velocity semblance panels, super-gathers are an important tool for increasing signal both for stacking and residual velocities. Though super-gathers are normally treated as conventional gathers, significant improvements in the quality of semblance panels are achieved by applying dip corrections. An application of the technique to 3D land dataset produces high quality semblance panels over complex geological structures where relatively steep dips are present. The size of super-gathers can be increased significantly beyond the point at which semblance panels would degrade without the corrections. Because the full-volume correction can be easily integrated with existing tools, it is likely to be useful for many different velocity analysis applications, including automatic picking and residual analysis after depth migration.

ACKNOWLEDGMENTS

This project was started while I was at Landmark Graphics Inc. I thank Landmark for continuing to allow me access to the code, data, and computing resources while completing the project at Stanford. Peter Hubral graciously hosted my summer stay at the Universität Karlsruhe.

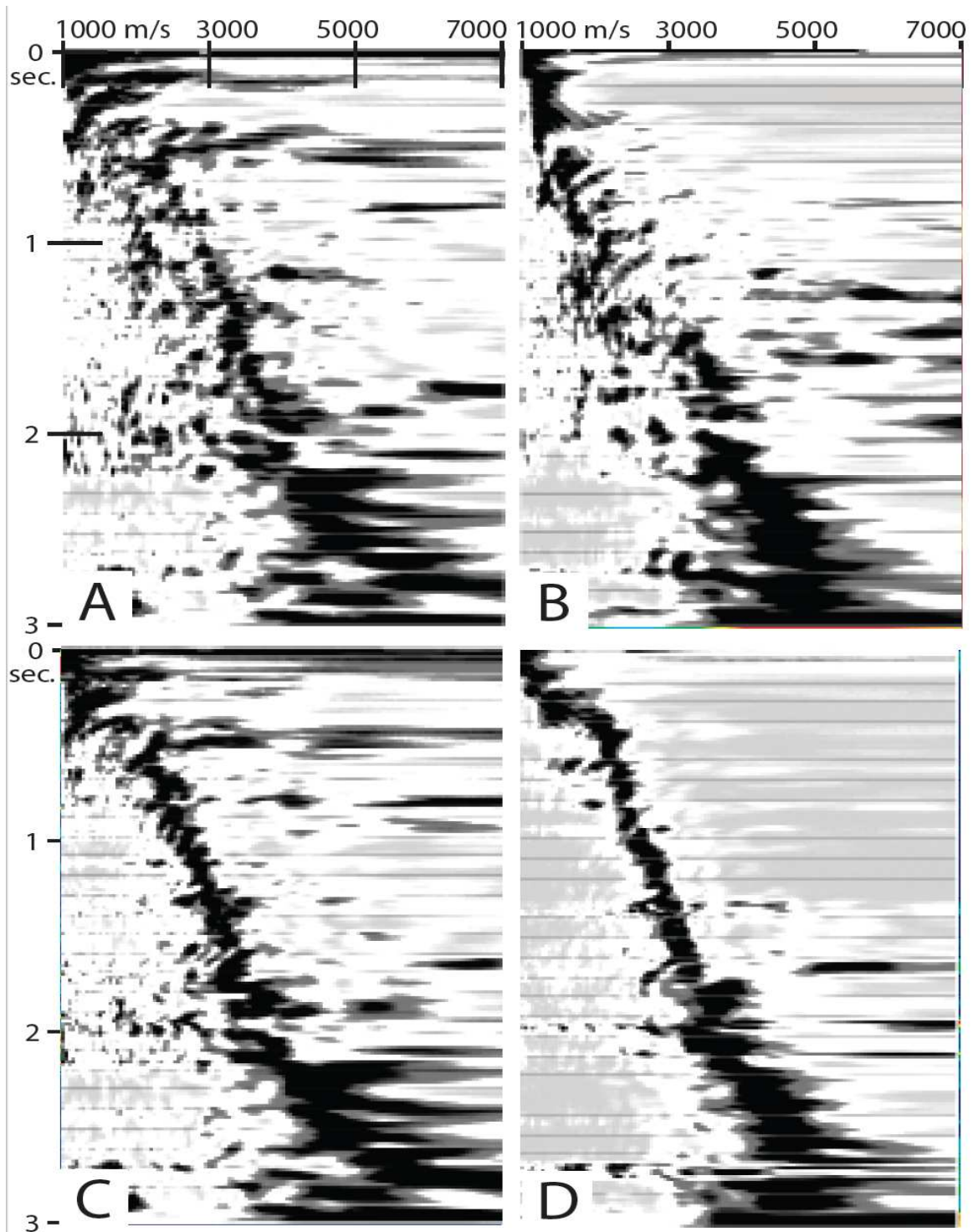


Figure 6: NMO semblance panels computed without dip corrections for 3x3 (A) and 11x11 (B) super-gathers; panels computed with dip corrections 3x3 (C) and 11x11 (D) super-gathers. The dip corrections improve the semblance quality for both the small and larger super-gathers. Note that without the correction, the smaller super-gather yields superior results while the opposite is true with the correction. `rgunther1-land_nmo` [NR]

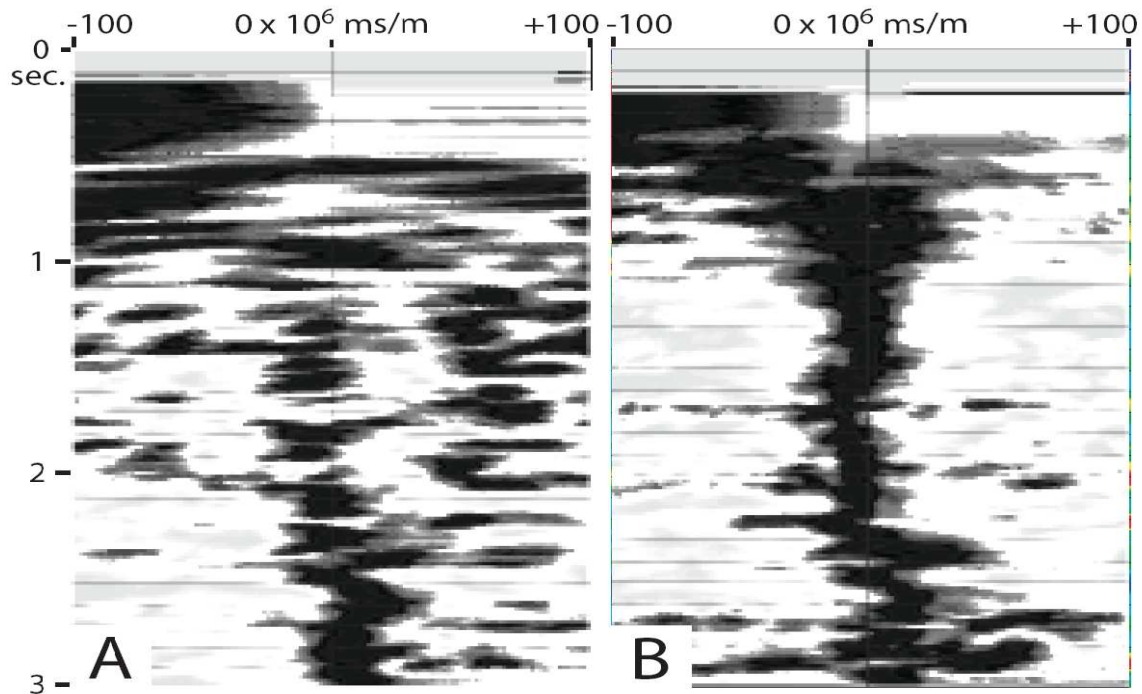


Figure 7: RMO semblance panels computed on an 11x11 super-gather without (A) and with (B) dip corrections. As for NMO velocity analysis, the dip corrections make the panel easier to pick. `rgunther1-land_rmo` [NR]

REFERENCES

- Claerbout, J., 1992, *Earth soundings analysis: processing versus inversion*: Blackwell Scientific Publications, Inc.
- Fomel, S., 2002, Applications of plane-wave deconstruction filters: *Geophysics*, **67**, no. 6, 1946–1960.
- Günther, R., 2006, Practical approaches to the common-reflection surface stack: Technical Program EAGE, Expanded Abstracts.
- Jäger, J. M. G. H., R. and P. Hubral, 2001, Common reflection-surface stack: image and attributes: *Geophysics*, **66**, no. 66, 97–109.

Aligned vertical fractures, HTI reservoir symmetry, and Thomsen seismic anisotropy parameters

James G. Berryman

ABSTRACT

The Sayers and Kachanov (1991) crack-influence parameters are shown to be directly related to Thomsen (1986) weak-anisotropy seismic parameters for fractured reservoirs when the crack/fracture density is small enough. These results are then applied to the problem of seismic wave propagation in reservoirs having HTI symmetry due to the presence of aligned vertical fractures. The approach suggests a method of inverting for fracture density from wave speed data.

INTRODUCTION

Aligned vertical fractures provide one commonly recognized source of azimuthal (surface angle dependent) seismic anisotropy in oil and gas reservoirs (Lynn *et al.*, 1995). While layering in the earth also results in seismic anisotropy (Backus, 1962), horizontal layering of isotropic rock produces vertical transversely isotropic (VTI) media, and could not produce horizontal transversely isotropic (HTI) symmetry without some very significant uplift phenomena being present simultaneously. Of course, anisotropic layers such as shale beds bring seismic anisotropy with them, but again this anisotropy will more typically be VTI, rather than HTI.

On the other hand, VTI earth media seem much easier to understand and analyze than HTI media. Nevertheless, when the source of the anisotropy is aligned vertical fractures, we can make very good use of the simpler case of horizontal fracture analysis by making a rather minor change of our point of view that easily gives all the needed results.

Together with the simplifications already noted, we can also understand very directly the sources of the anisotropy due to fractures by considering a method introduced by Sayers and Kachanov (1991). We find that elastic constants, and therefore the Thomsen (1986) parameters, can be very conveniently expressed in terms of the Sayers and Kachanov (1991) formalism. Furthermore, in the low crack density limit [which is also consistent with the weak anisotropy approach of Thomsen (1986)], we obtain direct links between the Thomsen parameters and the fracture properties. These links suggest a method of inverting for fracture density from wave speed data.

THOMSEN'S SEISMIC WEAK ANISOTROPY METHOD

Thomsen's weak anisotropy method (Thomsen, 1986), being an approximation designed specifically for use in velocity analysis for exploration geophysics, is clearly not exact. Approximations incorporated into the formulas become most apparent for greater angles θ from the vertical, especially for compressional and vertically polarized shear velocities $v_p(\theta)$ and $v_{sv}(\theta)$, respectively. Angle θ is measured from the \hat{z} -vector pointing into the earth.

For reference purposes, we include here the exact velocity formulas for P, SV, and SH seismic waves at all angles in a VTI elastic medium. These results are available in many places (Rüger, 2002; Musgrave, 2003), but were taken specifically from Berryman (1979) with some minor changes of notation. The results are:

$$v_p^2(\theta) = \frac{1}{2\rho} \{[(c_{11} + c_{44})\sin^2\theta + (c_{33} + c_{44})\cos^2\theta] + R(\theta)\} \quad (1)$$

and

$$v_{sv}^2(\theta) = \frac{1}{2\rho} \{[(c_{11} + c_{44})\sin^2\theta + (c_{33} + c_{44})\cos^2\theta] - R(\theta)\}, \quad (2)$$

where

$$R(\theta) = \sqrt{[(c_{11} - c_{44})\sin^2\theta - (c_{33} - c_{44})\cos^2\theta]^2 + 4(c_{13} + c_{44})^2\sin^2\theta\cos^2\theta} \quad (3)$$

and, finally,

$$v_{sh}^2(\theta) = \frac{1}{\rho} [c_{44} + (c_{66} - c_{44})\sin^2\theta]. \quad (4)$$

Expressions for phase velocities in Thomsen's weak anisotropy limit can be found in many places, including Thomsen (1986, 2002) and Rüger (2002). The pertinent expressions for phase velocities in VTI media as a function of angle θ , measured as before from the vertical direction, are

$$v_p(\theta) \simeq v_p(0) (1 + \delta \sin^2\theta \cos^2\theta + \epsilon \sin^4\theta), \quad (5)$$

$$v_{sv}(\theta) \simeq v_s(0) (1 + [v_p^2(0)/v_s^2(0)](\epsilon - \delta)\sin^2\theta \cos^2\theta), \quad (6)$$

and

$$v_{sh}(\theta) \simeq v_s(0) (1 + \gamma \sin^2\theta). \quad (7)$$

In our present context, $v_s(0) = \sqrt{c_{44}/\rho_0}$, and $v_p(0) = \sqrt{c_{33}/\rho_0}$, where c_{33} , c_{44} , and ρ_0 are two stiffnesses of the cracked medium and the mass density of the isotropic host elastic medium. We assume that the cracks have insufficient volume to affect the mass density ρ_0 significantly.

In each case, Thomsen's approximation has included a step that removes the square on the left-hand side of the equation, by expanding a square root of the right hand side. This step

introduces a factor of $\frac{1}{2}$ multiplying the $\sin^2 \theta$ terms on the right hand side, and — for example — immediately explains how equation (7) is obtained from (4). The other two equations for $v_p(\theta)$ and $v_{sv}(\theta)$, *i.e.*, (5) & (6), involve additional approximations as well that we will not attempt to explain here.

The three resulting Thomsen (1986) seismic parameters for weak anisotropy with VTI symmetry are $\gamma = (c_{66} - c_{44})/2c_{44}$, $\epsilon = (c_{11} - c_{33})/2c_{33}$, and

$$\delta = \frac{(c_{13} + c_{44})^2 - (c_{33} - c_{44})^2}{2c_{33}(c_{33} - c_{44})} = \left(\frac{c_{13} + c_{33}}{2c_{33}} \right) \left(\frac{c_{13} + 2c_{44} - c_{33}}{c_{33} - c_{44}} \right). \quad (8)$$

All three of these parameters can play important roles in the velocities given by (5)-(7) when the crack densities are high enough. If crack densities are very low, then the SV shear wave will actually have no dependence on angle of wave propagation. Note that the so-called anellipticity parameter $A = \epsilon - \delta$, vanishes when $\epsilon \equiv \delta$, which we will soon see does happen for low crack densities.

FRACTURED RESERVOIRS AND CRACK-INFLUENCE PARAMETERS

To illustrate the Sayers and Kachanov (1991) crack-influence parameter method, consider the situation in which all the cracks in the system have the same vertical (or z -)axis of symmetry. (We use 1,2,3 and x,y,z notation interchangeably for the axes.) Then, the cracked/fractured system is not isotropic, and we have the first-order compliance correction matrix for horizontal fractures, which is:

$$\Delta S_{ij}^{(1)} = \rho_c \begin{pmatrix} 0 & 0 & \eta_1 & & & \\ 0 & 0 & \eta_1 & & & \\ \eta_1 & \eta_1 & 2(\eta_1 + \eta_2) & & & \\ & & & 2\eta_2 & & \\ & & & & 2\eta_2 & \\ & & & & & 0 \end{pmatrix}, \quad (9)$$

where $i, j = 1, 2, 3$. The two lowest order crack-influence parameters from the Sayers and Kachanov (1991) approach are η_1 and η_2 . The scalar crack density parameter is defined, for penny-shaped cracks having number density $n = N/V$ and radius in the plane of the crack equal to a , to be $\rho_c = na^3$. The aspect ratio of the cracks is b/a .

Now it is also not difficult to see that, if the cracks were oriented instead so that all their normals were pointed horizontally along the x -axis, then we would have one permutation of this matrix and, if instead they were all pointed horizontally along the y -axis, then we would have a third permutation of the matrix. To obtain an isotropic compliance correction matrix, we can simply average these three permutations: just add the three ΔS 's together and then divide by three. [Note that this method of averaging, although correct for contributions linear in ρ_c , does not necessarily work for higher order corrections (Berryman, 2007).] This construction shows in part both the power and the simplicity of the Sayers and Kachanov (1991) approach. The connection to the isotropic case is of great practical importance, because it permits us to

estimate the parameters η_1 and η_2 by studying isotropic cracked/fractured systems, using well-understood effective medium theories (Zimmerman, 1991; Berryman and Grechka, 2006).

HORIZONTAL FRACTURES AND VTI SYMMETRY

Next consider horizontal fractures, as illustrated by the correction matrix (9). The axis of fracture symmetry is uniformly vertical, and so such a reservoir would exhibit VTI symmetry. The resulting expressions for the Thomsen parameters in terms of the Sayers and Kachanov (1991) parameters η_1 and η_2 are given by

$$\gamma_h = \frac{c_{66} - c_{44}}{2c_{44}} = \rho_c \eta_2 G_0, \quad (10)$$

and

$$\epsilon_h = \frac{c_{11} - c_{33}}{2c_{33}} = \rho_c [(1 + \nu_0)\eta_1 + \eta_2] \frac{E_0}{(1 - \nu_0^2)} \simeq \frac{2\rho_c \eta_2 G_0}{1 - \nu_0}. \quad (11)$$

The background shear modulus is G_0 , and the corresponding Poisson ratio is ν_0 . Young's modulus is $E_0 = 2(1 + \nu_0)G_0$. We also find that $\delta = \epsilon$ to the lowest order in the crack density parameter. We have chosen to neglect the term in η_1 in the final expression of (11), as this is on the order of a 1% correction to the term retained. Values of η_1 and η_2 can be determined from simulations and/or effective medium theories (Zimmerman, 1991; Berryman and Grechka, 2006). They depend on the elastic constants of the background medium, and on the shape of the cracks (assumed to be penny-shaped in these examples).

HTI RESERVOIR SYMMETRY FROM ALIGNED VERTICAL FRACTURES

Now the trick to get from horizontal fractures and VTI to aligned vertical fractures and HTI symmetry is relatively simple. We will not need to make any effort to relabel the c_{ij} 's. Rather we just change the meaning of the labels. As long as we stay mentally oriented in the reference frame of the fractures themselves, we can continue to view the z -direction as the symmetry axis and the xy -plane, as the plane of the fractures. The only change we need to make arises from the fact that the surface, where we shoot our seismic survey, is now at 90° from the fracture plane, whereas for horizontal fractures the surface was at 0° from the fracture plane. This observation implies that, wherever the angle θ (measured in radians) appeared in our previous formulas, now we must replace it by $\frac{\pi}{2} - \theta$ radians. Thus, $\sin^2 \theta \rightarrow \cos^2 \theta$ and vice versa in the formulas. This algorithm is exactly right only for those planes that are vertical and also perpendicular to the fracture plane, *i.e.*, at azimuthal angles $\phi = \pm \frac{\pi}{2}$. For all angles, we actually need to replace $\sin^2 \theta$ by $\cos^2 \theta \sin^2 \phi$. Then, when $\phi = 0$ or π , there is no angular dependence since we are in the plane of the fracture.

For the θ dependence, taking $\sin^2 \theta \rightarrow 1 - \sin^2 \theta$, is actually a handier way to proceed, because then we can reduce all the formulas to the same equivalent form as the one Thomsen had originally chosen — if we choose to do so. It is also helpful to backup one step in

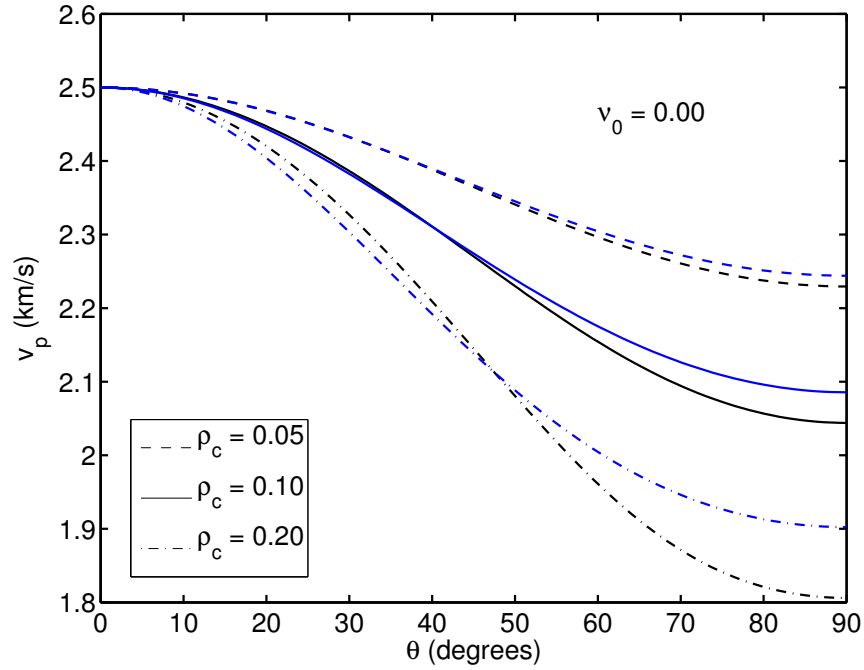


Figure 1: For aligned vertical cracks: examples of anisotropic compressional wave speed (v_p) for Poisson's ratio of the host medium $\nu_0 = 0.00$. Velocity curves in black are exact for the fracture model discussed in the text. The Thomsen weak anisotropy velocity curves for the same fracture model were then overlain in blue. jim1-FIG1 [NR]

the Thomsen derivation and restore squares, thereby “unexpanding” the square root. Certain approximations are then undone, and the final formulas we obtain will be more accurate.

If ϵ , δ , and γ are the Thomsen parameters for the VTI symmetry (horizontal fracture), then, for example,

$$v_{sh}^2\left(\frac{\pi}{2} - \theta\right) = v_s^2(0) \left[1 + 2\gamma \sin^2\left(\frac{\pi}{2} - \theta\right)\right] = v_s^2(0)(1 + 2\gamma) \left[1 - \frac{2\gamma}{1 + 2\gamma} \sin^2 \theta\right]. \quad (12)$$

From this result, we deduce that $\gamma \rightarrow -\gamma/(1 + 2\gamma)$. This is a rigorous statement for the form of the equation considered. Then, the weak anisotropy limit will be $\gamma \rightarrow -\gamma$, but this final step is not necessary or recommended for some of the higher crack densities considered here.

Similar calculations for v_p^2 and v_{sv}^2 give

$$v_p^2\left(\frac{\pi}{2} - \theta\right) = v_p^2(0) \left[1 + 2\delta \sin^2 \theta \cos^2 \theta + 2\epsilon \sin^2\left(\frac{\pi}{2} - \theta\right)\right] \quad (13)$$

and

$$v_{sv}^2\left(\frac{\pi}{2} - \theta\right) = v_s^2(0) \left[1 + 2[v_p^2(0)/v_s^2(0)](\epsilon - \delta) \sin^2 \theta \cos^2 \theta\right], \quad (14)$$

which lead to the results $\epsilon \rightarrow \frac{-\epsilon}{1+2\epsilon} \simeq -\epsilon$, and $\delta \rightarrow \frac{\delta-2\epsilon}{1+2\epsilon} \simeq \delta - 2\epsilon$. As a consistency check, note that $\epsilon - \delta \rightarrow (\epsilon - \delta)/(1 + 2\epsilon) \simeq (\epsilon - \delta)$. Similarly, the pertinent wave speeds are: $v_p(0) \rightarrow$

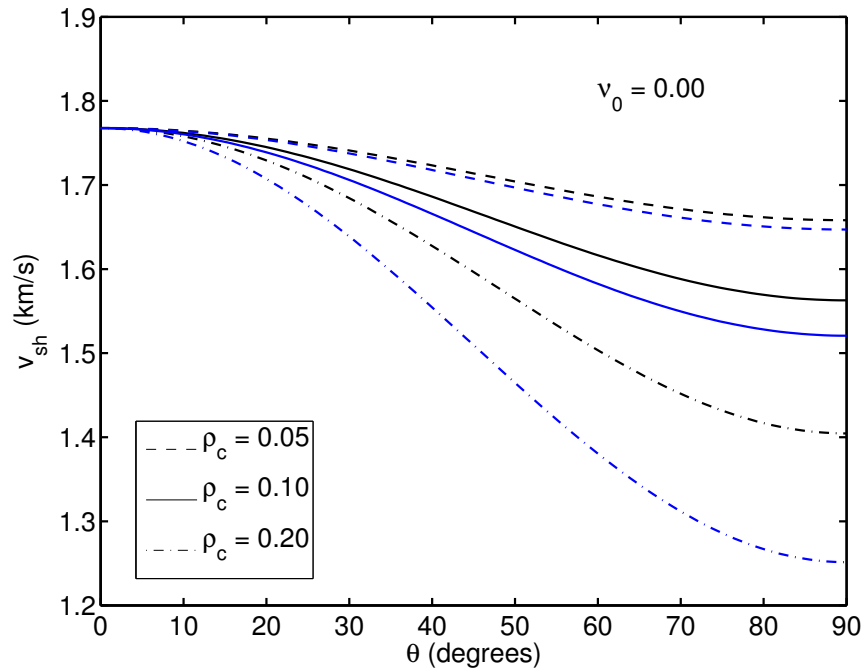


Figure 2: Same as Figure 1 for SH shear wave speed (v_{sh}). jim1-FIG2 [NR]

$\sqrt{c_{33}(1+2\epsilon)/\rho} = \sqrt{c_{11}/\rho}$ and $v_s(0) \rightarrow \sqrt{c_{44}(1+2\gamma)/\rho} = \sqrt{c_{66}/\rho}$ in (12), but the remaining velocity [$v_{sv}(0)$] does not change since $v_{sv}(\theta)$ (within Thomsen's weak anisotropy approximation) is completely symmetric in θ and therefore has to remain so, also with the same end points, after the switch from θ to $\frac{\pi}{2} - \theta$. These results were all known previously and can be found in Ruger (2002), p. 75.

Examples of these results for small ($\rho_c = 0.05$) and higher ($\rho_c = 0.1, 0.2$) crack densities [see Berryman and Grechka (2006) for details of the methods used to obtain all the Sayers and Kachanov crack-influence parameters from simulation data and Berryman (2007) for a full discussion of the reservoir application] are presented in Figures 1-6.

CONCLUSIONS

We find that the Sayers and Kachanov (1991) crack-influence parameters are ideally suited to analyzing the role of fracture mechanics in producing anisotropic elastic constants for aligned fractures in a reservoir exhibiting HTI symmetry. Discussion of the results obtained for the higher crack density examples presented in Figures 1-6 will be provided in a later publication. But the main ideas are already contained in Berryman and Grechka (2006) and Berryman (2007). One important conclusion from the modeling presented here is that the Thomsen weak anisotropy method is valid for crack densities up to about $\rho_c \simeq 0.05$, but should be replaced by better approximations, or exact calculations, if the crack density is $\rho_c \simeq 0.1$ or higher.

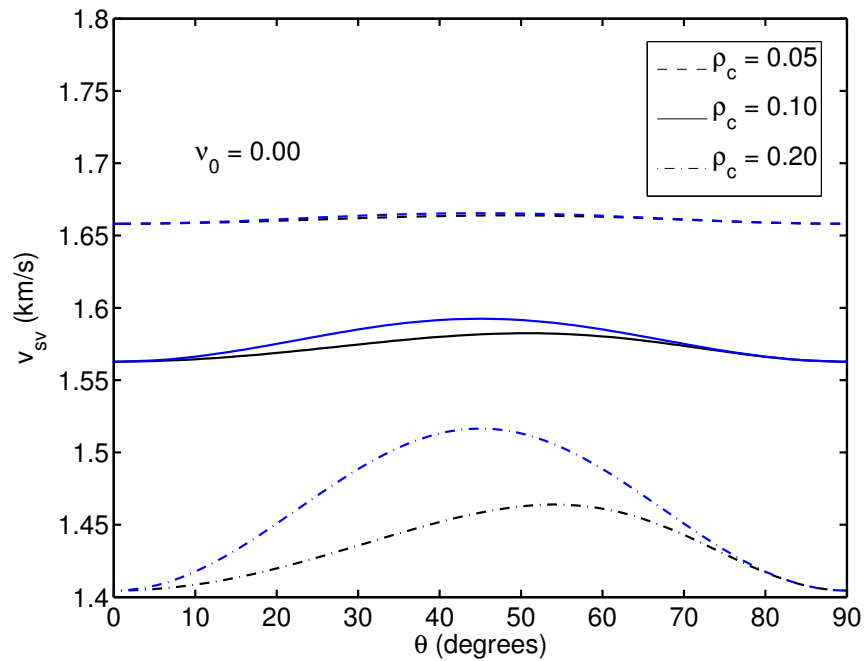


Figure 3: Same as Figure 1 for SV shear wave speed (v_{sv}). jim1-FIG3 [NR]

ACKNOWLEDGMENTS

The author thanks V. Grechka, M. Kachanov, S. R. Pride, and M. Schoenberg for helpful collaborations and conversations.

REFERENCES

- Backus, G. E., 1962, Long-wave elastic anisotropy produced by horizontal layering: *J. Geophys. Res.*, **67**, 4427–4440.
- Berryman, J. G., 1979, Long-wave elastic anisotropy in transversely isotropic media: *Geophysics*, **44**, 896–917.
- Berryman, J. G., 2007, Seismic waves in rocks with fluids and fractures: Submitted for publication.
- Berryman, J. G., and Grechka, V., 2006, Random polycrystals of grains containing cracks: Model of quasistatic elastic behavior for fractured systems: *J. Appl. Phys.*, **100**, 113527.
- Lynn, H. B., Simon, K. M., Layman, M., and Schneider, R., 1995, Use of anisotropy in P -wave and S -wave data for fracture characterization in a naturally fractured gas reservoir: *The Leading Edge*, **14**, 887–893.

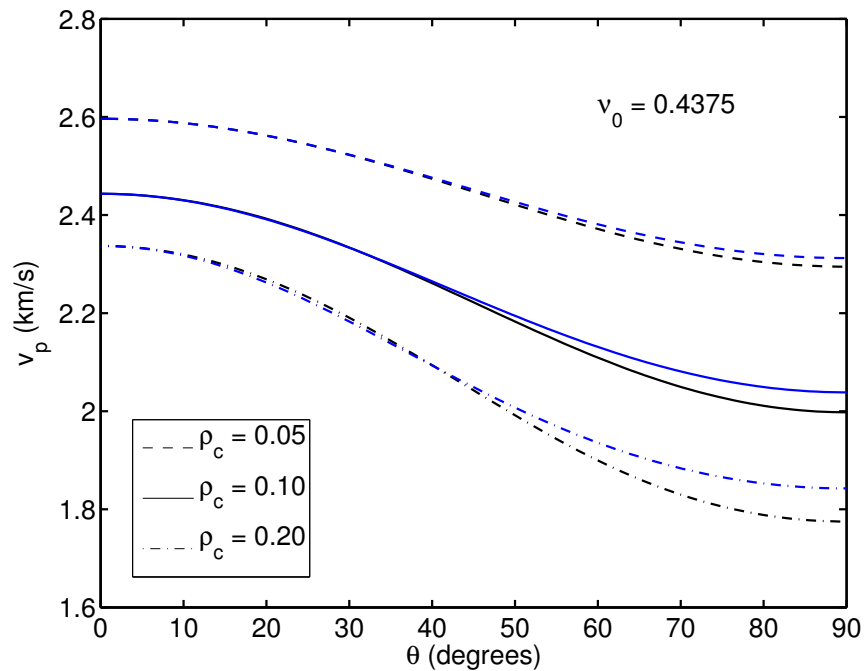


Figure 4: Same as Figure 1, but the value of $\nu_0 = 0.4375$. jim1-FIG4 [NR]

Musgrave, M. J. P., 2003, *Crystal Acoustics*: Acoustical Society of America, Leetsdale, Pennsylvania, Chapter 8.

Rüger, A., 2002, *Reflection Coefficients and Azimuthal AVO Analysis in Anisotropic Media*: Geophysical Monographs Series, Number 10, SEG, Tulsa, OK.

Sayers, C. M., and Kachanov, M., 1991, A simple technique for finding effective elastic constants of cracked solids for arbitrary crack orientation statistics: *Int. J. Solids Struct.*, **27**, 671–680.

Thomsen, L., 1986, Weak elastic anisotropy: *Geophysics*, **51**, 1954–1966.

Thomsen, L., 2002: *Understanding Seismic Anisotropy in Exploration and Exploitation*, 2002 Distinguished Instructor Short Course, Number 5, SEG, Tulsa, OK.

Zimmerman, R. W., 1991, *Compressibility of Sandstones*: Elsevier, Amsterdam.

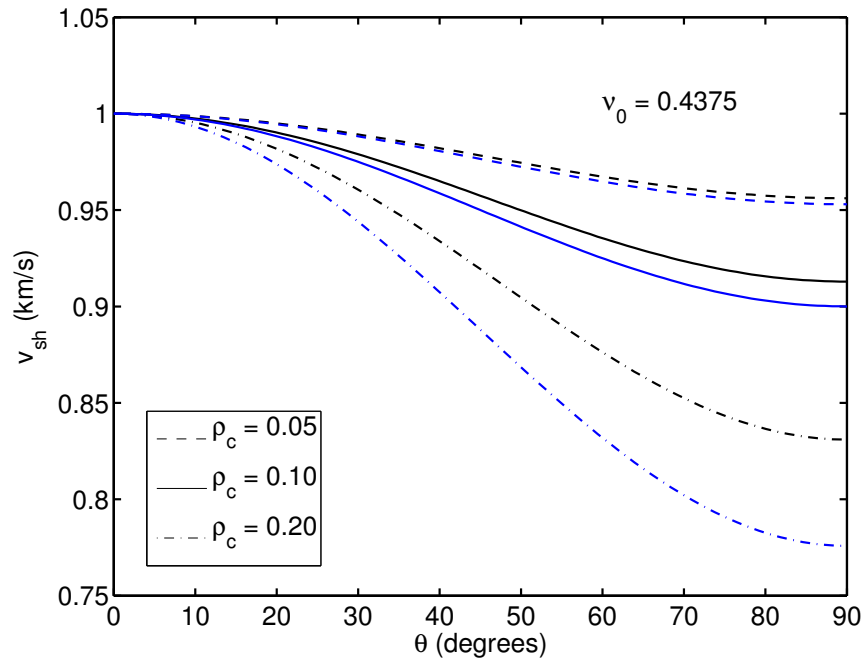


Figure 5: Same as Figure 2, but the value of $\nu_0 = 0.4375$. jim1-FIG5 [NR]

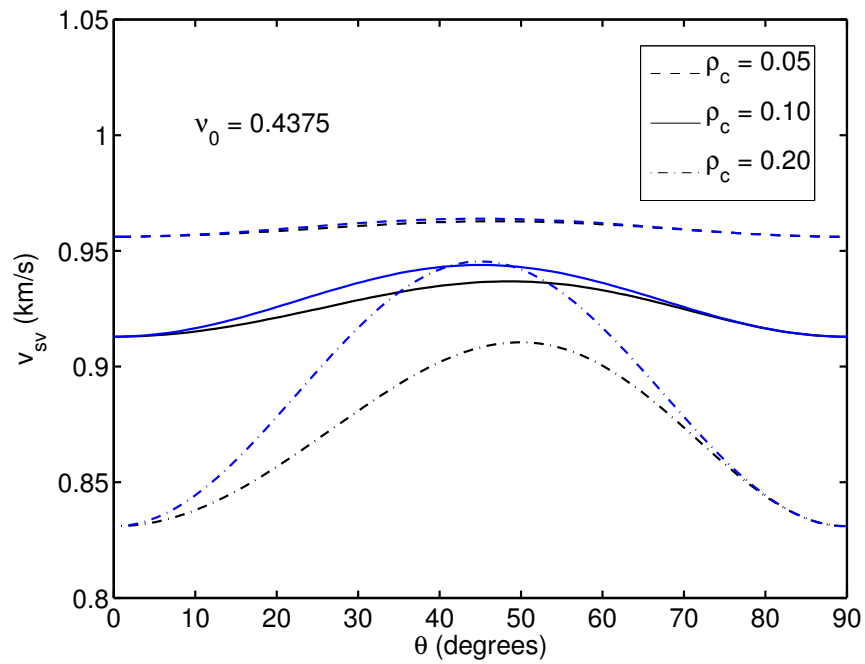


Figure 6: Same as Figure 3 for a different background medium having Poisson's ratio $\nu_0 = 0.4375$. jim1-FIG6 [NR]

Short Note

Moveout analysis with flattening

Robert G. Clapp

INTRODUCTION

Moveout analysis is an important component of many data processing steps. The most basic application is Normal Moveout (NMO), where curvature is related to velocity. Radon based multiple removal techniques take advantage of the differing moveout of primaries and multiples (Hampson, 1986). Migration velocity analysis often measures curvature in common reflection point gathers in either the offset domain or angle domain.

Moveout analysis involves testing potential trajectories by applying a series of moveout functions. A new domain is created where one (or more) of the axes is now a moveout parameter. The creation of this domain can be setup as an adjoint operation, inverse problem ((Lumley et al., 1994; Guitton and Symes, 1999), or in terms of semblance analysis. Often we want to choose a single parameter at each time (or depth) that accurately represents the moveout at the time (or depth). Unfortunately this a non-linear problem. Toldi (1985) and Symes and Carazzone (1991) discuss ways of linearizing the problem. The problem becomes more complicated if we wish to describe moveout by more than a single parameter. The volume formed by scanning over multiple moveout parameters results in very large model spaces. Previous authors have suggested sparse inversion techniques (Alvarez, 2006), or successive scanning.

Another approach to the problem is to use dip information to gain moveout information. Wolf et al. (2004) suggested applying a rough NMO correction then estimating the median of the implied v_{rms} from the dip information at a given zero offset traveltime τ . Guitton et al. (2004) built more directly on the flattening work of Lomask and Claerbout (2002); Lomask and Guitton (2006); Lomask (2006). Guitton et al. (2004) τ -based tomography problem (Clapp, 2001) based on the time-shifts calculated from flattening the data. The advantage of this formulation is that picking becomes unnecessary. The problem with these approaches, when applied to moveout analysis, is the non-linear nature of flattening can easily lead to unrealistic local minima and may not converge to a satisfactory result.

In this paper I also take advantage of the power of flattening while attempting to avoid its pitfalls by limiting the model space. The first approach is to set up an inverse problem from the time shifts needed to flatten a series of Common Reflection Point (CRP). I first invert

for a single parameter at each depth, and then two parameters. In the second approach I set up a non-linear inverse problem that relates dips directly to velocity. Both techniques show promise, but additional work is needed.

CHARACTERIZING RESIDUAL MOVEOUT

In migration velocity analysis there is always a debate on the best method to describe the moveout seen in CRP gathers. One approach is to measure and invert the moveout at many depths in each offset/angle of the CRP gather independently. Using this approach, complex residual moveouts can be accurately described. The downside is that these estimates are more prone to noise (cycle skipping for example). The other extreme is to use a single parameter (at many depth locations) that best describes the moveout as a function of offset or angle. A single parameter is more robust but in complex situations may not accurately describe moveout. In addition, selecting the parameter usually involves selecting the moveout with the maximum semblance at a given depth, a non-linear problem that can often lead to unrealistic solution if not properly handled (Clapp et al., 1998).

Often a good compromise between robustness and flexibility is to describe moveout with two parameters. Unfortunately, selecting these two linked parameters is more problematic than the single parameter approach. One approach is to scan over both parameters at all desired depths, for every CRP, and pick the maximum. In addition to being costly, this approach makes picking a consistent and spatially realistic model very challenging. A potentially better approach is outlined in Harlan (1998). He suggests a dual scanning approach: scan over the first-order term fitting the outer offsets, then scanning over the second-order term to best fit the middle offsets. This approach is more efficient than scanning over the entire model space. The dual scanning approach amounts to linearizing the problem around the first order term, with all of the associated linearization drawbacks. In addition spatial consistency is also problematic.

A general weakness of the scanning approach is that moveout is being determined from semblance amplitude. Flattening offers an interesting alternative to the scanning approach. Flattening inverts for a time shift field (moveout). By incorporating an operator that estimates moveout parameters from time shift field, arbitrary moveout descriptions can be estimated from dip.

FLATTENING REVIEW

The basic idea behind flattening (Lomask, 2006) is that the gradient measured at a time (or depth) horizon τ is equal to the dip \mathbf{p} measured at each point of the horizon.

$$\nabla \tau(x, y, t) = \mathbf{p}(x, y, \tau). \quad (1)$$

In order to obtain smoothness between horizons a regularization term is added to the problem. Defining the 3-D gradient operator as $\nabla = [\frac{\partial}{\partial x} \quad \frac{\partial}{\partial y} \quad \frac{\partial}{\partial t}]^T$ a new system of equations can be

built,

$$\mathbf{W}_\epsilon \nabla = \begin{bmatrix} \mathbf{I} & \mathbf{0} & \mathbf{0} \\ \mathbf{0} & \mathbf{I} & \mathbf{0} \\ \mathbf{0} & \mathbf{0} & \epsilon \mathbf{I} \end{bmatrix} \begin{bmatrix} \frac{\partial}{\partial x} \\ \frac{\partial}{\partial y} \\ \frac{\partial}{\partial t} \end{bmatrix}, \quad (2)$$

where \mathbf{I} is the identity matrix and ϵ is a scaling parameter. The residual is defined as

$$\mathbf{r} = \mathbf{W}_\epsilon \nabla \boldsymbol{\tau} - \mathbf{p} = \begin{bmatrix} \frac{\partial \boldsymbol{\tau}}{\partial x} \\ \frac{\partial \boldsymbol{\tau}}{\partial y} \\ \epsilon \frac{\partial \boldsymbol{\tau}}{\partial t} \end{bmatrix} - \begin{bmatrix} \mathbf{p}_x \\ \mathbf{p}_y \\ \mathbf{0} \end{bmatrix}. \quad (3)$$

The dips need to be measured along the horizon, making the problem non-linear. A Gauss-Newton approach can be used with linearizing about the current estimated horizon volume. Again following the approach of (Lomask, 2006), we

iterate {

$$\mathbf{r} = [\mathbf{W}_\epsilon \nabla \boldsymbol{\tau}_k - \mathbf{p}(x, y, \boldsymbol{\tau}_k)] \quad (4)$$

$$\Delta \boldsymbol{\tau} = ((\mathbf{W}_\epsilon \nabla)^T \mathbf{W}_\epsilon \nabla)^{-1} (\mathbf{W}_\epsilon \nabla)^T \mathbf{r} \quad (5)$$

$$\boldsymbol{\tau}_{k+1} = \boldsymbol{\tau}_k + \Delta \boldsymbol{\tau} \quad (6)$$

} ,

where the subscript k denotes the iteration number.

Two different approaches can be used for the linearized step (equation 5) The most efficient is to solve the problem a direct inverse in Fourier domain (Lomask, 2003). When space-domain weighting or model restriction (Lomask and Guitton, 2006) is needed, a space-domain conjugate gradient approach is warranted.

In general we deal with 2-D angle or offset gathers. The standard approach is to solve a 2-D flattening problem where $\boldsymbol{\tau}$ is a function of time/depth and offset. We revert to a 2-D gradient operator, and solve each CMP/CRP gather independently.

POST-FLATTENING INVERSION

There are two general approaches to calculating moveout parameters using the flattening methodology. The first approach is to perform parameter estimation in two phases. First, solve for the *non-linear* $\boldsymbol{\tau}$ field, then construct a linear problem to find the moveout parameters that best fit the $\boldsymbol{\tau}$ field.

The flattening algorithm provides a time-shift $\boldsymbol{\tau}$ field that is function of depth z , offset h , and CRP \mathbf{x} . As a first test we want to estimate moveout of a volume migrated using downward

continuation migration. Biondi and Symes (2003) demonstrated that residual moveout Δz can be approximated (assuming zero geologic dip) as a function of angle θ and depth z through

$$\Delta z = z\rho \tan(\theta)^2, \quad (7)$$

where ρ is the moveout parameter. We can estimate $\rho(z, \mathbf{z})$ as a global inverse problem. Defining the above moveout equation above as $\mathbf{B}\rho$ we obtain the objective function Q ,

$$Q(\rho) = |\tau - \mathbf{B}\rho|^2. \quad (8)$$

We can ensure spatial smoothness by introducing a roughener \mathbf{A} to the objective function to obtain,

$$Q(\rho) = |\tau - \mathbf{B}\rho|^2 + \epsilon^2 |\mathbf{A}\rho|^2, \quad (9)$$

where ϵ is scaling parameter.

To test the methodology I migrated a line from a 3-D North Sea dataset. Figure 1 displays two cross-sections of the migrated data (left) and the τ field (right) calculated from the volume. A moveout field ρ is then calculated from the τ field using a conjugate gradient algorithm to minimize equation 9. Figure 2 shows the resulting moveout field. The inversion approach has an additional advantage, it easy to assess where the moveout parameterization effectively described the time shifts and where it failed. Figure 3 shows the result of stacking the absolute value of the residual over the offset plane. Areas of high amplitude represent areas where a single parameter did not accurately describe τ .

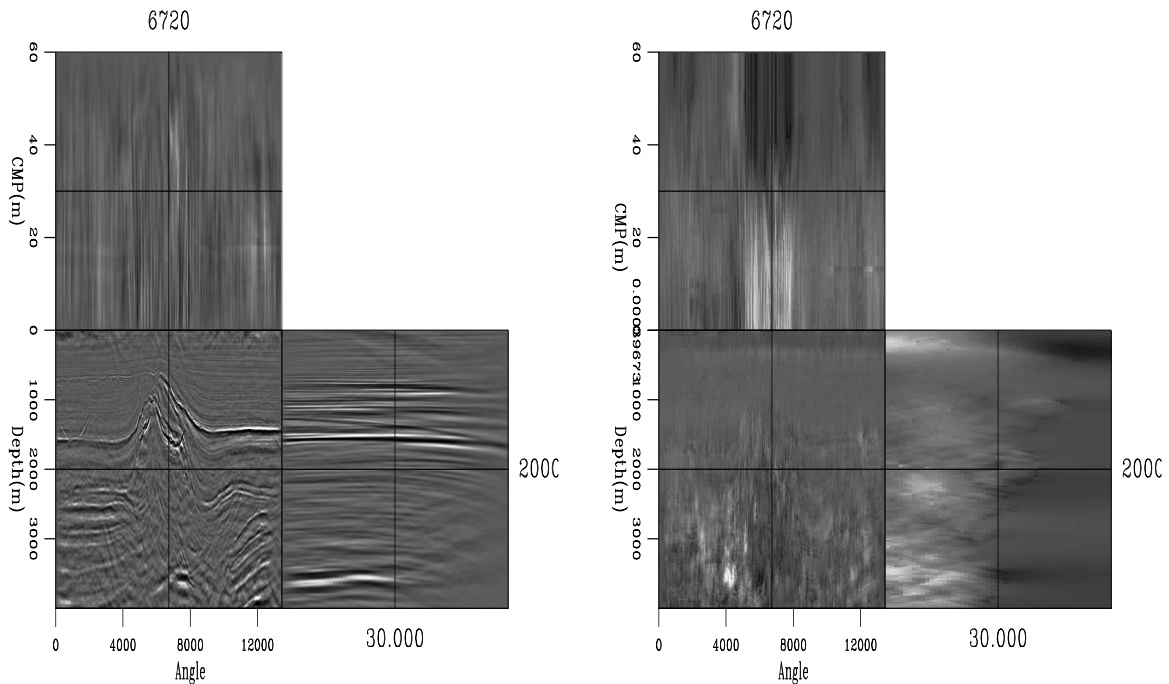


Figure 1: The left panel shows three cross-sections of the migrated image (depth, inline, angle). The right panel shows the time shifts calculated from the volume. [bob3-data](#) [ER]

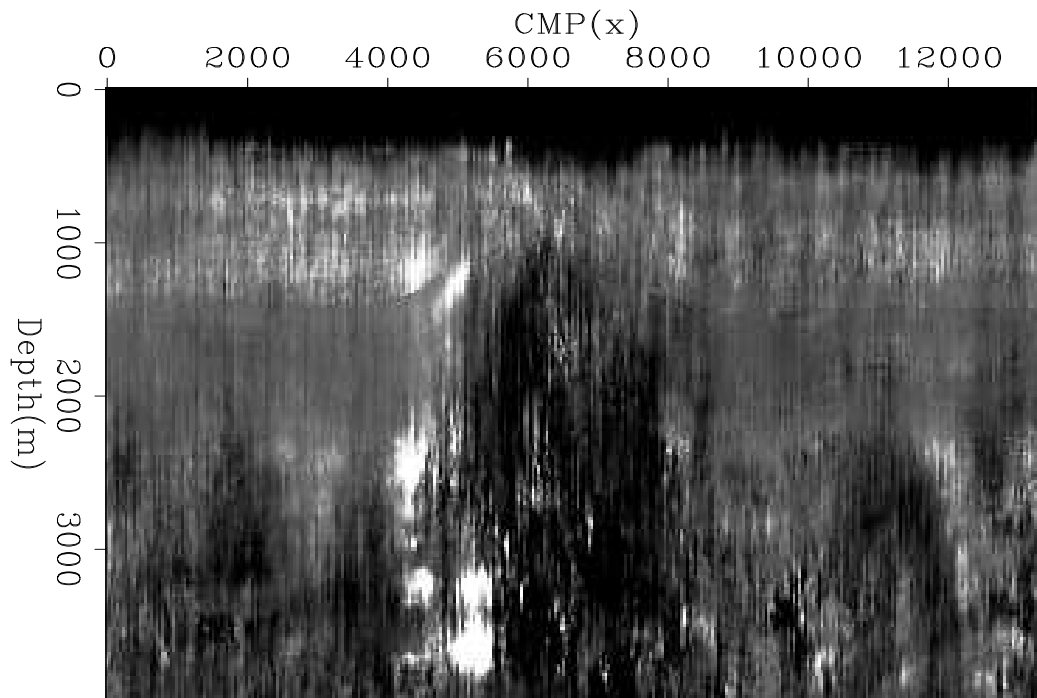


Figure 2: The result of inverting for the moveout parameter ρ from the time shifts shown in the right panel of Figure 1. `bob3-rho1` [ER]

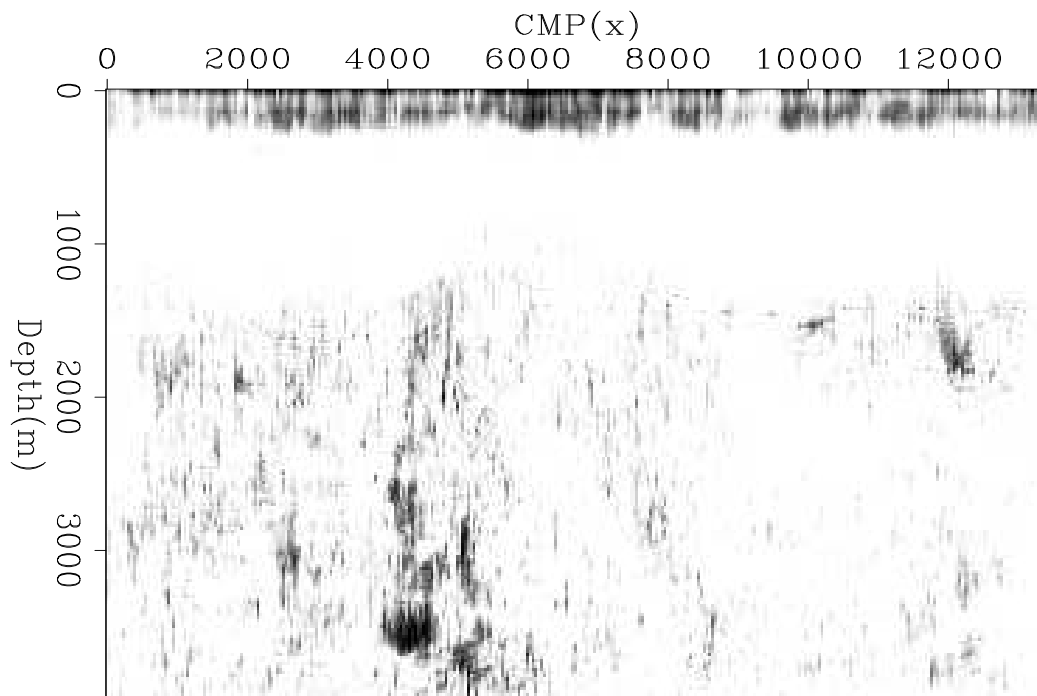


Figure 3: The spatial error fitting error associated with the time shifts shown in Figure 1 and the moveout parameter shown in Figure 2. `bob3-resid1` [ER]

Rather than solving for a single moveout parameter at each location, we can solve for multiple moveout parameters simultaneously. To test this approach I introduced a new operator \mathbf{C} that estimates the moveout parameter μ by searching for higher order moveout anomalies. For \mathbf{C} I chose an arbitrary moveout function,

$$\Delta z = \mu z \tan(\theta)^4 \quad (10)$$

that attempts to see if a higher polynomial of the same form as \mathbf{C} to help to describe the moveout. The optimization goal of equation (9) becomes

$$Q(\rho, \mu) = |\tau - \mathbf{B}\rho - \mathbf{C}\mu|^2 + \epsilon^2 |\mathbf{A}\rho|^2 + \epsilon^2 |\mathbf{B}\mu|^2. \quad (11)$$

Figure 4 shows the resulting ρ (left) and μ (right) fields. Note how similar the ρ field is to the one in Figure 2, indicating that a two-stage estimation approach would have yielded a similar result. Figure 5 shows the resulting residual. Note the decrease in some areas compared to Figure 3, but still showing areas where the moveout is significantly more complex.

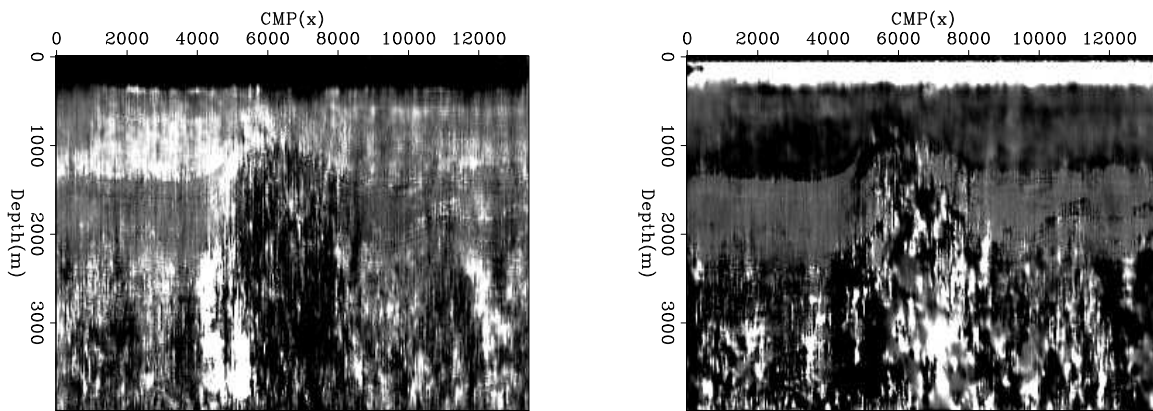
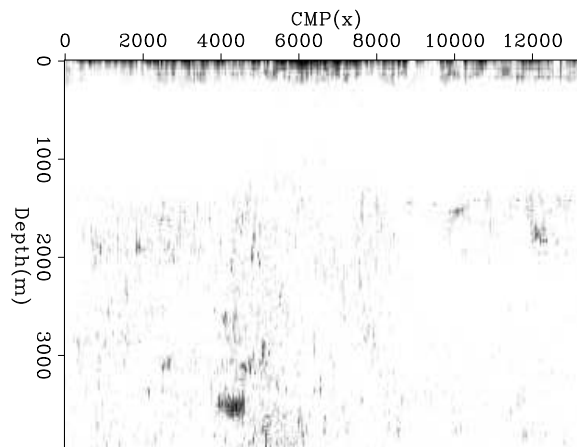


Figure 4: The result of inverting for both ρ (left panel) and μ (right panel). Note the similarity to the single parameter estimation shown in Figure 2. `bob3-rho2` [ER]

Figure 5: The fitting error associated with the two parameter fitting shown in Figure 4. `bob3-resid2` [ER]



The methodology of this section assumed that the τ field was accurate. The non-linear nature means this assumption is problematic, particularly when we are far from the correct

solution. In the context of the moveout problem, this means we are far from flat the defacto starting guess.

LIMITING FLATTENING MODEL SPACE

The two-stage approach of the last section is only applicable when the τ estimation is able to fully describe the moveout in the gather. When it cannot, another approach must be found. The left panel of Figure 6 is a synthetic CMP gather created by bandpassing random numbers, and then spraying them out with adjoint of NMO. The right panel of Figure 6 shows the result of estimating time shifts (7 Gauss-Newton steps) and then applying those time shifts to flatten the data. Note that the flattening approach has failed in several areas.

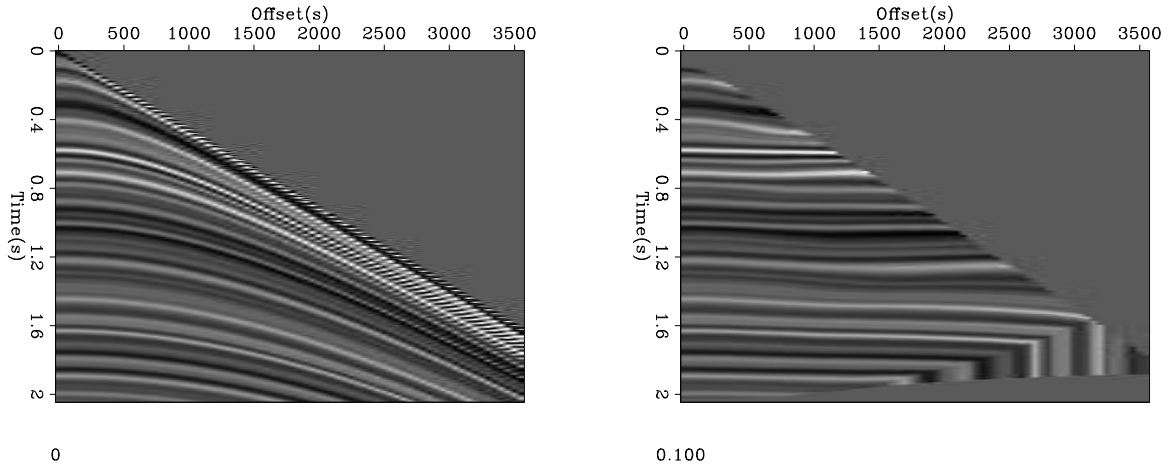


Figure 6: The left panel is a synthetic CMP gather. The right panel shows the result of flattening the CMP gather using the standard approach. Note the waviness of several reflectors due to the the non-linear nature of the flattening technique. bob3-syn [ER]

Estimation of the time shifts is problematic because the problem is inherently non-linear. One successful strategy is to try to start with an initial guess that is as close as possible to the correct solution. Another is to limit the model space to feasible candidates. In this simple case we know that the moveout is governed by the NMO equation. We can linearize the NMO equation that relates time shifts τ , zero offset time t_0 , offset h , and slowness s through

$$\tau = \sqrt{t_0^2 + h^2 s^2} - t_0 \quad (12)$$

around our initial slowness s_0 . We obtain an equation,

$$\Delta\tau = \frac{h^2 s_0}{\sqrt{t_0^2 + h^2 s_0^2}} h^2 s_0 \Delta s, \quad (13)$$

that relates $\Delta\tau$ to τs . The implied operator \mathbf{H} then helps to form the linearized optimization equation,

$$Q(\Delta s) = |\mathbf{W}_\epsilon \nabla \mathbf{H} \Delta s - \Delta \mathbf{p}|^2. \quad (14)$$

In practice we need to add an additional weighting operator \mathbf{W}_0 which accounts for areas effected wavelet stretch and for reflections that exist at zero offset, but not at larger offsets. As a result we must use a space-domain conjugate gradient scheme

$$Q(\Delta s) = |\mathbf{W}_0 \mathbf{W}_\epsilon \nabla \mathbf{H} \Delta s - \Delta \mathbf{p}|^2. \quad (15)$$

Figure 7 shows the flattened CMP gather using the slowness model space description. While not perfect, the result is significantly flatter than the alternative approach (right panel of Figure 6).

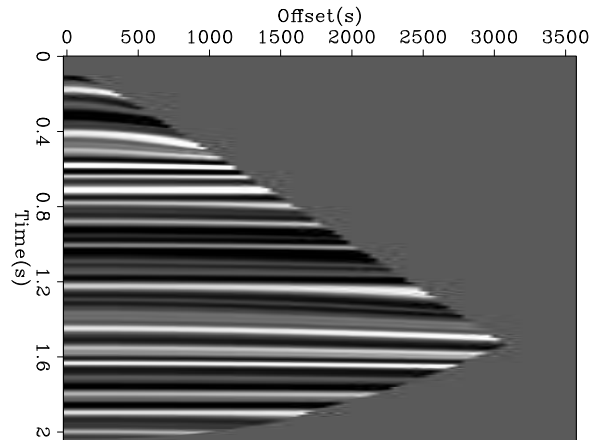


Figure 7: The flattened CMP gather using a Gauss-Newton scheme with the model space limited to hyperbolic moveout. The result is much flatter than the standard parameterization scheme show in the right panel of Figure 7. `bob3-cmp` [ER]

Figure 8 shows the result of applying both techniques to a CMP gather from the same North Sea dataset used in the previous section. The left panel is the raw gather, the center panel uses the conventional technique, and the right panel limits the moveout description to a single hyperbolic parameter. Note how both approaches fail at early times but the hyperbolic description provides noticeably better result.

CONCLUSIONS

Flattening is used to analyze moveout. Two different approaches are used. The first approach uses time shift information generated through flattening as the ‘data’ in inverting for one or more moveout parameters. The second approach directly relates dips to a moveout parameter. Both approaches show promise but additional work is needed.

ACKNOWLEDGMENTS

I would like to thank TotalFinaElf for providing the data used in this paper.

REFERENCES

Alvarez, G., 2006, Attenuation of 2d specularly-reflected multiples in image space: SEP-124.

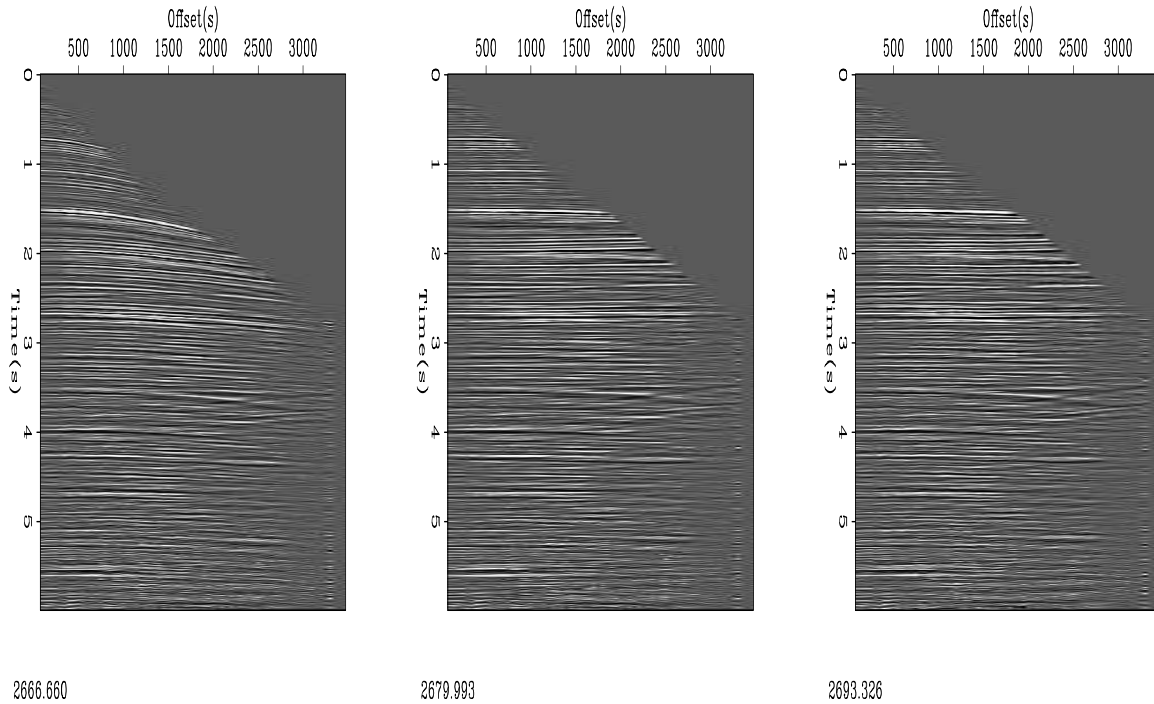


Figure 8: A CMP gather from the North Sea. The left panel shows the original gather. The center panel shows the result of using a standard parameterization for flattening. The right panel is the result using a hyperbolic parameterization. [bob3-elf] [ER]

Biondi, B. and W. Symes, 2003, Wavefield-continuation angle-domain common-image gathers for migration velocity analysis: SEG, 73rd Annual International Meeting., 2104–2107.

Clapp, R. G., P. Sava, and J. F. Claerbout, 1998, Interval velocity estimation with a null-space: SEP-97, 147–156.

Clapp, R. G., 2001, Geologically constrained migration velocity analysis: Ph.D. thesis, Stanford University.

Guitton, A. and W. W. Symes, 1999, Robust and stable velocity analysis using the Huber function: SEP-100, 293–314.

Guitton, A., J. Claerbout, and J. Lomask, 2004, First-order lateral interval velocity estimates without picking: SEP-115, 249–264.

Hampson, D., 1986, Inverse velocity stacking for multiple elimination: J. Can. Soc. Expl. Geophys., 22, no. 01, 44–55.

Harlan, W. S., 1998, A convenient approximation of transverse isotropy for higher-order moveout, prestack time migration, and depth calibration: <http://www.billharlan.com/pub/papers/aniso.pdf>.

Lomask, J. and J. Claerbout, 2002, Flattening without picking: SEP-112, 141–150.

- Lomask, J. and A. Guitton, 2006, Flattening with geological constraints: SEP-**124**.
- Lomask, J., 2003, Flattening 3-D data cubes in complex geology: SEP-**113**, 247–260.
- Lomask, J., 2006, Seismic volumetric flattening and segmentation: Ph.D. thesis, Stanford University.
- Lumley, D., D. Nichols, and T. Rekdal, 1994, Amplitude-preserved multiple suppression: SEP-**82**, 25–45.
- Symes, W. W. and J. J. Carazzone, 1991, Velocity inversion by differential semblance optimization: *Geophysics*, **56**, no. 5, 654–663.
- Toldi, J., 1985, Velocity analysis without picking: SEP-**43**.
- Wolf, K., D. Rosales, A. Guitton, and J. Claerbout, 2004, Robust moveout without velocity picking: SEP-**115**, 273–282.

Selective stacking in the reflection-angle and azimuth domain

Yaxun Tang

ABSTRACT

I analytically demonstrate the existence of artifacts in angle-domain common-image gathers (ADCIGs) caused by sparsely sampled wavefields from the perspective of shot-profile migration. The subsurface-offset domain common-image gather (SODCIG) is linearly related to the ADCIG in locally constant-velocity media when the wavefields are sufficiently well sampled, but not when the wavefields are poorly sampled. Hence, linear slant-stack or radial-trace transform in SODCIGs will produce ADCIGs with artifacts, which might hinder further interpretation or analysis and reduce the quality of the final stacking image. Instead of simply stacking along reflection angle and azimuth axes, I present a method to compute the stacking weights as functions of angle and azimuth and make the stacking process selective. My method is tested on the synthetic wide-azimuth version of the SEG/EAGE salt data set, where a cleaner image with higher signal-to-noise ratio is obtained.

INTRODUCTION

Seismic image quality is highly dependent on the acquisition geometry, or more specifically, on the illumination of the subsurface. Ideally, the best image is obtained when each subsurface image point is illuminated equally, which potentially requires a recording geometry both finely sampled and infinite in length. In the real world, however, we always have a limited recording geometry. For example, in the standard marine-streamer acquisition system, only narrow-azimuth data with limited offsets are acquired. Recent developments in multi-azimuth or wide-azimuth acquisition techniques (Michell et al., 2006; Keggin et al., 2006; Howard and Moldoveanu, 2006) provide a richer coverage in azimuth, and the subsurface can be better illuminated, especially in subsalt areas. Much better images are obtained because of improved subsurface illumination. Nevertheless, the reality can never meet the requirement for infinite recording geometry and infinitely dense sampling for shots and receivers. Illumination holes and aliasing may still happen in complex geologies. Poor illumination results in poor images, and related artifacts distort the migrated image, making it difficult to interpret. This effect is readily visible in the reflection-angle and azimuth domain, where illumination holes and related artifacts can be identified. They are by no means random or weak, and thus simple stacking can not attenuate them effectively.

In this paper, I briefly review methods for extracting subsurface-offset-domain common-image gathers (SODCIGs) and angle-domain common-image gathers (ADCIGs). I demon-

strate the effects of sparsely sampled wavefields on both SODCIGs and ADCIGs. I also demonstrate that the final image formed by simply stacking over the reflection-angle and azimuth axes without any weighting function suffers from artifacts caused by the poor illumination and has a low signal-to-noise ratio. Instead, I describe a simple but effective way to make the stacking process selective: we stack only those reflection angles and azimuths with good illumination. This method is tested on the wide-azimuth version of the SEG/EAGE salt data set, and a better image with higher signal-to-noise ratio is obtained.

EXTRACTING ANGLE-DOMAIN COMMON-IMAGE GATHERS

ADCIGs can be extracted either before applying an imaging condition (Prucha and Symes, 1999; Mosher and Foster, 2000; Xie and Wu, 2002; Soubaras, 2003) or afterward (Sava and Fomel, 2003; Biondi and Symes, 2004). The advantage of extracting the angle gathers after the imaging step is that it is a model-space processing, which offers more versatility and generally more efficiency. The same transformation can be used for images produced by source-receiver migration (Sava and Fomel, 2003), shot-profile migration (Rickett and Sava, 2002) and reverse time migration (Biondi and Shan, 2002).

There are basically two steps to extract the angle gathers after imaging: First, compute the SODCIGs. Second, transform the SODCIGs into ADCIGs. For source-receiver migration, the SODCIGs are immediately available after downward continuation of the wavefields; for shot-profile migration, a multi-offset imaging condition should be applied to get the SODCIGs (Rickett and Sava, 2002):

$$I(x, y, h_x, h_y) = \sum_{\omega} D^*(x - h_x, y - h_y, \omega) U(x + h_x, y + h_y, \omega), \quad (1)$$

where I is the image in the subsurface-offset domain, D is the source wavefield, $*$ means the complex conjugate, U is the receiver wavefield, x, y are the components of midpoint, h_x, h_y are the components of subsurface half offset, and ω is frequency. Sava and Fomel (2003) derived the following radial-trace transformation in the Fourier domain to transform the SODCIGs into ADCIGs in 2-D:

$$\tan \gamma = -\frac{k_{h_x}}{k_z} = -\frac{\partial z}{\partial h_x}, \quad (2)$$

where γ is the reflection angle, k_{h_x} is the offset wavenumber, and k_z is the depth wavenumber. The transformation is independent of geological dip in 2-D, but the 3-D formulation must be corrected for a crossline dip component. Tisserant and Biondi (2003) show that we can make this 3-D correction by re-writing the angle-gather transformation as

$$\tan \gamma = -\frac{|\mathbf{k}_h|}{k_z} \frac{1}{\sqrt{1 + \left(\frac{k_{m_x}}{k_z} \sin \beta + \frac{k_{m_y}}{k_z} \cos \beta \right)^2}}, \quad (3)$$

where β is the reflection azimuth, $|\mathbf{k}_h|$ is the absolute value of the offset wavenumber, k_{m_x} and k_{m_y} are the components of the midpoint wavenumber.

ARTIFACTS CAUSED BY SPARSELY SAMPLED WAVEFIELDS

As demonstrated in Rickett and Sava (2002), ADCIGs suffer from poor sampling of the source or receiver wavefield. This effect is not very obvious from the derivation in Sava and Fomel (2003); it is, however, more evident from the perspective of shot-profile migration. Appendix A analytically demonstrates that in locally constant-velocity media, when the receiver wavefield is densely sampled, the circular wavefronts of the downward continued receiver wavefields can be well reconstructed; hence the multi-offset imaging condition in equation (1) produces a linear relationship between subsurface half offset h_x and depth z for a specific CMP location x as follows:

$$z = -\tan \alpha x - \tan \gamma h_x, \quad (4)$$

where α is the geological dip and γ is the reflection angle. If we take the derivative of z with respect to h_x , we get

$$\tan \gamma = -\frac{\partial z}{\partial h_x} = -\frac{k_{h_x}}{k_z}, \quad (5)$$

which is exactly the same as equation (2). In other words, for well-sampled receiver wavefields, one shot will generate SODCIGs with a straight line. The slope of that line in local-offset domain is the tangent of the reflection angle γ . Hence, radial-trace or slant-stack transform in the subsurface-offset domain will produce artifact-free angle gathers, and a straight line in SODCIGs would be strictly mapped to a single point in the ADCIGs.

Let us consider the extreme case for poor sampling, where we have only one receiver. As demonstrated in Appendix B, when we have only one shot and one receiver, the multi-offset imaging condition in equation (1) no longer produces a linear relationship between subsurface half offset h_x and depth z . Instead z and h_x are non-linearly related as follows:

$$z^2 = -h_x^2 + (r-s)h_x + \frac{(r-s)^2}{[\tan(-\gamma-\alpha) + \tan(-\gamma+\alpha)]^2}, \quad (6)$$

where s and r are the source location and receiver location respectively, and α is the geological dip. In such situations, the linear transformation from subsurface-offset domain to angle domain will definitely produce unwanted artifacts. Note that though here I limit my discussion to the effect in ADCIGs caused by poorly sampled receiver wavefields, reciprocity implies that the same should be true for poorly sampled source wavefields.

For example, Figure 1 shows a synthetic shot gather for a flat reflector at $z = 2000$ meters, with a constant velocity $v = 4000$ m/s. The shot is located at $x = -1000$ meters. For an image point at $x = 0$ meter, $z = 2000$ meters, the reflection angle should be $\gamma = \arctan(1000/2000) = 26.6^\circ$. Figure 2(a) shows the migrated image obtained by using all the receivers shown in Figure 1. Figure 3(a) shows the SODCIG for surface location $x = 0$ meter; it shows a perfectly straight line intersecting at $(0, 2000)$ in the subsurface-offset domain (h_x, z) . Figure 4(a) shows the ADCIG obtained by slant-stacking the corresponding SODCIGs in Figure 3(a). This result also shows a point located at about 26.6° , which matches the theoretical result well. Figure

2(b), in contrast, shows the migration result obtained by using only one receiver located at $x = 1000$ meters. The image is an ellipse, which is basically a prestack impulse response. The SODCIG at $x = 0$ meter is shown in Figure 3(b), and as predicted by equation (6), it is a circle instead of a straight line in the subsurface-offset domain. The corresponding ADCIG is shown in Figure 4(b). Instead of a nicely focused point at 26.6° , we can identify a downward-frowning curve.

Figure 1: Synthetic shot gather for a flat reflector where the shot is located at $x = -1000$ meters. The modeling is done using finite difference.

`yaxun1-flat.shot` [CR]

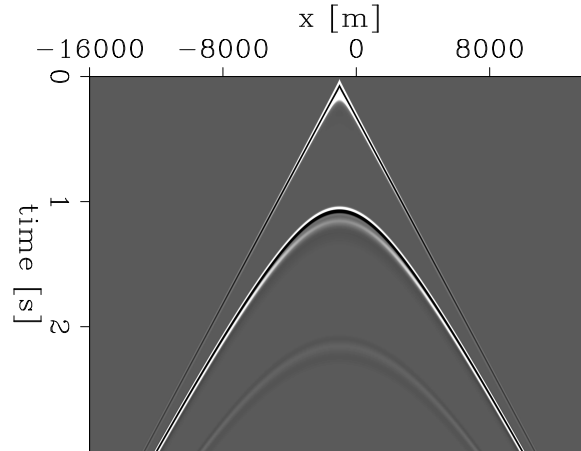
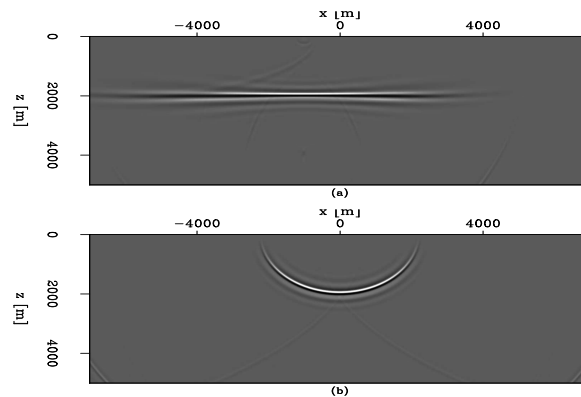


Figure 2: Migration results for only one shot. Panel (a) shows the migrated image for all the receivers shown in Figure 1, while (b) shows the migrated image for only one receiver located at $x = 1000$ meters.

`yaxun1-flat.img` [CR]



SELECTIVE STACKING BASED ON LOCAL SMOOTHING OF THE ENVELOPE FUNCTION

The downward-frowning artifacts observed in the previous section have a great influence on seismic angle-domain processing. They can distort the final image when we stack over the angle and azimuth axes, generating fake reflectors that can lead to misinterpretation. They can also affect the accuracy of residual-moveout-based velocity analysis, since with those frowning curves, it is difficult to predict the residual moveout accurately. There are four possible methods to get rid of those artifacts in angle gathers:

1. Define a non-linear transformation in the subsurface-offset domain to get an artifact-free angle gather.

Figure 3: SODCIGs at $x = 0$ meter for different results. (a) SODCIG extracted from the result in Figure 2(a), where a straight line is obtained, since the receiver wavefield is well sampled. (b) SODCIG extracted from the result in Figure 2(b), where a circle instead of a straight line is obtained, since the wavefield is extremely poorly sampled. `yaxun1-flat.sodcig` [CR]

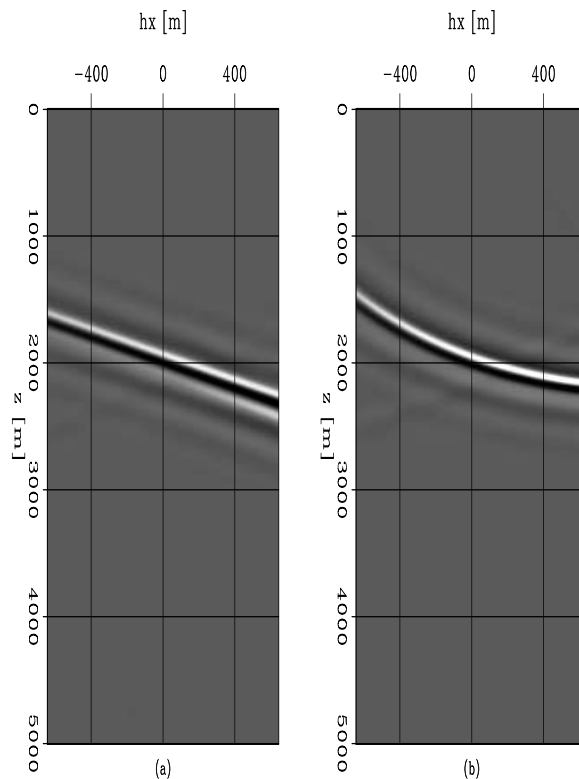
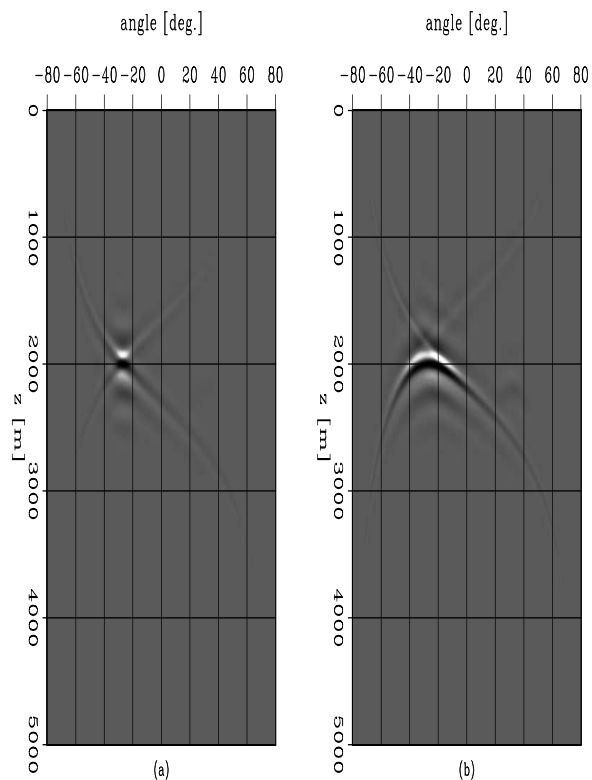


Figure 4: ADCIGs at $x = 0$ for different results. (a) ADCIG computed from Figure 3(a), where a nicely focused point at 26.6° is obtained, because the local offset gather in 3(a) is linear. (b) ADCIG computed from Figure 3(b), where a downward-frowning curve instead of a point is obtained, because the local offset gather in 3(b) is non-linear. `yaxun1-flat.adcig` [CR]



2. Densely interpolate the data before migration. This data-space interpolation is very helpful if the velocity structure is simple, but helps little when the velocity structure is complex.
3. Apply image-space interpolation. By assuming that reflectivities are changing smoothly along angles and azimuths and that any abrupt changes in amplitudes are caused by poor illumination or poor sampling, we can run least-squares inversion with regularization in the angle domain by smoothing along angles and azimuths to attenuate those artifacts (Prucha et al., 2000). Or equivalently, we can run least-squares inversion with differential-semblance regularization in the subsurface-offset domain (Valenciano, 2006; Tang, 2006). Both these methods are effective but computationally demanding.
4. Apply selective stacking by designing filters or weighting functions that ignore those artifacts, stacking only angles and azimuths with good illumination and dense sampling.

In this paper, I will concentrate mainly on the fourth method and describe a simple but effective way to design the weighting functions. As we know, when migrating with the correct migration velocity and with densely sampled and infinite recording geometry, the events in ADCIGs are aligned horizontally. In 2-D there are horizontal lines in the angle domain; in 3-D there are flat planes in the angle and azimuth domain, because with infinite acquisition geometry, all angles and azimuths should be illuminated. When we don't have densely sampled and infinite recording geometry, there are holes in the line in the 2-D case or holes in the plane in the 3-D case. The shape of holes can be fairly irregular, depending on the recording geometry and the geological structure of the subsurface. The goal of the method is to attenuate the artifacts and enhance the signal-to-noise ratio of the final image by stacking only those angles and azimuths that are well illuminated. I first compute the envelope of the 3-D angle gather, then apply 3-D local smoothing based on equation (7) to the computed envelope to get the weighting function,

$$W(z, \gamma, \beta) = \frac{1}{2L+1} \sum_{j=-L}^L s(j) E(z + j \Delta z, \gamma + j \Delta \gamma, \theta + j \Delta \beta), \quad (7)$$

where W is the weighting function for a particular CMP location. It is a function of depth z , reflection angle γ and reflection azimuth β . E is the envelope function, which can be computed via Hilbert transform. L is the half length of the moving window, and $s(j)$ determines the shape of the smoothing operator. In this paper I use a 3-D local boxcar smoothing operator, so $s(j) = 1$. A more sophisticated smoothing operator, such as a 3-D local Gaussian smoothing operator, could also be applied.

3-D SEG/EAGE SALT MODEL EXAMPLE

I tested the method discussed above on the 3-D wide-azimuth version of the SEG/EAGE salt data set. The wide-azimuth synthetic data was created by Sandia National Laboratory, it has 45 shots in total, with a shot interval of about 960 meters in both the inline and crossline directions. As can be seen in the plot of the shot layout in Figure 5, most of the shots are regularly

spaced, but some are not. The receiver geometry is a patching geometry, with minimum offset of about -2000 meters and maximum offset of about 2000 meters in both the inline and crossline directions. The plot of azimuth versus absolute offset is shown in Figure 6, which illustrates a fairly wide coverage of azimuth.

Figure 5: Shot layout. The horizontal axis is inline x , while the vertical axis is crossline y . Note most of the shots are regularly spaced, but several of them are not.

`yaxun1-segsalt.shot.layout` [CR]

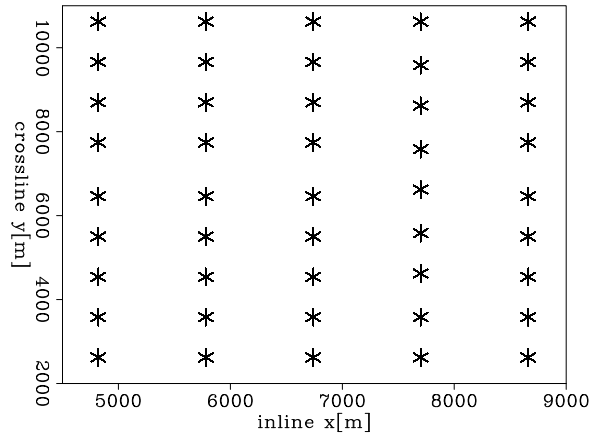
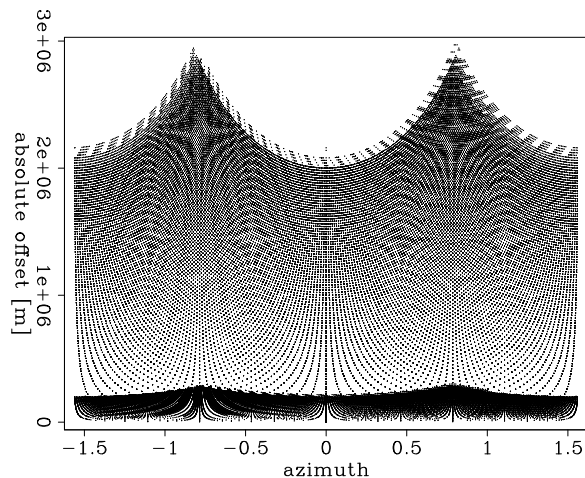


Figure 6: Azimuth vs. absolute offset plot. The horizontal axis is azimuth ranging from -1.5 to 1.5. The vertical axis is absolute offset [m] ranging from 0 to $3e+06$. The plot shows a dense, complex pattern of lines representing the relationship between azimuth and absolute offset for the shot layout.

`yaxun1-segsalt.off.azi` [CR]



The migrated image obtained by using shot-profile migration for all 45 shots is shown in Figure 7. Since there are only 45 shots and they are sparsely distributed, the SODCIGs and ADCIGs should have significant sampling induced artifacts. To save disk space and computation cost, the SODCIGs are not computed for all the image points in the model space; instead, the output image coordinate is restricted to within $[6580, 8480]$ for the inline direction and $[8460, 9920]$ for the crossline direction. I computed 25 half-offsets for both the inline and crossline directions and the spacing of half-local-offset equals 40 meters, twice as much as the receiver spacing, which is 20 meters. Hence the half-subsurface-offset ranges from -480 meters to 480 meters in both the inline and crossline directions.

Figure 8 shows the migrated image for the particular image size described above. The crosshairs indicate two different surface locations for the output SODCIGs, which are shown in Figure 9. From Figure 9 we can see that since the correct migration velocity is used, there is some focusing of energy at zero offset. However, the energy is not well focused because there

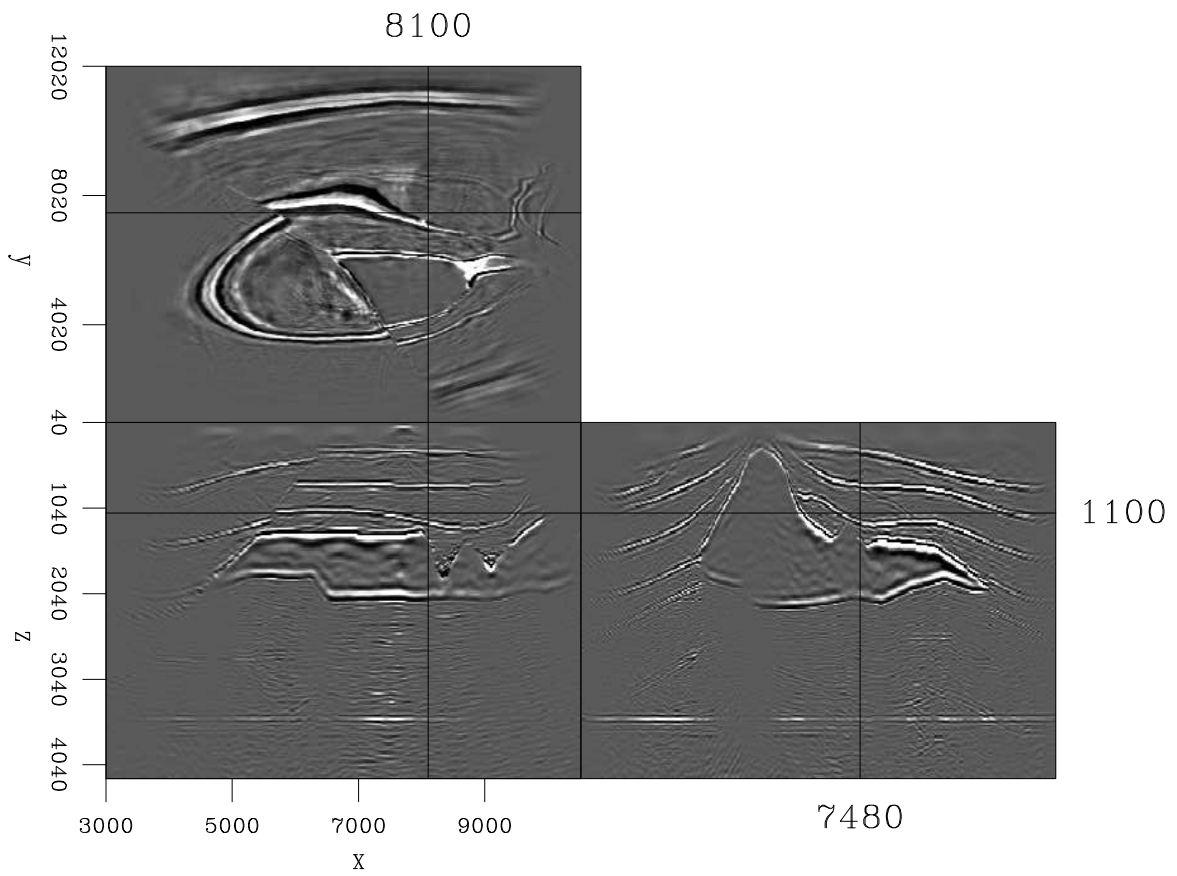


Figure 7: Shot-profile migration result of all 45 shots. `yaxun1-segsalt.img` [CR]

are only 45 shots, and thus at most 45 planes intersecting at zero-offset location, which are not sufficient to cancel the energy at non-zero offsets.

Since the sources are extremely sparsely located, and the receiver coverage is limited for each shot, we can identify some curved events in the SODCIGs in Figure 9. For the events above the salt, the curvatures are not very obvious, because the velocity model above the salt is relatively simple; however, we can still see that some of the events are bending at far offsets. For events that are below the salt, the curvatures are more obvious, because with the complex salt body and limited recording geometry, it is impossible to have the receiver wavefield well sampled.

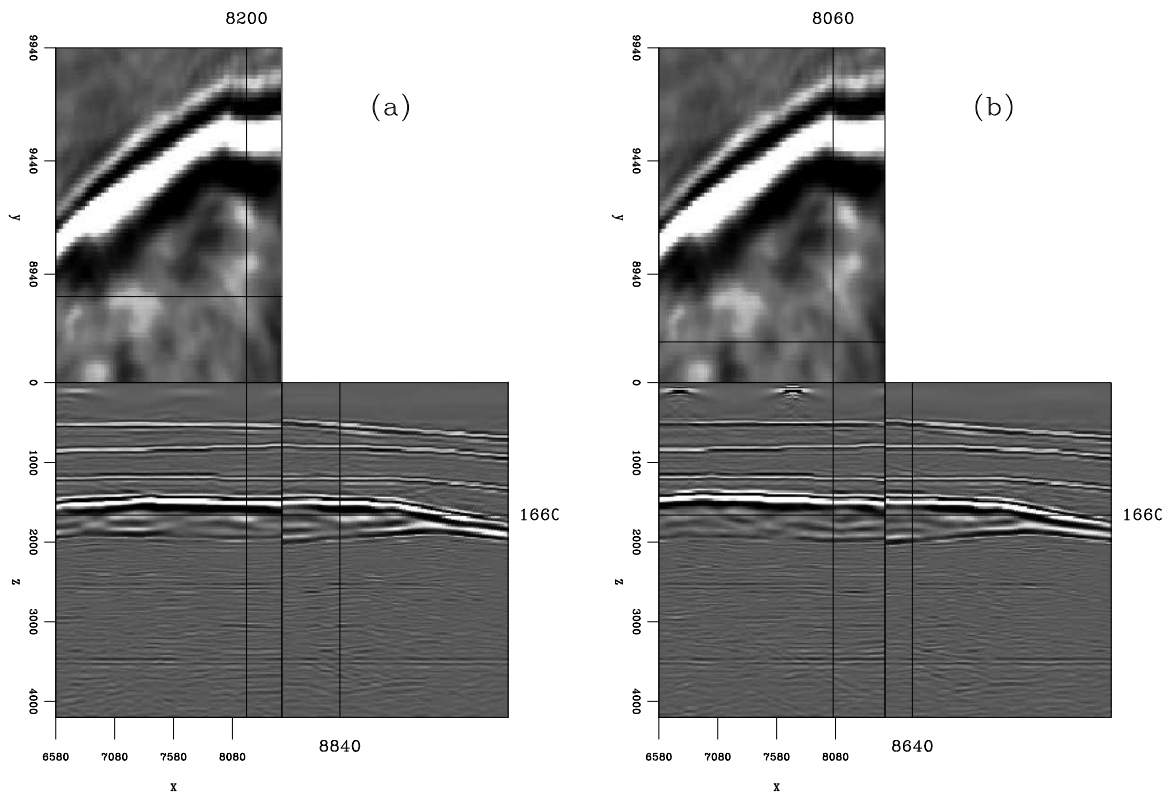


Figure 8: Migration result for the particular iamge size discribed in the text. The crosshairs indicate two different surface locations for output SODCIGs shown in Figure 9. (a) indicates the surface location at (8200,8840); while (b) indicates the surface location at (8060,8640).

`yaxun1-segsalt.off.loc` [CR]

SODCIGs are transformed into 3-D ADCIGs by using equation (3). The corresponding ADCIGs are shown in Figure 10. The computed azimuth range is from 0 to 180 degrees with a spacing of 5 degrees. Note the blobs in the depth slices in both (a) and (b), which are closely related to the shot locations.

As demonstrated in the previous section, linear transformation from SODCIGs to ADCIGs is prone to artifacts when the source or receiver wavefield is poorly sampled (sparsely distributed shot locations or receiver locations). Another possible reason for artifacts is large

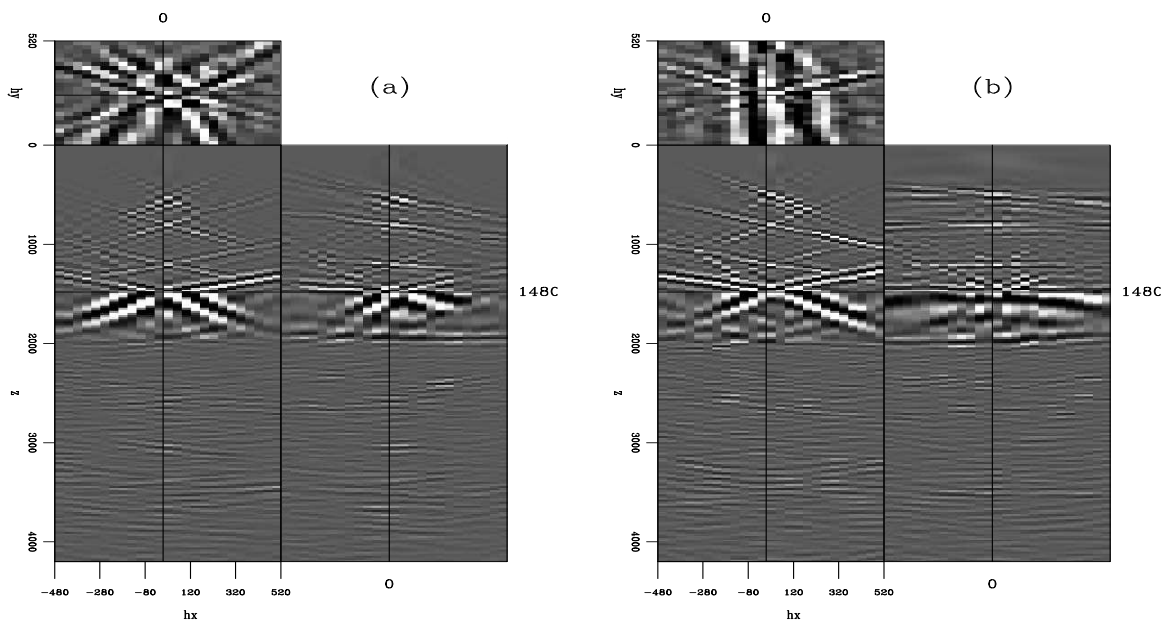


Figure 9: SODCIGs for two different surface locations shown in Figure 8. The left is the SODCIG extracted at (8200, 8840), while the right is the SODCIG extracted at (8060, 8640). The vertical axis in both figures is depth, the inline axis is h_x , and the crossline axis is h_y . `yaxun1-segsalt.off` [CR]

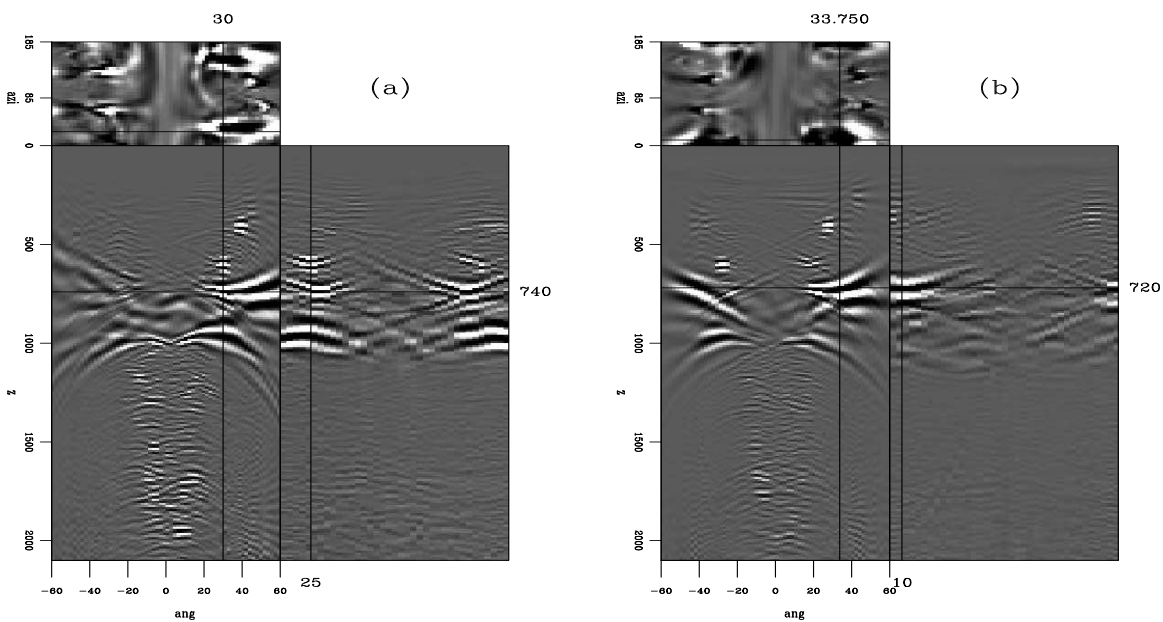


Figure 10: ADCIGs for two different surface locations shown in Figure 8. The left is the ADCIG extracted at (8200, 8840), while the right is the SODCIG extracted at (8060, 8640). The vertical axis in both figures is depth, the inline axis is reflection angle, and the crossline axis is reflection azimuth. `yaxun1-segsalt.ang` [CR]

velocity contrast in the vicinity of the image point, since the equations for subsurface-offset-to-angle transformation are valid only in media with locally constant velocity. Artifacts can be easily identified in ADCIGs for SEG/EAGE salt model as shown in Figure 10. We can find smeared energy (tails) in both near angles and far angles, especially in the top salt and base salt areas, where the velocity contrast is high, and in the subsalt area, where the wavefields are poorly sampled.

To form the final image cube, we have to stack the ADCIGs along both the reflection-angle and reflection-azimuth axes. As the transformation artifacts are not random, simple stacking without any weighting function might produce images with low signal-to-noise ratios, making interpretation difficult. The simply stacked image, shown in Figure 13(c), is quite noisy, especially in the subsalt. It is definitely difficult to interpret.

Instead of simply stacking along the angle and azimuth axes, we can apply weighting functions which attenuate unwanted artifacts to make the stacking process selective. The weighting functions are computed by using equation (7). Figure 11(b) shows the weighting function for the image point at (8200, 8840), while Figure 12 shows the weighting function for the image point at (8060, 8640). We can see that horizontally incoherent energy at near and far angles receives low weights, while horizontally coherent energy, where the actual reflection is located, receives high weights. Figure 11(c) and Figure 12(c) show the filtered results, in which the artifacts are greatly suppressed.

The weighting functions are computed for every image point and applied to the original ADCIGs, then the filtered ADCIGs are stacked together to form the final image. Figure 13(d) shows the result of using this kind of selective stacking. For comparison, Figure 13(a) shows the corresponding velocity model, Figure 13(b) shows the zero-offset image extracted from the SODCIG cube with $h_x = 0$ and $h_y = 0$, and Figure 13(c) shows the image obtained by simply stacking the ADCIGs without any weighting functions. It is quite obvious that the image in Figure 13(d), obtained by using selective stacking, has the highest signal-to-noise ratio and it is the cleanest among the three. Also notice the migration artifacts at the bottom of the image, which can be easily identified in Figures 13(b) and (c), but are greatly attenuated in Figure 13(d). The dipping reflector under the salt on the side panel, which is nearly invisible in Figure 13(b) and noisy in Figure 13(c), is clearly visible in Figure 13(d).

CONCLUSION AND DISCUSSION

I analytically demonstrated that when source or receiver wavefields are poorly sampled, subsurface-offset gathers are no longer linearly related to angle gathers. Slant-stack or radial-trace transform is prone to artifacts in such situations. This often happens when the underground velocity structure is very complex, since in complex geologies with limited recording geometries, it is difficult to have wavefields well sampled. To eliminate those artifacts, I presented a selective-stacking approach based on local smoothing of the envelope function. My test on the complex SEG/EAGE salt data set shows that by selectively stacking in the reflection angle and azimuth domain, a cleaner image with higher signal-to-noise ratio and less migration artifacts can be obtained.

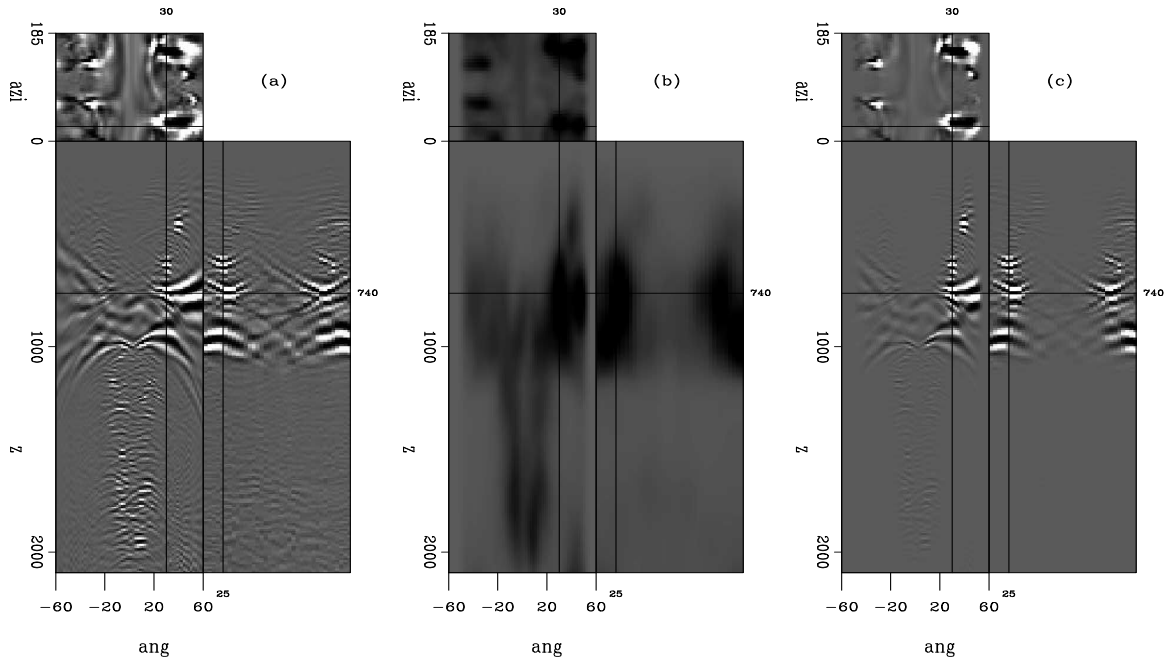


Figure 11: Filtering result for ADCIG at (8200, 8840). Panel (a) shows the original ADCIG, (b) is the computed weighting function via local smoothing of the envelope function, where dark color stands for high weight and light color stands for low weight. Panel (c) is (a) multiplied with (b), i.e. the filtered ADCIG. `yaxun1-segsalt.ang-2.filt` [CR]

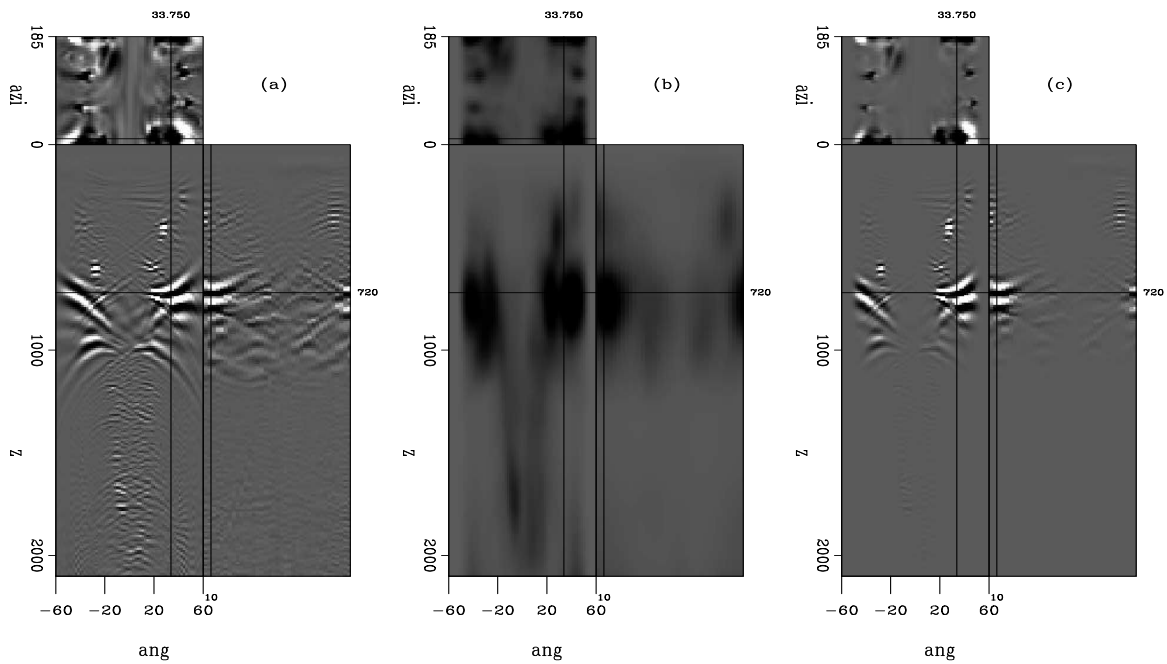


Figure 12: Filtering result for ADCIG at (8060, 8640). Panel (a) shows the original ADCIG, (b) is the computed weighting function via local smoothing of the envelope function, where dark color stands for high weight and light color stands for low weight. Panel (c) is (a) multiplied with (b), i.e. the filtered ADCIG. `yaxun1-segsalt.ang-3.filt` [CR]

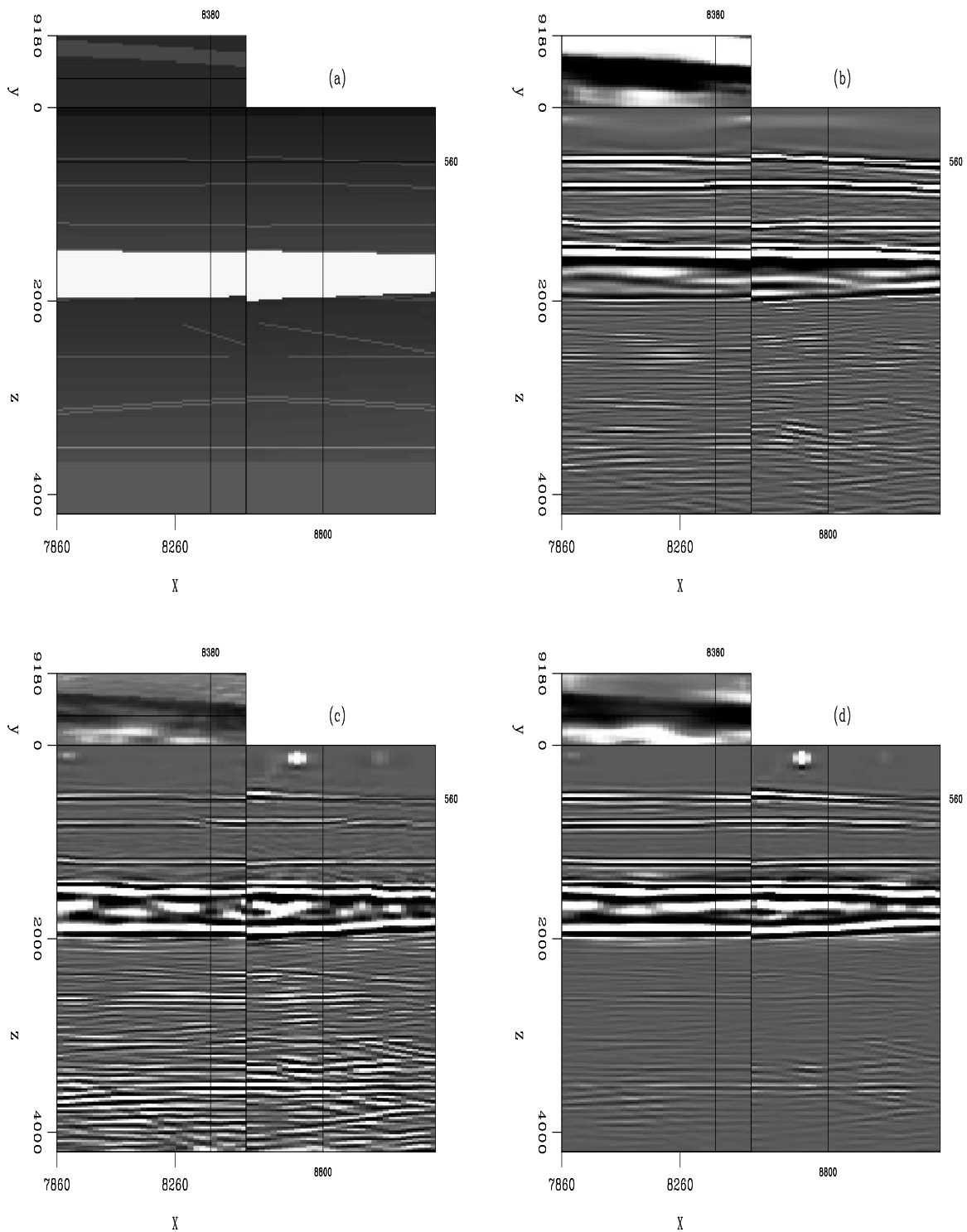


Figure 13: Comparison for different results. Panel (a) is the corresponding velocity model; (b) is the zero-offset image extracted from the SODCIG cube with $h_x = 0$ and $h_y = 0$; (c) is the result obtained by simple stacking without any weighting function; and (d) is the result obtained by selective stacking, with the weighting function computed by locally smoothing the envelope function of the ADCIGs. `yaxun1-segsalt.stack` [CR]

Though the method discussed in this paper is effective, it is purely based on signal processing. If the artifacts in the ADCIGs are coherent and strong, this signal-processing approach may not work well, because it tends to heavily weight strong energy. Instead, we can use the illumination of the subsurface as a reference for designing the weighting functions. The illumination can be measured in the least-square sense by computing the Hessian matrix. As illustrated in Valenciano and Biondi (2004), the Hessian is diagonal-dominated in well-illuminated areas, but the energy smears in areas that are not well illuminated, resulting in strong off-diagonal components. Therefore, the focus of energy in the diagonal of the Hessian can be a measure of illumination of the subsurface. We can further transform the Hessian into the reflection angle and azimuth domain, where well-illuminated reflection angles and azimuths will receive high energy, while poorly illuminated angles and azimuths will receive low energy. Therefore, we could design weighting functions based on the diagonal of the Hessian to attenuate unwanted artifacts and selectively stack those well-illuminated angles and azimuths to get a high-quality image. This methodology will be a future research topic.

ACKNOWLEDGMENTS

I would like to thank Guojian Shan for many insightful discussions on the derivation of the equations in Appendices A and B. I also would like to thank Brad Artman for providing the shot-profile migration code for migrating the SEG/EAGE salt model and Biondo Biondi for providing the code for extracting 3-D angle gathers.

REFERENCES

- Biondi, B. and G. Shan, 2002, Prestack imaging of overturned reflections by reverse time migration: 72nd Ann. Internat. Mtg., Soc. of Expl. Geophys., Expanded Abstracts, 1284–1287.
- Biondi, B. and W. Symes, 2004, Angle-domain common-image gathers for migration velocity analysis by wavefield-continuation imaging: *Geophysics*, **69**, 1283–1298.
- Howard, M. S. and N. Moldoveanu, 2006, Marine survey design for rich-azimuth seismic using surface streamers: 76rd Ann. Internat. Mtg., Soc. of Expl. Geophys., Expanded Abstracts, 2915–2919.
- Keggin, J., T. Manning, et al., 2006, Key aspects of multi-azimuth acquisition and processing: 76rd Ann. Internat. Mtg., Soc. of Expl. Geophys., Expanded Abstracts, 2886–2890.
- Michell, S., E. Shoshitaishvili, et al., 2006, Wide azimuth streamer imaging of mad dog: Have we solved the subsalt imaging problem?: 76rd Ann. Internat. Mtg., Soc. of Expl. Geophys., Expanded Abstracts, 2905–2909.
- Mosher, C. and D. Foster, 2000, Common angle imaging conditions for prestack depth migration: 70th Ann. Internat. Mtg., Soc. of Expl. Geophys., Expanded Abstracts, 830–833.

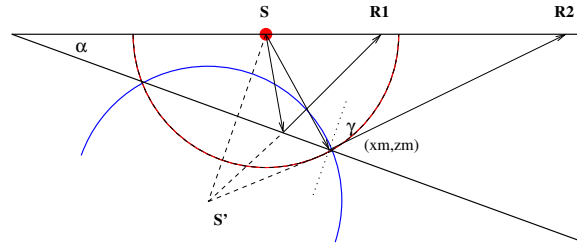
- Prucha, B. B., M. and W. Symes, 1999, Angle-domain common image gathers by wave-equation migration: 69th Ann. Internat. Mtg., Soc. of Expl. Geophys., Expanded Abstracts, 824–827.
- Prucha, M. L., R. G. Clapp, and B. Biondi, 2000, Seismic image regularization in the reflection angle domain: **SEP-103**, 109–119.
- Rickett, J. E. and P. C. Sava, 2002, Offset and angle-domain common image-point gathers for shot-profile migration: *Geophysics*, **67**, 883–889.
- Sava, P. C. and S. Fomel, 2003, Angle-domain common-image gathers by wavefield continuation methods: *Geophysics*, **68**, 1065–1074.
- Soubaras, R., 2003, Angle gathers for shot-record migration by local harmonic decomposition: 73rd Ann. Internat. Mtg., Soc. of Expl. Geophys., Expanded Abstracts, 889–892.
- Tang, Y., 2006, Least-squares migration of incomplete data sets with regularization in the subsurface-offset domain: **SEP-125**, 159–174.
- Tisserant, T. and B. Biondi, 2003, Wavefield-continuation angle-domain common-image gathers in 3-D: **SEP-113**, 211–220.
- Valenciano, A. A. and B. Biondi, 2004, Target-oriented computation of the wave-equation imaging Hessian: **SEP-117**, 63–76.
- Valenciano, A. A., 2006, Target-oriented wave-equation inversion with regularization in the subsurface offset domain: **SEP-124**.
- Xie, X. and R. Wu, 2002, Extracting angle domain information from migrated wavefield: 72nd Ann. Internat. Mtg., Soc. of Expl. Geophys., Expanded Abstracts, 1360–1363.

APPENDIX A

This appendix analytically derives SODCIGs for one shot and well-sampled receiver wavefields in locally constant-velocity media. Let's consider the SODCIG for a dipping reflector at image point (x_m, z_m) , as shown in Figure (A-1). The dipping angle is $-\alpha$, while the reflection angle at (x_m, z_m) is $-\gamma$ (assuming positive sign for angles measured in a clockwise direction). The red circle shows the source wavefront at some time t , which intersects the dipping reflector at (x_m, z_m) . If we put receivers for every location on the surface, i.e. the receiver wavefield is sufficiently densely sampled, when we downward continue or backward propagate the receiver wavefield, the circular wavefront, which is in blue, can be well reconstructed. It also intersects the dipping reflector at (x_m, z_m) at the same time t . Therefore, cross-correlation of the source wavefield and receiver wavefield will generate the image at (x_m, z_m) .

Figure A-1: When the receiver wavefield is sufficiently densely sampled, the actual circular wavefront in blue can be well reconstructed.

`yaxun1-dip.full.rec` [NR]



The equation for the source wavefront in red is

$$(x - s)^2 + z^2 = \left[\frac{(x_m - s)}{\sin(-\gamma + \alpha)} \right]^2, \quad (\text{A-1})$$

while the equation for the receiver wavefront in blue is

$$[x - s \cos(-2\alpha)]^2 + [z - s \sin(-2\alpha)]^2 = \left[\frac{(x_m - s)}{\sin(-\gamma + \alpha)} \right]^2. \quad (\text{A-2})$$

To get the local offset gather at x_m , we have to apply the multi-offset imaging condition described in equation (1) as follows, where h is the subsurface half-offset.

$$\begin{cases} (x - h - s)^2 + z^2 = \left[\frac{(x_m - s)}{\sin(-\gamma + \alpha)} \right]^2 \\ [x + h - s \cos(-2\alpha)]^2 + [z - s \sin(-2\alpha)]^2 = \left[\frac{(x_m - s)}{\sin(-\gamma + \alpha)} \right]^2 \end{cases} \quad (\text{A-3})$$

Therefore, by letting $x = x_m$ and subtracting the second equation from the first equation, we get

$$(x_m - h - s)^2 + z^2 = [x_m + h - s \cos(-2\alpha)]^2 + [z - s \sin(-2\alpha)]^2. \quad (\text{A-4})$$

After some algebra, we get

$$[2x_m - s(1 + \cos(-2\alpha))] [s(\cos(-2\alpha) - 1) - 2h] + (2z - s \sin(-2\alpha))s \sin(-2\alpha) = 0. \quad (\text{A-5})$$

Rearranging the above equation:

$$z = \frac{x_m s \sin^2(-\alpha) + x_m h - h s \cos^2(-\alpha)}{s \cos(-\alpha) \sin(-\alpha)} \quad (\text{A-6})$$

$$= \tan(-\alpha)x_m + \frac{x_m - s \cos^2(-\alpha)}{s \cos(-\alpha) \sin(-\alpha)}h \quad (\text{A-7})$$

$$= -\tan\alpha x_m + \frac{\frac{x_m}{s} - \cos^2(-\alpha)}{\cos(-\alpha) \sin(-\alpha)}h. \quad (\text{A-8})$$

From Figure (A-1), point (x_m, z_m) on the dipping reflector satisfies:

$$\tan(-\gamma + \alpha) = \frac{x_m - s}{z_m} \quad (\text{A-9})$$

$$\tan(-\alpha) = \frac{z_m}{x_m}. \quad (\text{A-10})$$

Multiplying them together yields

$$\tan(-\alpha)\tan(-\gamma + \alpha) = \frac{x_m - s}{x_m} = \frac{\frac{x_m}{s} - 1}{\frac{x_m}{s}}, \quad (\text{A-11})$$

so

$$\frac{x_m}{s} = \frac{1}{1 - \tan(-\alpha)\tan(-\gamma + \alpha)}. \quad (\text{A-12})$$

Substituting equation(A-12) into equation (A-8), we get:

$$z = -\tan\alpha x_m + \frac{\frac{x_m}{s} - \cos^2(-\alpha)}{\cos(-\alpha) \sin(-\alpha)}h \quad (\text{A-13})$$

$$= -\tan\alpha x_m + \frac{1}{1 - \tan(-\alpha)\tan(-\gamma + \alpha)} \frac{\cos^2(-\alpha)}{\cos(-\alpha) \sin(-\alpha)}h \quad (\text{A-14})$$

$$= -\tan\alpha x_m + \frac{1 - \cos^2(-\alpha)[1 - \tan(-\alpha)\tan(-\gamma + \alpha)]}{[1 - \tan(-\alpha)\tan(-\gamma + \alpha)] \cos(-\alpha) \sin(-\alpha)}h \quad (\text{A-15})$$

$$= -\tan\alpha x_m + \frac{\sin^2(-\alpha) + \sin(-\alpha)\cos(-\alpha)\tan(-\gamma + \alpha)}{\sin(-\alpha)\cos(-\alpha) - \sin^2(-\alpha)\tan(-\gamma + \alpha)}h \quad (\text{A-16})$$

$$= -\tan\alpha x_m + \frac{\sin(-\alpha) + \cos(-\alpha)\tan(-\gamma + \alpha)}{\cos(-\alpha) - \sin(-\alpha)\tan(-\gamma + \alpha)}h \quad (\text{A-17})$$

$$= -\tan\alpha x_m + \frac{\tan(-\alpha) + \tan(-\gamma + \alpha)}{1 - \tan(-\alpha)\tan(-\gamma + \alpha)}h \quad (\text{A-18})$$

$$= -\tan\alpha x_m + \tan(-\alpha - \gamma + \alpha)h \quad (\text{A-19})$$

$$= -\tan\alpha x_m - \tan\gamma h. \quad (\text{A-20})$$

Actually the above equation is true for each point (x, z) with dipping angle α and opening angle γ , so it can be rewritten as follows:

$$z = -\tan\alpha x - \tan\gamma h. \quad (\text{A-21})$$

Therefore, when the receiver wavefield is sufficiently densely sampled, the SODCIG is linearly related to the angle gather.

APPENDIX B

This appendix analytically derives SODCIGs for one shot and one receiver in locally constant-velocity media. Let's again consider a dipping reflector with the dip angle α , as shown in Figure B-1. The source is located at $(s, 0)$, while receiver is located at $(r, 0)$. Since there is only one receiver, when we downward continue or backward propagate the receiver wavefield, the receiver wavefront that intersects (x_m, z_m) is the green one shown in Figure B-1 instead of the blue one shown in Figure A-1.

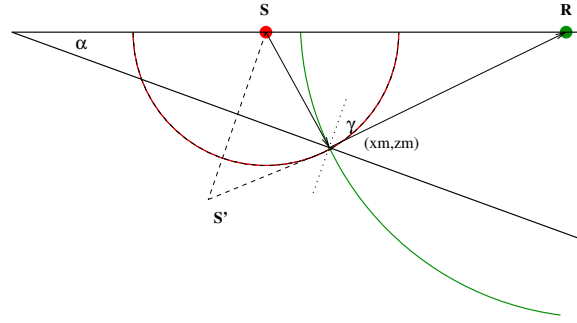


Figure B-1: In the extreme situation where there is only one receiver, the receiver wavefront is the one shown here in green, instead of the blue one shown in Figure A-1.

`yaxun1-dip.one.rec` [NR]

The image point at (x_m, z_m) on the dipping reflector certainly satisfies:

$$\tan(-\gamma + \alpha) = \frac{x_m - s}{z_m} \quad (\text{B-1})$$

$$\tan(-\gamma - \alpha) = \frac{r - x_m}{z_m}. \quad (\text{B-2})$$

Thus, we have:

$$z_m = \frac{x_m - s}{\tan(-\gamma + \alpha)} = \frac{r - x_m}{\tan(-\gamma - \alpha)}, \quad (\text{B-3})$$

which rearranges to

$$x_m = \frac{s \tan(-\gamma - \alpha) + r \tan(-\gamma + \alpha)}{\tan(-\gamma - \alpha) + \tan(-\gamma + \alpha)}. \quad (\text{B-4})$$

Since (x_m, z_m) is the intersecting point of the source wavefront and the receiver wavefront, it should satisfy the source wavefront equation:

$$(x - s)^2 + z^2 = \left[\frac{x_m - s}{\sin(-\gamma + \alpha)} \right]^2, \quad (\text{B-5})$$

and the receiver wavefront equation:

$$(x - r)^2 + z^2 = \left[\frac{r - x_m}{\sin(-\gamma - \alpha)} \right]^2. \quad (\text{B-6})$$

To get the SODCIG, we have to apply the multi-offset imaging condition described in equation (1) as follows, where h is the subsurface half-offset,

$$\begin{cases} (x - h - s)^2 + z^2 = \left[\frac{(x_m - s)}{\sin(-\gamma + \alpha)} \right]^2, \\ (x + h - r)^2 + z^2 = \left[\frac{(x_m - r)}{\sin(-\gamma - \alpha)} \right]^2. \end{cases} \quad (\text{B-7})$$

Therefore, by letting $x = x_m$ and summing the above two equations together, we can derive the relationship between z and h for surface location x_m :

$$(x_m - h - s)^2 + (x_m + h - r)^2 + 2z^2 = \left[\frac{x_m - s}{\sin(-\gamma + \alpha)} \right]^2 + \left[\frac{r - x_m}{\sin(-\gamma - \alpha)} \right]^2 \quad (\text{B-8})$$

From equation (B-4), it is easy to get:

$$x_m - s = \frac{s \tan(-\gamma - \alpha) + r \tan(-\gamma + \alpha)}{\tan(-\gamma - \alpha) + \tan(-\gamma + \alpha)} - s = \frac{(r - s) \tan(-\gamma + \alpha)}{\tan(-\gamma - \alpha) + \tan(-\gamma + \alpha)} \quad (\text{B-9})$$

and

$$r - x_m = r - \frac{s \tan(-\gamma - \alpha) + r \tan(-\gamma + \alpha)}{\tan(-\gamma - \alpha) + \tan(-\gamma + \alpha)} = \frac{(r - s) \tan(-\gamma - \alpha)}{\tan(-\gamma - \alpha) + \tan(-\gamma + \alpha)}, \quad (\text{B-10})$$

Substituting equations (B-9) and (B-10) into equation (B-8), after some algebra, we get

$$z^2 = -h^2 + (r - s)h + \frac{(r - s)^2}{[\tan(-\gamma - \alpha) + \tan(-\gamma + \alpha)]^2}. \quad (\text{B-11})$$

Obviously, in this situation, depth z is not linearly related to subsurface half-offset h . When $\alpha = 0$, i.e. for a flat reflector, the above equation can be simplified as follows:

$$z^2 = -h^2 + (r - s)h + \frac{(r - s)^2}{4 \tan^2 \gamma}. \quad (\text{B-12})$$

Anisotropic migration velocity analysis from residual moveout transformation in angle-domain common-image gathers

Pierre Jousselin and Biondo Biondi

ABSTRACT

We present the application of anisotropic migration velocity analysis (MVA) on synthetic data and on a real dataset acquired in the North Sea. The method we use to estimate anisotropic migration velocities is based on the computation and analysis of angle-domain common-image gathers (ADCIGs) in conjunction with anisotropic wavefield-continuation migration. Assuming flat reflectors and vertically transversely isotropic (VTI) media, we compute anisotropic velocity spectra from a residual moveout (RMO) transformation, based on the theoretical expression of the RMO in anisotropic ADCIGs as a function of perturbations in migration velocities.

In the first part of this paper, we briefly present the theory of ADCIGs and the derivation of the mathematical expression of the RMO function. In the second part, we analyze synthetic data with the method we propose to estimate anisotropic migration velocities. We demonstrate that our method is unable to resolve vertical velocities but nevertheless accurately estimates horizontal and normal moveout (NMO) velocities even for significant perturbations in the velocity model, provided the range of aperture angle is not too small. In the last part of this paper, we demonstrate on real data the validity of our estimation method, by showing it indicates the presence of velocity anellipticity in layers stratigraphically interpreted as anisotropic and for which well data do not match seismic data migrated under the assumption of isotropy.

INTRODUCTION

Since approximating the subsurface as an isotropic medium can be geologically unrealistic and since isotropic migration methods can give results inconsistent with well data, anisotropic migration has become an important focus of research and is now widely used. However, superior image quality and accurate reflector positioning require good estimates of anisotropic parameters.

Today, migration velocity analysis (MVA) is most commonly employed to estimate isotropic migration velocity in complex media. However, it is still less mature for anisotropic applications, and most recent work has developed anisotropic MVA only in conjunction with Kirchhoff migration (Tsvankin, 2001). The mathematical relationship that links residual moveout (RMO) in anisotropic angle-domain common-image gathers (ADCIGs) to anisotropic migration velocity errors (Biondi, 2005a,b) opens the way to new anisotropic MVA methods that

can be performed in conjunction with wavefield-continuation migration. These methods have the great advantage of being based on migrated gathers and allow the iterative estimation of anisotropic migration velocities.

In this paper, we present the results from computing anisotropic velocity spectra from RMO transformation in anisotropic ADCIGs assuming flat reflectors and vertically transversely isotropic (VTI) media. In the first part, we briefly present the theory of ADCIGs and the derivation of the mathematical expression of the RMO function. In the second part, we perform anisotropic MVA on synthetic data and analyze the accuracy and convergence of our estimation method. We demonstrate it does not resolve vertical velocities but nevertheless accurately estimates the horizontal and NMO velocities, even for significant perturbations, provided the range of aperture angle is not too small. We also show that when computing anisotropic velocity spectra as few approximations as possible must be made in order to attain accurate parameter estimates. In the last part, we perform anisotropic MVA on a real data set acquired in the North Sea. We demonstrate the validity of the method by showing it indicates the presence of velocity anellipticity in the layers stratigraphically interpreted as anisotropic, and for which well data do not match seismic data migrated under the assumption of isotropy.

RESIDUAL MOVEOUT IN ANISOTROPIC ADCIGS

In this section, we briefly present the theory of ADCIGs (Rickett and Sava, 2002; Sava and Fomel, 2003; Biondi and Tisserant, 2004) and the derivation of the mathematical expression of RMO in anisotropic ADCIGs as a function of errors in anisotropic velocity parameters (Biondi, 2005a,b; Jousselin and Biondi, 2006).

Generalized migration

Anisotropic ADCIGs are based on the generalization of integral migration to the computation of a prestack image that includes the subsurface-offset dimension (h_ξ) in addition to the usual image depth (z_ξ) and midpoint (m_ξ). Figure 1 illustrates the subsurface-offset dimension: the image point (m_ξ, h_ξ, z_ξ) belongs to the migration response of an impulse recorded at midpoint m_D , surface offset h_D and travel time t_D , provided that the travel time along the source and receiver paths (of length L_s and L_r , respectively) is equal to t_D .

Computation of ADCIGs

In 2-D, ADCIGs are computed for each midpoint by applying a slant-stack decomposition to the prestack image along the subsurface-offset axis. The kinematics of the angle-domain transformation are defined by the following change of variable:

$$\widehat{\gamma} = \arctan \left. \frac{\partial z_\xi}{\partial h_\xi} \right|_{m_\xi = \bar{m}_\xi}, \quad (1)$$

$$z_{\widehat{\gamma}} = z_\xi - h_\xi \tan \widehat{\gamma}, \quad (2)$$

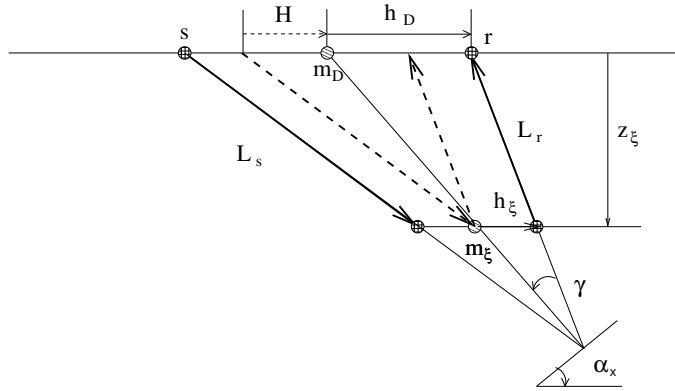


Figure 1: Illustration of generalized migration, where the prestack image is a function of the subsurface offset and γ and α_x are the group aperture and dip angles, respectively.

pierre1-imp-resp [NR]

where $z_{\hat{\gamma}}$ is the transformed image-point depth. Assuming flat reflectors and VTI media, Biondi (2005a) demonstrates that the angle $\hat{\gamma}$ is equal to the phase aperture angle $\tilde{\gamma}$, thereby simplifying equations 1 and 2:

$$\tilde{\gamma} = \arctan \left. \frac{\partial z_{\xi}}{\partial h_{\xi}} \right|_{m_{\xi} = \bar{m}_{\xi}}, \quad (3)$$

$$z_{\tilde{\gamma}} = z_{\xi} - h_{\xi} \tan \tilde{\gamma}. \quad (4)$$

RMO analysis in ADCIGs

When the migration velocity is correct and the image is focused at zero subsurface offset, transformation to the angle domain does not change the image-point depth and the reflections are imaged at the same depth for all aperture angles ($z_{\tilde{\gamma}} = z_{\xi} = \text{const}$). As a consequence, when migrated with the correct migration velocity, reflectors are mapped flat in ADCIGs. In contrast, when the reflections are not focused at zero offset, transformation to the angle domain maps the events to different depths for each different angle. The image-depth variability with aperture angle is described by the RMO function, which we want to measure and quantify as a function of the perturbation in anisotropic parameters. Below, we summarize the approach given by Biondi (2005a) to derive the expression of RMO in anisotropic ADCIGs. It consists of approximating the RMO by the first-order Taylor series expansion about the correct migration velocity.

The notation used in Biondi (2005a) is the following: the VTI velocity function parameterization is $\mathbf{V} = (V_V, V_H, V_N)$, where V_V is the velocity of a vertical ray, V_H is the velocity of a horizontal ray and V_N is the NMO velocity. It is equivalent to Thomsen's parameterization $\mathbf{V} = (V_V, \epsilon, \delta)$, since $V_H = V_V \sqrt{1 + 2\epsilon}$ and $V_N = V_V \sqrt{1 + 2\delta}$.

We define the perturbations in the VTI velocity function as a three-component vector $\boldsymbol{\rho} = (\rho_{V_V}, \rho_{V_H}, \rho_{V_N})$, where each component is a multiplicative factor for each migration velocity. The vector generates a perturbed velocity field, ${}_{\rho}\mathbf{V}$ defined by ${}_{\rho}\mathbf{V} = ({}_{\rho}V_V, {}_{\rho}V_H, {}_{\rho}V_N) = (\rho_{V_V} V_V, \rho_{V_H} V_H, \rho_{V_N} V_N)$.

From the analytic expression of the impulse response (derived from Figure 1) and geometric interpretation of the angle-domain transformation, Biondi (2005a) derives the first-order

derivatives of the image depth in the angle domain with respect to anisotropic parameter perturbations:

$$\frac{\partial z_{\tilde{\gamma}}}{\partial \rho_i} = -z_{\xi} \frac{(1 + \tan \tilde{\gamma} \tan \gamma)}{S(\gamma)} \frac{\partial S}{\partial \rho_i}, \quad (5)$$

where S is the slowness along the source and receiver rays.

Similarly, because residual moveout Δz_{RMO} is defined as the difference between the reflector movement at finite angle ($\tilde{\gamma}$) and the reflector movement at normal incidence ($\tilde{\gamma} = 0$), from equation 5, we can express the first-order derivatives of the residual moveout with respect to anisotropic parameter perturbations:

$$\frac{\partial \Delta z_{\text{RMO}}}{\partial \rho_i} = \left. \frac{\partial z_{\tilde{\gamma}}}{\partial \rho_i} \right|_{\tilde{\gamma}} - \left. \frac{\partial z_{\tilde{\gamma}}}{\partial \rho_i} \right|_{\tilde{\gamma}=0}. \quad (6)$$

The residual moveout Δz_{RMO} is eventually approximated by the first-order Taylor series expansion about the correct migration velocity ($\rho = 1$). The linearized expression is the following:

$$\Delta z_{\text{RMO}} = \left. \frac{\partial \Delta z_{\text{RMO}}}{\partial \rho_{V_V}} \right|_{\tilde{\gamma}, \rho=1} (\rho_{V_V} - 1) + \left. \frac{\partial \Delta z_{\text{RMO}}}{\partial \rho_{V_H}} \right|_{\tilde{\gamma}, \rho=1} (\rho_{V_H} - 1) + \left. \frac{\partial \Delta z_{\text{RMO}}}{\partial \rho_{V_N}} \right|_{\tilde{\gamma}, \rho=1} (\rho_{V_N} - 1). \quad (7)$$

Synthetic examples

The accuracy of the RMO function predicted from equations 5 to 7 is demonstrated in Biondi (2005a,b), for a large range of velocity perturbations. Figure 2 presents the ADCIGs obtained when a flat reflector is migrated with inaccurate migration velocity models. The data were modeled using the anisotropic parameters of the Taylor Sand (Tsvankin, 2001): $\epsilon = 0.110$ and $\delta = -0.035$. It was then migrated using: a) a velocity uniformly perturbed by $\rho_V = 0.99$, b) a velocity uniformly perturbed by $\rho_V = 0.9$, and c) an isotropic velocity with the correct vertical velocity. The predicted residual moveouts derived from equations 5 to 7 are superimposed. The solid line was computed when $\tan \gamma$ was derived from $\tan \tilde{\gamma}$ by applying equation A-2, whereas the dashed line was computed using the approximation $\tan \gamma \approx \tan \tilde{\gamma}$.

The predicted RMO functions accurately track the actual RMO functions when the perturbations are sufficiently small to be within the linearization accuracy range (Figure 2-a). Even when the perturbations are large (Figures 2-b and 2-c) and cause a substantial RMO, the predicted RMO functions are excellent approximations of the true RMO functions. In contrast, the approximation of the group angles with the phase angles (dashed lines in the figures) seriously lowers the accuracy of the predicted RMO functions.

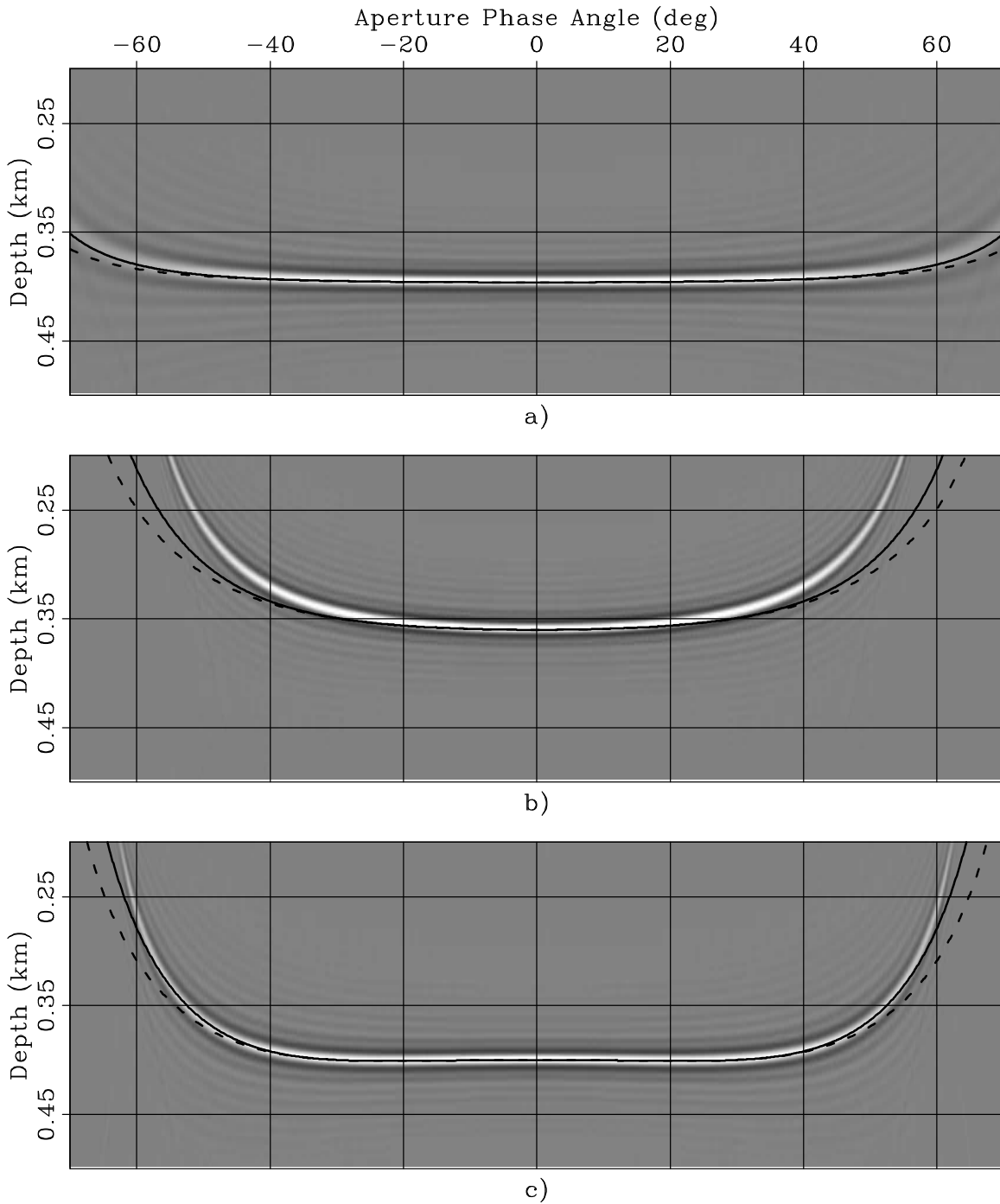


Figure 2: ADCIG obtained when data modeled using constant anisotropic parameters (Taylor Sand) have been migrated using: a) a velocity uniformly perturbed by $\rho_V = 0.99$, b) a velocity uniformly perturbed by $\rho_V = 0.9$, and c) an isotropic velocity with the correct vertical velocity. Superimposed onto the images are the RMO functions computed using equations 5 to 7. The solid line was computed when $\tan \gamma$ was derived from $\tan \tilde{\gamma}$ by applying equation A-2, whereas the dashed line was computed with the approximation $\tan \gamma \approx \tan \tilde{\gamma}$. pierre1-Aniso-rmo [ER]

ANISOTROPIC MIGRATION VELOCITY ANALYSIS OF SYNTHETIC DATA FROM RMO TRANSFORMATION IN ANISOTROPIC ADCIGS

In the preceding section, we derived the expression of the RMO in anisotropic ADCIGs as a function of anisotropic parameter perturbations and demonstrated its accuracy for different types of velocity model perturbations. In this section, we perform anisotropic MVA on the same synthetic data and analyze the accuracy and convergence of our estimation method. We also illustrate caveats in the computation of anisotropic velocity spectra and demonstrate that as few approximations as possible should be made in order to attain accurate anisotropic parameter estimates.

Estimation of the vertical velocity

First, we show that for flat reflectors and VTI media, vertical velocities cannot be estimated from reflection seismic data only. These results are consistent with Tsvankin (2001), who shows that P-wave signatures depend only on two combinations of V_V , δ and ϵ , and that vertical velocities cannot be estimated from reflection seismic data only.

For elliptical media, we demonstrate that the first-order derivative of the image-point depth with respect to vertical velocity perturbations is independent of the aperture angle so that the residual moveout is independent of the vertical velocity perturbations:

$$\frac{\partial z_{\tilde{\gamma}}}{\partial \rho_{V_V}} = -z_{\xi}, \quad (8)$$

$$\frac{\partial \Delta z_{\text{RMO}}}{\partial \rho_{V_V}} = \left. \frac{\partial z_{\tilde{\gamma}}}{\partial \rho_{V_V}} \right|_{\tilde{\gamma}} - \left. \frac{\partial z_{\tilde{\gamma}}}{\partial \rho_{V_V}} \right|_{\tilde{\gamma}=0} = 0. \quad (9)$$

As a consequence, vertical velocity perturbations cannot be estimated from RMO transformation.

For anelliptical media, we show numerically that the first-order derivative of the RMO with respect to vertical velocity perturbations is not significantly different from zero and does not allow the estimation of vertical velocity perturbations.

Estimation of the horizontal and NMO velocities

Since the vertical velocities cannot be estimated from RMO transformations in anisotropic ADCIGs, we computed the semblance values for ρ_{V_H} and ρ_{V_N} only. Figure 3 illustrates the velocity spectra computed at the image depth for the various ADCIGs illustrated in Figure 2. The various semblance panels are computed for various aperture angle ranges (30° , 45° and 60°). When computing the semblance of a velocity model, the first-order derivatives in equation 5 are computed around that velocity model, not around the one that was used for the migration. The group aperture angles are computed from phase aperture angles using equation A-2. The

parameterization of the estimated anisotropic parameters is done with the perturbations in the horizontal (ρ_{V_H}) and NMO velocities (ρ_{V_N}). For visualization purposes, Figure 4 illustrates the same semblance panels, but this time, the axes ρ_{V_H} and ρ_{V_N} have been normalized by the correct perturbations in the anisotropic migration velocities. As a consequence, in Figure 4, the true velocities lie in the center of the semblance panels. Several conclusions can be drawn from Figure 4.

- **Effect of the aperture angle:** As the range of the aperture angle increases, so does the residual moveout and the information about the true velocity model. As a consequence, the estimates of the anisotropic parameters become more accurate. Furthermore, as the range of the aperture angle increases, the relative constraints on the horizontal and NMO velocities become more even.
- **Accuracy of the estimation method:** For aperture angles around 30° , Figure 4 illustrates that the velocity perturbations are unresolved (especially ρ_{V_H}). For aperture angles larger than 45° , the largest semblance values are found close to the center of the semblance panels, demonstrating the accuracy of the estimation method. However, the largest semblance values are not exactly centered, but slightly shifted toward the upper left, indicating that the anisotropic migration velocities tend to be underestimated. This is consistent with Figure 2 that illustrates that the predicted RMO functions underestimate the absolute value of the true RMOs.
- **Convergence of the estimation method:** Table 1 displays the values of $\rho_{V_H} - 1$ and $\rho_{V_N} - 1$ for the maximum semblance velocity models, as a function of the aperture angle range. These quantities are equivalent to the percentage error in V_H and V_N estimates. Table 1 indicates that starting from an isotropic model or a uniform perturbation of $\rho_V = 0.9$, the estimation method improves the estimates of V_H and V_N by reducing the percentage errors to less than 2%. However, it also shows that for a velocity model uniformly perturbed by $\rho_V = 0.99$, the estimation method may neither converge nor improve the accuracy of the migration velocity model since for a 60° aperture angle range, the estimation error is still of the order of 1% (i.e. the starting velocity model error).
- **Trade-off between the anisotropic migration velocities:** Figure 4 shows a negative trade-off between ρ_{V_H} and ρ_{V_N} , because a perturbation in V_H can be balanced by a perturbation of the opposite sign in V_N , and result in a very small net change in the predicted RMO function. This negative trade-off has an important practical consequence: it justifies the joint-estimation of ρ_{V_H} and ρ_{V_N} . The successive estimation of ρ_{V_H} and ρ_{V_N} may lead to a much poorer convergence rate.

Caveats in the computation of velocity spectra

Eventually, we illustrate the caveats in the computation of anisotropic velocity spectra and demonstrate that as few approximations as possible should be made in order to attain accurate anisotropic parameter estimates. As equation 5 shows, the predicted RMO is a function

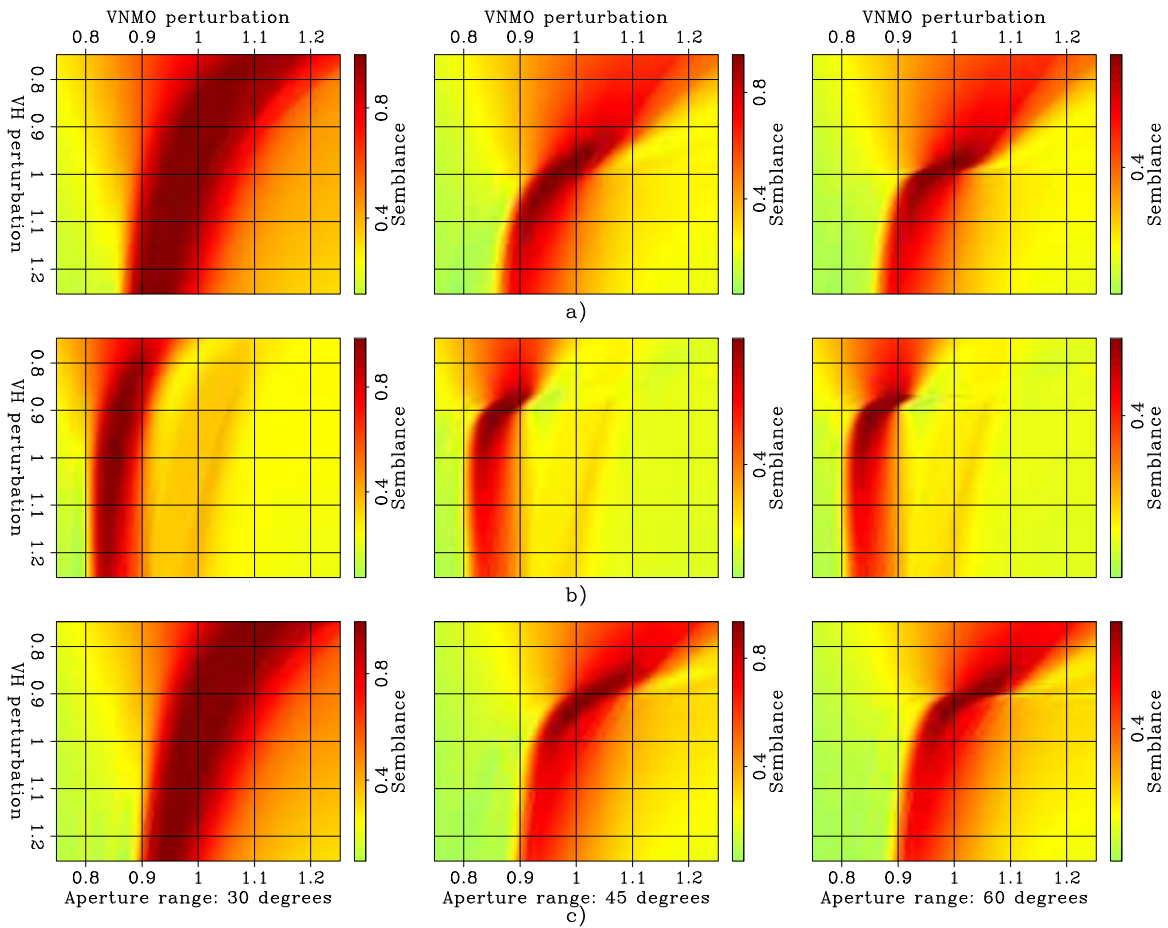


Figure 3: Velocity spectra obtained at the image depth when data modeled with a constant anisotropic velocity model (Taylor Sand) have been migrated using: a) a velocity uniformly perturbed by $\rho_V = 0.99$, b) a velocity uniformly perturbed by $\rho_V = 0.9$, and c) an isotropic velocity with the correct vertical velocity. The various semblance panels are computed for various aperture angle ranges (30° , 45° and 60° from left to right). The parameterization of the estimated anisotropic velocity model is done with the perturbations in the horizontal (ρ_{V_H}) and in the NMO velocity (ρ_{V_N}). The correct perturbation values are: a) $\rho_{V_H} = 0.99$ and $\rho_{V_N} = 0.99$, b) $\rho_{V_H} = 0.9$ and $\rho_{V_N} = 0.9$, and c) $\rho_{V_H} = 0.905$ and $\rho_{V_N} = 1.037$. pierre1-Comb-VelSpec-group [ER]

Velocity model perturbation	Initial perturbation	Range of aperture angles		
		[0,30]	[0,45]	[0,60]
1 % uniform perturbation	(-1.0%, -1.0%)	(-3.5%, +5.0%)	(-2.5%, +2.0%)	(-1.0%, +0.5%)
10 % uniform perturbation	(-10.0%, -10.0%)	(-4.5%, +7.0%)	(-3.0%, +0.0%)	(-1.5%, -1.5%)
Isotropic model with right V_V	(-9.5%, +3.7%)	(+1.5%, -3.5%)	(-2.0%, +1.5%)	(+0.5%, +0.0%)

Table 1: Values of $(\rho_{V_H} - 1, \rho_{V_N} - 1)$ for the maximum semblance velocity model, as a function of the aperture angle range.

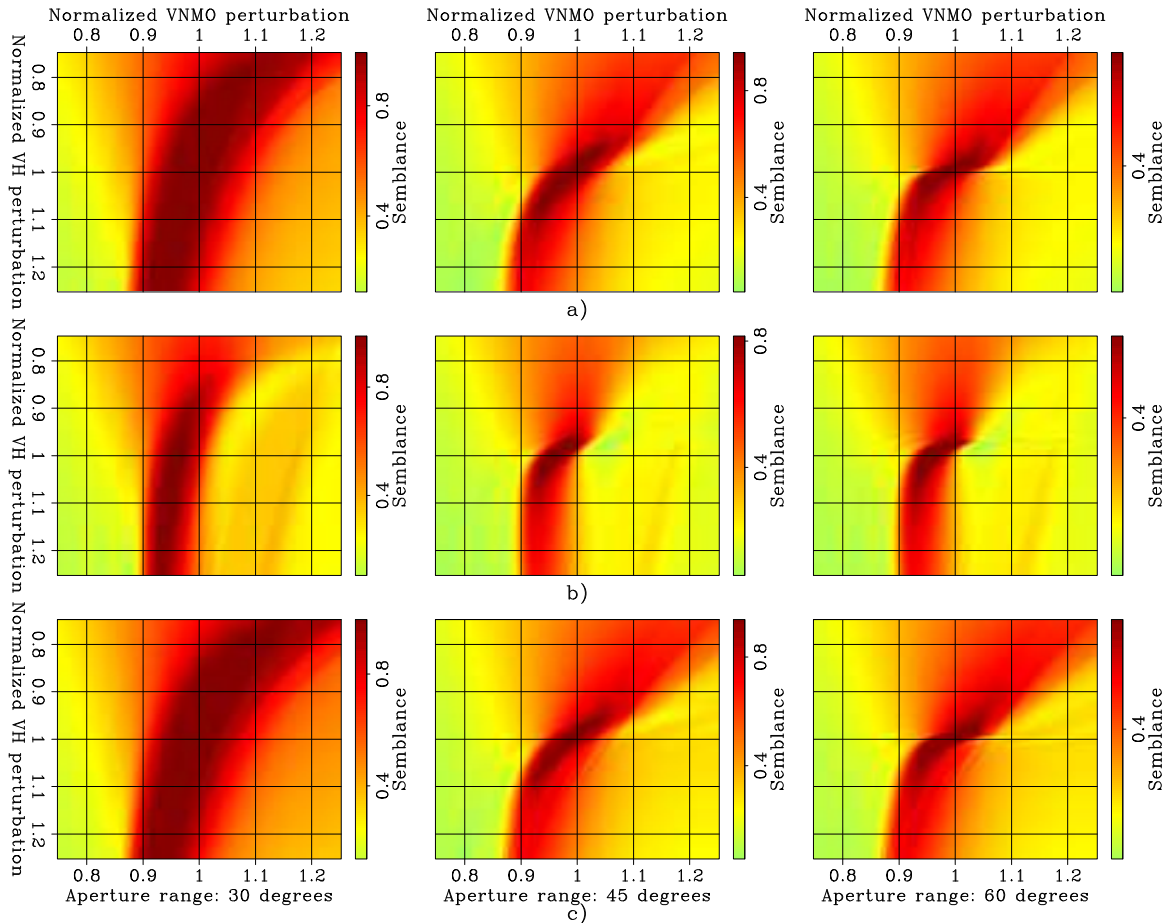


Figure 4: Velocity spectra obtained at the image depth when data modeled with a constant anisotropic velocity model (Taylor Sand) have been migrated using: a) a velocity uniformly perturbed by $\rho_V = 0.99$, b) a velocity uniformly perturbed by $\rho_V = 0.9$, and c) an isotropic velocity with the correct vertical velocity. The various semblance panels are computed for various ranges of aperture angles (30° , 45° and 60° from left to right). The parameterization of the estimated anisotropic velocity model is done with ρ_{VH} and ρ_{VN} by the correct perturbation values. `pierre1-Comb-VelSpec-group_centrd` [ER]

of both phase and group aperture angles. Phase aperture angles are computed by applying post-processing slant-stacks on the prestack migrated image (equation 3). Group aperture angles have to be derived from phase aperture angles. Figure 5 illustrates the velocity spectra computed when approximating the group aperture angles with the phase aperture angles. It shows the inaccuracy of the estimates of the anisotropic parameters for large velocity perturbations. Figure 6 illustrates the velocity spectra computed when the first-order derivatives in equation 5 are computed around the migration velocity model and not the velocity model whose semblance we compute. The group aperture angles are computed from phase aperture angles using equation A-2. Figure 6 illustrates the inaccuracy of the anisotropic parameter estimates for large velocity perturbations. It indicates that when computing velocity model semblances, first-order derivatives of the RMO functions have to be estimated independently for each velocity model.

ANISOTROPIC MIGRATION VELOCITY ANALYSIS ON REAL DATA FROM RMO TRANSFORMATION IN ANISOTROPIC ADCIGS

In this section, we perform anisotropic migration velocity analysis on real data and demonstrate the validity of our estimation method, by showing it indicates the presence of anellipticity in layers stratigraphically interpreted as anisotropic and for which well data do not match seismic data migrated under the assumption of isotropy. We first present the geologic setting and imaging challenges of the Alwyn field, where the data set was acquired. We then compute anisotropic velocity spectra.

Geologic setting

The Alwyn field is located in the UK sector of the North Sea, about 440 kilometers northeast from Aberdeen. The geologic setting is a tilted block structure with three reservoir formations (Figure 7): the Brent reservoir (top) produces oil, the Staffjord reservoir (middle) produces gas and the Triassic reservoir (bottom) produces oil. Existing 3D isotropic prestack time-migration (PSTM) and prestack depth-migration (PSDM) images are considered insufficient for structural understanding of the different fault blocks of this fluvial formation.

Imaging challenges

Several imaging challenges associated with Alwyn are well illustrated in Figure 8 that shows the seismic crossline of the migrated cube obtained by CGG in 2003 after isotropic Kirchhoff prestack migration. It shows the following different challenges encountered in the area of interest:

- First, the reflectors and faults below the BCU horizon (strong reflector at around 3.5 km depth) are moderately well focused.

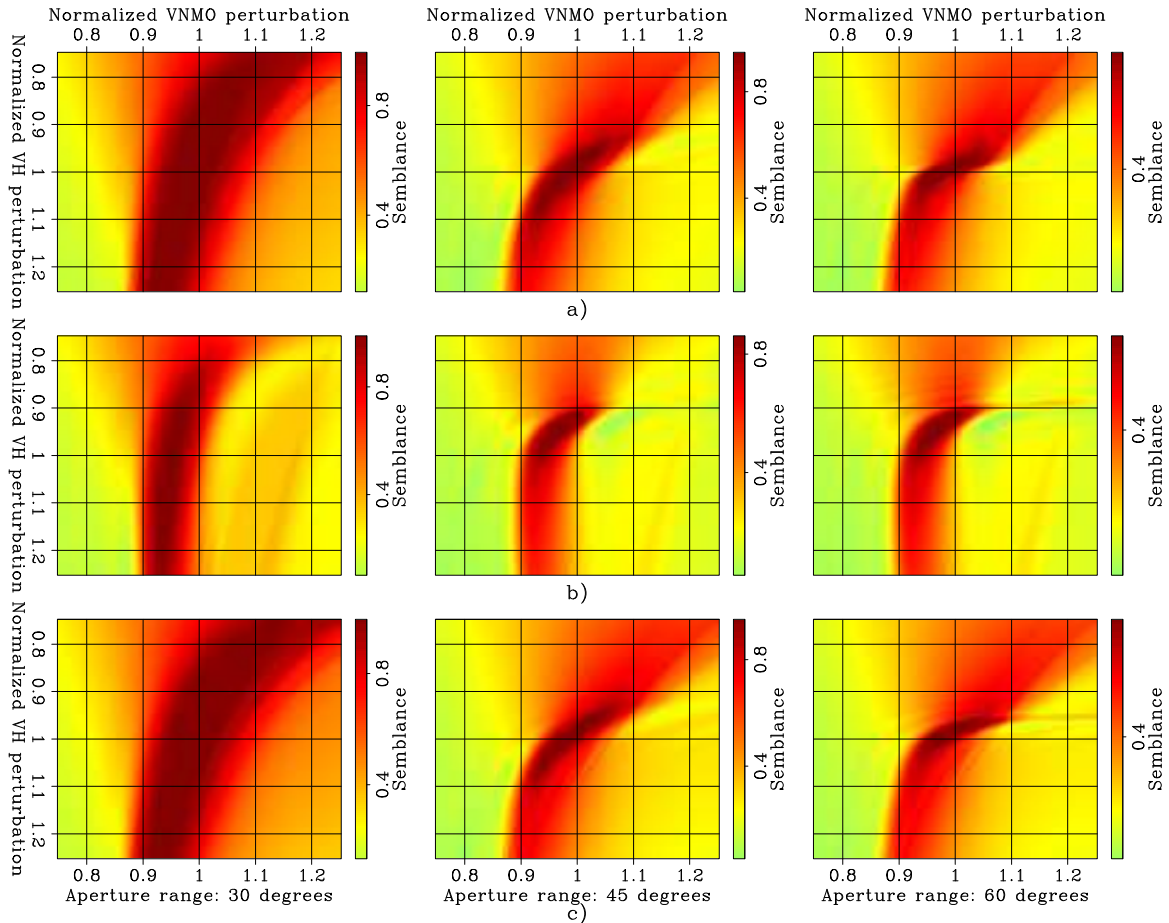


Figure 5: Velocity spectra obtained when the group aperture angles are approximated as equal to the phase aperture angles. The data have been modeled with a constant anisotropic velocity model (Taylor Sand) and then migrated using: a) a velocity uniformly perturbed by $\rho_V = 0.99$, b) a velocity uniformly perturbed by $\rho_V = 0.9$, and c) an isotropic velocity with the correct vertical velocity. The different semblance panels are computed for different ranges of aperture angles (30° , 45° and 60° , from left to right). The parameterization of the estimated anisotropic velocity model is done with ρ_{V_H} and ρ_{V_N} normalized by the correct perturbation values. `pierre1-Comb-VelSpec-phase_centrd` [ER]

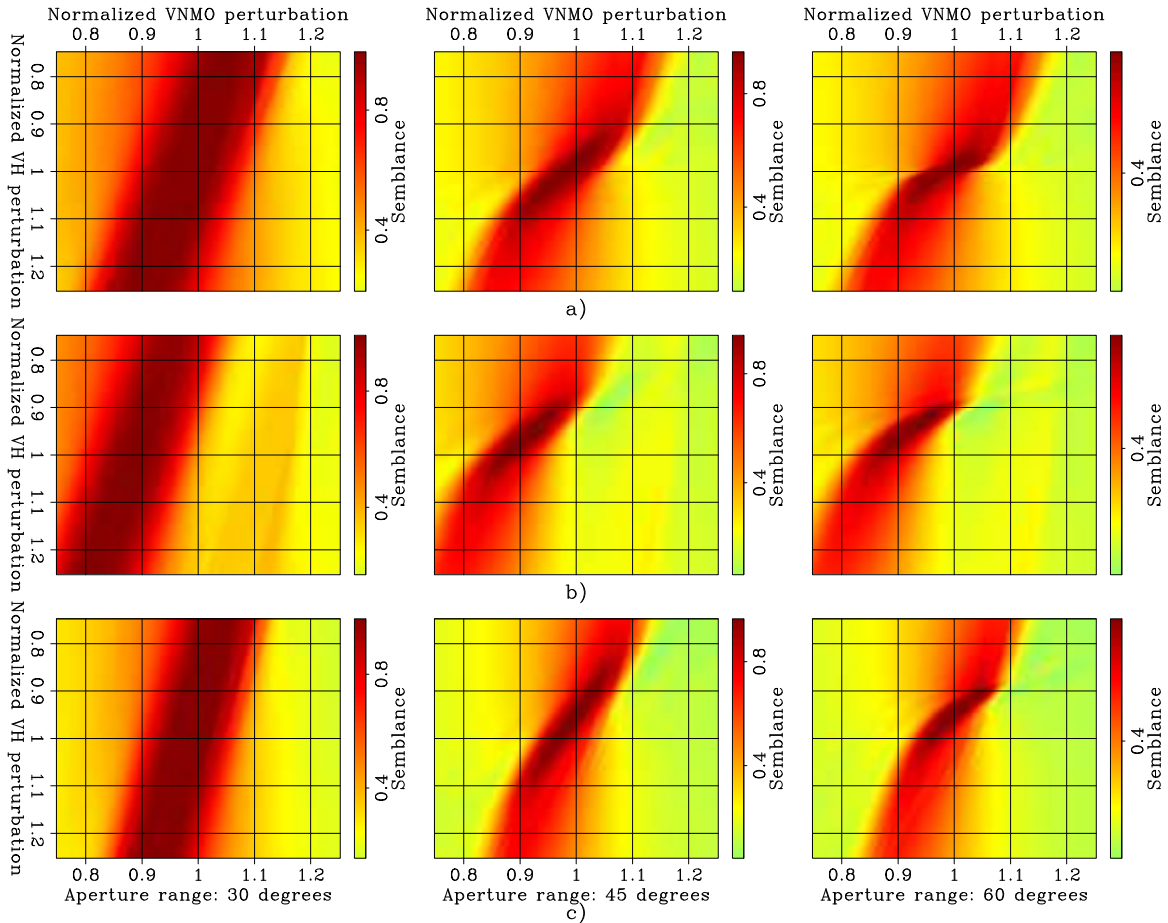


Figure 6: Velocity spectra obtained when the first-order derivatives in equation 5 are computed around the migration velocity model. The group aperture angles are computed from phase aperture angles using equation A-2. The data have been modeled with a constant anisotropic velocity model (Taylor Sand) and then migrated using: a) a velocity uniformly perturbed by $\rho_V = 0.99$, b) a velocity uniformly perturbed by $\rho_V = 0.9$, and c) an isotropic velocity with the correct vertical velocity. The different semblance panels are computed for different ranges of aperture angles (30° , 45° and 60° , from left to right). The parameterization of the estimated anisotropic velocity model is done with ρ_{V_H} and ρ_{V_N} , normalized by the correct perturbation values. `pierre1-Comb-VelSpec-group_approx_centrd` [ER]

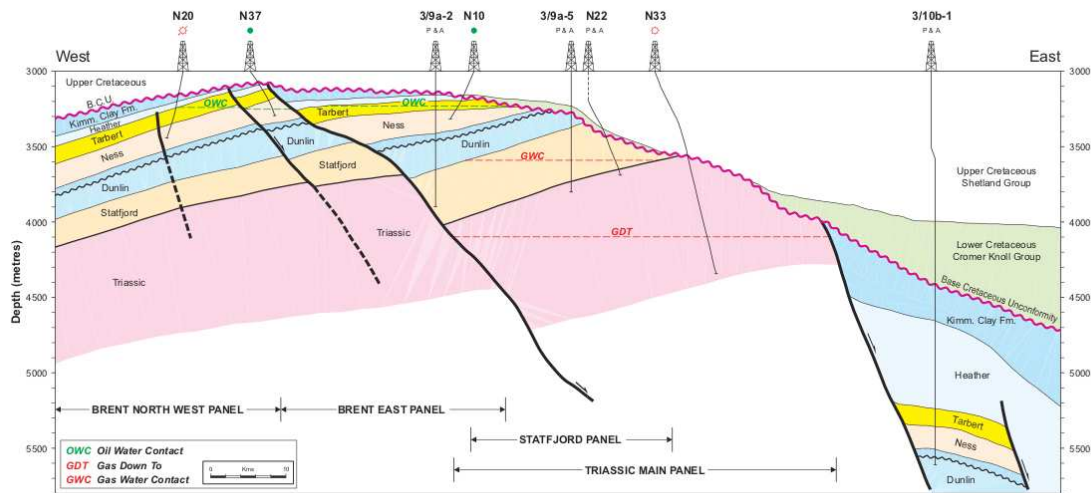


Figure 7: Geological section of the Alwyn field operated by TOTAL UK. pierre1-Section
[NR]

- Second, a complex channel at around 1.0 km depth distorts the underlying horizons and especially the Balder horizon (strong and continuous reflector at around 1.5 km depth), affected by pull-ups (for example, at inlines 630, 660 and 700).
- Third, strong multiples contaminate the lower part of the image as well as strong migration smiles due to limited crossline acquisition aperture.

Furthermore, anisotropy is commonly observed in the North Sea. In the Alwyn field, the thick layer between the Top Chalk horizon (at around 2.2 km depth) and the BCU horizon is made of chalk, a sedimentary carbonate rock whose main mineral (calcite) has an anisotropic crystalline structure. The anisotropy of this layer, if not taken into account in the migration, can result in poor imaging of the underlying layers.

Description of the available data

TOTAL UK provided us with the data from the 2001 acquisition (preprocessed recently by Veritas), the isotropic interval velocity model developed by CGG in 2003, and the data from 15 nearby wells.

- **Acquisition area** In 2001, approximately 260 km² of 3D seismic full-fold data was acquired with an interleaved acquisition. The available seismic data spans 180 km².
- **2001 survey acquisition parameters** The main parameters of the acquisition are illustrated in Figure 9. The shotpoint interval is 18.75 meters. The bin size of the data preprocessed by Veritas in 2006 is 6.25 meters by 18.75 meters, corresponding to a stacking fold of 108.

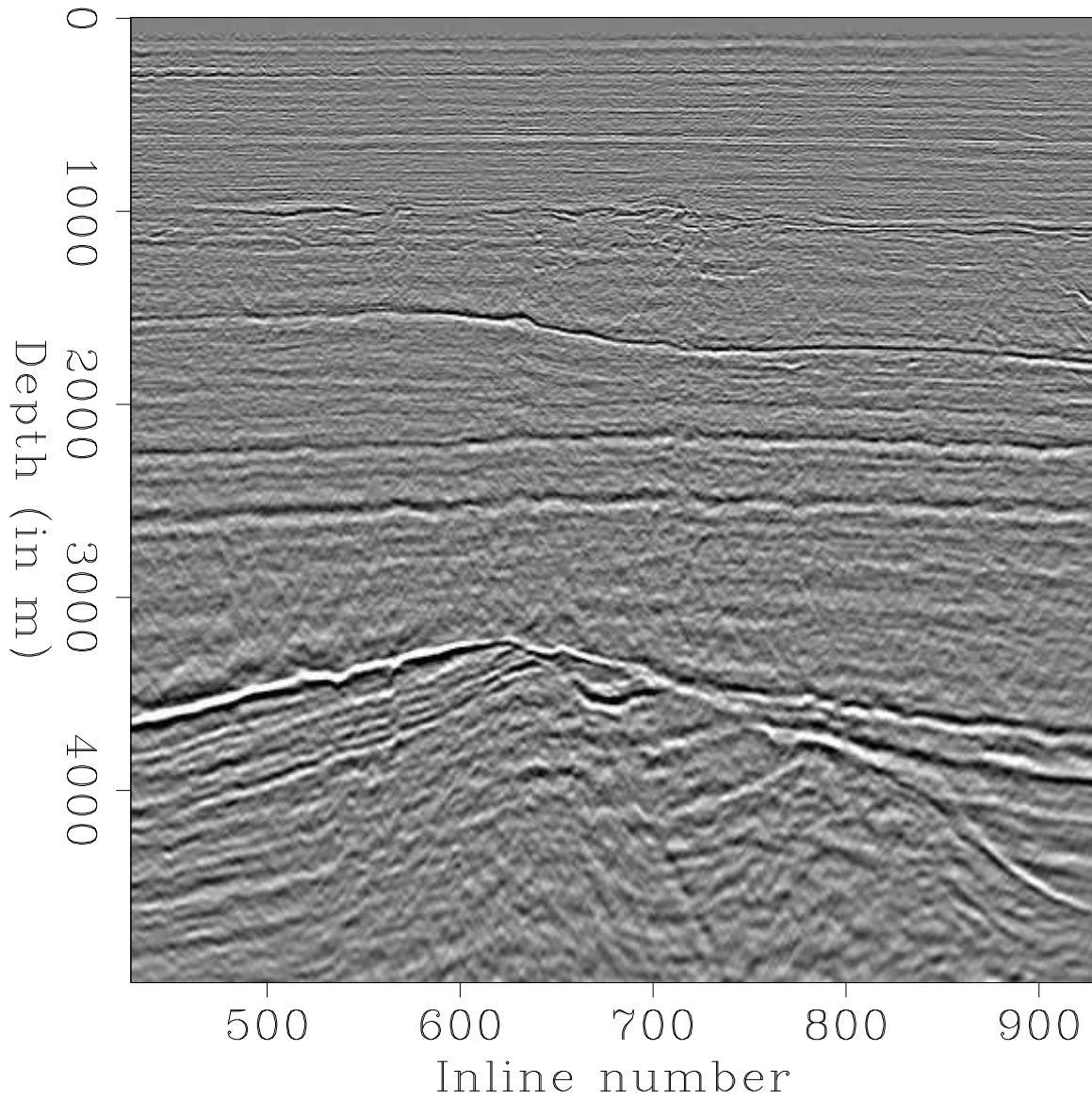
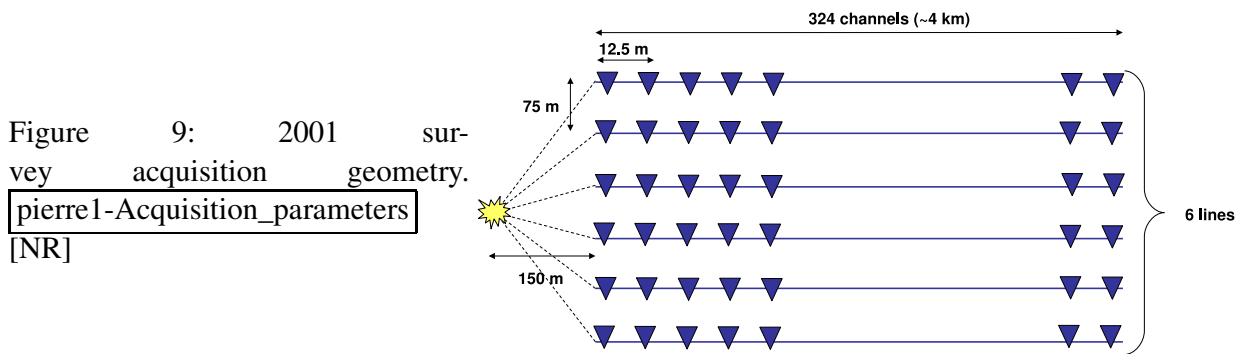


Figure 8: Crossline 1999 of CGG 2003 PSDM cube obtained after isotropic Kirchhoff prestack migration. The distance between two inlines is equal to 18.75m. `pierre1-Section_Crossline_1999` [CR]



- Isotropic Velocity model** We were provided with the final isotropic interval velocity depth model computed by CGG. The blocky velocity model was first built in time using the interpreted time-horizons, the surface seismic stacking velocities and the compaction gradients given by the wells. It was then updated by layer-stripping. Two different updating methods were used. The first one was to compute CRP scans and perform normal-ray update. The second method was to pick residual curvature and perform multi-offset velocity updates. Figure 11 illustrates the final isotropic velocity model for Line 750.

Migration of the data

We restricted ourselves to 2D anisotropic migration velocity estimation and to mild dips. For that reason, we selected a line where crossline and inline dips are limited (Line 750 illustrated in Figure 10). As illustrated, the geologic structure along line 750 is relatively flat, and the assumption of flat reflectors is reasonable. This allows us to use the analytical expression of the RMO in ADCIGs presented by Biondi (2005b) and to compute anisotropic velocity spectra. Furthermore, it has the advantage of having a nearby well. This gives us useful vertical velocity constraints when building the anisotropic velocity model.

In our estimation procedure, we use an anisotropic source-receiver migration program and first perform an isotropic migration of the data starting from the interval vertical velocity model developed by CGG (Figure 11). The migration result is illustrated in the Figure 10.

Analysis of ADCIGs and computation of anisotropic velocity spectra

We compute ADCIGs from the prestack migrated image by applying post-processing slant stacks (Rickett and Sava, 2002; Sava and Fomel, 2003). The ADCIGs at three different locations are illustrated in Figure 12. It can be observed that up to 2 km depth, reflectors are imaged flat in ADCIGs, meaning that the migration velocity obtained by CGG is correct and that no anisotropy in those layers is needed. However, we can observe that below the Balder horizon (strong reflector at around 1.7 km depth), the reflectors start curving downward, indicating that the estimated isotropic migration velocity is larger than the true migration velocity. That result is consistent with the sonic velocity recorded in well 3_9a-8, located at 32.83 km along

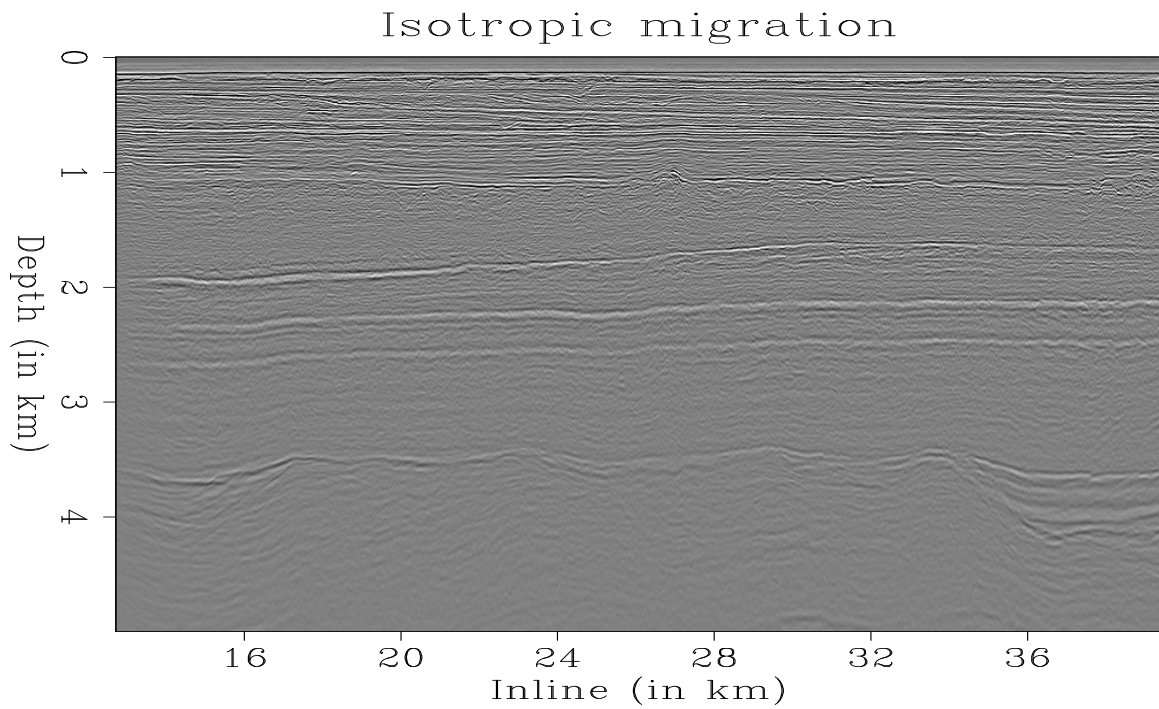


Figure 10: Line 750: Migration result obtained after isotropic source-receiver migration.
`pierre1-Section-iso-750` [CR]

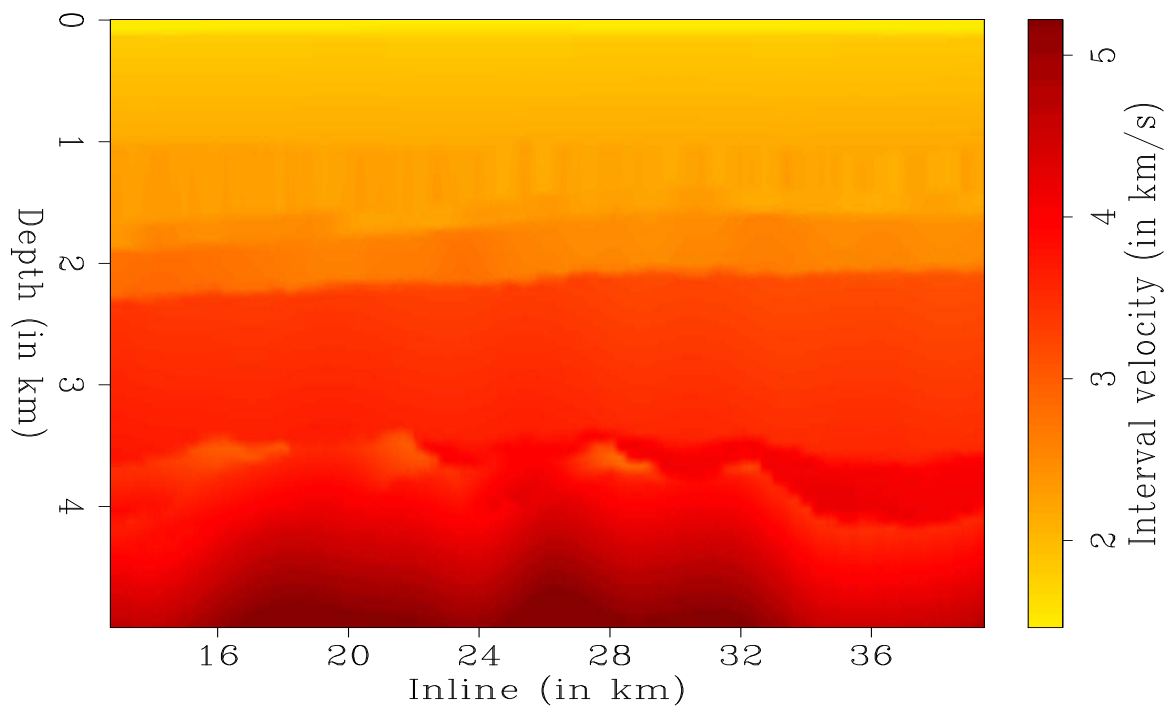


Figure 11: Line 750: Starting isotropic interval velocity model obtained by CGG (2003).
`pierre1-Velocity-750` [CR]

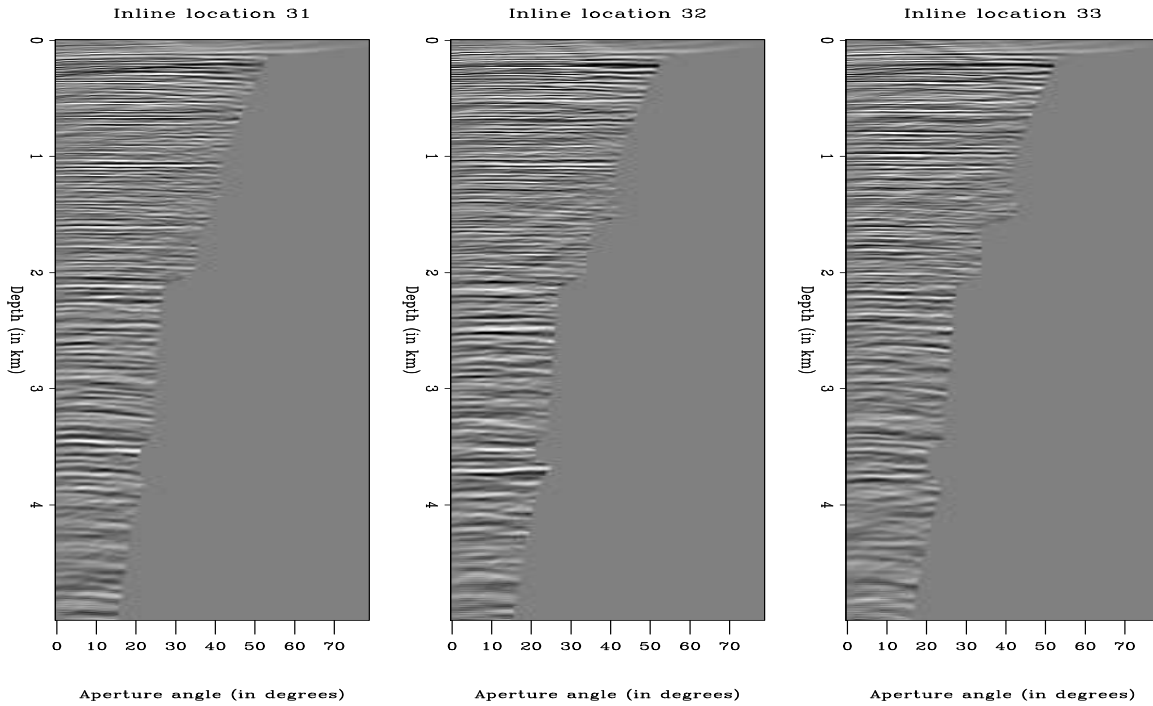


Figure 12: Line 750: ADCIGs at different locations obtained after isotropic migration. pierre1-ADCIGs [CR]

the CMP axis on line 750. Figure 13 presents the estimates of the interval vertical velocity obtained from surface seismic data, measurement of sonic velocity and checkshot. It illustrates that the vertical velocity estimated from surface seismic data — under the assumption of isotropy — is accurately estimated down to a depth of around 2 km and is overestimated deeper between the Balder and BCU horizons. This overestimation is due to the presence of anisotropic rocks under the Balder layer. The velocity measured from surface seismic data (V_N) is equal to the vertical velocity (V_V) under the assumption of isotropy and flat layers. However, in an anisotropic medium, for flat layers and a VTI model, the expression of the NMO velocity becomes $V_N = V_V \sqrt{1 + 2\delta}$, where δ is the first Thomsen parameter. Since the velocity measured from seismic data, V_N , is larger than the velocity measured from sonic logs and checkshots, the anisotropic parameter δ probably can not be considered zero and takes significantly positive values.

Finally, we computed anisotropic velocity spectra from the three different ADCIGs illustrated in Figure 12. The first series of velocity spectra are semblance panels of ρ_{V_N} (Figure 14). The velocity spectra are computed by trying to fit the RMO curves in ADCIGs with only ρ_{V_N} . Figure 14 illustrates that the V_N was well estimated by CGG since high semblance values are centered around perturbation values close to zero.

Semblance panels of ρ_{V_H} are presented in a second series of velocity spectra (Figure 15). The second series of velocity spectra is semblance panels of ρ_{V_H} . The velocity spectra are computed by trying to fit the RMO curves in ADCIGs with only ρ_{V_H} , assuming that V_N is

Figure 13: Comparison of the vertical velocities at the location of well 3_9a-8. The different velocities are estimated from seismic surface data (assuming isotropy), measurement of sonic velocity and checkshots. `pierre1-Sonic_log` [NR]

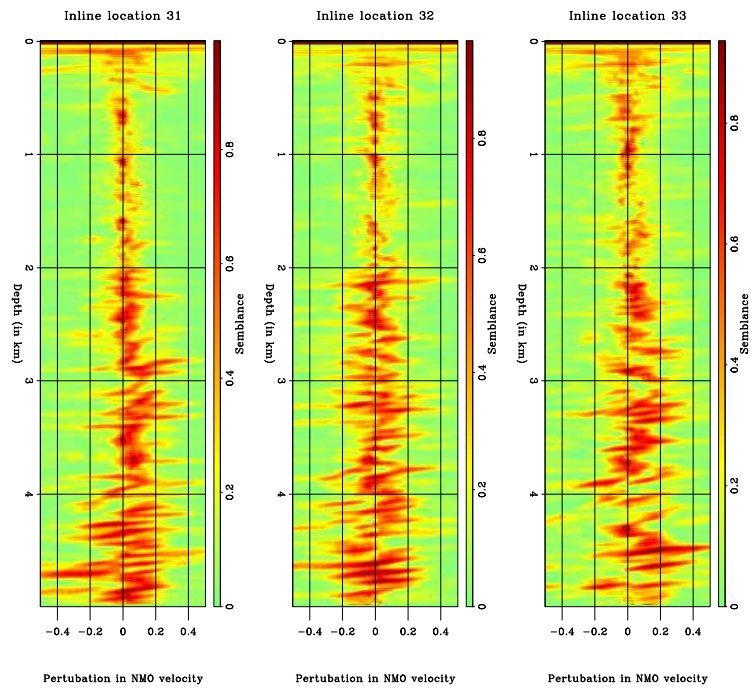
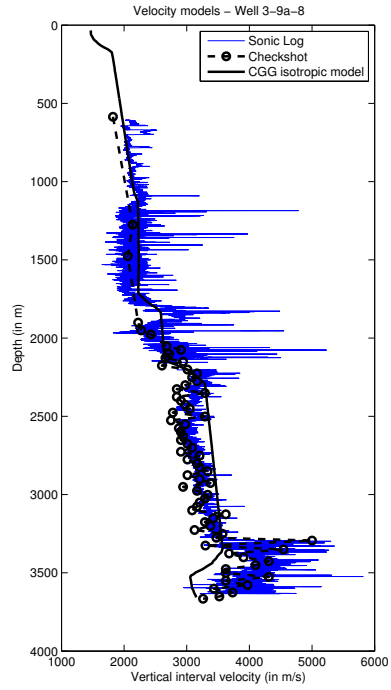


Figure 14: Velocity spectra computed at different inline locations by trying to fit the RMO curves in ADCIGs with only ρ_{VN} . `pierre1-VN_spectra` [CR]

correct. Figure 15 illustrates the presence of anisotropy at a depth greater than 2 km. More specifically, the fact that the energy is centered at negative values of the horizontal velocity perturbations indicates that the horizontal velocity we used for the migration is smaller than the true horizontal migration velocity. Since our migration was isotropic, we assumed that $V_H = V_N = V_V$. As a consequence, we can infer that below 2 km depth, the anisotropic parameter ϵ probably should not be set to zero and will take significant positive values ($V_H = V_V \sqrt{1 + 2\epsilon}$).

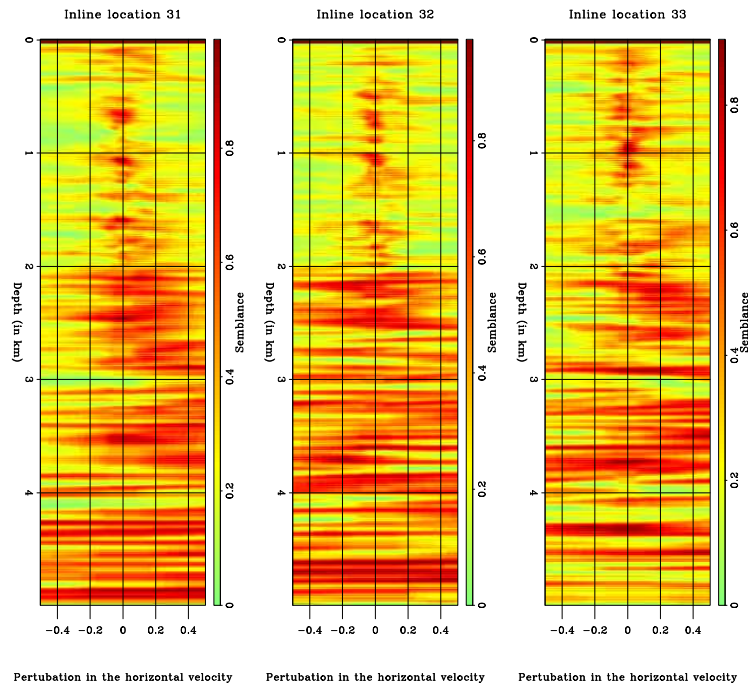


Figure 15: Velocity spectra computed at different inline locations by trying to fit the RMO curves in ADCIGs with only perturbations in the horizontal velocities. pierre1-VH_spectra [CR]

CONCLUSIONS

We presented an anisotropic migration velocity analysis (MVA) method based on the computation and analysis of angle-domain common-image gathers (ADCIGs) in conjunction with anisotropic wavefield-continuation migration. This method is based on the assumption of flat reflectors and vertically transversely isotropic (VTI) media but could also be generalized to dipping reflectors and tilted transversely isotropic (TTI) media. Our method has the great advantage of being based on migrated gathers and allows the iterative estimation of anisotropic parameters. We analyzed synthetic data to determine the accuracy and convergence of the estimation method. We showed that vertical velocities could not be resolved by our method but that even if we used a first-order approximation of the RMO function, picking the anisotropic migration velocities in semblance panels improves the overall anisotropic parameter estimation. We performed anisotropic MVA on a real data set acquired in the North Sea. Starting

from an isotropic velocity model, we demonstrated the validity of our estimation method by showing it indicates the presence of anellipticity in the layers that are stratigraphically interpreted as anisotropic and for which well data do not match seismic data migrated under isotropy assumption.

ACKNOWLEDGMENTS

We would like to thank TOTAL for making the real data set available for SEP through the generous efforts of Jérôme Guilbot et Frédéric Joncour.

REFERENCES

- Biondi, B. and T. Tisserant, 2004, 3-D angle-domain common-image gathers for migration velocity analysis: *Geophysical Prospecting*, **52**, 575–591.
- Biondi, B., 2005a, Angle-domain common image gathers for anisotropic migration: SEP-**123**.
- Biondi, B., 2005b, Residual moveout in anisotropic angle-domain common image gathers: SEP-**123**.
- Dellinger, J. and F. Muir, 1985, Two domains of anisotropy: SEP-**44**, 59–62.
- Jousselin, P. and B. Biondi, 2006, Residual moveout in anisotropic angle-domain common image gathers with dipping reflectors: SEP-**124**.
- Rickett, J. and P. Sava, 2002, Offset and angle-domain common image-point gathers for shot-profile migration: *Geophysics*, **67**, 883–889.
- Sava, P. and S. Fomel, 2003, Angle-domain common-image gathers by wavefield continuation methods: *Geophysics*, **68**, 1065–1074.
- Tsvankin, I., 2001, *Seismic Signatures and Analysis of Reflection Data in Anisotropic Media*: Elsevier Science.

APPENDIX A

PHASE AND GROUP ANGLES AND VELOCITIES

In anisotropic wave propagation the phase angles and velocities are different from the group angles and velocities. In this appendix we briefly review the concepts of phase and group angles and velocities and the relationships between these physical quantities.

The transformation from phase velocity \tilde{V} to group velocity V is conventionally defined as the following (Tsvankin, 2001):

$$V = \sqrt{\tilde{V}^2 + \left(\frac{d\tilde{V}}{d\tilde{\theta}}\right)^2}, \quad (\text{A-1})$$

where $\tilde{\theta}$ is the phase propagation angle. The associated transformation from phase angles to group angles θ is defined as:

$$\tan\theta = \frac{\tan\tilde{\theta} + \frac{1}{V}\frac{d\tilde{V}}{d\tilde{\theta}}}{1 - \frac{1}{V}\frac{d\tilde{V}}{d\tilde{\theta}}\tan\tilde{\theta}}. \quad (\text{A-2})$$

Dellinger and Muir (1985) propose, and heuristically motivate, the following symmetric relations for the inverse transforms:

$$\tilde{S} = \sqrt{S^2 + \left(\frac{dS}{d\theta}\right)^2}, \quad (\text{A-3})$$

where \tilde{S} and S are respectively the phase slowness and the group slowness, and

$$\tan\tilde{\theta} = \frac{\tan\theta + \frac{1}{S}\frac{dS}{d\theta}}{1 - \frac{1}{S}\frac{dS}{d\theta}\tan\theta}. \quad (\text{A-4})$$

We use the heuristic relation in equation A-4 to derive some of the analytical results presented in this paper. Furthermore, we use all the above relationships to compute the kinematic numerical results presented in this paper.

Mapping of 3-D multiples to image space: An example with a Gulf of Mexico dataset

Gabriel Alvarez

ABSTRACT

I migrate a real 3D seismic dataset from the Gulf of Mexico with shot profile migration and use it to illustrate the mapping of 3D multiples from data space to image space. The dataset contains specular water-bottom multiples, peg-leg multiples associated with a large, shallow salt body, and diffracted multiples originating at the salt edges. Both the water bottom and the salt body have significant cross-line dip which makes it difficult to model the trajectory of the multiples. The location of the multiples in the image domain is severely affected by the presence of the salt and thus do not follow the geometry of the multiple-generating interface. As a consequence, some multiples could easily be interpreted as primaries. I show, by computing subsurface offsets for one sail-line, that the multiples map away from the zero-subsurface offset as they would in a purely 2D model.

INTRODUCTION

In complex subsurface areas, the propagation trajectory of primaries and multiples can be very complex. Therefore, in these areas, data-space methods to attenuate multiples based on their residual moveout after NMO correction (Hampson, 1986) are likely to fail because NMO may not flatten the primaries and because the residual moveout of the multiples may depart significantly from being parabolic or hyperbolic.

The data-space alternative is SRME (Verschuur et al., 1992). Since SRME uses the data itself to predict the multiples, the complexity of the multiple trajectory is not an issue. Furthermore, no knowledge whatsoever is required about the subsurface. The problem with SRME, specially with 3D data, is that it requires regular, fine sampling, and large apertures in both the inline and cross-line directions. With standard streamer acquisition, and in the presence of cable feathering, these conditions are unlikely to be met in practice. In the cross-line direction in particular, cost and logistic considerations dictate that sampling be coarse and apertures small. The remedy is to apply large-scale interpolation of near offsets and streamers and extrapolation of cross-line offsets. In addition, data regularization is required to deal with cable feathering. A lot of research is currently being carried out on how to address these issues in a way that allows fast and accurate estimation of the multiple model.

An alternative to data-space methods is to attenuate the multiples after migration, *i.e.* in the image domain (Sava and Guitton, 2003). The main advantage of the image domain is that prestack migration can unravel the complex propagation of both primaries and multiples. In Subsurface Offset Domain Common Image Gathers (SODCIGs), the primaries are focused near the zero subsurface-offset line whereas the multiples are smeared along a curve toward the negative subsurface offsets (Alvarez, 2005). Although identification of the multiples is simple in SODCIGs, they are not the ideal domain to attenuate them. Instead, we can transform the SODCIGs to Angle Domain Common Image Gathers (ADCIGs) that are a function of the reflection and azimuth angle (Biondi and Tisserant, 2004). In this domain, the primaries will be flat as a function of the aperture angle for the azimuth of the reflection plane, but will have curvature for other azimuths. The multiples, on the other hand, will not be flat even for the azimuth of the multiple-generating interface, but will instead exhibit a residual moveout that in 2D can be approximated, to a first order, by a simple trigonometric equation (Alvarez, 2005). This equation in turn can be used as the kernel of a Radon transform to focus the primaries and multiples to separate regions of the Radon domain, thereby allowing for their attenuation.

Here I use a real 3D dataset from the Gulf of Mexico to illustrate the mapping of the multiples to image space. The dataset, provided by VeritasDGC, was acquired over a complex salt body with structure in both the inline and the cross-line directions. The water-bottom itself dips about 11 degrees in the cross-line direction making the mapping of the multiples in the image-space cube difficult to predict. The presence of the salt distorts the multiples so much that in many cases it is difficult to discern with certainty which events are multiples and which events are primaries in the migrated cube. An important tool for that purpose are the SODCIGs where the multiples can be identified by their tendency to map toward the negative subsurface offsets. I illustrate this situation by computing SODCIGs for one sail-line. The goal is to compute SODCIGs inline and crossline for the entire area, but at the time of writing this report the results are not yet available. I show that even in the SODCIGs for one sail-line, however, the multiples are identifiable and clearly distinguishable from the primaries.

DESCRIPTION OF THE DATA

Geometry of acquisition

The 3D dataset consists of 20 sail lines each with four active streamers and dual flip-flop shooting. The separation between streamers is 160 m and between receivers is 25 m. The shot interval is 37.5 m (between the flip and the flop). The minimum offset inline is 240 m and each streamer has 288 receivers for a maximum inline offset of 7175 m. Figure 1 shows the acquisition template. Figure 2 shows a map view of the subset of the shots used in this study. Although most sail lines were straight in the East-West direction, a few had significant curvature.

The strong currents present in the area caused significant feathering. Figure 3 shows an example for the sail-line at cross-line distance 11440 m. For most shots, the feathering was in the same South-North direction. Figure 4 shows the fold of coverage that in some places

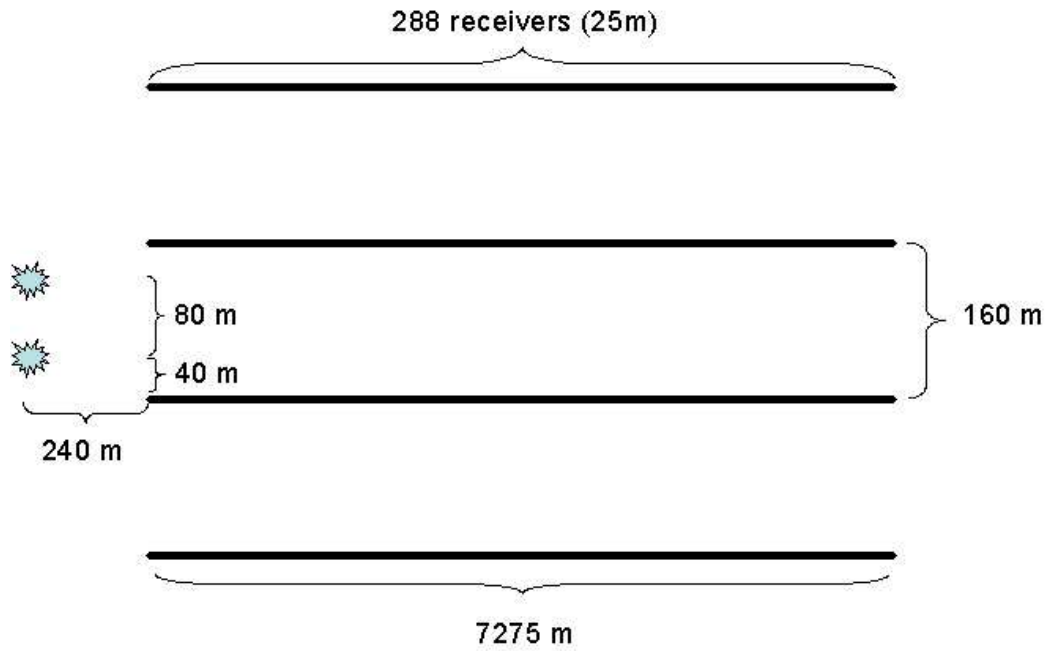


Figure 1: Sketch of the basic acquisition geometry `gabriel1-acq_sketch1` [NR]

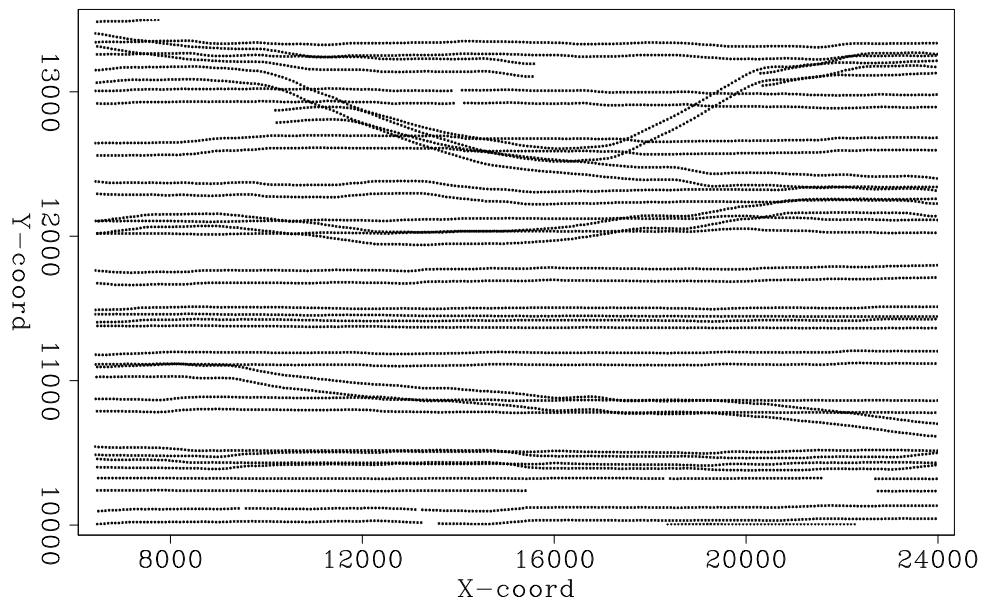


Figure 2: Map view of the source locations. `gabriel1-shots_map` [CR]

depart significantly from its design value of 48. Some of the short source lines in Figure 2 we acquired as infill to avoid large coverage holes.

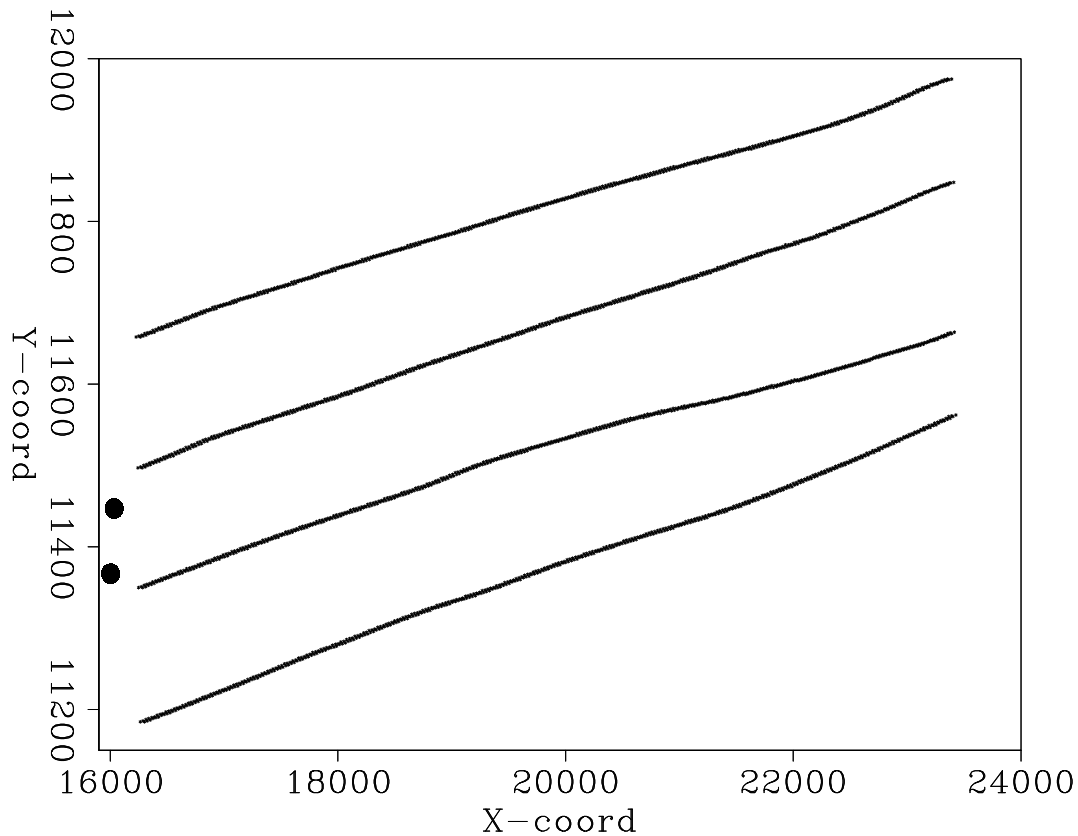


Figure 3: Map view of the receiver cables for one shot illustrating typical feathering. [gabriel1-feathering](#) [CR]

Velocity model

The velocity model (provided by Norsk Hydro), shows a large, complex salt body with steeply dipping flanks in both inline and cross-line directions (Figure 5). The water-bottom itself dips in some places as much as 11 degrees in the cross-line direction, although it is relatively flat in the inline direction.

Raw data

Figure 6 shows a typical shot record with the traces ordered one streamer after the next. The traveltimes are relative to an arbitrary reference. The water-bottom multiple is seen in the close-up look from one the streamers in Figure 7 at about 4 s on the near offset trace. Notice also the diffractions and complex moveout of some of the reflectors due to the 3D nature of the subsurface and the complex wave propagation it produces.

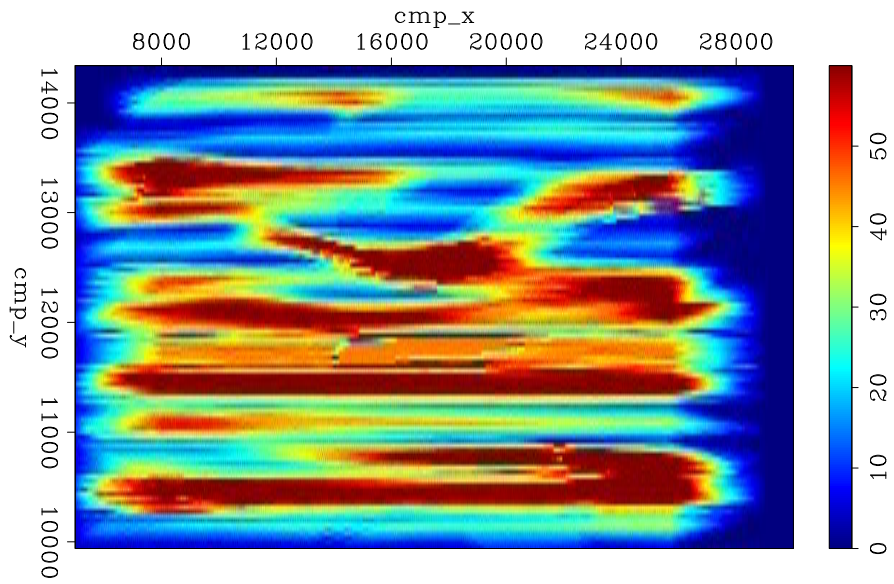


Figure 4: Fold map illustrating relatively uniform coverage. `gabriel1-fold` [CR]

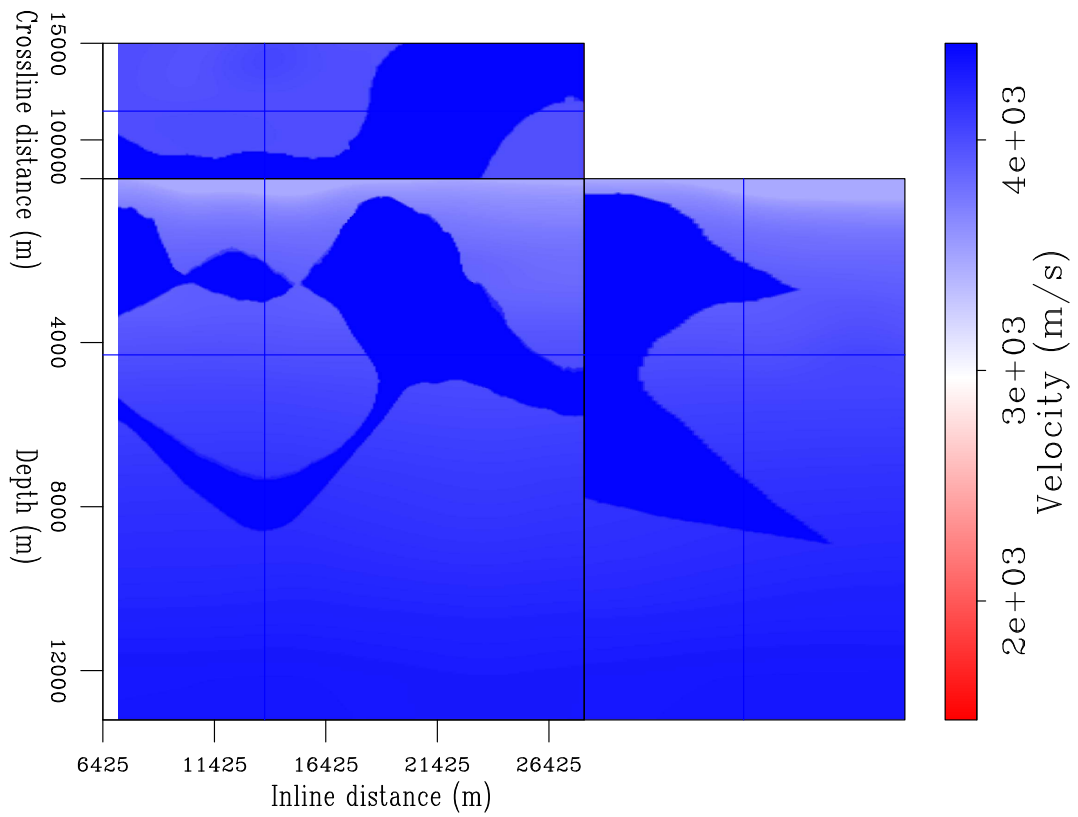


Figure 5: Subsurface velocity model. Note the strong dips in both the inline and cross-line directions. `gabriel1-vmodel` [CR]



Figure 6: A typical shot record showing the data from the four streamers. `gabriel1-shot1` [CR]

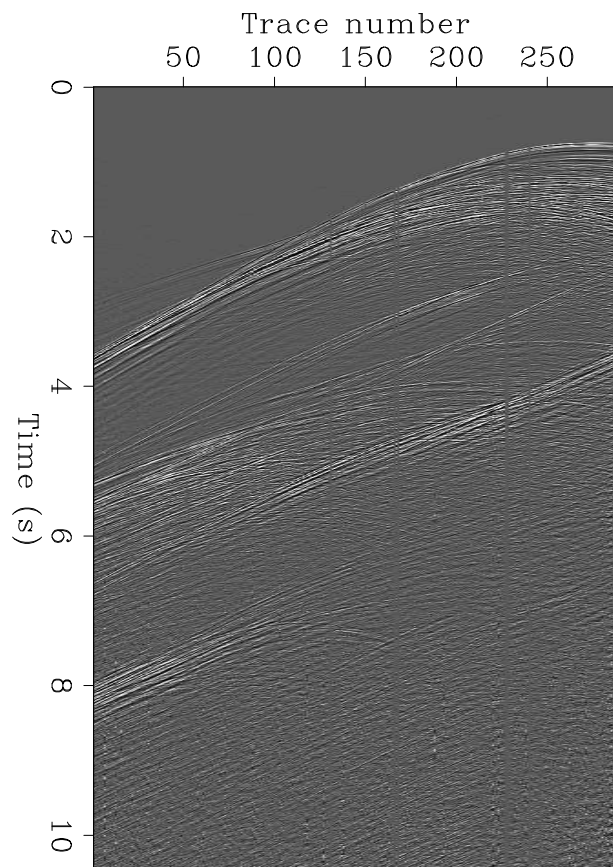


Figure 7: A close-up view of the shot for one of the streamers. `gabriel1-shot_str1` [CR]

SHOT PROFILE MIGRATION

In order to efficiently migrate the data with shot profile migration, I removed the time samples before the water-bottom arrival and compensated by applying a linear frequency shift to the source wavelet. The propagation through the water layer was done in two depth steps and from there down the depth sampling was 10 m. For the sake of computer time, only two reference velocities were used to propagate the data at each depth step. These reference velocities were computed with Lloyd's algorithm (Clapp, 2004). The aperture in the inline direction was 9 km (1.2 km in front of the streamer and 0.6 km at the end of the streamer) and the cross-line aperture was 4.8 km (2.4 km in the up-dip direction and 1.4 km in the down-dip direction). Four hundred frequencies were used from 6 to 40 Hz. Figure 8 shows an inline and a cross-line sections taken from the migrated cube. The depth axis is with respect to an arbitrary reference. The inline section is at crossline 10240 m and the crossline section is taken at inline 12000 m. The migrated data was filtered in depth and a gain proportional to the depth squared was applied for display purposes. Since it is not easy to identify the multiples in Figure 8, I

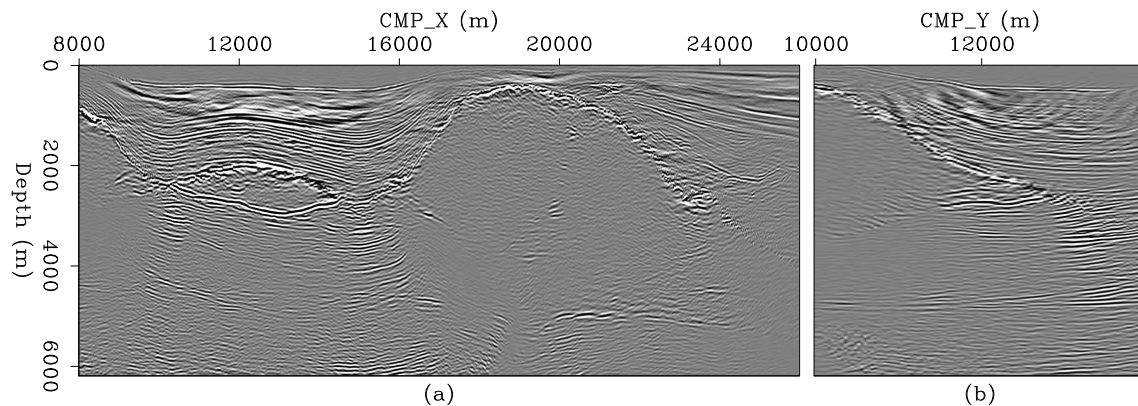


Figure 8: Shot profile migration. Panel (a) is the inline section at crossline 11440 m. Panel (b) is the crossline section at inline 12000 m. [gabriel1-mignooffs1](#) [CR]

windowed the image below the salt body between 8000 and 16000 m in the inline direction as shown in Figure 9. The crossing events are an indication of the presence of the migrated multiples and their interference with the legitimate, possibly weak subsalt primaries. Again, it is not immediately obvious which of these reflections are primaries and which are multiples without the help of prestack migrated images as a function of subsurface offset or aperture and azimuth angles. Computing subsurface offsets, however, is very expensive and at the time of this report I have computed only inline subsurface offsets and only for one sail line. The results are presented in the next section.

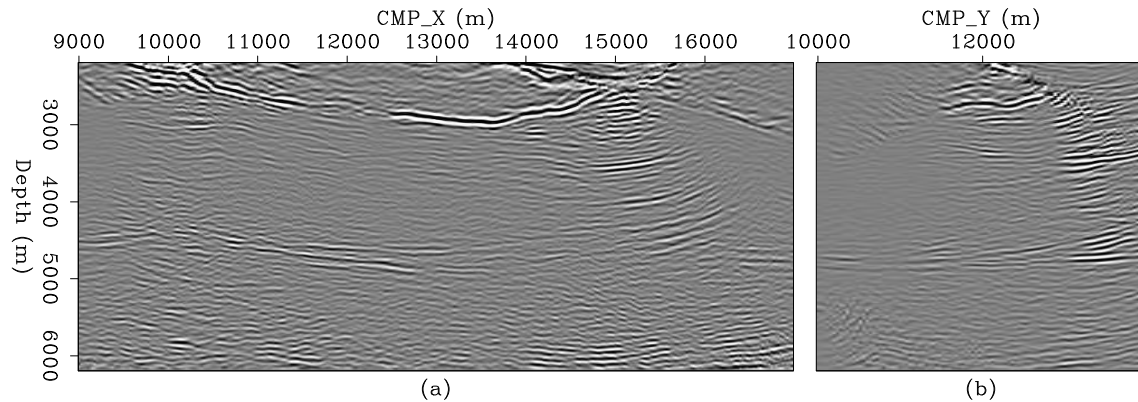


Figure 9: Close up view of the migrated cube to show the interference between the multiples and the weak subsalt primaries. Panel (a) is the inline section at crossline 11440 m. Panel (b) is the crossline section at inline 12000 m. gabriel1-mignooffs1_win [CR]

DISCRIMINATION OF MULTIPLES

Inline image gathers

Figure 10 shows the same inline section as in Figure 8 but this time taken from the migration of only one sail line. Notice that the salt boundaries are poorly imaged because of the complexity of the salt geometry in the cross-line direction. Much more data needs to be migrated from the cross-line direction in order to get these reflections as can be seen by comparing with Figure 8. The right hand panel is now a subsurface offset gather taken at the center of the window in Figure 9 (CMP position 13200 m). Although not all the multiples are imaged in this migration because of the lack of cross-line data as indicated for the salt reflections, those imaged can be identified by their moveout away from zero toward the negative subsurface offsets in the offset gather. Notice in particular the multiple at about 4 km depth and -400 m subsurface offset. Figure 11 shows three subsurface offset gathers taken at different lateral positions. The first SODCIG (panel (a)), taken at about the center of the window in Figure 9(a) (CMP position 13200 m), shows evidence of multiples at about 4000 m depth at -400 m half-subsurface offset. This multiple is difficult to identify in Figure 9 because it essentially stacks out. It is, however visible in the constant subsurface offset section of panel (b) in Figure 12 (left oval). The second SODCIG (panel (b)), taken below the big salt body in Figure 8(a) (CMP position 20800 m) shows no clear evidence of multiples below the salt. The strong event below 20000 m and about 5000 m in Figure 8 is actually the base of the salt and the events below it are subsalt primaries (see also the oval in panel (a) of Figure 12). The last SODCIG, (panel c), taken where the sediments meet the salt flank (CMP position 24900 m), show evidence of multiples below 4000 m depth. To further illustrate this point, Figure 12 shows a comparison between the image taken at zero subsurface offset, which should be mostly (but not exclusively) primaries, and that obtained at -400 m half-subsurface offset, which should be mostly multiples. Notice in particular the multiple above a depth of 3000 m to the right of the inline distance of 24000 m as indicated by the right oval. Also notice the flattish event at about 4000 m depth and 13000 m

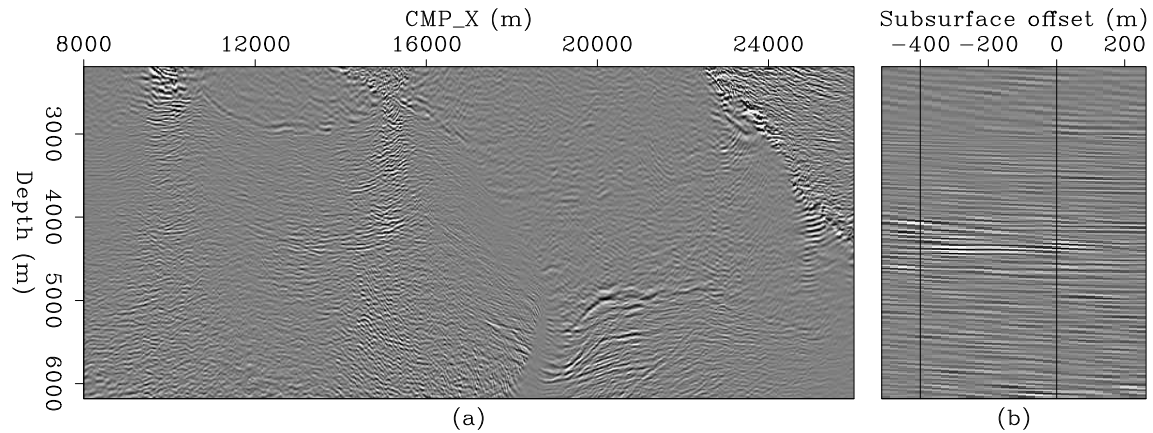


Figure 10: Migration of one sail line. The left panel is an inline subsurface offset common image gather. [gabriel1-2dmigoffs1](#) [CR]

inline distance (left oval). This is likely to be a multiple obscuring the weak primaries. Since I

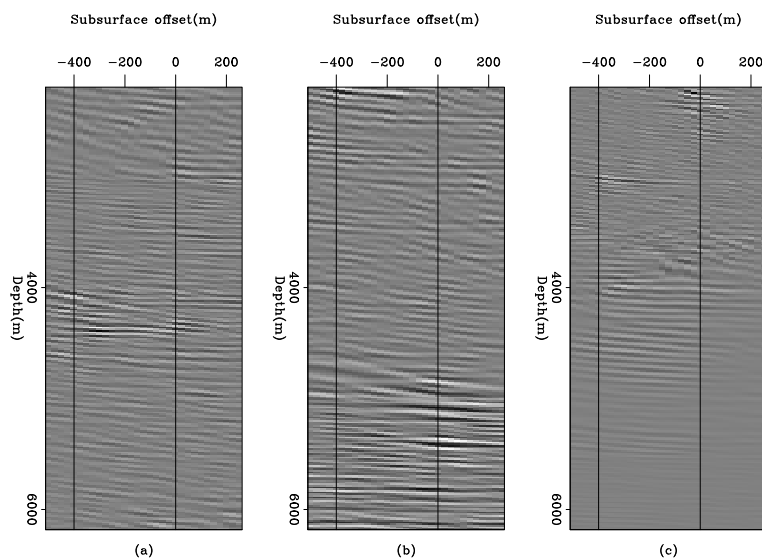


Figure 11: Subsurface offset common image gathers taken at lateral positions (a): 13200 m, (b): 20800 m and (c): 24930 m. [gabriel1-2dsodcigs1](#) [CR]

expect to attenuate the multiples in ADCIGs rather than SODCIGs, it is interesting to see how the multiples in this 2D migration are mapping to ADCIGs. This is illustrated in Figure 13 that shows ADCIGs for the same SODCIGs shown in Figure 11. Again, notice in panel (a) the down curvature of the multiple at about 6000 m at zero aperture angle. There seems to be another multiple at above 7000 m depth. In contrast, no clear evidence of multiple can be seen in the ADCIG in panel (b). In panel (c) there is some evidence of multiples at a depth of about 6300 m depth but at the same depth there seem to be primaries as well. The situation will probably be more clear once the ADCIG is computed after migrating all the data.

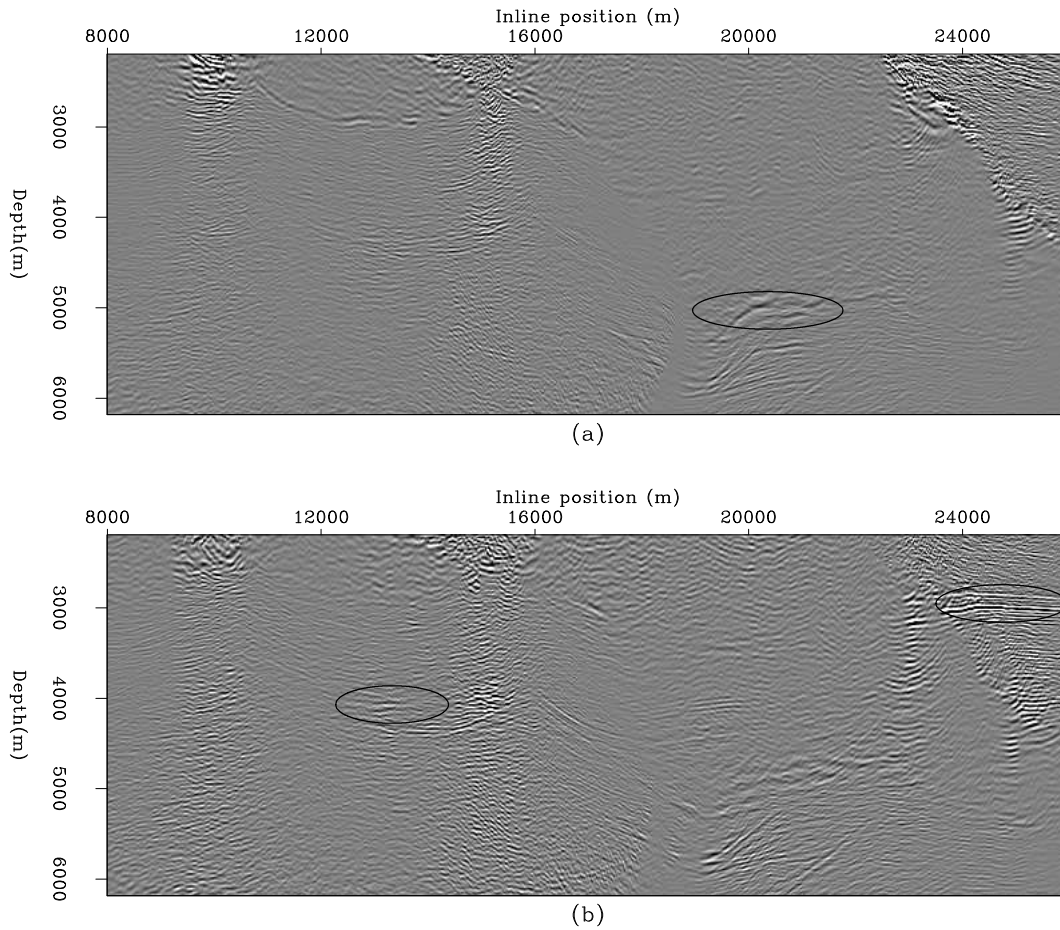


Figure 12: Common subsurface offset sections taken at (a): 0 and (b): -400 m half-subsurface offset. [gabriel1-2dcoffs1](#) [CR]

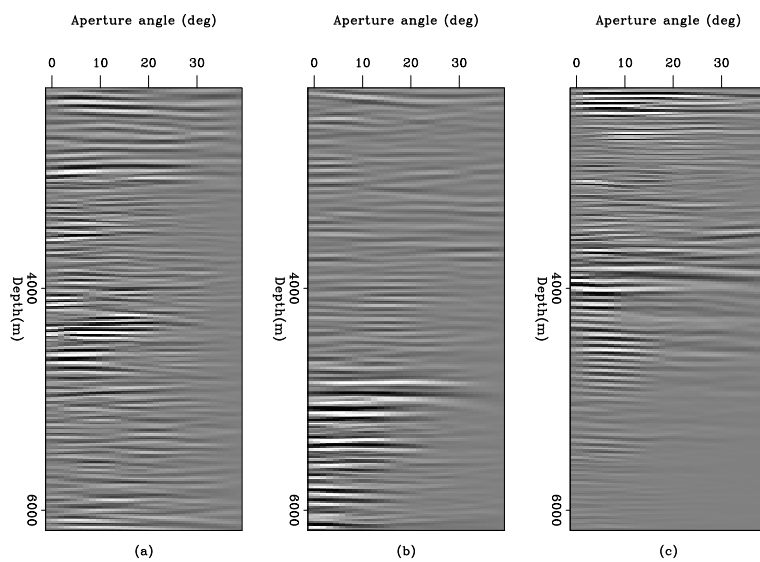


Figure 13: Angle domain common image gathers corresponding to the subsurface offset domain common image gathers in Figure 11 [gabriel1-2dadcigs1](#) [CR]

DISCUSSION

In complex areas, the image space is an attractive domain to attenuate the multiples, provided that we can design a Radon transform to separate them from the primaries. The presence of large salt bodies and in particular their steeply dipping salt flanks in the cross-line direction severely distort the imaging of the multiples. A full 3D migration is necessary to image the multiples. In order to discriminate between primaries and multiples, and to attenuate the multiples, we need to compute prestack image gathers as a function of subsurface offset or aperture and azimuth angles. Computing prestack images is expensive, but they can be used not only to attenuate the multiples but also to assess the accuracy of the migration velocity model and even to back project residual moveout information into velocity corrections. The expense of computing the full prestack image (inline and cross-line subsurface offsets and from them angle gathers as a function of aperture angle and reflection azimuth) is thus well worth.

At a relatively small additional cost (an additional convolution), it is attractive to use the image space version of SRME to get an initial estimate of the multiple model (Artman et al., 2007). I expect, however, that diffracted multiples, and specular multiples from reflections with a significant cross-line dip components, will not be accurately modeled. For these multiples, exploiting their particular behavior in terms of their residual moveouts as a function of aperture angle and reflection azimuth, is the best way to attenuate them.

CONCLUSION AND FUTURE WORK

Complex subsurface distorts multiples and make their identification difficult in the image space. We can either compute an approximate multiple model with an image space version of SRME or, better, compute full 3D angle gathers in order to exploit the different characteristics of the residual moveout of the multiples and the primaries as a function of aperture angle and reflection azimuth to attenuate them. This is the focus of my current research.

ACKNOWLEDGMENTS

I would like to thank VeritasDGC for providing the dataset and Dr. Jan Pajchel of Norsk Hydro for providing the velocity model and for his help in securing permission to use the dataset.

REFERENCES

- Alvarez, G., 2005, Mapping of water-bottom and diffracted 2D multiple reflections to image space: , Stanford Exploration Project, SEP-123., 129-154.
- Artman, B., G. Alvarez, and K. Matson, 2007, Image-space surface-related multiple prediction: Geophysics. Accepted for publication.

- Biondi, B. and T. Tisserant, 2004, 3D angle-domain common-image gathers for migration velocity analysis: *Geophysical Prospecting*, **62**, 575–591.
- Clapp, R., 2004, Reference velocity selection by a generalized lloyd method: 74th Annual International Meeting, SEG, Expanded Abstracts, 981–984.
- Hampson, D., 1986, Inverse velocity stacking for multiple elimination: *Canadian Journal of Exploration Geophysicists*, **22**, 44–55.
- Sava, P. and A. Guitton, 2003, Multiple attenuation in the image space: 73rd Annual International Meeting, SEG, Expanded Abstracts, 1933–1936.
- Verschuur, D., A. Berkhout, and C. Wapenaar, 1992, Adaptive surface-related multiple elimination: *Geophysics*, **57**, 1166–1167.

Improving multiple prediction in image space using ADCIGs for limited-offset recordings

Madhav Vyas

ABSTRACT

Auto-convolution is a convenient way of generating multiple models and is the basis for Surface Related Multiple Prediction (SRMP). The completeness of the multiple model, however, relies on recording all the primary paths that contribute to multiple generation. In practice, with limited offset recordings and in areas of complex subsurface geometries (especially steep dips), we might record only the multiple path and not the primary, leading to incomplete multiple models. In image space, this translates to modeling multiples at fewer opening angles than are actually present. In this article, I show that the Angle Domain Common Image Gathers (ADCIGs) of multiple models provide useful angular information which may be used to infill or extrapolate missing angles and account for the missing multiples in the model generated using SRMP.

INTRODUCTION

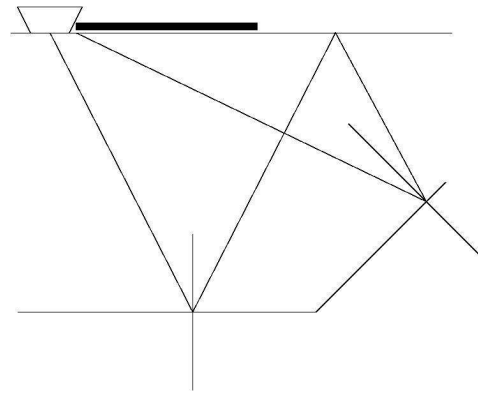
Removing multiples from seismic data is essential to producing interpretable subsurface images. Multiples can be categorized on the basis of kinematics and the mechanism of generation. Multiples can be of different types, including specularly reflected or diffracted multiples, peg-leg multiples, surface-related multiples or inter-bed multiples. Strong surface related multiples associated with the free surface are common in marine surveys. With the increase in marine acquisition, surface-related multiples have received more attention, and techniques for handling and removing these multiples have improved.

Kinematics of surface-related multiples can be predicted by auto-convolution of recorded data (Anstey and Newman, 1966). However, due to discrepancies between modeled and observed multiples in terms of their amplitudes and frequency content, direct subtraction is not possible. Various iterative and adaptive subtraction schemes have been proposed in the past to address this issue. The problem of multiple removal can also be attacked in image space instead of in the data domain (Sava and Guitton, 2003, 2005; Alvarez et al., 2004). There are some intuitive reasons to prefer image-space prediction over data-space modeling. First, the image space is much smaller than the data space, and hence there are associated computational savings. Second, if we assume perfect knowledge of the velocity, discriminating between multiples and primaries with the help of common-image-point gathers (offset and angle) is fairly straightforward.

Artman and Matson (2006) extended the SRMP approach through commutability of wave-field extrapolation and convolution to predict multiples in image space during shot-profile migration. The image-space SRMP algorithm is computationally cheaper than first carrying out SRMP in the data space and then migrating the data and the multiple model independently to the image space. However, since SRMP is based on convolving recorded data with itself, it yields perfect multiple prediction only when we record all the primary paths that lead to multiple generation. This is true when either our recording geometry is infinite or the subsurface structure is flat. In practice, neither of the aforesaid conditions are likely; in addition, there are situations when the primary escapes the recording geometry, but the corresponding multiple, after hitting a steeply dipping reflector bounces back in and gets recorded. Figure 1 shows the ray path for one such possibility. It is not possible to predict this multiple using SRMP, because we do not record the contributing primaries.

Figure 1: A ray path illustrating the situation where the primary escapes the recording geometry but the multiple bounces back and gets recorded.

`madhav1-raypath` [NR]



It is difficult to model such multiples; however, image space gives us a better chance to handle them. We can make use of the redundancy present in the image space to address this problem. Multiple events in the data space migrate to a single point in image space (if perfect multiple velocity) but with different opening angles, and a missing event in data space translates to a missing angle in image space. If we can spread the information consistently from one opening angle to another, we may be able to reconstruct the missing part of the multiple model. When the migration velocity is perfect, events in the image space will appear flat in the angle domain, and we can easily infill the missing angles to reconstruct the multiple model. But in general, multiples have very different velocities than the primaries recorded at similar times and show curvature in the angle domain when migrated with the true velocity. The task of infilling is thus not as straightforward as it is for flat gathers. There are two ways to approach this: either we can migrate with the multiple velocity, do infilling and then demigrate, or alternatively, we can use Radon-style transforms to infill gathers with curvature.

In this article I first demonstrate the problem using a simple synthetic example and then illustrate a possible corrective approach. I give a second example using the Sigsbee model, which is a more realistic case.

THEORY - SRMP

A multiple event can be modeled or predicted by convolution of two primary traces. Only surface-related multiples (multiples that reflect at the surface) can be estimated by such a prediction scheme. Understanding the assumption of convolving raw traces with themselves rather than with the primaries, multiple prediction (SRMP) can be written in the Fourier domain (Berkhout and Verschuur, 1997) as

$$M(\mathbf{x}_g; \mathbf{x}_s, \omega) = \sum_{\mathbf{x}_a} R(\mathbf{x}_g; \mathbf{x}_a, \omega) R(\mathbf{x}_a; \mathbf{x}_s, \omega), \quad (1)$$

where R is the data-space volume of shot-gathers defined at geophone (x_g) and source (x_s) locations on the acquisition surface. M is the multiple model and ω is the frequency. Equation 1 is a trace-by-trace operation to produce the multiple prediction with any geophone-source combination. Artman and Matson (2006) showed that equation 1 can be re-written in terms of wavefields ($U(\mathbf{x}, \mathbf{x}_s)$) as

$$M_{z=0}(\mathbf{x}; \mathbf{x}_s, \omega) = \sum_{\mathbf{x}_a} U_{z=0}(\mathbf{x}; \mathbf{x}_a, \omega) U_{z=0}(\mathbf{x}_a; \mathbf{x}_s, \omega). \quad (2)$$

With a little bit of algebra and the use of reciprocity, Artman and Matson (2006) also showed that equation 2 reduces to

$$m_z(\mathbf{x}, \mathbf{h}) = \sum_{\mathbf{x}_s} \sum_{\omega} U_z(\mathbf{x} + \mathbf{h}; \mathbf{x}_s, \omega) U_z(\mathbf{x} - \mathbf{h}; \mathbf{x}_s, \omega), \quad (3)$$

where m_z is the multiple model in image space defined at the image coordinates, surface location x and offset h . A direct analogy can be drawn between equation 3 and the imaging condition for shot-profile migration, the difference being that the shot wavefield is now replaced by the receiver wavefield.

Using the scheme proposed above, multiple prediction can be carried out in the image space, which is theoretically equivalent to doing SRMP in the data space, followed by migration. In this article, I use both the image-space SRMP and data-space SRMP to generate multiple models.

SYNTHETIC DATA

I generate a synthetic data set using finite-difference modeling for the velocity model given in Figure 2. The velocity model is a combination of a flat layer and a layer having a dip of 30 degrees. The simulation is done with a free surface condition to model multiple events as well. I modeled about 225 shots with offsets ranging from -8000 ft to 8000 ft and shot spacing of 40 ft. Figure 3 is a sample shot record corresponding to a shot located at a surface location of 5000 ft. In the given shot record we have primaries and both first- and second-order multiples coming from the flat as well as the dipping reflector. There are also different types of first-order multiples having varied trajectories, including multiple bounces on the flat layer,

multiple bounces on the dipping layer and one bounce each on the flat and dipping layers. Finally, there are second-order multiple events which have higher degrees of freedom in terms of possible ray combinations and have further complicated trajectories. Most of the multiple analysis carried out henceforth focuses on first order multiples.

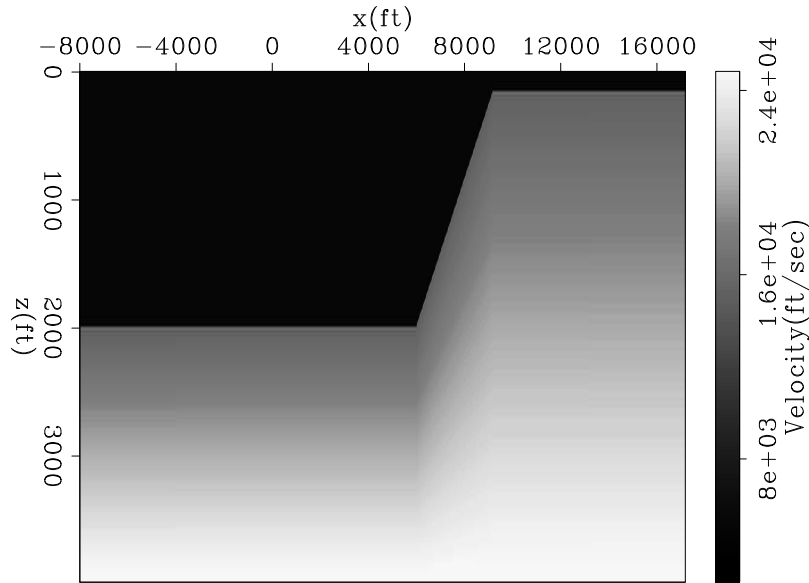


Figure 2: Velocity model used for modeling the synthetic data `madhav1-vel.dip1` [ER]

First Order Multiples - Analytics

To identify different multiples and to understand their behavior, I analytically modeled the ray paths for all possible first-order multiple events for the given synthetic model. For simplicity of referencing to these events I use the nomenclature given in Table 1.

Table 1. Nomenclature for different first order multiples.

Type	Ray-path	Name
1	Both the bounces on the flat part	FF
2	First bounce on the flat part and second on the dipping	FD
3	First bounce on the dipping part and second on the flat	DF
4	Both the bounces on the dipping part	DD

Equations 4 and 5 give the travel time and offset as a function of θ (take-off angle) for the event FF,

$$t(\theta) = \frac{4d}{V \cos \theta}, \quad (4)$$

$$h(\theta) = 4d \tan \theta. \quad (5)$$

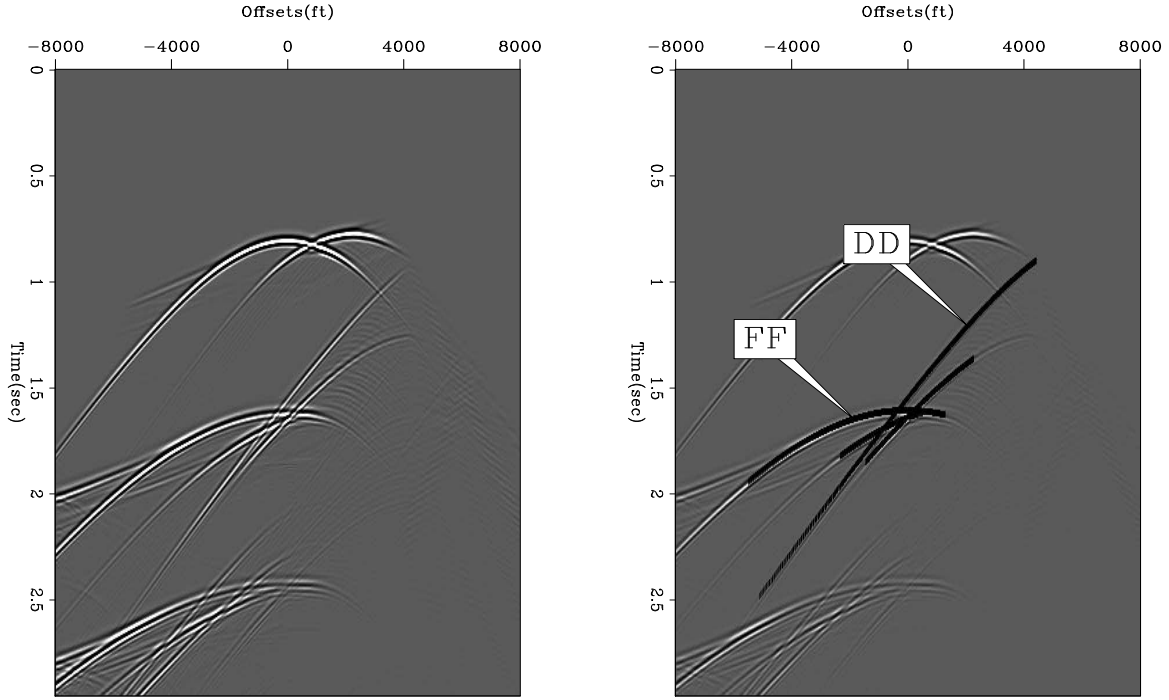


Figure 3: (a) A shot record corresponding to a shot located at a surface location of 5000. (b) Shot record with first order multiples modeled analytically overlaid on them madhav1-shot5000 [CR]

In the equations above, d is the depth of the flat reflector, V is the velocity, and h and t are offset and travel time respectively. There are different conditions and constraints on the value of θ depending on the shot location, which determines the range of take-off angles where these events take place and get recorded. Equations 6 and 7 give the expressions for travel time and offsets for the event FD.

$$t(\theta) = \frac{1}{V} \cdot \left\{ \frac{2d}{\cos\theta} + \frac{(x_d + \frac{d}{\tan\alpha} - x_s - 2d \tan\theta)(\sin\alpha)}{\cos(\alpha - \theta)} \cdot \left[1 + \frac{\cos\theta}{\cos(2\alpha - \theta)} \right] \right\} \quad (6)$$

$$h(\theta) = [\sin\theta - \cos\theta \tan(2\alpha - \theta)] \cdot \frac{\sin\alpha}{\cos(\alpha - \theta)} \cdot \left[x_d + \frac{d}{\tan\alpha} - x_s - 2d \tan\theta \right] + 2d \tan\theta \quad (7)$$

In these equations, x_d is the horizontal location where the dipping reflector meets the flat layer, x_s is the source location and α is the dip of the dipping reflector. There are two other possibilities for the first-order multiples: DF and DD. Travel time and offsets are given in equations 8 and 9 for the first category and equations 10 and 11 for the second category.

$$t(\theta) = \frac{1}{V} \left\{ \left(x_d + \frac{d}{\tan\alpha} - x_s \right) \frac{\sin\alpha}{\cos(\theta - \alpha)} \left[1 + \frac{\cos\theta}{\cos(2\alpha - \theta)} \right] + \frac{2d}{\cos(2\alpha - \theta)} \right\} \quad (8)$$

$$h(\theta) = \left(x_d + \frac{d}{\tan\alpha} - x_s \right) \cdot \frac{\sin\alpha}{\cos(\theta - \alpha)} \cdot \{ \sin\theta - \cos\theta \tan(2\alpha - \theta) \} - 2d \tan(2\alpha - \theta) \quad (9)$$

$$t(\theta) = \frac{1}{V} \cdot [x_d + \frac{d}{\tan \alpha} - x_s] \cdot \frac{\sin \alpha}{\cos(\theta - \alpha)} \times \\ \times \left[1 + \frac{\cos \theta}{\cos(2\alpha - \theta)} + \frac{\cos \theta}{\cos(2\alpha - \theta)} \cdot \frac{\cos(\theta - \alpha)}{\cos(3\alpha - \theta)} + \frac{\cos \theta}{\cos(4\alpha - \theta)} \cdot \frac{\cos(\theta - \alpha)}{\cos(3\alpha - \theta)} \right] \quad (10)$$

$$h(\theta) = [x_d + \frac{d}{\tan \alpha} - x_s] \cdot \frac{\sin \alpha}{\cos(\theta - \alpha)} \cdot [\sin \theta \\ - \cos \theta \tan(2\alpha - \theta) - \frac{\cos \theta \cdot \cos(\theta - \alpha)}{\cos(3\alpha - \theta)} \cdot \{\tan(2\alpha - \theta) + \tan(4\alpha - \theta)\}] \quad (11)$$

Once again, all the above equations are functions of the parameter θ and are valid only for a range of θ values corresponding to angles at which the event actually takes place. On Figure 3 (b) are overlaid the first-order multiple events modeled using the above equations.

Surface Related Multiple Prediction

The next step is to model these multiples using SRMP. Ideally, when we record all the offsets, SRMP could perfectly model surface-related multiples. In this section I test how the SRMP algorithm performs when we do not have access to far offsets. To simulate this situation, I throw away half the modeled offsets, keeping only the offsets from -4000 ft to 4000 ft instead of -8000 ft to 8000 ft. We would expect SRMP to fail for events that bounce back into the recording geometry (Figure 1). For the given synthetic example, first-order multiples that have either one or both bounces on the dipping surface bounce back into the recording geometry (FD,DF,DD). In the subsequent analysis we focus on the multiple which gets back into the recording geometry after bouncing twice on the dipping surface (DD), though the same may apply to other kinds of multiple events as well.

To estimate first-order multiples using SRMP, we need to record two primary paths that contribute to the multiple. In Figure 4, I draw a crossplot corresponding to a shot at a surface location of 5000 ft. Where on X axis is the offset at which the multiple DD is actually recorded, and on Y axis is the offset of both the primaries contributing to this multiple. Note that for the multiple recorded at an offset of about -4000 ft, the corresponding primaries are recorded at offsets of -5800 ft and -1800 ft. When we limit the maximum recording offset to -4000 ft, we will not be able to model this multiple event as one of the primary events will not be recorded. Likewise, any multiple event having either of its primaries recorded at offsets greater than 4000 ft will not be modeled. The circled portion in the figure indicates that the multiples recorded at offsets between -4000 ft and -2000 ft will not be modeled as one of the contributing primaries come at an offset greater than the maximum recording offset (4000 ft). The maximum recording offset would thus limit us to be only able to model multiples recorded at offsets of -2000 ft or less.

Figure 5 shows the shot gather, the multiple model created using SRMP, and the gather after adaptively subtracting the multiple model. Notice that the tail of the particular multiple event DD is not modeled between offsets of -2000 ft to -4000 ft (circled), as predicted by the crossplot in Figure 4.

Figure 4: Crossplot between offsets of recorded multiples and primaries contributing to those multiples
madhav1-offsets [NR]

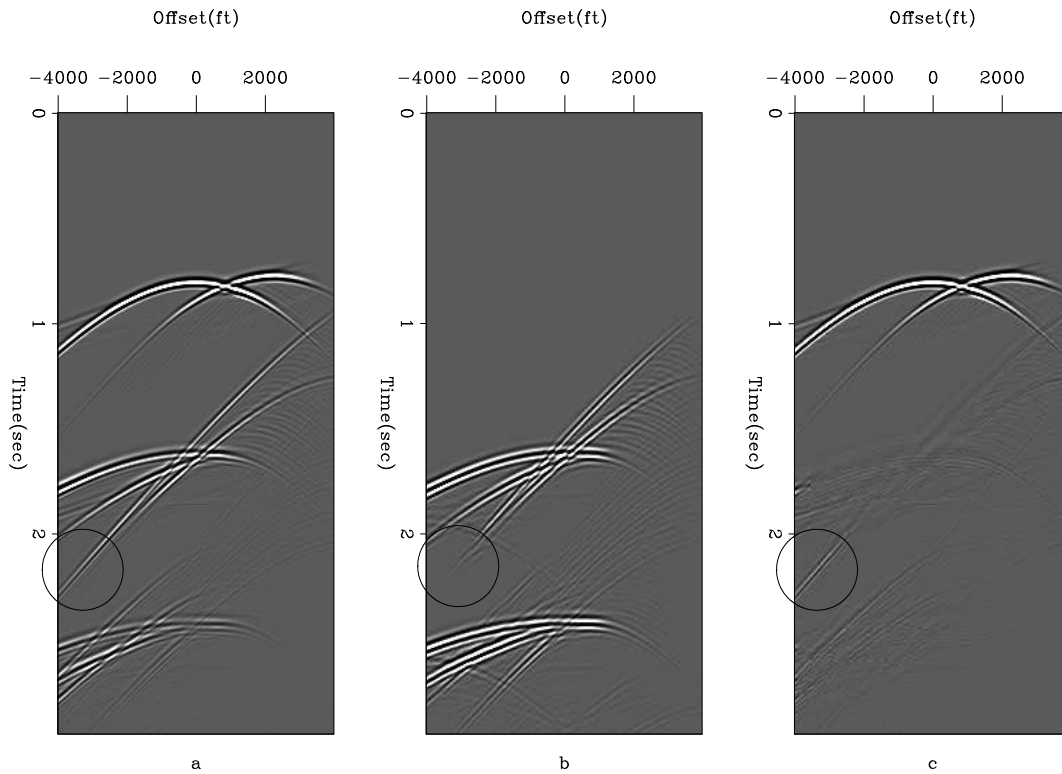
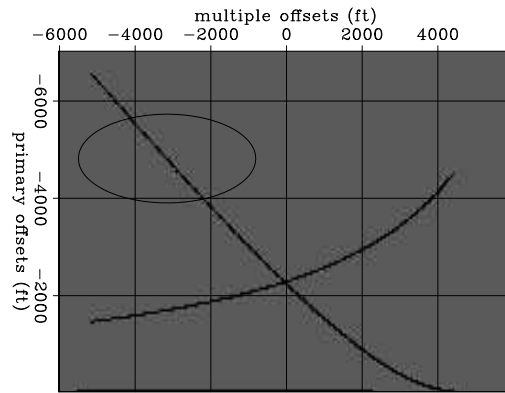


Figure 5: The (a) shot gather, (b) the multiple model and (c) the gather after subtracting the multiple model
madhav1-srme.so.5000 [CR]

Once we migrate the data after subtracting the multiple model obtained using SRMP, we expect to see some remains of the multiples in the image space, since we were unable to completely model all the multiple events. Figure 6 compares the two images obtained by migrations carried out on the data with and without multiple subtraction. The image obtained from the data after removing the multiple model is devoid of the flat portion of the first-order multiple, but some portion corresponding to the dipping layer remains. This dipping multiple in the image space corresponds to the event DD in data space; we were not able to model this perfectly because of limited-offset recording. Some multiple energy also remains in the bottom portion of the image, corresponding to the second-order multiple energy, but here I limit the analysis to the first-order multiple events.

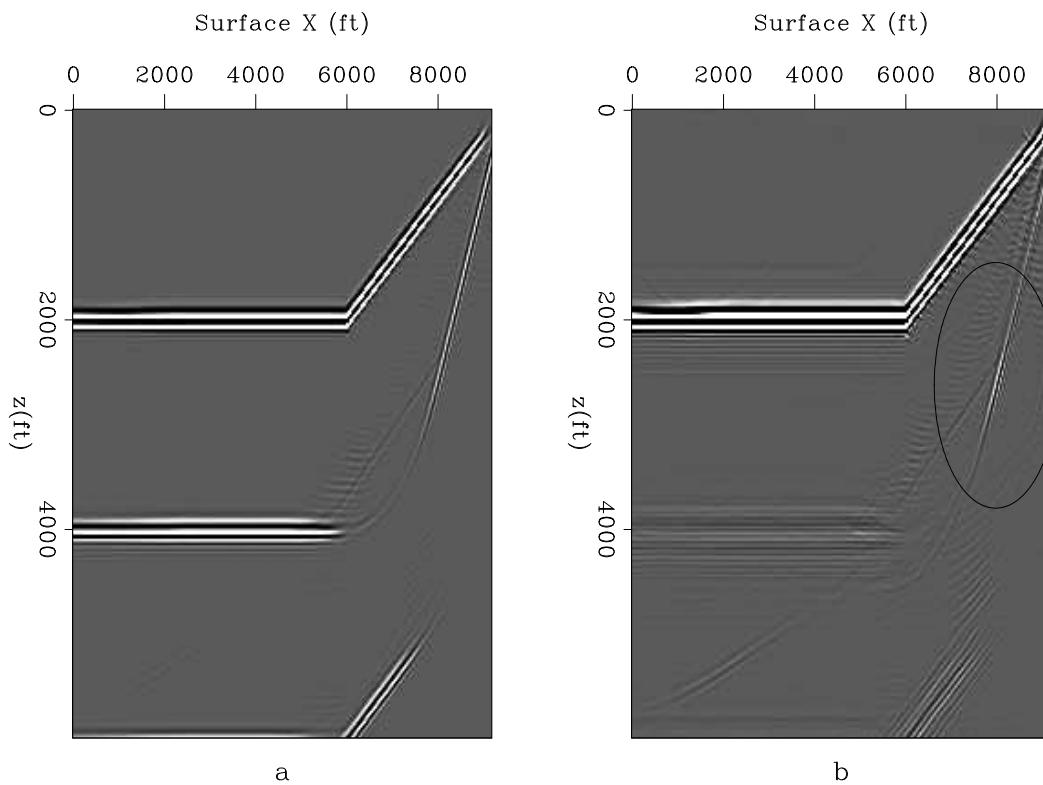


Figure 6: Image obtained by migrating the data (a) before multiple removal and (b) after multiple removal [madhav1-compim] [CR]

Use of ADCIGs

There are many events in data space that migrate to the same point in image space (if the migration velocity is perfect), but with different opening angles. In the class of events discussed above, because of limited recording geometries we do not expect to model all those angles. However, if we can capture some subset of angles, we can make use of the ADCIGs to infill these missing angles and generate a more complete multiple model. When migration velocity is same as the multiple velocity, this reduces to simple interpolation or extrapolation, because

events will be perfectly flat in the ADCIGs. In cases of imperfect velocity, Radon-style transforms can be used to accomplish the same goal.

To illustrate the point, I extract an ADCIG corresponding to a surface location of 8000 ft (where the dipping multiple persists). Figure 7 (a) is the ADCIG of the recorded data and shows angles at which the multiple is actually illuminated. Figure 7 (b) displays the illumination range of the modeled multiple. Note that the modeled multiple is missing at far angles where the recorded multiple exists. This indicates that SRMP in this case was unable to model far angles. Figure 7 (c) is the ADCIG for the data obtained after removing the multiple model generated using SRMP (data space removal). Again, we were able to get rid of multiple energy close to zero offset, but we still have multiple energy at far offsets.

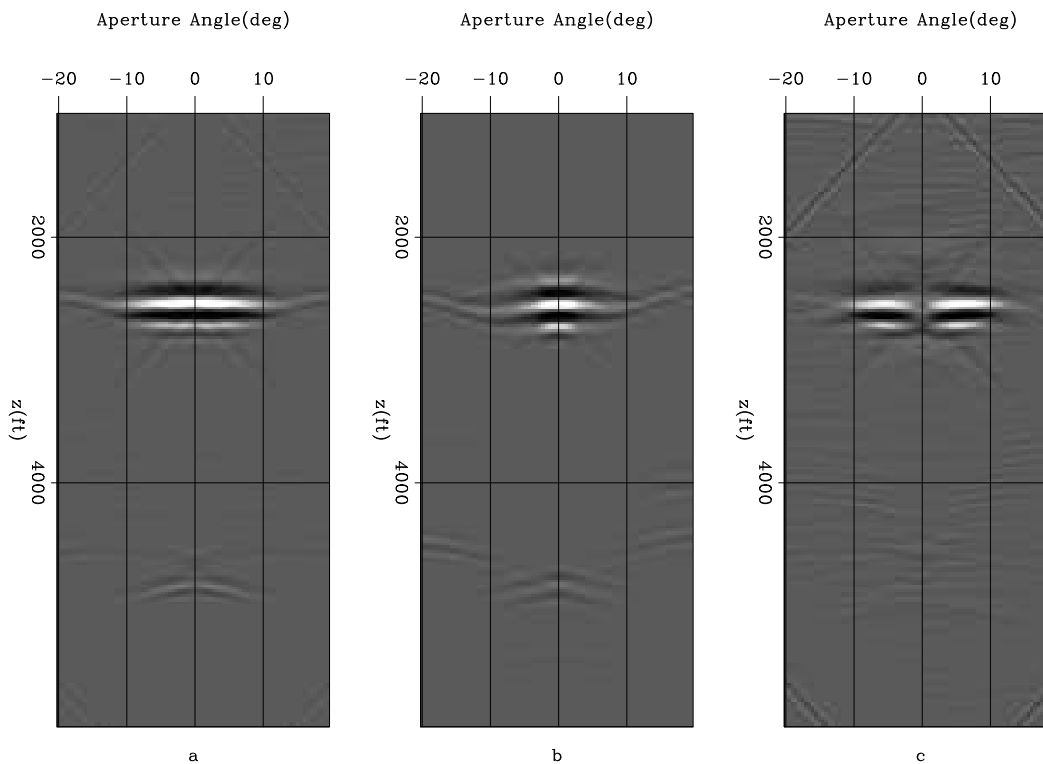
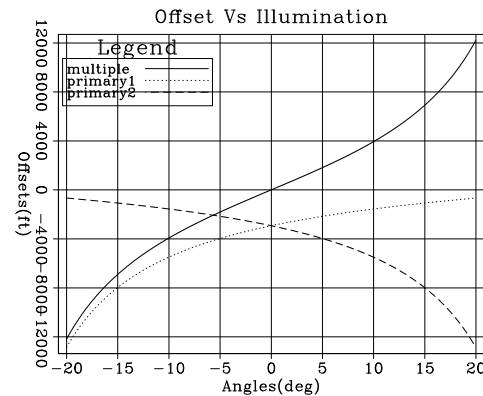


Figure 7: ADCIGs for (a) complete data (b) multiple model and (c) data after removing the multiple model madhav1-ADCIG [CR]

For a given velocity model and recording geometry, we can analytically compute the angles up to which we will be able to model a particular multiple, and the angles up to which it will be actually recorded. The multiple event DD maps as a dipping reflector with twice the dip in image space. ADCIGs above also show the angular illumination for this multiple event. Figure 8 shows a plot between illumination angle and offsets for an image point located at the multiple event, with twice the dip of the original and having an X position of 8000 ft. The plot shows the relation between surface offsets and illumination angles for the first-order multiple event DD along with the two primaries that contribute towards it. It can be noticed from the plot that if we limit our recording from -4000 ft to 4000 ft, the multiple will be illuminated from -10 to +10 degrees. To model this multiple we need to record both the primaries that

contribute towards it. The plot shows that for limited offsets we record both primaries only in an angular range of -5 to $+5$ degrees. This would be the range in which we will be able to model the multiple, which reiterates the inability of SRMP to model multiples at far opening angles, with such geometries and limited offsets.

Figure 8: The relation between recording offsets and opening angles for the multiple event with several bounces on the dipping layer, and the primaries that contribute to it, for an image point corresponding to the X position of 8000 ft. madhav1-angoff
[NR]



To obtain Figure 7 (c) we constructed the multiple model in the data space, removed it from the data and then migrated it to image space and constructed ADCIGs. Equivalently, this process could have been carried out in image space, in which case we would migrate the data and the multiple model independently to the image space and then do the subtraction.

Reconstructing missing angles

The advantage of working with image-space SRMP is that we have access to angle-domain information, which can be used to infill the missing angles in the multiple model. When using the perfect migration velocity, angle gathers look flat and extrapolating farther angles is fairly straightforward. A simplistic approach like stacking along angles and then spraying the normalized energy to other angles (stack and spray) can work well in case of flat gathers.

I use the algorithm proposed by Alvarez and Guitton (2006) (matching filters and adaptive subtraction) as a tool for removing multiples. If the image space subtraction is carried out on an ADCIG by ADCIG basis, the algorithm tries to account for the differences in amplitudes as well as the illumination range of modeled and recorded multiples. Adaptive matching works well for the ADCIGs corresponding to this example. When we do multiple removal in the data domain, we also use adaptive subtraction, but it is easier to match the missing parts in the angle domain, since the patterns are much simpler. If the velocity is perfect, events in the angle domain are flat. Secondly, in the angle domain we can enhance the performance of adaptive subtraction using the stack-and-spray approach or the Radon transforms in the case of complex situations, which is difficult to do when we are dealing with subtraction in the data domain.

In Figure 9, I compare angle gathers for the original multiple model, the reconstructed multiple model generated using a stack-and-spray approach, and the one reconstructed using the adaptive-matching algorithm. Once we reconstruct the missing angles, we can carry out the process of subtraction.

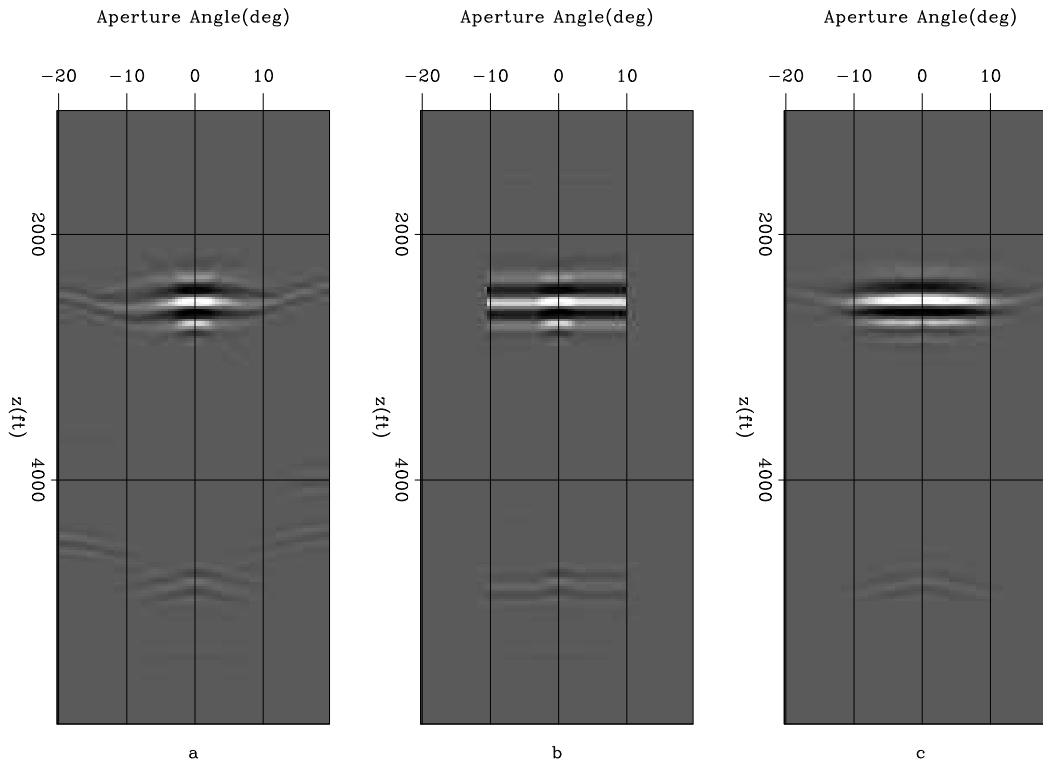


Figure 9: ADCIG for (a) multiple model and reconstructed multiple model using (b) stack and spray and (c) adaptive approach `madhav1-recon` [CR]

Finally, let us compare the image and the ADCIGs created by doing multiple removal in the data space to the one created in the image space using adaptive subtraction, working on one ADCIG at a time. Figure 10 is the result of multiple removal in the data space followed by migration, and Figure 11 is the result of multiple modeling in the image space followed by adaptive subtraction. The ADCIGs on right show the remains of the multiple energy in the former case at high angles, but nearly all the energy is gone in the latter.

SIGSBEE

Moving to a more realistic and complex subsurface geometry, in this section I discuss the application of SRMP on the Sigsbee data set. Figure 12 and 13 show the Sigsbee velocity model and the migrated image respectively. Figure 14 shows the corresponding multiple model in the image space. The side face in these figures is a representative ADCIG corresponding to sediments, left of the salt body. Since we migrate with the correct velocity, primaries appear flat in the ADCIGs, and multiples show a frown since they are migrated with velocities higher than their actual velocities.

The complex velocity model and especially the salt body cause the multiples to image in a very complicated fashion. It is difficult to identify even the water-bottom multiples that image underneath the salt body. Our goal here is to analyze multiples modeled by SRMP

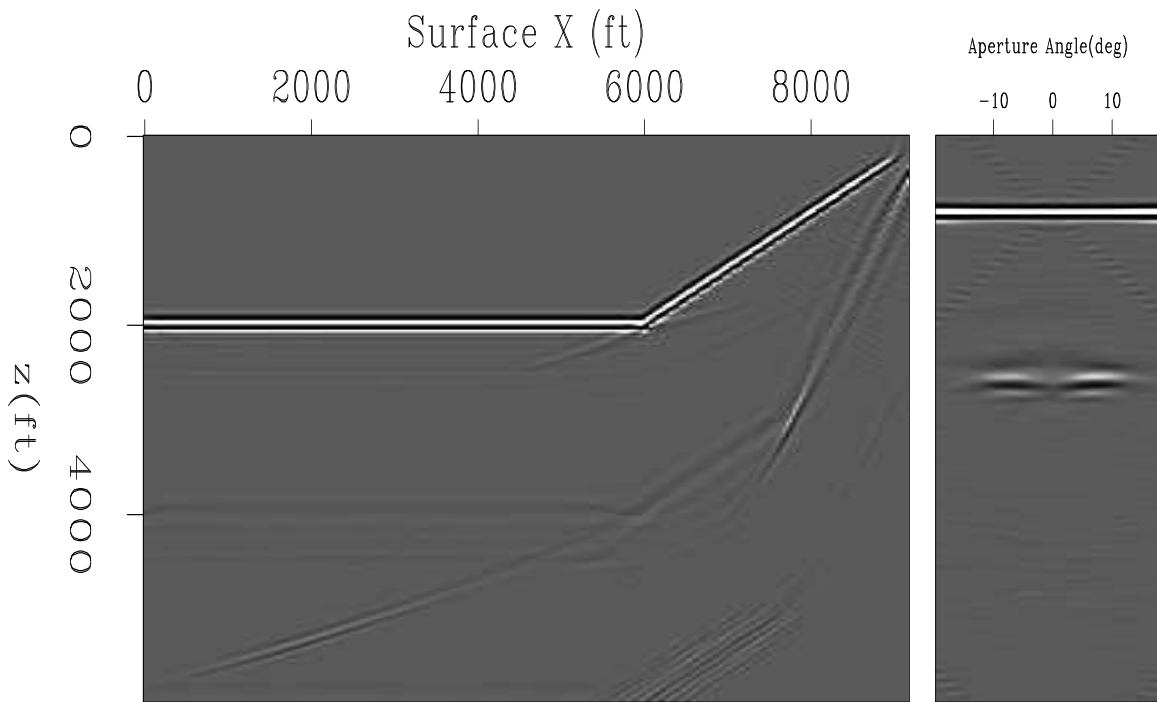


Figure 10: Image and a representative ADCIG at a surface location of 8000, created by data space multiple removal followed by migration `madhav1-imgbf` [CR]

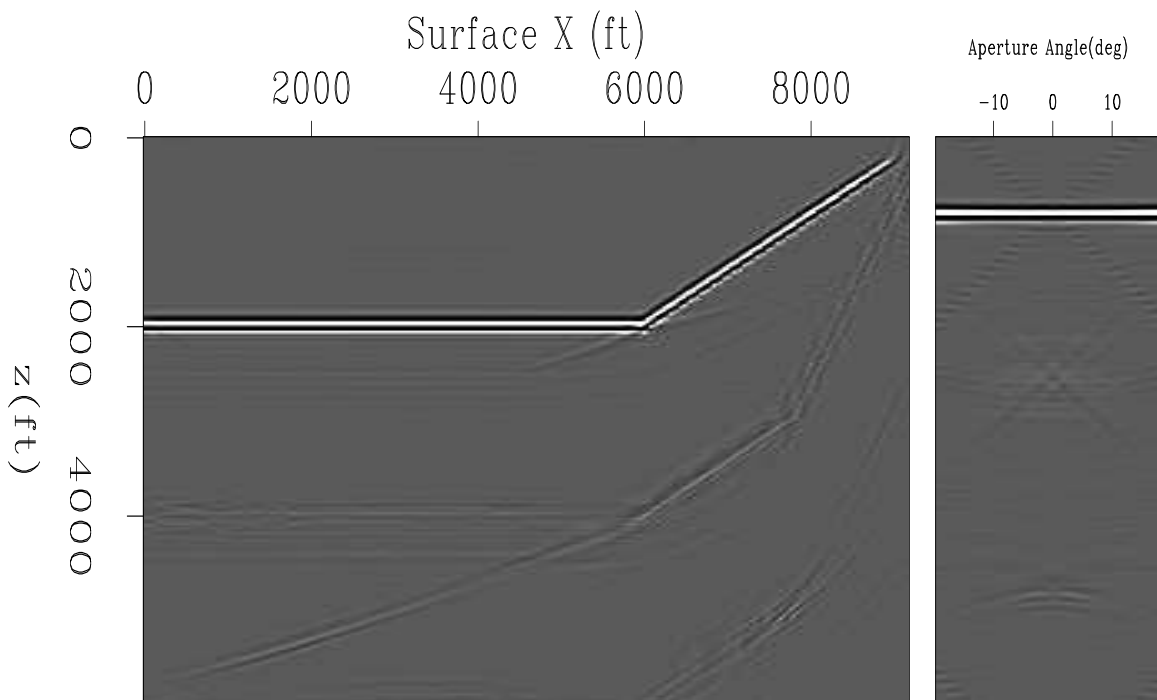


Figure 11: Image and a representative ADCIG at a surface location of 8000, created by image space multiple removal `madhav1-imgaf` [CR]

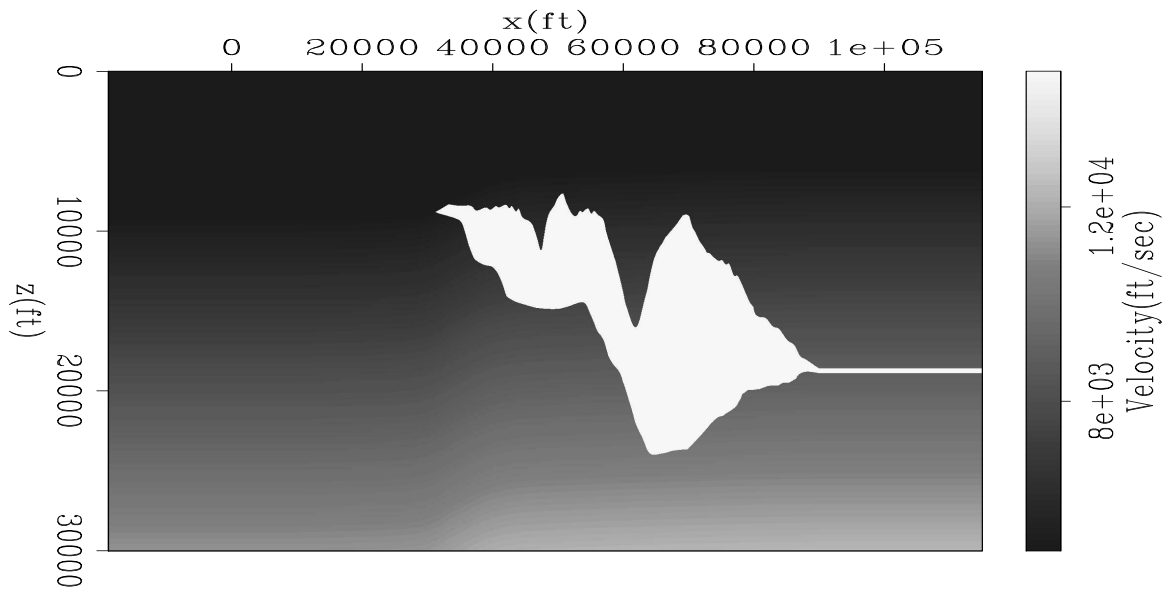


Figure 12: Velocity model for the Sigsbee data `madhav1-vel.sig` [NR]

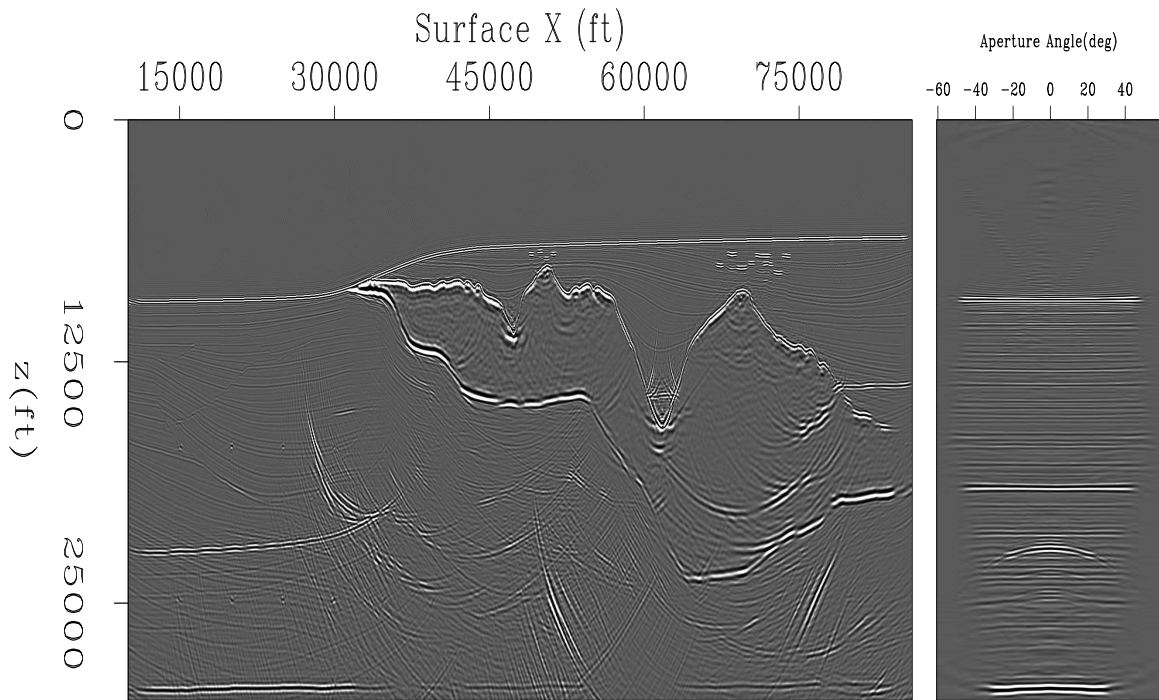


Figure 13: Image and a representative ADCIG for Sigsbee data migrated with the true velocity `madhav1-imgtr.sig` [CR]

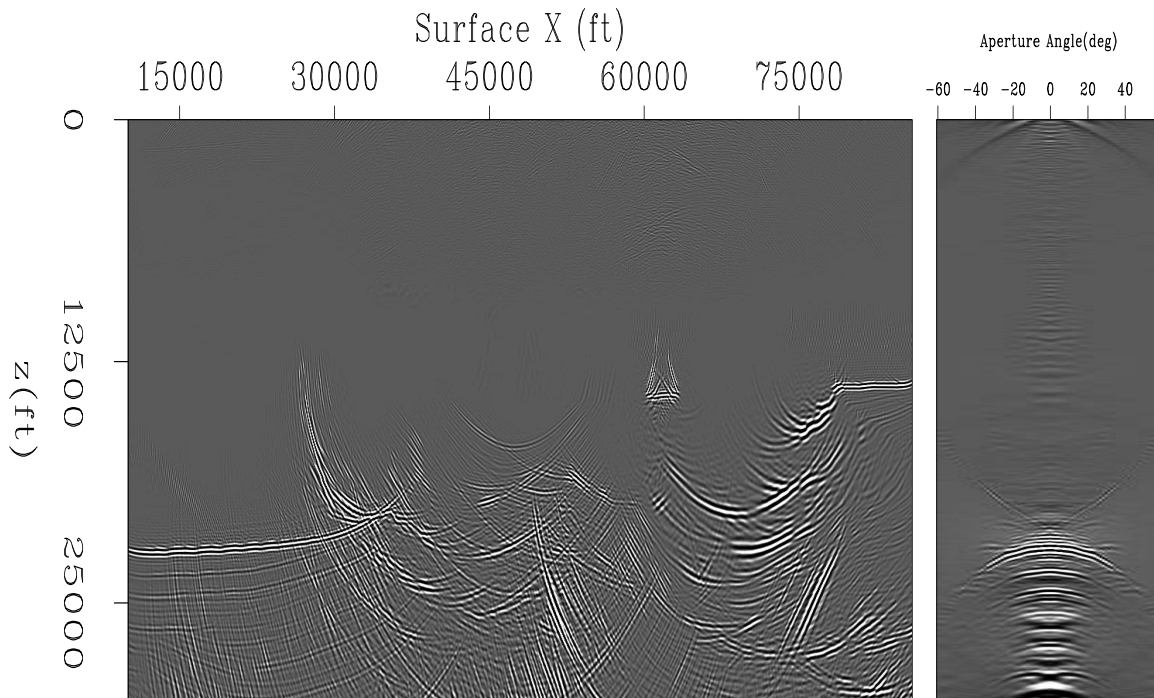


Figure 14: Multiple model (in image space) and a representative ADCIG for the Sigsbee data migrated with the true velocity `madhav1-mult.rsig` [CR]

and improve our estimate if we have some missing parts in our model. Ideally, we would like to look at multiples in a domain where they can be easily identified and understood. To accomplish this I use water velocity as the migration velocity. Not all multiples travel at the water velocity, but many that emanate from shallow layers almost do that. Figures 15 and 16 show the image and the multiple model, with an ADCIG on the side. The first- and second-order water-bottom multiples look much more interpretable as we used water velocity for migration. These multiple events also appear flat in ADCIGs.

The Sigsbee data set has offsets of about 30000 ft. To illustrate the limitations of SRMP in the case of limited-offset recordings, I retain only near offsets (5000 ft) to model the multiples. In Figure 17, I compare the image (top) with the multiple model (bottom). Second-order multiples corresponding to the dipping part of the water bottom and salt canyon are present in the image but are not modeled using SRMP (compare circled events). These events correspond to the ray paths that tend to bounce back into the recording geometry, which we could not model because of limited recording offsets.

To demonstrate the possible use of angle gathers in SRMP, I focus on the dipping part of the first-order water-bottom multiple. The dip of that part is about 10° . Figure 18 (a) shows the ADCIG drawn from the image around the location of the dipping water bottom. Figure 18 (b) is the ADCIG of the multiple model at the same location. The first-order water-bottom multiple (at about a depth of 15000 ft) is illuminated at a much wider range of angles than it is actually modeled. If we subtract the multiples in the data space and then migrate the resulting

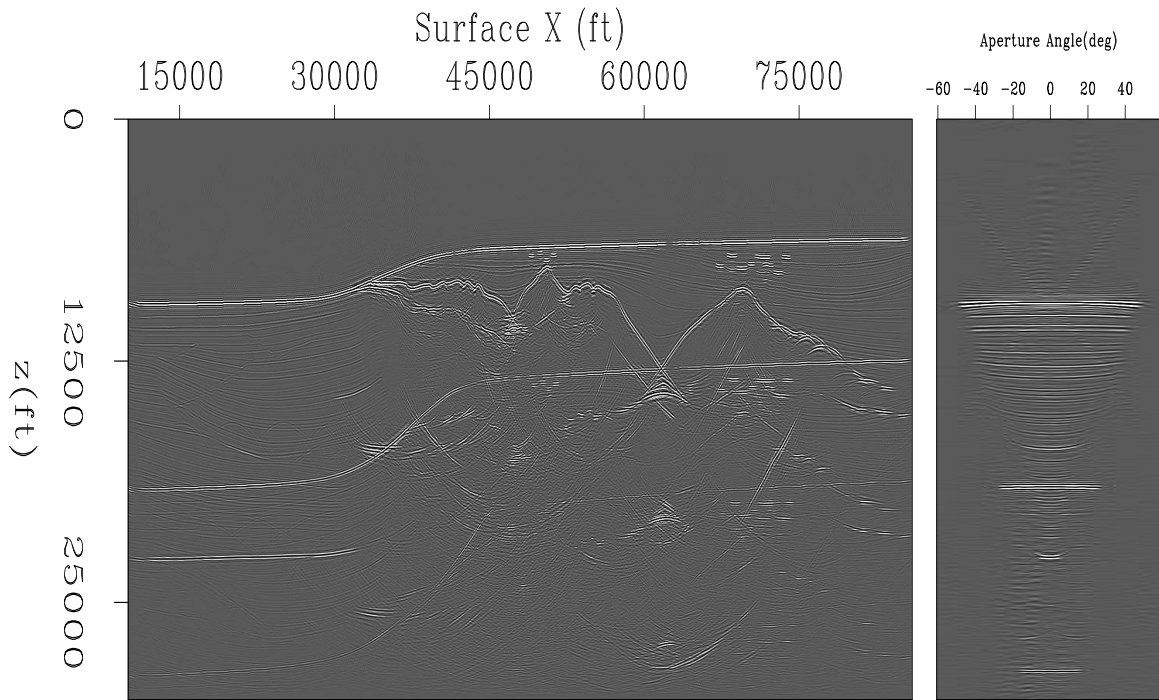


Figure 15: Image and a representative ADCIG for Sigsbee data migrated with the water velocity `madhav1-imgwv.sig` [CR]

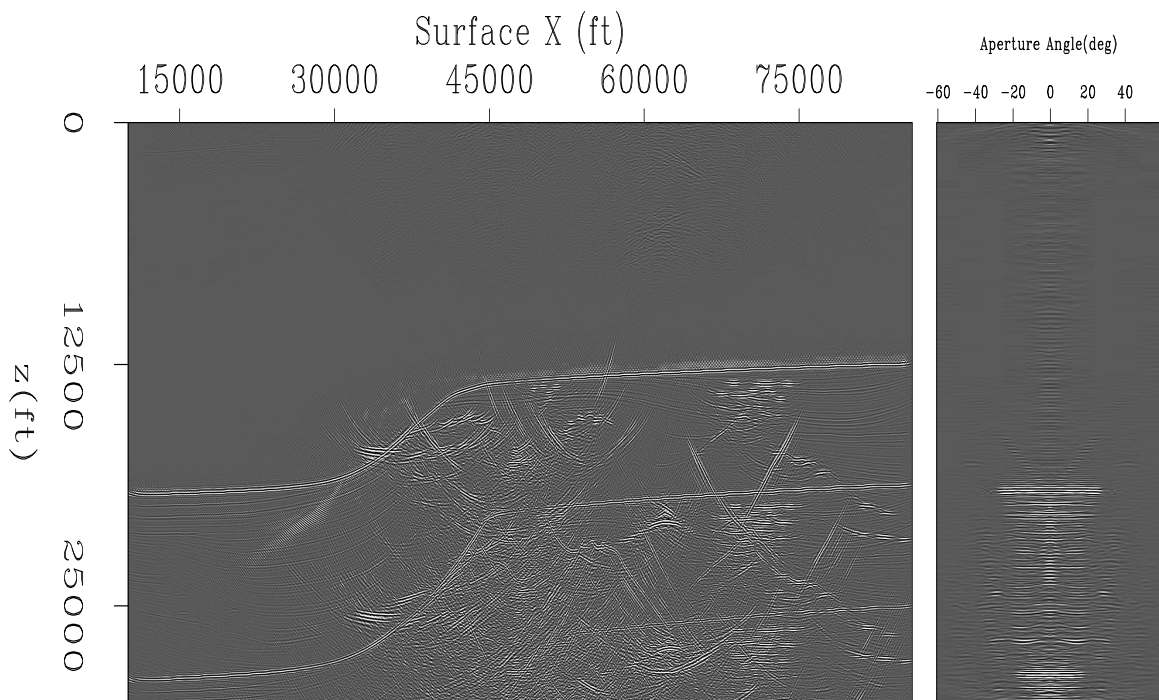


Figure 16: Multiple model (in image space) and a representative ADCIG for the Sigsbee data migrated with the water velocity `madhav1-mulwv.sig` [CR]

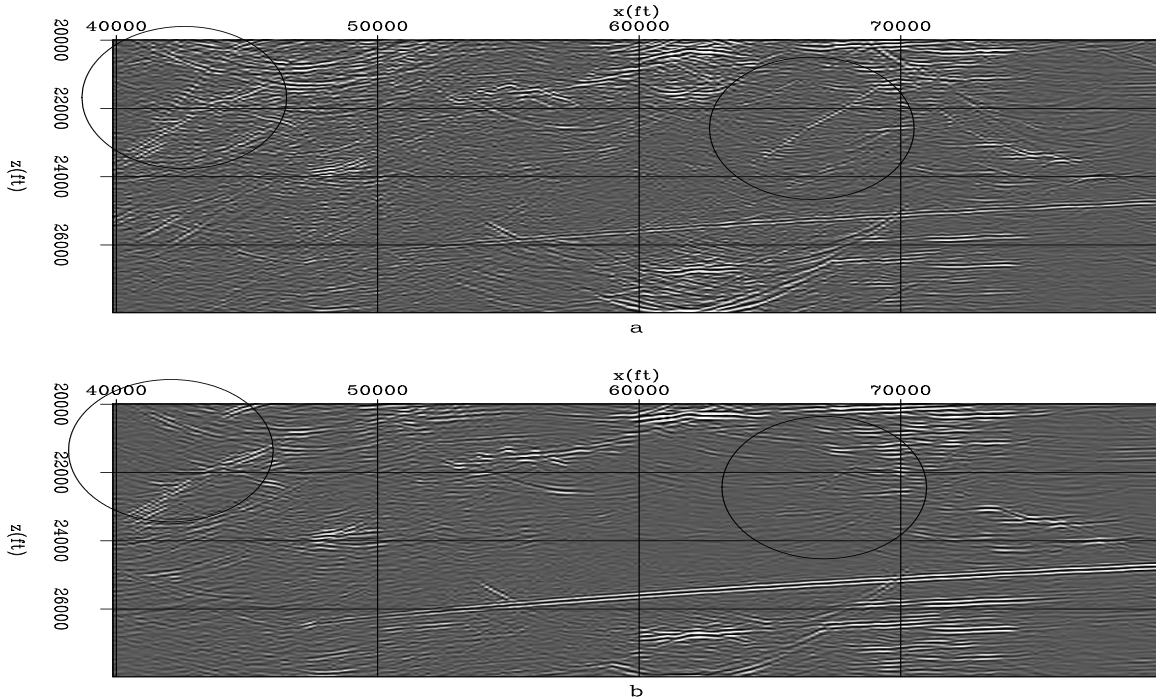


Figure 17: A window extracted from the (a) image and (b) the multiple model after migrating with the water velocity. madhav1-smloff.com [CR]

data set, our image has some remnants of the multiple, which is understandable, since we did not model all the multiples that we recorded. Figure 18 (c) is the ADCIG from the same location, but corresponding to the data for which we subtract modeled multiples in the data space. For the specific water-bottom multiple, the energy is removed close to the zero opening angle but is present at higher opening angles. This observation is similar to the one in the simple synthetic example discussed in the previous section.

As in the simple synthetic example applying adaptive subtraction in the image domain gives us a better chance of removing this class of multiples. This is because in the angle space, multiples appear flat when migrated with the perfect velocity, and it is relatively straightforward for the matching filters to adaptively match the pattern of recorded multiples. When the velocity is not perfect, and multiples show curvature, it may be better to use Radon transforms to reconstruct missing multiples at higher opening angles. To draw a comparison for the given example, I plot in Figures 19 (a), (b) and (c) the ADCIG for the modeled multiple, the reconstructed multiple using the matching filter, and the multiple-free gather after subtraction in image space. The angle gather looks relatively cleaner after subtraction in the image domain (right panel).

Since we carried out migration with the water velocity, we now demigrate with the water velocity and re-migrate with the true velocity to obtain a multiple-free image. This proposition appears expensive, but may be useful when the multiple noise is overwhelming. Again, an alternative may be to use the true velocity but use Radon transforms to infill missing angles

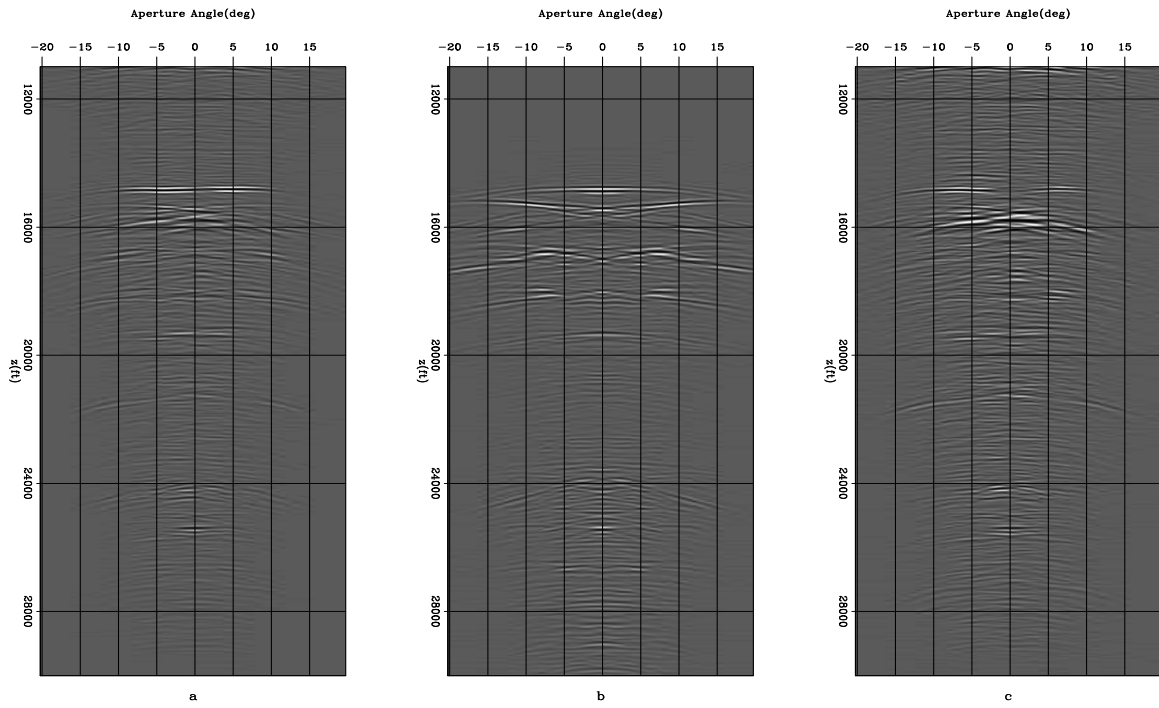


Figure 18: ADCIG for (a)the image, (b) the multiple model and (c) the image after multiple removal in the data domain `madhav1-adcig.sig` [CR]

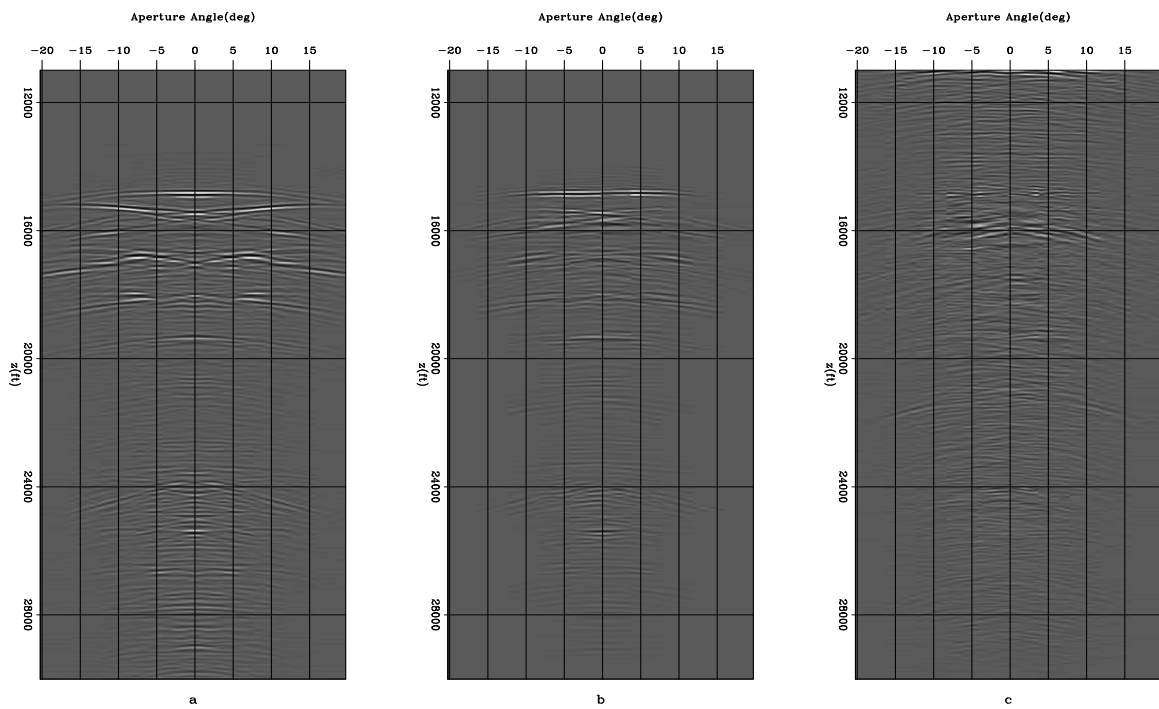


Figure 19: ADCIG for (a) the multiple model, (b) the reconstructed multiple model and (c) the image after multiple removal in image domain `madhav1-adcig2.sig` [CR]

and assist adaptive subtraction in the angle domain.

DISCUSSION AND CONCLUSIONS

Surface-related multiple prediction works well for predicting the free-surface multiples, but, as shown through a series of tests and examples, it fails for certain ray paths where the subsurface geometry is complicated, and we have access to only small offsets. Though data-space and image-space SRMP are mathematically equivalent, image-space subtraction gives us a better chance of reconstructing the missing parts of the multiple model because of the redundancy associated with the image space. In the present analysis we used angle gathers as a preferred domain of reconstruction.

In the presence of complicated structures and salt bodies, multiples migrate to the image space in a fairly complicated fashion when we use the true migration velocity. The use of the multiple velocity for migration takes us to a domain where multiples are identifiable and appear flat in ADCIGs. We may carry out the process of reconstruction relatively easily in this domain. But the drawback is that this should be followed by the process of demigration and migration, making it computationally very expensive. As discussed earlier, we may also use Radon-style transforms for reconstruction, which should work even when the multiples are not absolutely flat in ADCIGs. This allows us to migrate with the true velocity in one step, avoiding the extra steps of migration and demigration. Although the performance of the Radon transform depends upon how many angles we actually have, in the case of a very narrow range of angles, the spectrum would be very smeared, and effective reconstruction would not be possible.

To illustrate these points, in the examples above I retain only very small offsets, which might appear unrealistic for the inline direction. However, there is a trade-off between the offsets and dip of the structure; for instance, if dip is very high, SRMP can fail even for large recording offsets. Furthermore, in 3D surveys, along with many limitations of SRMP, extremely limited crossline offsets might be a concern for even a gently dipping water bottom. The heuristic extension of the idea discussed here would be that in 3D, a multiple event might be perfectly modeled for some azimuths, but not all. In that case we may spread information across azimuths to reconstruct the multiple model, like we did across aperture angles in the 2D case.

ACKNOWLEDGMENTS

The author would like to thank the SMAART JV for the Sigsbee dataset. I would like to thank Biondo Biondi for his guidance and suggestions through out this work. Also I would like to thank Bob Clapp and Gabriel Alvarez for very useful and insightful discussions that helped shape the project.

REFERENCES

- Alvarez, G. and A. Guitton, 2006, Simultaneous adaptive matching of primaries and multiples with non-stationary filters: *SEP*, **125**, 61–75.
- Alvarez, G., B. Biondi, and A. Guitton, 2004, Attenuation of diffracted multiples in angle-domain common-image gathers: 74th Annual International Meeting, SEG, Expanded Abstracts, 1301–1304.
- Anstey, N. A. and P. Newman, 1966, The sectional auto-correlogram and the sectional retro-correlogram: *Geophysical Prospecting*, **14**, No.4, 389–426.
- Artman, B. and K. Matson, 2006, Image-space surface-related multiple prediction: *SEP*, **125**, 47–60.
- Berkhout, A. J. and D. J. Verschuur, 1997, Estimation of multiple scattering by iterative inversion, part i: theoretical considerations: *Geophysics*, **62**, no. 5, 1586–1595.
- Sava, P. and A. Guitton, 2003, Multiple attenuation in the image space: 73rd Annual International Meeting, SEG, Expanded Abstracts, 1933–1936.
- Sava, P. and A. Guitton, 2005, Multiple attenuation in the image space: *Geophysics*, **70**, 10–20.

Residual multiple attenuation using AVA modeling

Claudio Guerra

ABSTRACT

Residual multiple attenuation is a common process applied towards the end of the seismic processing flow. Its main objective is to decrease the energy of migrated residual multiples. This process can be time-consuming. I present a method which uses amplitude-versus-angle (AVA) modeling to simulate primary events and adaptive subtraction to estimate residual multiples and residual-multiple-attenuated data. The method is applied on angle-domain common-image gathers (ADCIGs) from a 2D data set from the Gulf of Mexico that is contaminated with residual multiples. This method is simple, fast and, depending on the parameterization of the adaptive subtraction, can preserve primary reflection amplitudes.

INTRODUCTION

Conventional time and depth imaging considers that the input data is made up of only primary reflections. Because of this basic assumption, much effort is spent attenuating events considered as noise. In the marine case, multiple reflections are the most important noise. If not successfully attenuated, multiple reflections can bias velocity estimation, and after migration, give rise to images contaminated with residual multiples which can make interpretation difficult. For example, such contamination may severely interfere with AVA analysis.

In marine data processing, it is a common practice to run residual multiple attenuation as one of the later steps — after migration, for instance. The multiple-attenuation tests do not access every line of 3D data, and the evaluation of the efficacy of the attenuation is performed along control lines. Since the multiple-attenuation parameters are optimized for the control lines, unfortunately, sometimes, a surprising amount of residual-multiple energy is left and is spread by migration over the entire migrated data set. Sometimes, the evaluation of the multiple attenuation is performed by inspecting post-stack migrated data, or even stacked volumes. Since this ignores the effect of pre-stack migration on the multiple-attenuated data, it can allow residual multiples to appear, manifesting as crosshatched patterns and high-frequency migration noise resembling overmigrated events.

Another very common process after pre-stack migration is automatic residual-moveout correction to mitigate the effects of velocity inaccuracies, which aims to align reflectors horizontally to improve the stacking power and better constrain the data for AVA analysis. Consequently, a method which relies on the flatness of the gathers is a natural process to attenuate

ate residual multiples after automatic residual-moveout correction. However, the problem of residual moveout will not be addressed in this work.

Weglein (1999) classified multiple-attenuation methods into two main categories: (1) filtering methods and (2) prediction methods. The most widely used filtering methods rely on differences in traveltimes between primaries and multiples to separate them in appropriate domains where multiples can be filtered out (Hampson, 1987). Since, regardless of the domain, primaries and multiples normally overlap, particularly at small reflection angles and offsets, the filtering is not perfect; therefore, some of the primary energy can be attenuated, or some of the multiple energy is left out (crosstalk). Prediction methods simulate multiples by auto-convolution of shot gathers and then subtract them from the original data using nonlinear adaptive subtraction (Verschuur et al., 1992). As prediction methods became popular, filtering methods inherited the nonlinear adaptive subtraction to attack the crosstalk problem. So, filtering methods can be used to estimate multiples by exploring the same differences between them and primaries as before, but instead of simply filtering them out, a possible approach is to subtract the estimated multiples from the original data using nonlinear adaptive-subtraction schemes. This provides more flexibility to solve specific problems.

Generally, residual-multiple attenuation is performed by filtering methods, by zeroing the residual-multiple energy (along with some primary energy) or by using nonlinear adaptive subtraction. Choo et al. (2004) devised a method to perform residual-multiple attenuation in a different manner. They apply AVA inversion to simulate the primaries and then estimate the residual multiples using nonlinear adaptive subtraction. Although many details of their work are unpublished, the method I present here is, in essence, very similar to the one proposed by them. The method simulates the primaries according to an AVA curve, adjusts amplitude and phase of the simulated primaries to the amplitude and phase of the original data by applying filters computed in a nonlinear adaptive strategy, subtracts the adjusted primaries from the original data to get an estimate of the residual multiples, and, finally, obtains the attenuated data by nonlinear adaptive subtraction. This approach solves the AVA modeling problem globally.

The method is applied on angle-domain common-image gathers (ADCIGs) of a Gulf of Mexico (GOM) 2D data subjected to multiple attenuation after migration. The data set contains very complex multiple patterns (Alvarez et al., 2004).

DESCRIPTION OF THE METHOD

Aki and Richards (1980) stated that, up to 40° , the *p-wave* reflection coefficients, $R(\theta)$, as a function of the incidence angle, θ , can be approximated by

$$R(\theta) = A + B \sin^2 \theta + C \tan^2 \theta, \quad (1)$$

where A, B and C are parameters related to the average and contrasts of the elastic properties of the limiting layers. Therefore, if it is possible to determine these parameters, one can simulate the amplitudes of primary events at every depth or time step. I refer to the simulation of the primary amplitudes as AVA modeling. The aim of this work is not to invert the AVA parameters

for rock and fluid properties, but just to obtain a reasonable estimate of the primaries to be further used in a residual-multiple-attenuation sequence.

The AVA modeling problem can be addressed by solving locally, for every different depth (or time) step, the normal equations $(\mathbf{G}^T \mathbf{G})\hat{\mathbf{m}} = \mathbf{G}^T \mathbf{d}$, where $\hat{\mathbf{m}}$ are the estimated AVA parameters, \mathbf{G} has the column vector form $[\mathbf{1}, \sin^2\theta_i, \tan^2\theta_i]$ and \mathbf{d} is the ADCIG (or a CMP gather after NMO). The simulated primaries are obtained by using the estimated AVA parameters in equation (1). One problem that arises from this local solution is that the AVA parameters are not constrained to be smooth along depth. This can lead to anomalous amplitudes in the simulated primaries for a certain depth.

In the present approach, the AVA modeling problem consists of determining the three parameters A, B and C of equation (1) by solving the following data fitting problem:

$$\mathbf{Lm} = \mathbf{d}, \quad (2)$$

where \mathbf{L} in matrix form is

$$\begin{bmatrix} \mathbf{1}_1 & \mathbf{S}_1 & \mathbf{T}_1 \\ \mathbf{1}_2 & \mathbf{S}_2 & \mathbf{T}_2 \\ \mathbf{1}_3 & \mathbf{S}_3 & \mathbf{T}_3 \\ \vdots & \vdots & \vdots \\ \mathbf{1}_{n_1} & \mathbf{S}_{n_1} & \mathbf{T}_{n_1} \end{bmatrix} \quad (3)$$

which has dimension $n_1 n_2 \times 3n_1$, \mathbf{m} is the model-parameter vector ($3n_1$ elements), and \mathbf{d} is the data vector ($n_1 n_2$ elements), where n_1 and n_2 are the number of samples in depth (or time) and the number of traces in the ADCIG, respectively. $\mathbf{1}_j$, \mathbf{S}_j and \mathbf{T}_j are $n_2 \times n_1$ matrices consisting of 1, $(\sin^2 \theta_i)$ and $(\tan^2 \theta_i)$ along their j -th column entries, respectively. i stands for the reflection-angle indexes.

Generally, in ADCIGs, residual multiples are more persistent at near angles, because of insufficient moveout difference between them and the flattened primaries. Additionally, at the farthest angles, stretch occurs. To avoid these imperfections in the input data, the fitting goal is to minimize the residual,

$$\mathbf{0} \approx \mathbf{M}(\mathbf{Lm} - \mathbf{d}), \quad (4)$$

where \mathbf{M} is a selector operator which applies the appropriate internal and external mutes.

If unrealistic variations of the AVA parameters with depth are an issue, the following regularization goal can be introduced:

$$\mathbf{0} \approx \epsilon \mathbf{Dm}, \quad (5)$$

where \mathbf{D} is the derivative operator along depth and ϵ is the regularization parameter. As usual, care must be taken when choosing ϵ not to destroy any recoverable residual moveout information and not to spread simulated primaries to angles at which they originally do not occur.

To accelerate the solution, the problem can be solved with preconditioning (Claerbout and Fomel, 2001), using the transformation $\mathbf{m} = \mathbf{Cp}$, where $\mathbf{C} = D^{-1}$ and \mathbf{p} is the preconditioned variable. Finally, the fitting goals reduce to

$$\begin{aligned}\mathbf{0} &\approx \mathbf{M}(\mathbf{LCp} - \mathbf{d}) \\ \mathbf{0} &\approx \epsilon \mathbf{p}.\end{aligned}\tag{6}$$

The final model is obtained with $\mathbf{m} = \mathbf{Cp}$. I use conjugate-gradients to solve the inverse problem.

After the determination of the three AVA parameters for every depth step, primaries are simulated by computing the reflection coefficient for all reflection angles using equation (1). Of course, the method relies on the flatness of the reflectors in the CIG to correctly extract the 3 parameters of the AVA curve.

To get the residual-multiple-attenuated data, the adaptive subtraction must be applied in two steps. The first one aims to obtain an estimate of the residual multiples. This is done by subtracting the adjusted version of the simulated primaries from the original data. Amplitude and phase adjustments are achieved by the convolution of the simulated primaries with a prediction-error Wiener filter.

As the estimated residual multiples may contain some primary information (mainly at small reflection angles), I use the strategy proposed by Guitton et al. (2001), the so-called ‘subtraction method,’ in which two different prediction-error filters (PEFs), which model primaries and multiples, are computed. Their method allows regularization, to decrease the crosstalk between multiples and primaries. The corresponding fitting goals are

$$\begin{aligned}\mathbf{0} &\approx \mathbf{m}_n \\ \mathbf{0} &\approx \epsilon \mathbf{m}_s \\ \text{subjected to } \Leftrightarrow \mathbf{d} &= \mathbf{S}^{-1} \mathbf{m}_s + \mathbf{N}^{-1} \mathbf{m}_n\end{aligned}$$

after preconditioning, with $\mathbf{s} = \mathbf{S}^{-1} \mathbf{m}_s$ and $\mathbf{n} = \mathbf{N}^{-1} \mathbf{m}_n$. In the preconditioning equations, \mathbf{s} represents the primaries, \mathbf{n} the multiples; \mathbf{N}^{-1} and \mathbf{S}^{-1} represent deconvolution with PEFs for multiples and primaries, respectively; \mathbf{m}_n is the multiple model content and \mathbf{m}_s is the primary model content. Finally, the estimated primaries are obtained by $\hat{\mathbf{s}} = \mathbf{d} - \mathbf{N}^{-1} \mathbf{m}_n$. All PEFs are computed with conjugate-gradients.

EXAMPLES

The method is applied on ADCIGs of a Gulf of Mexico (GOM) 2D data. The data have been migrated with shot-profile algorithm and the transformation from subsurface-offset to angle was performed after imaging. The ADCIGs have been subjected to multiple attenuation using the apex-shifted tangent-squared radon transform (Alvarez et al., 2004). Figure 1, which corresponds to the stack of ADCIGs without multiple-attenuation, shows complex patterns of multiples, especially below the edges of the salt, corresponding to diffracted multiples. Around

a depth of 3500 m, the first-order multiple of the sea bottom is probably distorted due to the alternation between fast and slow velocities. The fitting goal I used to simulate the primaries is the one given in equation (6).

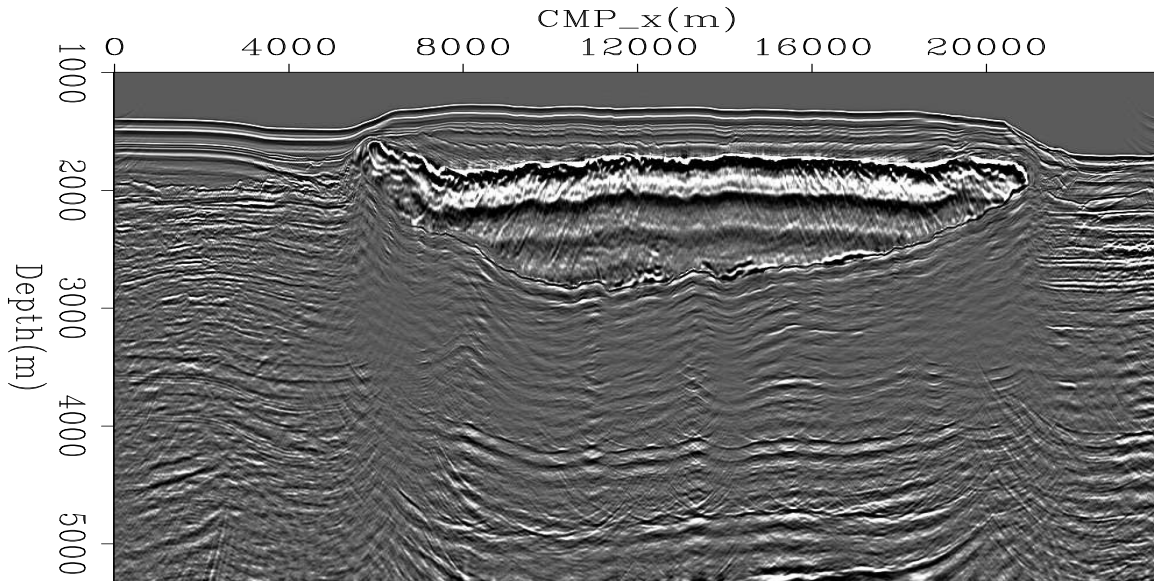


Figure 1: Migrated data without multiple attenuation – stacked data. Notice strong migrated multiples, especially below the edges of the salt, corresponding to migrated diffracted multiples. `claudio1-migstk` [ER]

The results are shown in CIGs near CMP locations 2000, 12000, and 20000 m, in zero-angle sections, and in stacked sections. Figures 2, 3 and 4 illustrate the ADCIGs. In all of the figures are shown in panel (a) the original ADCIG, panel (b) the residual-multiple-attenuated, panel (c) the estimated residual multiples, and panel (d) the simulated primaries. The residual-multiple panels tell us that not only multiples, but every non-flat event in the ADCIG is considered noise to be attenuated (e.g. kinematic effects due to illumination problems and artifacts due to the transformation from subsurface offset to reflection angle). Primaries with significant residual moveout may also be considered events to be attenuated, so it is important to consider the application of residual-moveout correction before the residual-multiple attenuation to preserve the primary information. In this particular case, the velocity model seems to be less accurate for deeper reflectors. The estimated primary panels show significant residual-multiple attenuation, specially at smaller reflection angles.

Another issue in methods that rely on the moveout difference between primaries and multiples is the persistence of multiples in the near angles (or offsets) due to insufficient moveout difference between them and the primaries. In sub-salt regions, this problem is especially prominent in ADCIGs because of the poor illumination of larger angles. To guarantee that residual multiples in the near-angle range do not interfere with the computation of the simulated primaries, I applied an internal mute, roughly below depth=3000 m between angles -10° and 10° . At the CMP location 12000 m; what may seem to be primaries in the near angle are actually residual multiples, as can be clearly seen in the zero-angle section (Figure

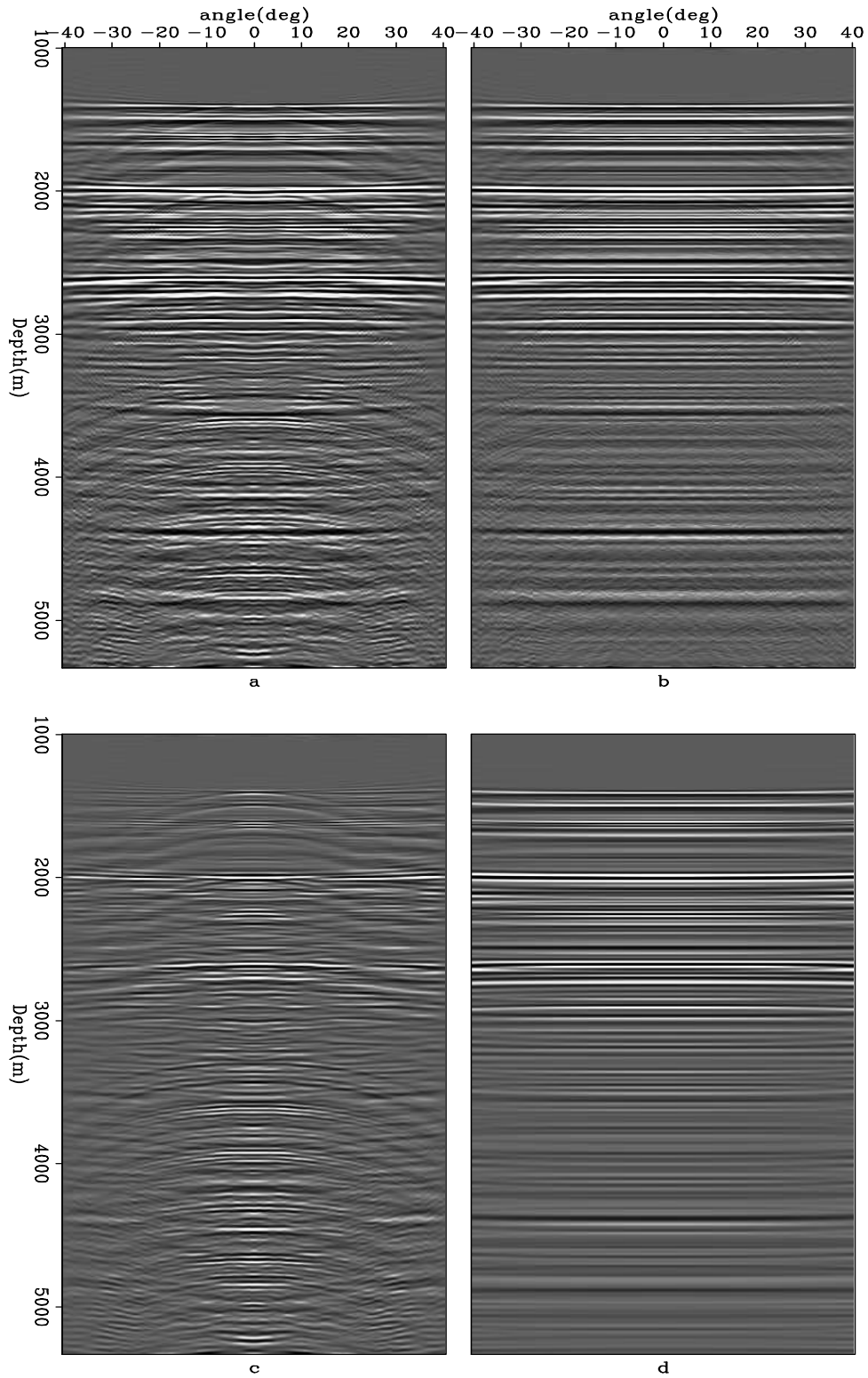


Figure 2: ADCIG — CMP location 2000 m. (a): multiple-attenuated data; (b): residual-multiple-attenuated data; (c): estimated multiples; and (d): simulated primaries. Notice significant residual-multiple attenuation, specially at smaller reflection angles. [claudio1-cig02000](#) [CR]

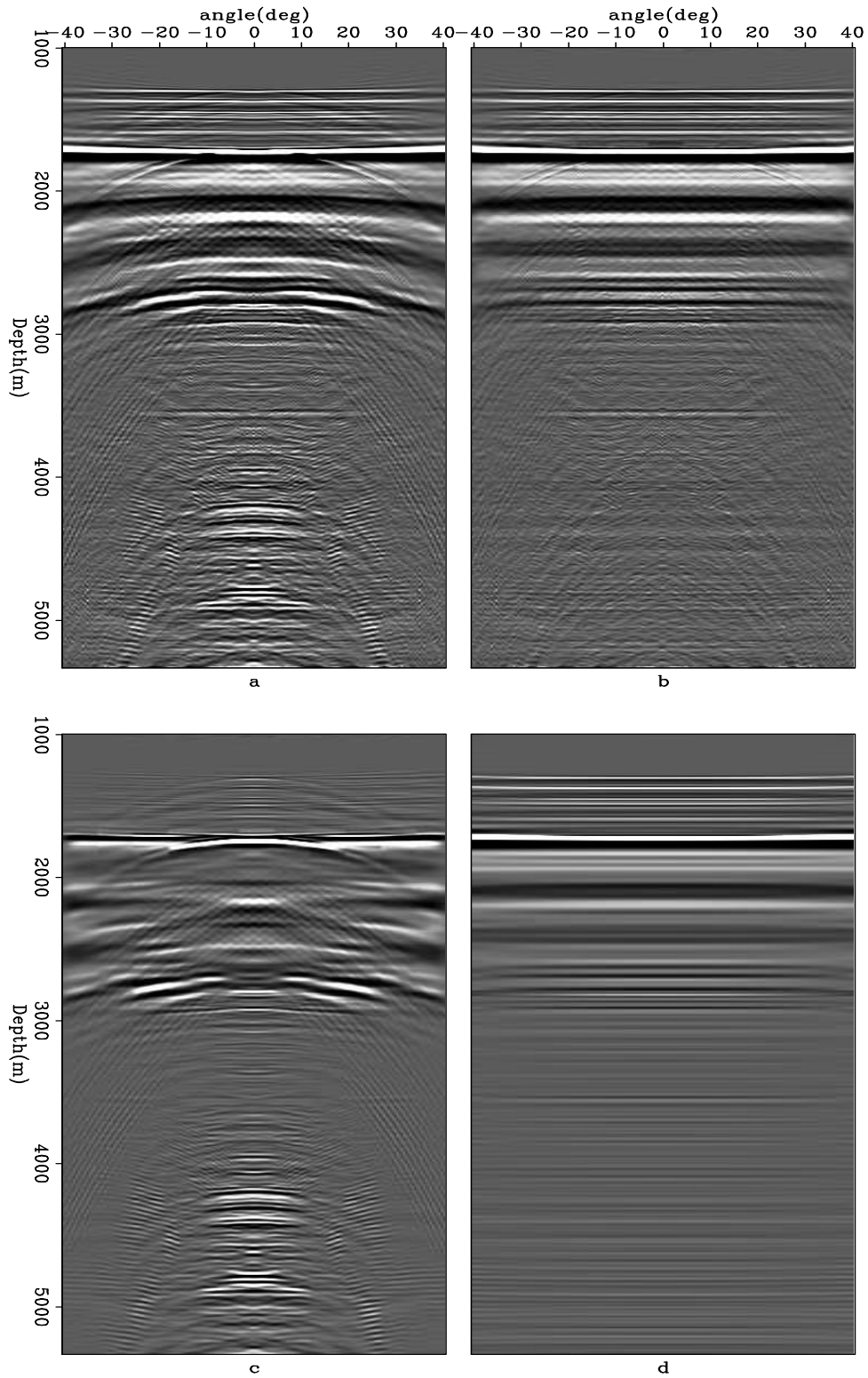


Figure 3: ADCIG — CMP location 12000 m. (a): multiple-attenuated data; (b): residual-multiple-attenuated data; (c): estimated multiples; and (d): simulated primaries. Notice significant residual-multiple attenuation, specially at smaller reflection angles. [claudio1-cig12000](#) [CR]

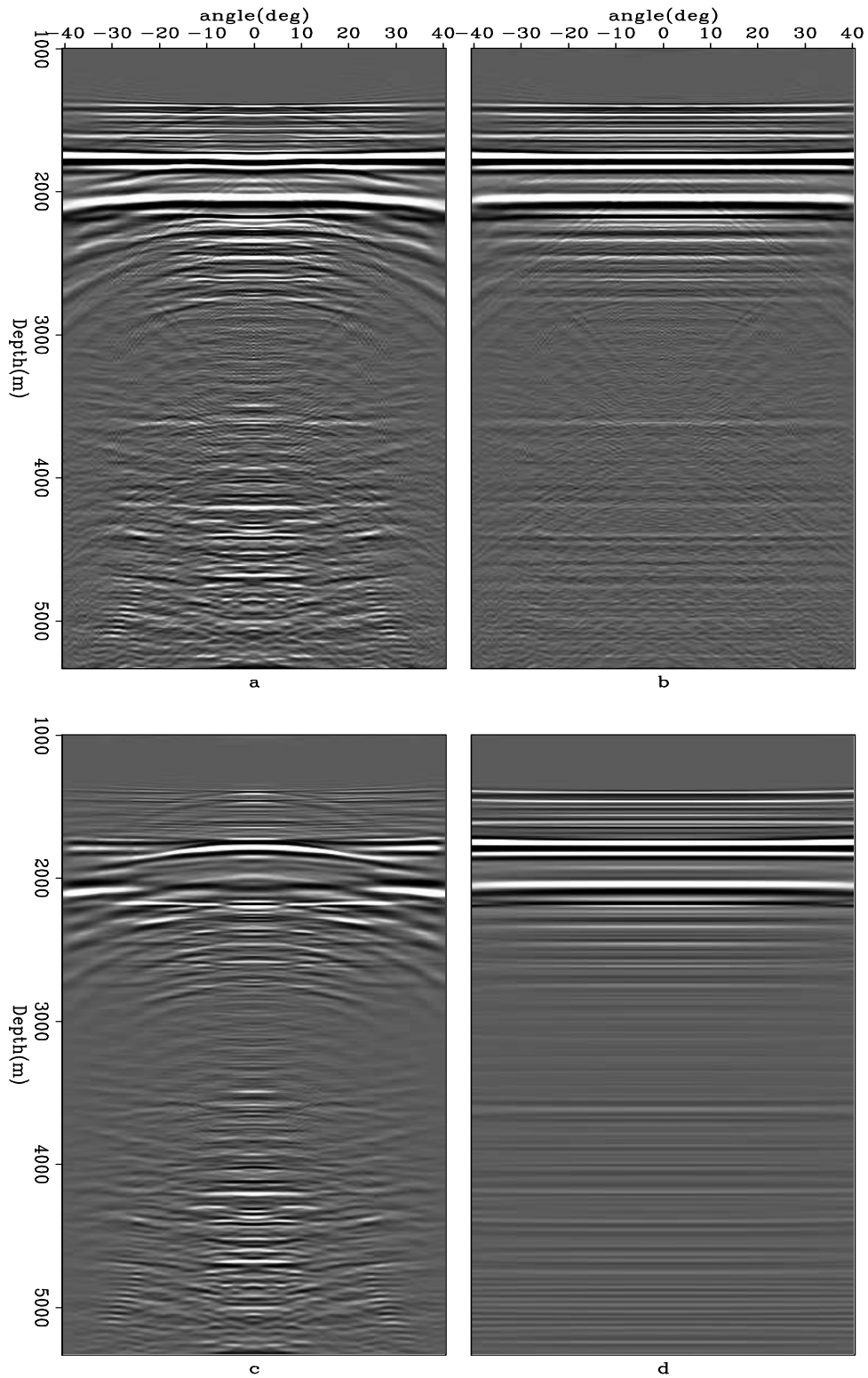


Figure 4: ADCIG — CMP location 20000 m. (a): multiple-attenuated data; (b): residual-multiple-attenuated data; (c): estimated multiples; and (d): simulated primaries. Notice, in the estimated residual-multiples panel, the apex of diffracted multiples (around depth = 3700 m) located at reflection angles = $\pm 20^\circ$. `claudio1-cig20000` [CR]

5). The zero-angle section of the residual-multiple-attenuated data in Figure 6 shows that a low-frequency content of the residual multiples remains after the process. Figure 7 shows details of the zero-angle sections. As can be seen by inspecting the Figures 7a and 7b, after the residual-multiple attenuation, some reflectors have been revealed. This final result obtained for the near-angle section has great impact in AVA analysis. Unfortunately, it is very difficult to observe a typical reflector below the edge of the salt body, in the zero-reflection-angle gathers, making it hard to evaluate the efficacy of the method in preserving primaries in such a complex geology. However, as can be observed in Figures 7c and 7d, the residual multiples are not as strong as before.

Interestingly, below the edges of the salt body where diffracted multiples are more prominent, parts of the residuals of diffracted multiples, which look like migration smiles dipping to the right, remain untouched (e.g. CMP location 20000 m). Conversely, diffracted migrated multiples dipping to the left are well attenuated. By inspecting the corresponding ADCIG, (Figure 4) one can see that the apex of the untouched diffracted multiples (around depth = 3700 m and reflection angles = $\pm 20^\circ$) is out of the internal mute (roughly 10°) applied. Additionally, their tops are relatively flat. Therefore, they give rise to “false” simulated primaries and are not attenuated at all.

Disregarding the imperfections which break the assumption of flatness, by comparing the original and the attenuated ADCIGs we can see that the results are promising. Most of the residual-multiple energy has been attenuated.

In spite of the simplicity of the assumptions, the method provides a cleaner image for interpretation, as the comparison of Figures 8 and 9 shows. A zoomed version is presented in Figure 10.

CONCLUSIONS

I present a simple and fast method, based on AVA modeling, to obtain simulated primaries for estimating residual multiples, in such a way that they can be further attenuated. The method relies on the flatness of the input CIGs. I apply the method to a GOM 2D data set which has strong residual multiples with complex geometries. The method proves its efficiency in attenuating residual multiples, yielding cleaner images than the original ones. In principle, any residual noise which does not obey the flatness criteria in a CIG can be attenuated by the method.

ACKNOWLEDGMENTS

I thank Gabriel Alvarez, Guojian Shan and Madhav Vyas for discussions and suggestions, and Antoine Guitton for the program to perform adaptive subtraction. I also thank WesternGeco for providing the data set.

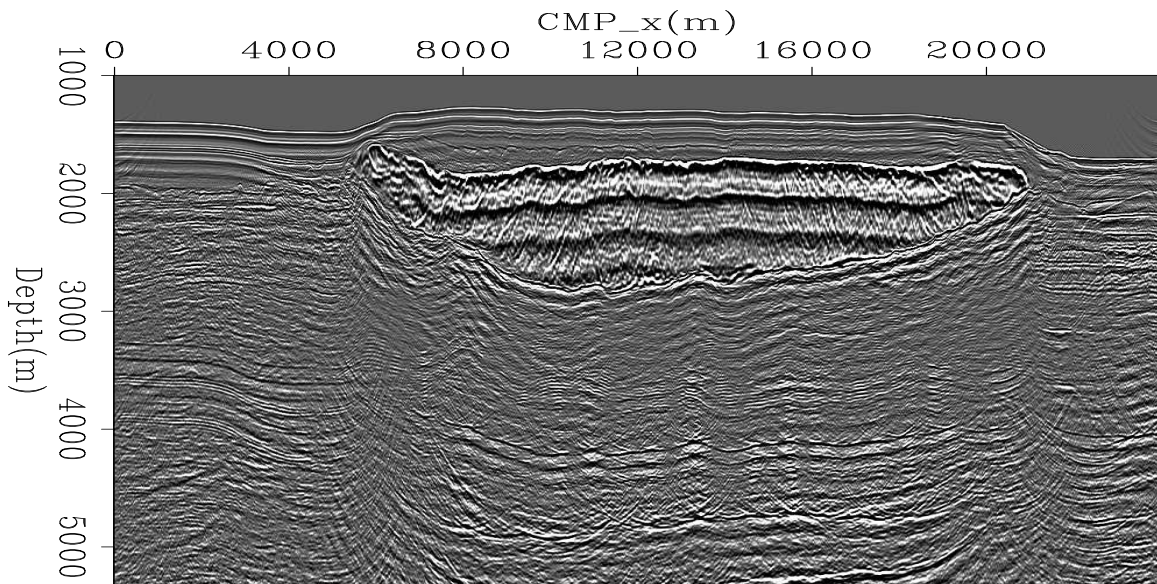


Figure 5: Multiple-attenuated data — zero-angle section. Strong migrated multiples make interpretation of primaries impossible. `claudio1-or00deg` [ER]

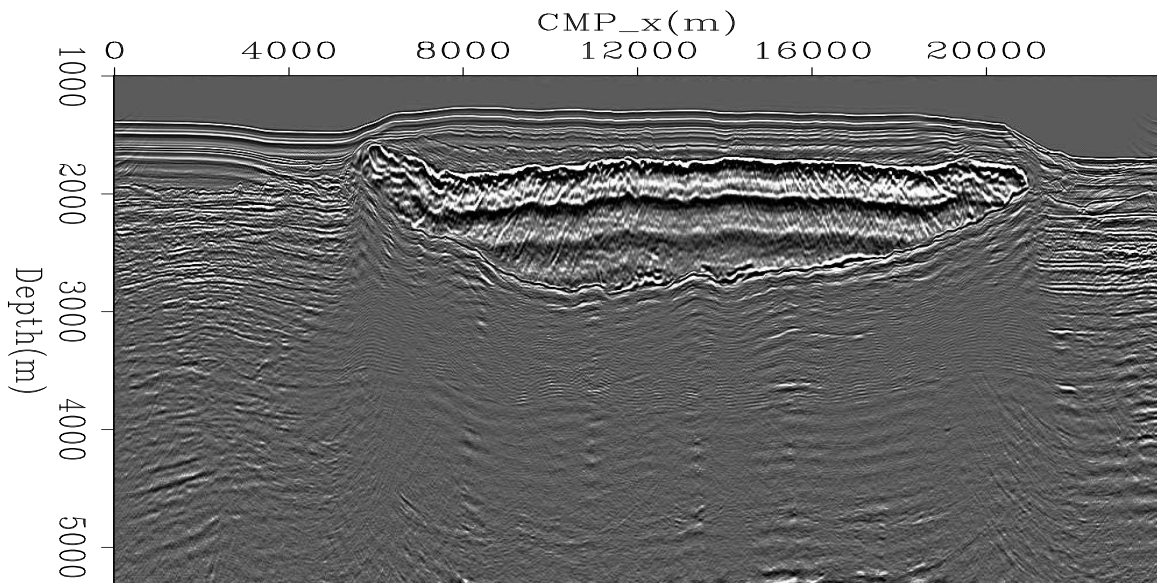


Figure 6: Residual-multiple-attenuated data — zero-angle section. Residual multiples have been attenuated. `claudio1-pest00deg` [ER]

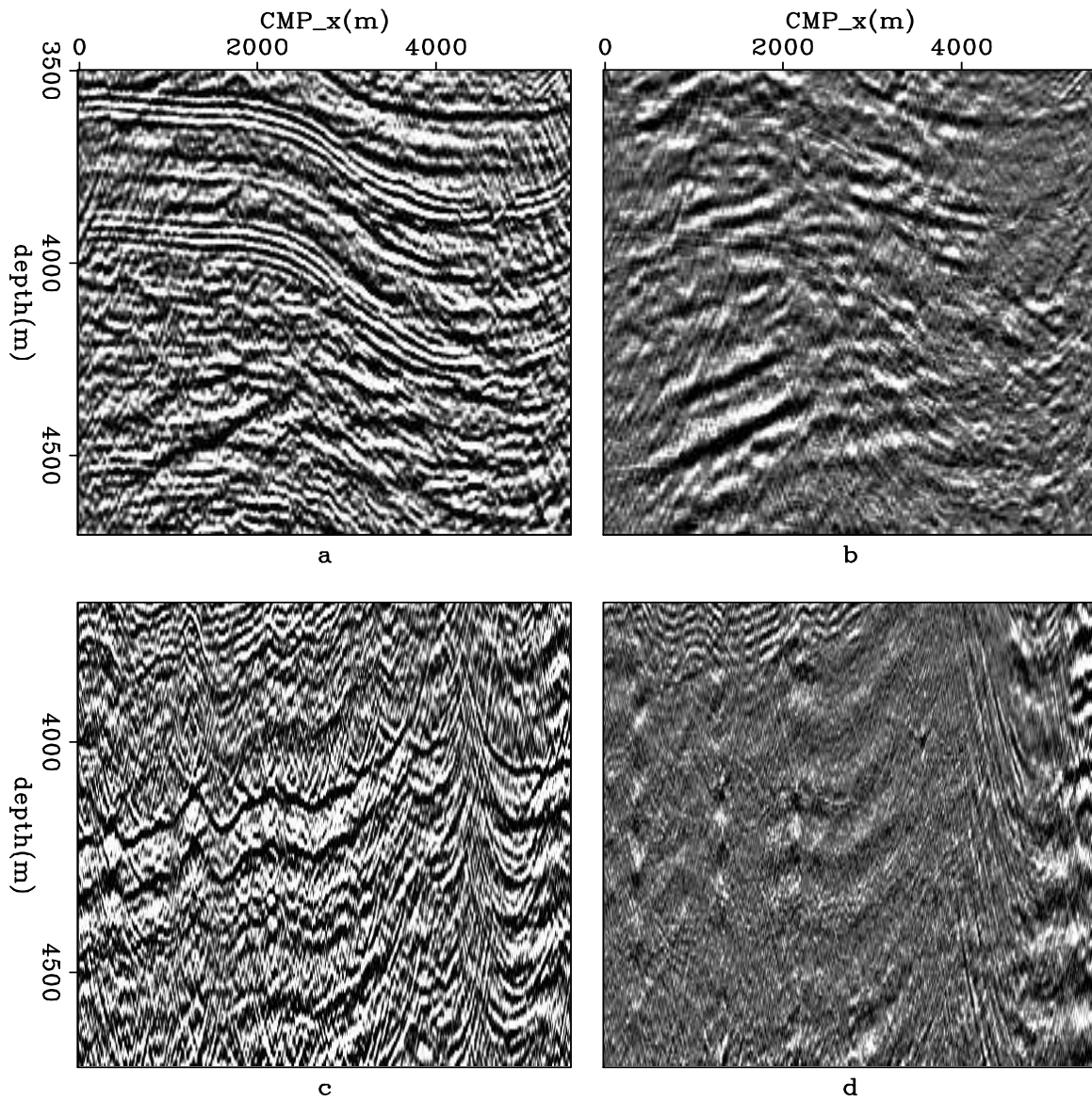


Figure 7: Details of Figures 5 and 6 — zero-angle sections. (a) and (c): multiple-attenuated data. (b) and (d): residual-multiple-attenuated data. [claudio1-zzo](#) [ER]

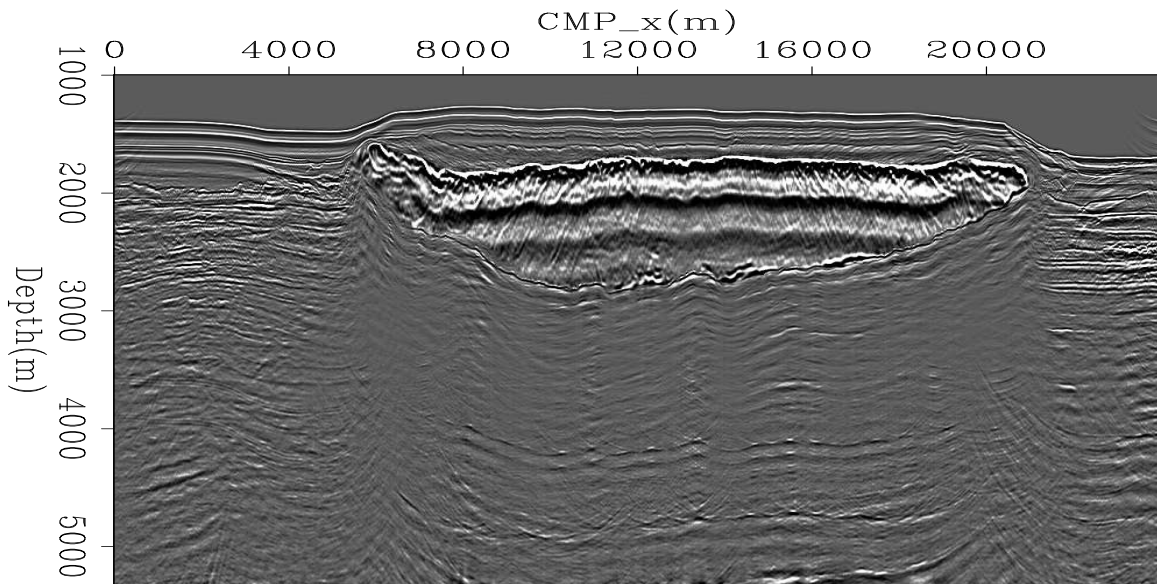


Figure 8: Multiple-attenuated data — stacked data. Residual multiples dominate the deeper portion of the data. [claudio1-orstk](#) [ER]

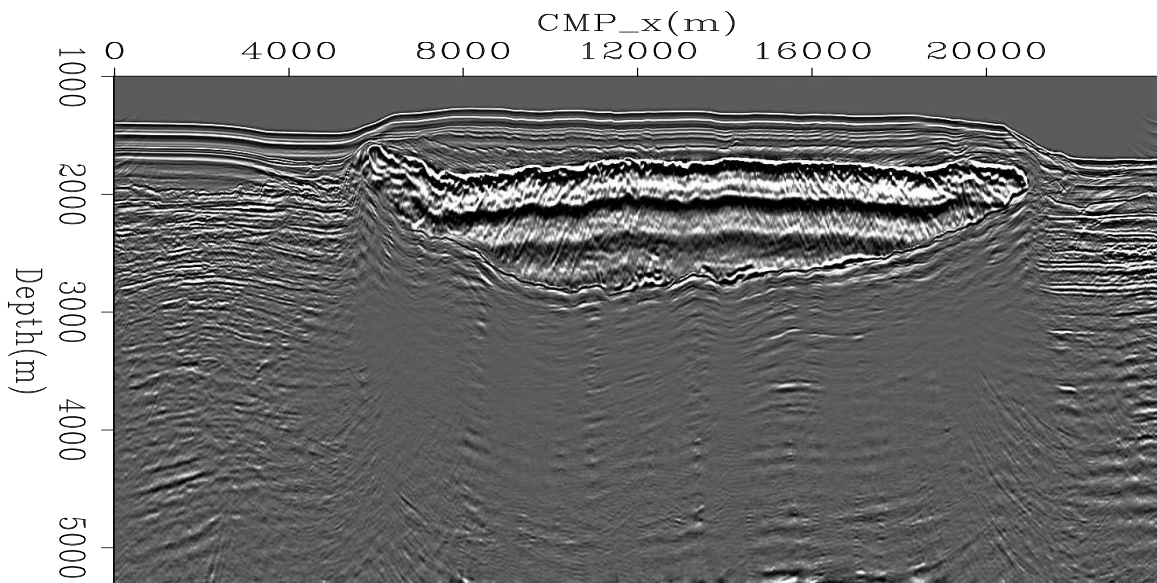


Figure 9: Data after residual-multiple attenuation — stacked data. The final data is much cleaner than the multiple-attenuated data. [claudio1-peststk](#) [ER]

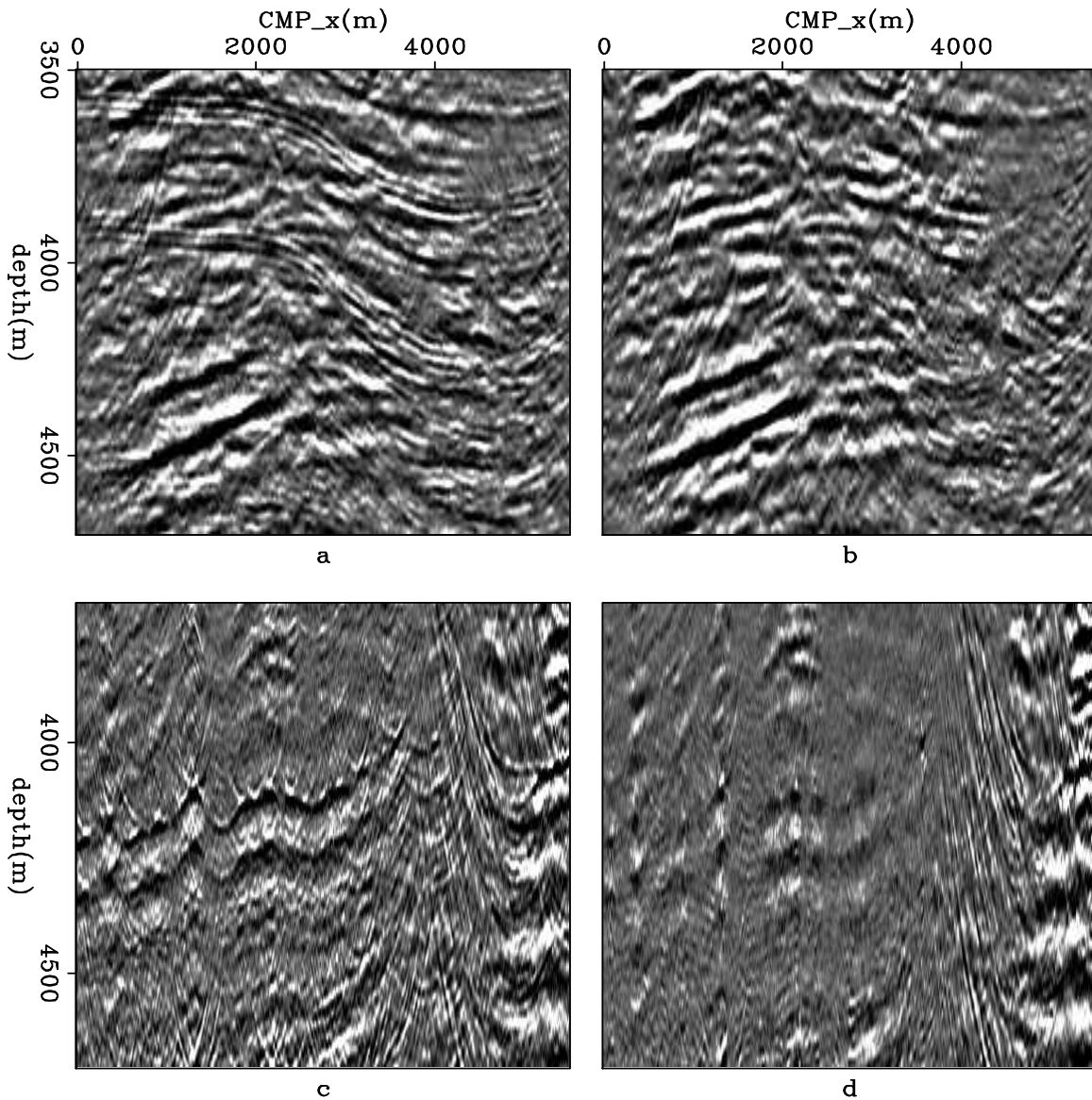


Figure 10: Details of Figures 8 and 9 at the same portion as shown in Figure 7 — stacked data. (a) and (c): multiple-attenuated data. (b) and (d): residual-multiple-attenuated data. Notice persistent multiples in the original data on panels (a) and (c) and how attenuated they are on panels (b) and (d). [claudio1-zstk](#) [ER]

REFERENCES

- Aki, K. and P. Richards, 1980, Quantitative seismology: W.H. Freeman and Co.
- Alvarez, G., B. Biondi, and A. Guitton, 2004, Attenuation of diffracted multiples with an apex-shifted tangent-squared radon transform in image space: *SEP-115*, 139–152.
- Choo, J., J. Downton, and J. Dewar, 2004, Lift: A new and practical approach to noise and multiple attenuation: *First Break*, **22**, no. 5, 39–44.
- Claerbout, J. and S. Fomel, 2001, Image estimation by example: Geophysical soundings image reconstruction: <http://sepwww.stanford.edu/sep/p/rof/gee2.06.pdf>.
- Guitton, A., M. Brown, J. Rickett, and R. Clapp, 2001, A pattern-based technique for ground-roll and multiple attenuation: *SEP-108*, 249–274.
- Hampson, D., 1987, The discrete Radon transform: A new tool for image enhancement and noise suppression: *Soc. of Expl. Geophys., 57th Ann. Internat. Mtg, Soc. Expl. Geophys., Expanded Abstracts, Session:BP3.CSEG*.
- Verschuur, D. J., A. J. Berkhout, and C. P. A. Wapenaar, 1992, Adaptive surface-related multiple elimination: *Geophysics*, **57**, no. 9, 1166–1177.
- Weglein, A. B., 1999, Multiple attenuation: An overview of recent advances and the road ahead: *The Leading Edge*, **18**, no. 1, 40–44.

Short Note

A New Build Environment for SEP

Ben Witten, Bill Curry, and Jeff Shragge

INTRODUCTION

The Stanford Exploration Project (SEP) has been at the forefront of computational reproducible research for many years. Beginning with the introduction of *active* (a-doc) and *interactive* (i-doc) documents by Claerbout (1990), SEP progressed to reproducible scripting using *cake* (Nichols and Cole, 1989) and archiving on CD-ROMS to ensure that entire reports, along with original codes and processing flows, could be distributed easily and cheaply. An additional change occurred around SEP-89 when the more flexible GNU Make software was introduced at SEP (Schwab and Schroeder, 1995). Testing of the reproducible workflows to ensure complete repeatability became common practice by SEP-77 (Prucha et al., 1999).

In the summer 2006, SEP began transitioning from the Make system to SCons (Software Construction), an open-source software construction based on the Python scripting language. The transition was largely inspired by the work of (Fomel and Hennenfent, 2007), who released the RSF/Madagascar package for generating geophysical (and more general processing) work flows. A main goal of this project was harnessing the scripting power of Python into a package for generating and checking the processing flow rules. Using the RSF/Madagascar as a model, SEP adapted and reengineered certain aspects of the package that were not completely tooled for SEP's research, development and computer environment. One of the main goals was to facilitate an easy transition to SCons for all SEP personnel by retaining a lot of the Make functionality. However, due to the use of a different scripting language and reproducibility philosophy, we have included a number of new features reported herein.

INTRODUCTION TO SCONS

Recently, SEP decided to transition from Make to SCons build tool. Part of the motivation for this change was that SCons has numerous advantages over GnuMake:

- Build rules are written in the more flexible Python scripts;
- SConstruct files containing build rules are easy to learn and edit;
- Improved ability to check for dependencies and parameter changes;

- SCons has the functionality to create multiple build environments (e.g. 32 and 64-bit); and
- SCons can execute build rules in parallel.

The adapted RSF package also contains:

- Built-in *pdflatex* software that generates .pdf reports with the up-to-date SEG standard;
- An improved and efficient method for transforming LaTeX documents to html and wiki formats using the modern *latex2html* and *latex2wiki* programs.

We discuss each of these points in the sections below.

Python

Because SCons is written in Python, it has numerous advantages when writing processing flows, such as:

- Users can write their own build rules, tailored to their specific needs;
- Loops, conditions and string substitutions are easily incorporated into the build file; and
- Lists can be used in build rules.

Dependency Checking

SCons uses MD5 signatures to check dependencies rather than timestamps. This improves dependency checking by:

- Ensuring updated build if the MD5 signatures changes, which occurs when any aspect of a file changes; and
- Including the build rules in the dependency check, so changing parameters in the build rule updates the MD5 signature.

COMPILING WITH SCONS

Because SCons is designed for software development, the amount of code written to generate the SEP SCons compiling environment is relatively small. However, in order to remain consistent with the philosophy of automatic generation of build rules for programs that is present in the SEP make environment, some deviation from a standard SCons environment was necessary.

The SEP SCons environment scans through C, Fortran77/90/95, Loptran, and Ratfor77/90 files present in the source directory. The source files are then scanned for files which they depend upon (listed in use or include statements) and build rules are automatically generated for all programs and objects in that directory. As such, no manual writing of compiling rules in the SConstruct is necessary, although the user may opt to and turn off the automatic build rule generation.

The current implementation of the build environment is contained in two files, *SEPDefs.py* and *SEPProg.py*. The first file contains definitions of variables in a build environment that are site-specific, such as the location of the compiler and compile options. The second file contains several subroutine calls that automatically generate the build rules for the code in the source directory.

Current limitations with the scanning of source files mean that there can currently only be one module per file, and the file name must match the name of the module contained in the file. This will change with time, of course.

BUILD RULES

It was important to keep the SCons syntax similar to the Make syntax so that everyone is comfortable using it. We have created rules for different types of files and figures. Below is an example of a Make rule and the same rule in SCons. The Makefile rule is given by,

```
RESDIR=./Fig
%.v: %.H
    <${*.H} Grey >/dev/null gainpanel=a pclip=100 title=${*} out=${@}
${RESDIR}/images.v: image1.v image2.v image3.v
    vp_SideBySideAniso image1.v image2.v image3.v > ${@}
```

We assume all “.H” files are already made. In the Make rule, we have the targets followed by a colon, then the dependencies. The next lines are indented and give the commands. Here we have two rules: one to make “.v” files from “.H” files and a second to combine the .v files into a single figure. The % are used as command line wild cards, \$* call dependencies, such as RESDIR, \$@ is the target. Now look at the same rule in SCons.

```
RESDIR= './Fig'
ResultER(RESDIR+'images.v',[' image 1.H' ,'im age2. H',' image 3.H' ],
'''
    <${SOURCES[0]} Grey >/dev/null gainpanel=a pclip=100 title="image 1" out=image1.v;
    <${SOURCES[1]} Grey >/dev/null gainpanel=a pclip=100 title="image 2" out=image2.v;
    <${SOURCES[2]} Grey >/dev/null gainpanel=a pclip=100 title="image 3" out=image3.v;
    vp_SideBySideAniso image1.v image2.v image3.v > ${TARGET}
''')
```

In the SCons rule, we have combined both of the previous Make rules. In SCons, first you give the target (or list of targets) then the dependency (or list of dependencies) and then the commands. The triple quotes mean that the command is broken up into more than one line. We can replace a string with a variable. In this case, `./Fig` has been replaced by `RESDIR`. Targets and sources can be referred to as `${SOURCES[i]}` or `${TARGETS[i]}` if there are multiple sources or targets, where `i` is the position in the list on the first line. If there is only one source or target they can be called in the build rule as `${SOURCE}` or `${TARGET}`.

In Make there was no way to distinguish between different build objects except with the `RESULTSER/RESULTSCR/RESULTSNR` listed at the top of the Makefile. In SCons we adapted rules from RSF for different objects:

- Flow is used to build intermediate files;
- Plot used to view intermediate figure files; and
- `ResultER`, `ResultCR`, `ResultNR`, which are easily-, conditionally-, and con-reproducible results.

The Result commands are used to create anything that should not be removed when a clean is used. `ResultER` is an easily reproducible result. If there is any change in the rule or the dependency that figure will be rebuilt. `ResultCR` is a conditionally reproducible result that has one of the following properties:

- require large or proprietary data set
- require parallel processing or special software
- or take 20 minutes or more to build

SCons handles a CR result by first checking to see if the file exists. If the file does not exist, then it is created using the provided build rule. If the file does exist, then it checks to make sure there are rules to build all of the dependencies for that file. If so, then nothing is done. If at least one rule to build a dependency is missing then the build aborts and gives an error message to that effect. `ResultNR` serves to let the “tex” portion know there is a figure and as a place to put commands for figures that could be build, but the data has been lost.

CONCLUDING REMARKS

In this paper, we describe the benefits of switching build environments from Make to SCons. We have also shown the basic framework of how SCons works for SEP and how a user can take advantage of SEP’s SCons environment.

REFERENCES

- Claerbout, J. F., 1990, Active documents and reproducible results: SEP-**67**, 139–144.
- Fomel, S. and G. Hennenfent, 2007, Reproducible computational experiments using scon: 32nd IEEE International Conference on Acoustics, Speech, and Signal Processing.
- Nichols, D. and S. Cole, 1989, Device independent software installation with CAKE: SEP-**61**, 341–344.
- Prucha, M. L., R. G. Clapp, et al., 1999, Reproducible research - results from sep-100: SEP-**102**, 249–252.
- Schwab, M. and J. Schroeder, 1995, Reproducible research documents using GNUmake: SEP-**89**, 217–226.

Accelerating subsurface offset gathers for 3D seismic applications using FPGAs

Oliver Pell and Robert G. Clapp

ABSTRACT

For shot profile migration construction of subsurface offset gathers can be the dominant cost. By implementing the subsurface offset gather computation on a MAX-1 accelerator card with a Xilinx Virtex-4 Field Programmable Gate Array (FPGA), we obtain 20x speed-up over a state-of-the-art Opteron system. By reducing data precision further speed-up can be achieved, at minimal image degradation.

INTRODUCTION

Downward continued based migration often provides higher quality migration results. For velocity estimation and lithological determination they require a change in strategy compared to Kirchhoff based approaches. In Kirchhoff based approaches moveout and amplitude information are evaluated as a function of offset. For downward continuation based methods angle gathers are constructed from subsurface offset gathers (de Bruin et al., 1990; Prucha et al., 1999; Biondi and Symes, 2004).

The cost of constructing the subsurface offset gathers is trivial for source-receiver migration methods based on the Double Square Root (DSR) equation (Claerbout, 1985) but can be a dominant cost in shot profile and plane wave methods (Rickett and Sava, 2002). With the increased use of wide azimuth geometries (Michell et al., 2006) and the resulting 3-D angle gathers, over 90% of CPU cycles can be spent in constructing the subsurface offset gathers.

Hardware accelerators are emerging as a powerful solution to computationally intensive problems. A standard desktop PC or cluster node can be augmented with additional hardware dedicated to providing substantially increased performance for particular applications. Research projects have shown (He et al., 2004; Zhang et al., 2005; Cheung et al., 2005; Sano et al., 2007) that FPGA-based hardware accelerators can offer order-of-magnitude greater performance than conventional CPUs, provided the algorithm to be accelerated performs a large number of operations per data point.

Constructing subsurface offset gathers involves a significant number of operations for each data point, making it an ideal candidate for acceleration. We implement subsurface offset gather construction on a FPGA. We show that a 20x speed-up is achievable using 32-bit precision. Further we demonstrate that 40x speed-up can be achieved by using a lower precision

representation of the data, with minimal image degradation.

ANGLE GATHERS FROM SHOT PROFILE MIGRATION

Claerbout (1971, 1985) noted that you could simulate sources and receivers in the subsurface by applying the DSR equation to the wavefield recorded at the surface. For 3-D source-receiver based migration methods a 4-D volume (cmpx,cmpy, hx, hy) is downward continued and the zero-time, zero-offset portion of the volume is the image of the subsurface at that depth. In shot profile migration the source and receiver wavefields are downward continued separately by the Single Square Root (SSR) equation. To obtain an image I at a given depth z and location \mathbf{x} :

$$I(\mathbf{x}, z) = \sum_s \sum_w S(\mathbf{x}, z, \mathbf{w}, s) G^*(\mathbf{x}, z, \mathbf{w}, s), \quad (1)$$

where S is the source wavefield, G is the receiver wavefield, w is the temporal frequency, and s is the shot index.

de Bruin et al. (1990), Prucha et al. (1999) and Biondi and Symes (2004) all provided mechanisms to create reflectivity as a function of angle based on the focusing of the energy around zero-offset. In source-receiver migration, the analysis is naturally done by analyzing the focusing in the \mathbf{h} plane. In shot profile migration \mathbf{h} does naturally occur. Rickett and Sava (2002) explained how to create subsurface offset for shot profile migration by cross-correlating the source and receiver fields by various shifts. As a result subsurface offset volumes can be created by applying:

$$I(\mathbf{h}, \mathbf{x}, z) = \sum_s \sum_w S(\mathbf{x} - \mathbf{h}, z, \mathbf{w}, s) G^*(\mathbf{x} + \mathbf{h}, z, \mathbf{w}, s). \quad (2)$$

The cost of constructing these sub-surface offset gathers can be significant. The cost of downward continuing a single shot a single depth step is dominated by the FFT cost which grows by $(n \log n)$ with the size of the data n . The cost of constructing the subsurface offset gathers is on the order of $nh * n$, where nh is the number of subsurface offsets. Constructing a 2-D subsurface offset gather can be the dominant cost in shot profile migration. To construct a 3-D subsurface offset gather as part of the migration, over 95% of the compute time is common.

STREAMING PROCESSORS

Traditionally, performance increases have come from microprocessor frequency scaling. However, due to power and other constraints, scaling looks to only deliver modest performance improvements in the future. In the future large performance improvements demanded by computationally intensive applications must come from exploiting parallelism. Intel and AMD

are scaling up the number of cores per chip and processors per node in order to higher degrees of Symetric Multi-Processor (SMP). Existing software has to be modified to take advantage of potentially modest speed improvements that remain limited by a machine's memory bandwidth. The change in software presents an opportunity to move beyond conventional processors to custom accelerators. These accelerators offer the potential of much higher performance by delivering parallelism that is tailored to a particular application. In particular, streaming processors offer a route around the "memory wall" by maximising operations performed per data item retrieved from memory. Stream processors can be implemented using Field-Programmable Gate Arrays (FPGAs) and can speed up highly parallel applications by over an order of magnitude. FPGA acceleration has been successfully demonstrated in a variety of application domains including computational finance (Zhang et al., 2005), fluid dynamics (Sano et al., 2007), cryptography (Cheung et al., 2005) and seismic processing (He et al., 2004).

COMPUTING WITH FPGAS

FPGAs are Complementary Metal Oxide Semiconductor's (CMOS) technology based chips containing logic which can be configured to any digital circuit and a limited number of memory elements including RAMs and registers. In fact, FPGAs can be re-configured several times per second, offering a flexible substrate for application specific circuits. The price of reconfigurability is a 10x slower clock frequency compared to today's state-of-the-art Pentium and Opteron processors. Modern FPGAs contain on the order of 10^5 independent logic cells, all of which can operate in parallel. This massive parallelism more than compensates for the 10x reduction in clock frequency versus a state-of-the-art CPU, delivering orders of magnitude more compute power within a reasonable power budget. FPGAs have shown excellent potential as hardware accelerators for a wide class of applications. Compute-intensive algorithms can be mapped directly into parallel FPGA hardware, tightly coupled to a conventional CPU through a high-speed I/O bus, enabling key hotspots in an application to be accelerated by over an order-of-magnitude. The performance potential of FPGAs arises from exploiting *stream processing*. In a typical CPU, instructions are executed sequentially (Figure 1). Despite the high clock frequency, data throughput can be quite limited since there is limited scope for parallelism, even in modern superscalar processors with vector (SIMD) units. For many algorithms a streaming approach (Figure 2) delivers significant benefits. FPGA stream processors operate continuously on streams of data. Data is transferred to the accelerator once, over a high-speed I/O bus such as PCI Express, then it passes from one processing element to the next as it is required for each operation. The FPGA circuit computes one or more results each and every cycle without any of the control overhead associated with CPU conditionals, loops, etc. On-chip memory implements a custom "perfect cache" which retains data on-chip for precisely as long as it is required for the computation. A large number of compute units operating in parallel overcome the compute limitations of the CPU, while the on-chip storage structure and MISD (multiple instruction, single data) operation significantly mitigate the memory limitations of the CPU. Stream processors show potential for accelerating seismic applications operating on large datasets, since only a small fraction of the data needs to be stored on-chip

at any one time. This makes the approach scalable to multi-dimensional problems with tens of gigabytes of data, since the primary storage medium remains CPU main memory. FPGAs are usually regarded as hard to program, with building FPGA accelerators essentially being a matter of hardware design. We develop this accelerator at a higher level of abstraction using the ASC (Mencer, 2006) compiler. ASC, A Stream Compiler for FPGAs, provides a software-like interface to FPGA design based on C++, while retaining the performance of hand-designed circuits. At the top level, ASC code closely resembles C code, allowing a relatively low cost transition from a C-based software implementation to the FPGA hardware implementation. One key difference between ASC and a conventional imperative programming language is that the standard semantics for all operations performed in parallel and all operators are vector operations performed on streams of data. To transfer code to an FPGA accelerator we identify loops to be accelerated, then re-write those loops in ASC code, replacing the original loop with code which transfers data to/from the accelerator. For example, a C loop can describe a vector increment operation as below:

```
int i;
int a[SIZE], b[SIZE];
for (i = 0; i < SIZE; i++)
    b[i] = a[i] + 1;
```

This can be rewritten for FPGA implementation as:

```
STREAM_START;
    HwInt a(IN), b(OUT);
    b = a + 1; // Loop is implicit
STREAM_END;
```

The loop has been replaced with `STREAM_START` and `STREAM_END` declarations, which identify the boundaries of the code to be implemented on the FPGA. The integer arrays *a* and *b* are declared as Hardware Integer type variables, one input and one output. This ASC code can be compiled using GCC producing an executable which, when executed, generates an FPGA circuit.

Figure 1: When computing with a microprocessor, instructions are executed sequentially on data items retrieved from memory.

`bob1-microproc` [NR]

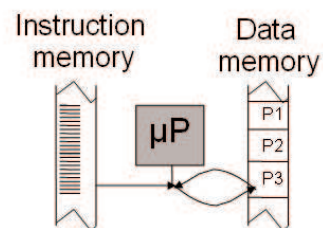
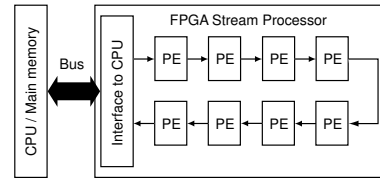


Figure 2: Computing with an FPGA involves “streaming” data through an FPGA which has been configured to implement a function. Here two input arrays are transferred, processed, and a single output array is produced.



`bob1-streaming` [NR]

FPGA ACCELERATION

FPGA’s require that memory is accessed through the processor and transferred to the FPGA. In order to obtain a meaningful speed advantage a large number of operations must be performed for each data point. The density of arithmetic operations per data item is the key to the potential for acceleration. Algorithms which use a transferred data item only once (such as the vector add example above) are unlikely to accelerate, since the overhead of transferring the data across the bus is significant, however algorithms such as an offset gather which use each data item many times will accelerate significantly. Because FPGA accelerators dedicate specific resources to each operation executed, there is a maximum size to the code segment that can be executed on-chip. This depends on not only the size of the FPGA but also the complexity of the operations. Additions and multiplications can be implemented more densely than divisions, square roots and complex functions (*sin*, *cos* etc) so algorithms in which adds and multiplies are dominant will accelerate particularly well. This is common in seismic applications. In contrast to conventional processors, which support a fixed set of data representations (typically integer and IEEE floating point) FPGAs offer the potential for the data representation to be customised to the application. This allows acceleration to be maximised subject to desired accuracy constraints. The dynamic range of migration data is such that floating point representations are not necessary, so our FPGA implementation uses fixed-point data. Fixed point arithmetic can be implemented more densely and with lower latency on FPGAs than floating point, so allowing for increased acceleration without loss of accuracy.

SUBSURFACE OFFSET IMAGING CONDITION ON THE FPGA

The shot profile imaging condition has a high arithmetic density, meeting the requirements for FPGA acceleration. The zero time part of the imaging condition (Equation 2), which requires a summing over all frequencies nf . In addition each input point is going to be used in nh cross-correlations. Despite the high arithmetic density of the offset gather, the arithmetic capabilities of the FPGA are substantially in excess of that required so acceleration is limited by the rate at which data can be streamed across the bus from main memory to the accelerator. In this case, the performance is limited by:

$$\max(nf \times 2, nh) \times bw \quad (3)$$

where bw is the number of bits used to represent each value. This condition arises because the PCI-Express bus is symmetric, providing limited input and output bandwidth. Two arrays (**S** and **G**) containing nf data items per coordinate are sent to the FPGA and one array (**I**) is sent from the FPGA back to the processor, containing nh data items per coordinate. By reducing the number of bits stored for each value from 32 to 16 the performance of the operation can be doubled, with negligible degradation in the output image. The on-chip memory requirement is $O(nf \times nh)$, well within the capabilities of modern FPGAs for hundreds of frequencies and dozens of subsurface offsets. This allows very large datasets to be processed easily with only a small fraction stored on-chip at any one time.

RESULTS

To test the applicability of this approach we compared the result of constructing angle gathers for the 2-D Marmousi synthetic dataset. Figure 3 show the zero-subsurface offset image obtained from implementing the imaging step of shot profile migration on both the processor and the FPGA. The images are indistinguishable.

The left panel of Figure 4 shows an angle gather constructed from the CPU implementation of the imaging condition. The remaining panels show the same angle gather obtained from the FPGA implemented imaging condition with decreasing floating point precision. Note that visually the kinematics are identical.

To test the speed-up offered by the FPGA implementation we ran a larger 3-D problem. Specifically the cost of constructing 41 subsurface offset gathers from 500 inline CMPS, 400 crossline cmnps, 200 frequencies, and 41 subsurface offsets. We compare our FPGA implementation to a 2.8Ghz AMD Opteron-based PC with 12GB of RAM. The software implementation was written in C and compiled using both *gcc* and the Intel C Compiler with full optimization, the average of three runs was selected. The FPGA accelerator was implemented on a Maxeler MAX-1 FPGA platform equipped with a Xilinx Virtex-4 FX100 FPGA. The accelerator circuit consumes 58% of the logic resources of the device and runs at 125Mhz. Table 1 shows the runtimes for the gather operation at a single depth and shot, carried out both in software and on the FPGA. The FPGA computes the gather 19–21 times faster than the software using 32-bit data, or 35–42 times faster than the software using 16-bit data. This degree of acceleration transforms the application space, instead of the subsurface offset gather being dominant the time spent computing it is now insignificant as a portion of the overall runtime.

FUTURE WORK

In the future we plan to implement other portions of the shot profile algorithm on an FPGA. The streaming approach should offer significant speed-up for both applying the SSR equation and the 2-D FFTs.

The same subsurface imaging condition is used in both plane wave and reverse time mi-

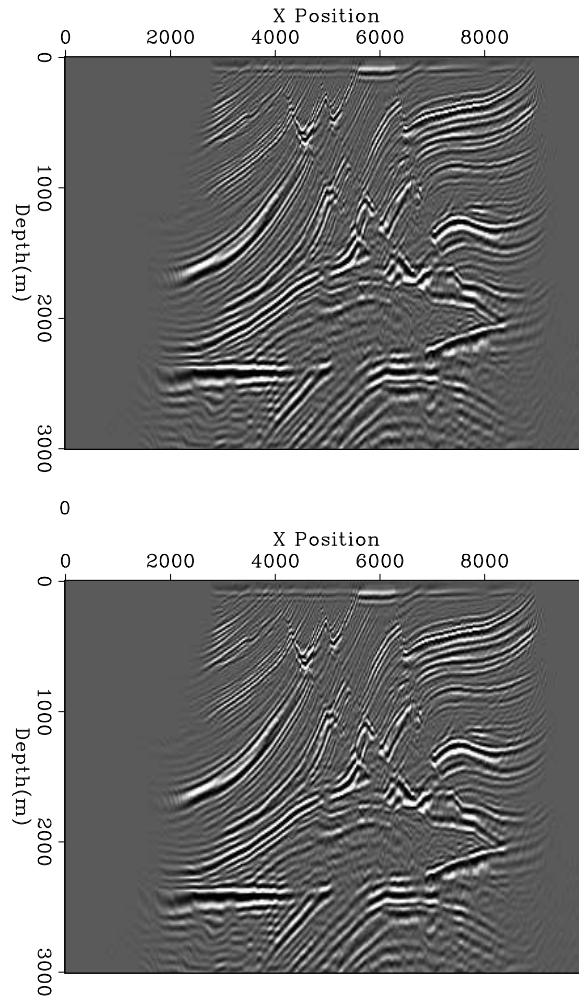


Figure 3: Comparison of the zero-subsurface offset image from implementing the shot profile imaging condition on the processor (top) and the FPGA (bottom). `bob1-mig` [NR]

1

ny	T_{sw}	T_{fpga32}	Speed-up	T_{fpga16}	Speed-up
1	0.041	0.002	21x	0.001	41x
50	1.48	0.073	20x	0.042	35x
100	2.76	0.149	19x	0.075	37x
200	6.40	0.311	21x	0.150	42x

Table 1: Performance comparison of FPGA and 2.8GHz AMD Opteron. T_{sw} is the time in seconds for the software version. T_{fpga32} is the time for the FPGA processing 32-bit data, T_{fpga16} is the time for the FPGA processing 16-bit data. Speed-up is shown for both data sizes.

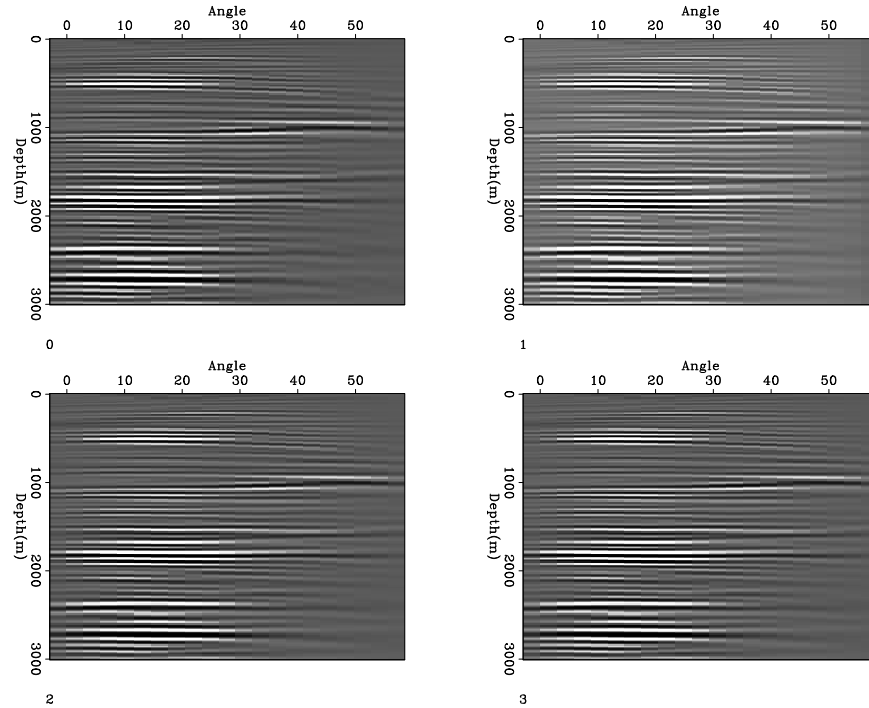


Figure 4: The same angle gather obtained by various implementation of the shot profile imaging condition. The top-left panel shows the result from a CPU based implementation. The remaining panels show various FPGA implementations. Note that they are visually kinematically identical. `bob1-gath` [NR]

gration. Incorporating a FPGA based imaging condition into either would be trivial. Reverse time migration, where the cost of propagating the source and receiver wavefield is order and magnitude more than Fourier based methods, is another exciting opportunity for a FPGA based solution.

CONCLUSION

We implemented the sub-surface offset imaging condition for shot profile migration on a FPGA. We showed that a factor of 40x speed up can be obtained compared to a conventional processor.

ACKNOWLEDGEMENTS

The second author would like to thank the sponsors of the Stanford Exploration Project for financial support.

REFERENCES

- Biondi, B., and Symes, W., 2004, Angle-domain common-image gathers for migration velocity analysis by wavefield-continuation imaging: *Geophysics*, **69**, no. 5, 1283–1298.
- Cheung, R., Telle, N., Luk, W., and Cheung, P., 2005, Customisable elliptic curve cryptosystems: *IEEE Transactions on Very Large Scale Integration Systems*, **13**, no. 9, 1048–1059.
- Claerbout, J. F., 1971, Toward a unified theory of reflector mapping: *Geophysics*, **36**, no. 36, 467–481.
- Claerbout, J. F., 1985, *Imaging the Earth's Interior*: Blackwell Scientific Publications.
- de Bruin, C. G. M., Wapenaar, C. P. A., and Berkhout, A. J., 1990, Angle-dependent reflectivity by means of prestack migration: *Geophysics*, **55**, no. 09, 1223–1234.
- He, C., Lu, M., and Sun, C., 2004, Accelerating seismic migration using FPGA-based coprocessor platform: Accelerating seismic migration using FPGA-based coprocessor platform:, *IEEE Symp. Field Programmable Custom Computing Machines 2004*.
- Mencer, O., 2006, ASC: A stream compiler for computing with FPGAs: *IEEE Transactions on Computer-Aided Design*, **25**, no. 9, 1603–1617.
- Michell, S., Shoshitaishvili, E., Chergotis, D., Sharp, J., and Etgen, J., 2006, Wide azimuth streamer imaging of mad dog; have we solved the subsalt imaging problem?: Wide azimuth streamer imaging of mad dog; have we solved the subsalt imaging problem?., *Soc. of Expl. Geophys.*, 76th Ann. Internat. Mtg., 2905–2909.
- Prucha, M., Biondi, B., and Symes, W., 1999, Angle-domain common image gathers by wave-equation migration: Angle-domain common image gathers by wave-equation migration:, *Soc. of Expl. Geophys.*, 69th Ann. Internat. Mtg, 824–827.
- Rickett, J. E., and Sava, P. C., 2002, Offset and angle-domain common image-point gathers for shot-profile migration: *Geophysics*, **67**, no. 03, 883–889.
- Sano, K., Iizuka, T., and Yamamoto, S., 2007, Systolic architecture for computational fluid dynamics on FPGAs: Systolic architecture for computational fluid dynamics on FPGAs:, *IEEE Symp. Field Programmable Custom Computing Machines 2007*.
- Zhang, G. L., Leong, P. H. W., Ho, C. H., Tsoi, K. H., Cheung, C. C. C., Lee, D.-U., Cheung, R. C. C., and Luk, W., 2005, Reconfigurable acceleration for monte carlo based financial simulation: Reconfigurable acceleration for monte carlo based financial simulation:, *IEEE Intl. Conf. Field Programmable Technology 2005*.

SEP ARTICLES PUBLISHED OR IN PRESS

- Artman, B., G. Alvarez, and K. Matson, 2007, Image-space surface-related multiple prediction: *Geophysics*, **72**, S113–S122.
- Artman, B., 2006, Imaging passive seismic data: *Geophysics*, **71**, SI177–SI187.
- Bevc, D. and B. Biondi, 2005, Which depth imaging method should you use? A road map through the maze of possibilities: *The Leading Edge*, **24**, 602–606.
- Biondi, B. and D. Bevc, 2005, Seismic imaging of complex structures by reflection seismic data *in* Levander, A. and G. Nolet, Eds., *Data Analysis and Imaging with Global and Local Arrays*: American Geophysical Union, in press, 137–148.
- Biondi, B., 2006a, Prestack exploding-reflectors modeling for migration velocity analysis: 76th Ann. Internat. Mtg., Soc. of Expl. Geophys., Expanded Abstracts, SVIP 1.5.
- Biondi, B. L., 2006b, 3D Seismic Imaging: Society of Exploration Geophysicists.
- Biondi, B. L., 2006c, Concepts and Applications in 3D Seismic imaging: Society of Exploration Geophysicists, in press.
- Biondi, B., 2007a, Angle-domain common image gathers from anisotropic migration: *Geophysics*, **72**, S81–S91.
- Biondi, B., 2007b, Residual moveout in anisotropic angle-domain common-image gathers: *Geophysics*, **72**, S93–S103.
- Brown, M. P. and A. Guitton, 2005, Least-squares joint imaging of multiples and primaries: *Geophysics*, **70**, S79–S89.
- Clapp, R. G., 2006, Amo inversion to a common azimuth dataset: 76th Ann. Internat. Mtg., Soc. of Expl. Geophys., Expanded Abstracts, SI 3.4.
- Gray, S., D. Trad, B. Biondi, and L. Lines, 2006, Towards wave-equation imaging and velocity estimation: *Recorder*, **31**, 47–53.
- Guitton, A., B. Kaelin, and B. Biondi, 2006, Least-square attenuation of reverse time migration artifacts: 76th Ann. Internat. Mtg., Soc. of Expl. Geophys., Expanded Abstracts, 2348–2352.
- Guitton, A., B. Kaelin, and B. Biondi, 2007, Least-squares attenuation of reverse-time-migration artifacts: *Geophysics*, **72**, G19–G23.
- Guitton, A., 2005, Multiple attenuation in complex geology with a pattern-based approach: *Geophysics*, **70**, V97–V107.
- Haines, S., A. Guitton, and B. Biondi, 2007a, Seismoelectric data processing for surface surveys of shallow targets: *Geophysics*, **72**, G1–G8.

- Haines, S., S. Pride, S. Klemperer, and B. Biondi, 2007b, Seismoelectric imaging of shallow targets: *Geophysics*, **72**, G9–G20.
- Jousselin, P. and B. Biondi, 2006, Residual moveout in anisotropic angle-domain common-image gathers with dipping reflectors: 76th Ann. Internat. Mtg., Soc. of Expl. Geophys., Expanded Abstracts, 224–228.
- Lomask, J. and A. Guitton, 2006, Flattening with geological constraints: 76th Ann. Internat. Mtg., Soc. of Expl. Geophys., Expanded Abstracts, INT 3.2.
- Lomask, J., R. G. Clapp, and B. Biondi, 2007, Application of image segmentation to tracking 3d salt boundaries: *Geophysics*, in press.
- Rosales, D. and B. Biondi, 2006, Converted-wave azimuth moveout: *Geophysics*, **71**, pp. S99–S110.
- Rosales, D. A., S. Fomel, and B. Biondi, 2007, Angle-domain common-image gathers for converted-wave: *Geophysics*, in press.
- Sava, P. and A. Guitton, 2005, Multiple attenuation in the image space: *Geophysics*, **70**, V10–V20.
- Sava, P., B. Biondi, and J. Etgen, 2005, Diffraction-focusing migration velocity analysis with application to seismic and GPR data: *Geophysics*, **70**, U19–27.
- Shan, G. and B. Biondi, 2006, Imaging steep salt flank with plane-wave migration in tilted coordinates: 76th Ann. Internat. Mtg., Soc. of Expl. Geophys., Expanded Abstracts, SPMI 2.3.
- Shan, G., 2006, Optimized implicit finite-difference migration for vti media: 76th Ann. Internat. Mtg., Soc. of Expl. Geophys., Expanded Abstracts, SPMI 2.2.
- Shragge, J., 2006a, Differential mesh generation: 76th Ann. Internat. Mtg., Soc. of Expl. Geophys., Expanded Abstracts, SM 2.1.
- Shragge, J., 2006b, Non-orthogonal Riemannian wavefield extrapolation: 76th Ann. Internat. Mtg., Soc. of Expl. Geophys., Expanded Abstracts, SM 2.7.
- Shragge, J., 2007, Waveform inversion by one-way wavefield extrapolation: *Geophysics*, in press.
- Tang, Y. and R. G. Clapp, 2006, Selection of reference-anisotropy parameters for wavefield extrapolation by Lloyd's algorithm: 76th Ann. Internat. Mtg., Soc. of Expl. Geophys., Expanded Abstracts, ANI 2.7.
- Witten, B. and J. Shragge, 2006, Quaternion-based signal processing: 76th Ann. Internat. Mtg., Soc. of Expl. Geophys., Expanded Abstracts, SPNA 3.8.

SEP PHONE DIRECTORY

Name	Phone	Login Name
Alvarez, Gabriel	723-1250	gabriel
Ayeni, Gboyega	723-3187	gayeni
Berryman, James	–	berryman
Biondi, Biondo	723-1319	biondo
Cardoso, Claudio	723-3187	claudio
Claerbout, Jon	723-3717	jon
Clapp, Bob	725-1334	bob
Curry, Bill	723-6006	bill
De Zan, Francesco	723-9282	francesco
Guitton, Antoine	–	antoine
Gunther, Roland	725-5462	rgunther
Jousselin, Pierre	723-1250	pierre
Lau, Diane	723-1703	diane
Shan, Guojian	723-0463	shan
Shragge, Jeff	723-0463	jeff
Tang, Yaxun	723-1250	tang
Valenciano, Alejandro	723-9282	valencia
Vyas, Madhav	723-0463	madhav
Witten, Ben	723-6006	ben

SEP fax number: (650) 723-0683

E-MAIL

Our Internet address is “*sep.stanford.edu*”; i.e., send Jon electronic mail with the address “*jon@sep.stanford.edu*”.

WORLD-WIDE WEB SERVER INFORMATION

Sponsors who have provided us with their domain names are not prompted for a password when they access from work. If you are a sponsor, and would like to access our restricted area away from work, visit our website and attempt to download the material. You will then fill out a form, and we will send the username/password to your e-mail address at a sponsor company.

STEERING COMMITTEE MEMBERS, 2006-2007

Name	Company	Telephone	E-Mail
Raymond Abma	BP	(281) 366-4604	abmar1@bp.com
Dimitri Bevc	3DGeo	(408) 450-7840	dimitri@3dgeo.com
Biondo Biondi	SEP	(650) 723-1319	biondo@sep.stanford.edu
Henri Calandra (Co-chair, 2nd year)	Total E&P USA	(713) 647-394x	henri.calandra@total.com
Luis L. Canales	WesternGeco	(713) 806-5271	lcanales@houston.westerngeco.slb.com
Jon Claerbout	SEP	(650) 723-3717	jon@sep.stanford.edu
Richard Cook	Shell	(713) 245-7195	richard.cook@shell.com
Helmut Jakubowicz	CGGVeritas	+44 1293 443219	helmut_jakubowicz@veritasdgc.com
Stewart A. Levin (Co-chair, 1st year)	Landmark Graphics	(303) 488-3062	salevin@lgc.com

Print - from: pdx to: 3400 S Hemlock St, Tolovana Park, OR 97145 - Go... <http://maps.google.com/maps?f=d&hl=en&saddr=pdx&daddr=3400+S...>



Start **PDX - Portland Intl Airport**
Portland, OR 97218
 End **3400 S Hemlock St**
Tolovana Park, OR 97145
 Travel **92.5 mi (about 2 hours 17 mins)**

Directions

1. Head southeast	470 ft
2. Continue on NE Airport Way	2.1 mi 4 mins
3. Take the I-205 S ramp to Portland (I-84)/Salem	3.1 mi 4 mins
4. Take the I-84 W exit 21B to Portland	5.4 mi 6 mins
5. Take the I-5 S ramp to Salem/Beaverton	1.5 mi 2 mins
6. Take the I-405 ramp to City Center/Beaverton (US-26)	0.3 mi
7. Merge into I-405 N	0.6 mi 1 min
8. Take the US-26 W exit 1D to Beaverton	74 mi 1 hour 32 mins
...	
➔ 9. Bear right onto the US-101 S ramp to Cannon Beach/Tillamook	495 ft
➔ 10. Bear right at US-101	3.1 mi 3 mins
11. Continue on Oregon Coast Hwy	1.3 mi 1 min
12. Continue on US-101	0.8 mi 1 min
➔ 13. Bear right onto the ramp	0.1 mi
➔ 14. Bear right onto the E Warren Way ramp	92 ft
➔ 15. Turn right at E Warren Way	115 ft
⬅ 16. Turn left at S Hemlock St	36 ft
17. Arrive at 3400 S Hemlock St Tolovana Park, OR 97145	

Overview



Start



End



Map data ©2006 NAVTEQ™

Research Personnel

Gabriel Alvarez received a B.S. degree in Physics from the National University of Colombia in 1985 and an M.Sc. in Geophysics from the Colorado School of Mines in 1995, where he was a member of the Center for Wave Phenomena. From 1989 to 2000, he worked at the Instituto Colombiano del Petroleo (ICP), the Research and Development Division of Ecopetrol, the National Oil Company of Colombia. Joined SEP in 2000, and is currently working towards a Ph.D. in geophysics at Stanford University.



Gboyega Ayeni received his B.Sc. in Applied Geophysics from Obafemi Awolowo University, Nigeria in 2004. He was a Shell scholar at University of Leeds, where he obtained an M.Sc with Distinction in Exploration Geophysics. Gboyega joined SEP in September 2006 to work towards his Ph.D in Geophysics. He is a member of SEG, EAGE, AGU and AAPG.



James G. Berryman received a B.S. degree in physics from Kansas University (Lawrence) in 1969 and a Ph.D. degree in physics from the University of Wisconsin (Madison) in 1975. He subsequently worked on seismic prospecting at Conoco. His later research concentrated on seismic waves in rocks and sediments – at AT&T Bell Laboratories (1978-81) and at Lawrence Livermore National Laboratory (1981-), where he is currently a physicist in the Energy and Environment Directorate. He received the Maurice Anthony Biot Medal of the ASCE in May, 2005, for his work in the mechanics and acoustics of porous media containing fluids. Continuing research interests include acoustic, seismic, and electrical methods of geophysical imaging and studies of waves in porous media. He is a member of APS, AGU, ASA, and SEG.



Biondo L. Biondi graduated from Politecnico di Milano in 1984 and received an M.S. (1988) and a Ph.D. (1990) in geophysics from Stanford. SEG Outstanding Paper award 1994. During 1987, he worked as a Research Geophysicist for TOTAL, Compagnie Française des Pétroles in Paris. After his Ph.D. at Stanford, Biondo worked for three years with Thinking Machines Co. on the applications of massively parallel computers to seismic processing. After leaving Thinking Machines, Biondo started 3DGeo Development, a software and service company devoted to high-end seismic imaging. Biondo is now Associate Professor of Geophysics and leads SEP efforts in 3-D imaging. He is a member of SEG and EAGE.



Robert Clapp received his B.Sc. (Hons.) in Geophysical Engineering from Colorado School of Mines in May 1993. He joined SEP in September 1993, received his Masters in June 1995, and his Ph.D. in December 2000. He is a member of the SEG and AGU.



William Curry graduated in 2000 from the University of Alberta with a B.Sc. (Hons.) in Geophysics, and received his M.S. from SEP in 2002. From 1998-1999, he worked as a seismic interpreter with Jet Energy Corporation in Calgary, Canada. During the summer of 2002 he interned with Marathon Oil in Houston, in 2005 he interned with ExxonMobil Exploration Co., and in 2006 interned with 3DGeo Development. Bill is a student member of the EAGE, IEEE, SEG, and SIAM.



John Etgen works for BP in Houston. He spends his time taking good ideas from SEP (and a few other places), coding them up, and processing huge surveys with them. He finally learned to love the 45 degree equation just last year.



Roland Günther received his B.Sc. in physics with a minor in computer science from Stanford University in 2004. Subsequently, he worked at Landmark Graphics, Inc. in Denver, CO, focusing on the development of ProMAX and SeisSpace. He joined SEP in 2006 to pursue a Ph.D. in geophysics.



Claudio Guerra received his B.Sc. in Geology from Federal University of Rio de Janeiro, Brazil in 1988 and a M.Sc. from State University of Campinas, Brazil in 1999. Since 1989, he has been working for Petrobras, Brazil. He joined SEP in 2006 and is currently pursuing a Ph.D. in geophysics at Stanford University. He is member of SEG and SBGf.



Pierre Jouselin received his M.Sc. in General Engineering with distinction from the Ecole Nationale Supérieure des Mines de Paris in July 2005. During his studies, Pierre had a one year professional experience in London and worked as an intern in different areas of research in applied mathematics (Financial mathematics for Ca-lyon, Seismic imaging for WesternGeco and Geostatistics for the French National Statistics Institute). In September 2006, TOTAL sponsored him to join SEP. He is currently pursuing a M.Sc. in geophysics at Stanford University. He is a member of SEG.



Guojian Shan received his B.Sc. in Mathematics School of Peking University in July, 1998. From 1998 to 2001, he studied in Institute of Computational Mathematics and Scientific/Engineering Computing, Chinese Academy of Sciences (CAS), and received his M.S. in Applied Mathematics in July, 2001. He joined SEP in 2001 and is currently working towards a Ph.D. in geophysics. He is a member of the SEG.



Jeff Shragge graduated in 1998 with a BScH in Honours Physics from Queen's University in Kingston, Canada. After completing a MSc degree in 2001 in teleseismic imaging at the UBC in Vancouver, Canada, he spent 2001 and 2002 working for a small geophysical consulting company based out of Woburn, MA. He joined SEP in 2002, and is working towards a Ph.D. in Geophysics. His main research interest is migration and wavefield inversion. He is a member of SEG and AGU.



Yaxun Tang received his B.Sc. (Jul. 2003) and M.Sc. (Aug. 2005) in Geophysics from School of Ocean and Earth Science, Tongji University, Shanghai. He joined SEP in 2005 and is currently working towards a Ph.D. in Geophysics at Stanford University. He is a member of SEG.



Alejandro A. Valenciano received a B.Sc. degree in Physics from Havana University (Cuba) in 1994, and a M.Sc. in Physics from Simon Bolivar University (Venezuela) in 1998. He worked in the Earth Science Department of PDVSA-INTEVEP from 1995 to 2001. He joined SEP to work towards a Ph.D in geophysics in the Fall of 2001.



Madhav Vyas received a B.S and M.S in Exploration Geophysics from Indian Institute of Technology, Kharagpur, India in 2005. He interned with Geological Survey of India in 2002 and Reliance Industries Ltd., Exploration and Production Division in 2004. He joined SEP in 2005 and is currently pursuing a Masters in Geophysics at Stanford University.



Ben Witten received his B.S. in Applied Mathematics from Columbia University in May 2005. Ben worked as a research assistant at the University of Oklahoma, School of Geology and Geophysics, during the summers of 2002-2004. He joined SEP in 2005 and is currently pursuing a Ph.D. in geophysics at Stanford University.

